UC Berkeley
UC Berkeley Electronic Theses and Dissertations

Title

Molecular and Cellular Mechanisms of Acute and Viral Nociception

Permalink

https://escholarship.org/uc/item/0hs6b76c

ISBN

9798288866319

Author

Mali, Sonali S

Publication Date

2025-05-15

Peer reviewed|Thesis/dissertation

eScholarship.org Powered by the California Digital Library
University of California

Molecular and Cellular Mechanisms of Acute and Viral Nociception

By

Sonali S. Mali

A dissertation submitted in partial satisfaction of the

requirements for the degree of

Doctor of Philosophy

in

Neuroscience

in the

Graduate Division

of the

University of California, Berkeley

Committee in charge:

Professor Diana M. Bautista, Chair
Professor Marla B. Feller
Professor Ellen A. Lumpkin
Professor Sarah A. Stanley

Spring 2025

Abstract

Molecular and Cellular Mechanisms of Acute and Viral Nociception

by

Sonali S. Mali

Doctor of Philosophy in Neuroscience

University of California, Berkeley

Professor Diana M. Bautista, Chair

Nociceptors are specialized sensory neurons that detect harmful or potentially harmful stimuli and trigger protective responses such as pain, sneezing, and coughing. These neurons densely innervate the epithelia of barrier tissues like the skin and airway, where they convert environmental threats, such as mechanical force, noxious temperatures, chemical irritants, and pathogens, into neural signals that drive rapid reflexes and coordinated physiological defenses. During my PhD, I investigated the mechanisms by which epithelial and neuronal cells coordinate to detect mechanical force and pathogens, initiate defense responses, and how viruses such as SARS-CoV-2 exploit these systems to drive symptoms and potentially enhance transmission.

In Chapter I, I review the molecules, cells, and circuits that mediate nociception and their emerging roles in acute airway defense, allergic inflammation, and respiratory infection. In Chapter II, I use the *Drosophila melanogaster* larvae as a model to demonstrate that epidermal cells are not passive bystanders but active mechanosensors; these cells respond to mechanical force via the store-operated calcium signaling molecules Stim and Orai, and their activation is sufficient to drive nociceptor activity, escape behavior, and mechanical hypersensitivity. These findings highlight an evolutionarily conserved role for epithelial cells as modulators of nociceptive signaling.

Next, I investigate how SARS-CoV-2, the virus responsible for COVID-19, can perturb nociceptor function through two distinct mechanisms. In Chapter III, I focus on the papain-like protease (PLpro), a viral protein essential for SARS-CoV-2 replication and immune evasion, that is released by infected epithelial cells. I demonstrate that PLpro can directly activate mouse airway-innervating and human stem cell-derived nociceptors and trigger rapid sneezing, coughing, and pain-like behaviors in mice. These studies revealed that PLpro acts through the host ion channel TRPA1, a key transducer of noxious stimuli, to initiate these reflexive behaviors. Moreover, SARS-CoV-2 infection of sensory neurons induces transcriptional changes that selectively impact nociception, upregulating the same TRPA1-CGRP signaling axis directly activated by PLpro. This work defines a novel molecular mechanism by which a respiratory virus can hijack host sensory neurons to drive disease symptoms and potentially facilitate its transmission.

In Chapter IV, I characterize a second SARS-CoV-2 protein, ORF3a, as a calcium-permeable, nonselective cation channel using structural, electrophysiological, and imaging approaches. ORF3a exhibits biophysical properties reminiscent of nociceptive ion channels such as TRPV1, P2X7, and OSCA, making it poised to alter host cell physiology such that it can modulate neuronal excitability and immunity. Taken together, these studies reveal new molecular and cellular mechanisms by which epithelial and neuronal cells detect environmental and viral stimuli to initiate protective responses.

Acknowledgements

I often feel like a very small person inside a very large trench coat, standing on the shoulders of many. As such, this dissertation is a collective accomplishment of everyone who has guided, supported, and inspired me along the way. But for me, this community is the most meaningful achievement of all.

I cannot imagine becoming the scientist I am today without the support of my advisor, Diana Bautista. I am deeply grateful to have been seen as a whole human, and to have been given the freedom, and the patience, to follow my curiosities in all their depth and divergence. And most of all, I am grateful for your unrelenting belief in me, that, in turn, taught me to believe in myself. I owe much of my scientific development to my time at the Marine Biological Laboratory in Woods Hole, particularly because I was fortunate to work with Takeshi Morita, Yalda Moayedi, Jay Parrish, Ellen Lumpkin, and Diana. They showed me the kind of scientist I aspire to be: creative, rigorous, and deeply committed to their students, and through them, to the future of science.

In the many years of grad school, doing science never lost its fun. And for that, I'm grateful to the many wonderful scientists I had the opportunity to collaborate with and learn from. Thank you to Cliff Vuong for being a sounding board for experiments, inspiring clever solutions (and excuses to superglue), and for taking down metaphorical and literal doors to make science happen. I am grateful for Zhongyan Gong –my baymate, secret project co-conspirator, and friend– whose brilliant mind I've been lucky to pick again and again. I am also grateful to Ricardo Silva and Alexander Flamm for trusting me as a mentor and for approaching science with infectious (pun absolutely intended) energy and enthusiasm. Ricky and Alex's relentless efforts led to the key discoveries of the roles of PLpro, and working with them taught me how deeply fulfilling it can be to ask hard questions together. And to Lara Ocumen, Ifechukwu Okeke, Uyen Vo, Michael Hsiao, Christopher Cook, Abigail Mende, and Odilia Liu –thank you for letting me learn alongside you and for challenging me to become a better scientist in the process. And lastly, thanks to my thesis committee, Marla Feller, Sarah Stanley, and Ellen, whose thoughtful guidance and incisive feedback strengthened my project at a critical juncture.

I feel wildly (in the fullest sense of the word) lucky to have Julia Bleier and Vinson Fan as my adventure pals, up the summit of mountains and through mountains of injustice. And to MKP, Chloe McCollum, Danielle Spitzer, Vivian Tran, Justin Zhong, Joyner Cruz, Lisa Strong, and my east bay (and beyond) Strava friends– thank you for joining me on bike, on foot, and in the water, for some of the best parts of grad school. And thank you Erin Aisenberg, Kamran Ahmed, and Julia for making HT a place that was always safe and full of laughter.

Thank you to San Francisco mandal (and especially Hina Dave) for filling my stomach and my soul, and the SF kishoris, Shreya Suthar, Leah Patel, Aagna Modi, Vidita Bhatt, Diya Patel, Anjali Dave, and Prayosha Daraji, for your endless kindness and encouragement. To Michelle Reid and Deena Patel– thank you for being there through

the highest and lowest parts of this journey. Your friendships are empowering and liberating, and, for that reason, an act of revolution. I am also grateful to Naomi Latorraca, Rose Hill, Holly Gildea, Krisha Aghi, and Christine Liu, whose support and solidarity remind me that I, too, belong in science.

It still comes as a surprise to me that I chose to pursue science, but I am grateful to Rajesh Sardar and Andrea Hohmann, who generously gave this teenager a place in their labs and have aspired on my behalf ever since.

I am grateful to my grandparents, Sudha and Rasik Mali, and my dad, Sunil Mali, whose courage and resilience as immigrants in this country paved the way for this life of opportunity.

Vishaal Mali, thank you for always having my back, for pushing me to aim higher, and for keeping me grounded, as only a little brother can. Vishaal, I am so proud of you.

In hindsight, it should be no surprise that I fell in love with science. Mom (Vibhuti Mali, not the Movable Objective Microscope), thank you for nurturing a curiosity about the world around us and within us, and for instilling a deep commitment to making both better. I would not be here without your courage to imagine and advocate for a world more just, more curious, and more possible than the one you were given.

And, Madhu Tanna, *Ba*, from whom anything and everything that is good in me comes. I dedicate this thesis to you, in honor of your enduring love and sacrifice.

Table of Contents

Chapter I: Molecules, Cells, and Circuits of Nociception in Airway Defense and Disease

Principles of Somatosensory Signaling Across Species 1
The Structural and Functional Organization of Airway Nociceptors 3
Roles for Airway Nociceptors in Allergy and Asthma 8
Roles for Airway Nociceptors in Respiratory Infection 10

Chapter II: Drosophila Epidermal Cells Are Intrinsically Mechanosensitive and Modulate Nociceptive Behavioral Outputs

Summary & Introduction 15
Results 16
Discussion 50
Methods 52

Chapter III: SARS-Cov-2 Papain-Like Protease Activates Nociceptors to Drive Sneeze, Cough, and Pain

Summary & Introduction 68
Results 69
Discussion 91
Methods 92

Chapter IV: Cryo-EM Structure of SARS-Cov-2 ORF3a in Lipid Nanodiscs

Summary & Introduction 98
Results 100
Discussion 123
Methods 124

Conclusion 132

References 134

Appendix 151

Chapter I: Molecules, Cells, and Circuits of Nociceptors in Airway Defense and Disease

We must be able to breathe, a process necessary for sustaining life and maintaining homeostasis. However, the airways are continually exposed to environmental insults, making rapid defensive responses, such as coughing, sneezing, and gasping, critical for survival. To protect against such threats, organisms have evolved highly conserved protective mechanisms that can quickly detect and respond to harmful stimuli. Nociceptors, the sensory neurons responsible for recognizing harmful or potentially harmful stimuli, initiates these protective reflexes. Derived from the Latin word *"nocere,"* meaning "to harm," nociception encompasses diverse molecular and cellular pathways that detect a wide array of insults, including mechanical forces, noxious temperatures, chemical irritants, toxins, and biological threats like pathogens and inflammatory mediators.

Airway nociceptors express a diverse array of receptors, including ion channels, G-protein-coupled receptors (GPCRs), and cytokine receptors, that allow them to detect mechanical, thermal, chemical, and inflammatory signals. Activation of these receptors alters the membrane potential of the neuron, initiating the process of **sensory transduction**, where external stimuli are converted into electrical signals. This change in the membrane potential generates action potentials that relay information to the central nervous system, allowing for rapid detection and response to environmental threats. By converting environmental stimuli into neural signals, these sensory neurons serve as a key interface between the airways and the brain. These specialized neurons orchestrate rapid protective responses ranging from nearly instantaneous reflexive behaviors to coordinated physiological adaptations to promote airway homeostasis in the face of a dynamic environment. Advances in mouse genetics, single-cell RNA sequencing, and neural circuit tracing tools have driven a surge of new studies uncovering the cells and circuits that mediate airway physiology. Here, I will provide an overview of our current understanding of the cells, molecules, and circuits that mediate airway nociception across diverse physiological and pathological contexts.

Principles of Somatosensory Signaling Across Species

Nociception is broadly conserved across diverse animal taxa, and nociceptors drive a variety of protective behaviors. Studies from classical model organisms such as worms (*Caenorhabditis elegans*), fruit flies (*Drosophila melanogaster*), and rodents including mice (*Mus musculus*) and guinea pigs (*Cavia porcellus*) have provided foundational insights into the cells and molecules that mediate nociception[1–3]. Despite differences in anatomy and behavior, studies across these species reveal conserved cells and molecules of nociceptive signaling.

Nociception is an Evolutionarily Conserved Protective System

In Drosophila larvae, somatosensory neurons are organized into four classes of multidendritic (md) neurons, Class I through Class IV, based on their dendritic complexity and function. The cell bodies of these neurons are arranged in a stereotyped

pattern along the body wall, with their dendrites arborizing beneath the epidermis and their axons projecting to the ventral nerve cord to drive specific motor outputs in response to sensory cues. Class I neurons are involved in proprioception, Class II and III neurons detect gentle touch and innocuous temperatures, Class III noxious cold, and Class IV neurons respond to harsh mechanical, thermal, and noxious stimuli[4]. *Drosophila* larvae display a rapid rolling escape response when attacked by parasitic wasps, a behavior triggered by polymodal nociceptors, specifically Class IV neurons.[5–7]. Activation of these neurons is sufficient to drive escape behavior, making this model a powerful tool for identifying key molecular transducers of nociception, such as *painless*[8] and *trpa1*[9,10], members of the transient receptor potential (TRP) channel family. *Drosophilae* continue to serve as a valuable model for studying nociceptor development, sensitization, and neural circuitry, providing insights that may be conserved across animal nociception. Similarly, mammalian nociceptors are generally polymodal, like *Drosophila* larval Class IV neurons. However, mammalian somatosensory neurons are pseudounipolar, with cell bodies located in the dorsal root ganglia; they likewise project centrally to terminate in the spinal cord, functionally analogous to the ventral nerve cord, to drive motor responses. Interestingly, in both *Drosophila* larvae and mammals, the role of neurons that detect innocuous touch in modulating nociceptive responses, whether through gating or facilitation, remains incompletely understood[11–14].

While *Drosophila* and mice have offered powerful genetic tools for dissecting nociceptive circuits, guinea pigs have historically played a key role in studying airway physiology. Foundational electrophysiological studies in guinea pigs have significantly advanced our understanding of airway-innervating neurons[15,16]. Studies from guinea pigs have elucidated the role for two key sensory transduction channels, transient receptor potential vanilloid 1 (TRPV1) and transient receptor potential ankyrin 1 (TRPA1) as critical detectors of noxious stimuli that mediate cough reflexes[17–19]. Because the occurrence and identification of cough and sneeze responses in mice has been controversial, researchers have traditionally relied on guinea pigs, whose respiratory anatomy and physiology more closely resembles that of humans. Nonetheless, the power of mouse genetics has driven concerted efforts to improving methods for measuring respiratory and airway reflexes in mice[20–26]. These advancements have paved the way for identifying the cells and circuits that regulate airway defense mechanisms.

Epithelial-Neural Signaling in Somatosensory Function

Epithelial–neuronal signaling is increasingly recognized as a critical axis of somatosensation, and particularly in the context of nociception. In both vertebrates and invertebrates, somatosensory neurons densely innervate epithelial surfaces and have been traditionally viewed as the primary detectors of noxious and innocuous stimuli. However, recent studies have shown that epithelial cells can themselves detect thermal, mechanical, and chemical cues and modulate neuronal output in response.

Merkel cells are among the first and best-characterized examples of epithelial sensory transducers. These specialized epithelial cells detect light touch via the

mechanosensitive channel Piezo2 and form synaptic contacts with low-threshold Aβ afferents, which also express Piezo2[27–29]. Optogenetic experiments have shown that activating Merkel cells can drive action potential firing in these neurons, while silencing them reduces neuronal responses to touch. Merkel cells directly signal to sensory neurons via norepinephrine. Although both Aβ afferents and Merkel cells use Piezo2 to detect force, Merkel cells are specifically required for the sustained component of neuronal firing, thereby tuning the afferent response to mechanical stimuli.

Keratinocytes also play key roles in sensory transduction and respond to both innocuous and noxious mechanical stimuli [30–32]. Optogenetic activation and inhibition of keratinocytes can modulate nocifensive behavioral responses which depend on ATP released from keratinocytes and activation of neuronal P2X4 receptors[30,31]. Keratinocyte-expressed Piezo1 contributes, in part, to this mechanical sensitivity and has been linked to keratinocyte-mediated pain responses[32]. Meanwhile, another study finds that both *Drosophila* larvae epidermal cells and human keratinocytes require store-operated calcium signaling for stretch-activated calcium responses. Similar to mice, *Drosophila* larvae epidermal cells also drive neuronal responses and behavior, via epidermal vesicle release, but the signaling molecule remains unknown[33]. Beyond mechanosensation, keratinocytes also play roles in thermosensation. They express ion channels such as TRPV3 and TRPV4, which respond to warming and cooling[34], and contribute to heat- and cold-evoked nocifensive behaviors in a manner that depends on P2X4 signaling[35]. In addition to ATP, keratinocytes can release molecules such as TSLP, which directly activate sensory neurons and drive itch responses, further highlights their role as active participants in somatosensory signaling[36]. These findings highlight the broad sensory roles of keratinocytes in detecting both mechanical and thermal cues and modulating neuronal activity.

Epithelial contributions extend beyond the skin. In the gut and airways, epithelial cells release neurotransmitters such as serotonin and ATP in response to sensory cues and modulate afferent activity[25,26,37]. The fact that epithelial and neuronal cells can detect overlapping stimuli, but with different kinetics and signaling pathways, supports a model in which epithelial input serves to amplify, tune, or gate nociceptor activity. This coordination may allow for more flexible and context-dependent behavioral responses to environmental threats.

Structural and Functional Organization of Airway Nociceptors

Mammalian airway defense

To protect themselves from inhaled irritants, pathogens, and allergens, mammals rely on rapid and coordinated airway defense mechanisms. In the upper airways, comprised of the nasal cavity, pharynx, and larynx, these defenses include sneezing, coughing, nasal secretions, and nose-directed behaviors such as rubbing or wiping. Sneezing and coughing are powerful expulsive reflexes that help clear irritants from the airways, generating approximately 40,000 and 3,000 droplets in humans, respectively[38]. Nasal secretions dilute and flush out harmful substances, while rubbing and wiping physically remove irritants and mucus from the nasal passages. In the lower airways, comprised of

the trachea, bronchi, and lungs, additional defenses include mucus production and airway-guarding reflexes such as apnea, glottic closure, and bronchoconstriction. These reflexes serve to restrict airflow to prevent further inhalation of harmful substances and facilitate their clearance through mechanical or mucosal means. Mucus plays a central role throughout the respiratory tract by trapping inhaled particles and microorganisms, which are then cleared via ciliary transport or cough. Although acutely protective, persistent or dysregulated activation of these responses can become maladaptive, contributing to conditions such as allergic rhinitis, chronic cough, and asthma. These **nocifensive** responses–protective behaviors triggered by noxious or irritating stimuli– are initiated by anatomically organized and functionally distinct nociceptors that innervate the upper and lower airways, detect irritants, and drive motor responses via central neural circuits and secretory responses through their interactions with epithelial cells and immune mediators.

Molecular transducers of airway nociception

Two key sensory transduction channels expressed by nociceptors are TRPV1 (transient receptor potential vanilloid 1) and TRPA1 (transient receptor potential ankyrin 1). TRPV1 is a heat- and capsaicin-sensitive non-selective cation channel expressed by a major subset of airway nociceptors. In addition to noxious heat and capsaicin, the active component of chili peppers, TRPV1 is directly activated by acidic pH and endogenous lipid mediators and contributes to reflexes such as cough, bronchoconstriction, and mucus secretion[39]. TRPA1 is a non-selective cation channel expressed in a subset of TRPV1-expressing neurons and serves as a sensor for environmental irritants. These include various reactive and oxidative compounds such as ozone, hydrogen peroxide, chlorine, and other reactive oxygen species (ROS) found in smog, cigarette smoke, and tear gas[40–44]. TRPA1 activation drives irritant-induced cough, airway inflammation, and bronchoconstriction[39,45,46].

In addition to their direct activation by irritants, TRPV1 and TRPA1 can also be sensitized or indirectly activated by inflammatory mediators acting through G protein-coupled receptors and other upstream signaling pathways. For example, the endogenous lipid sphingosine-1-phosphate (S1P) activates nociceptors via S1PR3, a G protein-coupled receptor known to modulate TRPV1 and TRPA1 activity[47,48], and drives inflammation-independent bronchoconstriction[49]. Another notable example is histamine, that activates nociceptors via TRPV1[50] to trigger sneezing[21]. Additionally, mediators released during allergy or infection, as well as allergens and pathogens themselves, can directly activate nociceptors, often through these channels; this will be discussed in later sections.

Cellular architecture of airway nociception

Nociceptors are specialized subsets of somatosensory and vagal sensory neurons, defined by their ability to detect noxious stimuli. Airway-innervating nociceptors reside in four major sensory ganglia: the trigeminal, jugular, nodose, and, to a lesser extent, the dorsal root ganglia (DRG). These pseudounipolar neurons extend peripheral projections to various regions of the airways and central projections to distinct areas of the

brainstem and spinal cord, where they interface with respiratory and reflexive motor circuits. They are primarily unmyelinated C-fiber neurons, although a subset of nociceptors are thinly myelinated A-delta fibers. The trigeminal and dorsal root ganglia contain the cell bodies of somatosensory neurons that innervate the body, including the skin and viscera. The jugular and nodose ganglia contain vagal sensory neurons that innervate internal organs. Although the jugular and nodose ganglia are anatomically difficult to distinguish in mice, they have distinct developmental origins: jugular neurons arise from the neural crest, like those in the trigeminal and DRG, whereas nodose neurons derive from the epibranchial placode[51]. These sensory projections, referred to as **afferents**, convey information from the periphery (i.e., the airway epithelium) to the central nervous system. In response to afferent activation, brainstem integration centers engage **efferent** motor pathways that drive protective reflexes such as sneeze, cough, and bronchoconstriction.

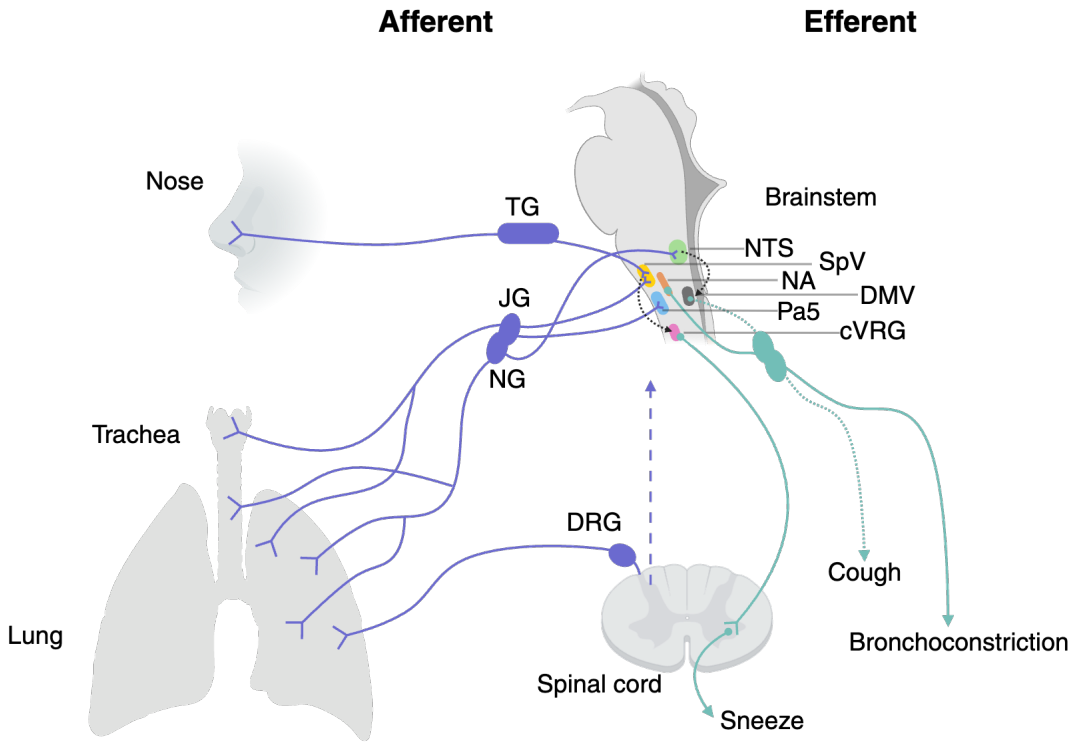

Figure 1. Neuroanatomical organization of afferent and efferent pathways that drive airway reflexes.
Airway nociceptors arise from four major sensory ganglia: the trigeminal ganglion (TG), jugular ganglion (JG), nodose ganglion (NG), and dorsal root ganglia (DRG). These afferent neurons detect noxious stimuli across distinct regions of the airway and project centrally to specialized brainstem nuclei to initiate protective reflexes. Trigeminal afferents innervating the nasal cavity detect irritants and project to the paratrigeminal nucleus (Pa5, blue) spinal trigeminal nucleus (SpV, yellow) where they can initiate the sneeze reflex via downstream activation of the caudal ventral respiratory group (cVRG, pink) and spinal motor neurons. Jugular afferents innervating the larynx and trachea

project to Pa5 and the SpV, while nodose afferents project primarily to the nucleus of the solitary tract (NTS, green), a key integrative center for interoceptive signals and initiating cough. Lung-innervating DRG neurons send signals to the brain via their projections that enter the spinal cord. Central integration by brainstem autonomic and respiratory centers (nucleus ambiguus (NA, orange), dorsal motor nucleus of the vagus (DMV, gray), and cVRG) engages efferent motor circuits that trigger sneeze, coordinate the cough motor program, and elicit bronchoconstriction. Brainstem sensory nuclei relay information to supraspinal centers involved in perception, emotion, and voluntary control, while higher brain regions can also modulate these reflexes. Abbreviations: TG, trigeminal ganglion; JG, jugular ganglion; NG, nodose ganglion; DRG, dorsal root ganglion; NTS, nucleus of the solitary tract (green); SpV, spinal trigeminal nucleus (yellow); Pa5, paratrigeminal nucleus (nucleus paratrigeminalis) (blue); NA, nucleus ambiguus (orange); DMV, dorsal motor nucleus of the vagus (gray); cVRG, caudal ventral respiratory group (pink).

I. Nasal nociceptors

Nociceptors from the trigeminal ganglia innervate the nasal cavity, nasopharynx, and the skin around the nares, as well as the rest of the face and head. This area represents the most external interface of the airway and thus, highly exposed to environmental irritants. Trigeminal nociceptors detect these threats and initiate rapid nocifensive responses including sneezing, nasal secretions, and nose-directed behaviors like rubbing or wiping[21,52]. Their central projections terminate in the spinal trigeminal nucleus and related regions of the brainstem, where they connect with circuits mediating both somatic reflexes and autonomic responses (Fig. 1). Recent work has begun to uncover the molecular mechanisms underlying sneeze reflex initiation. Nasal sensory neurons, expressing TRPV1 and MrgprC11, release the neuropeptide neuromedin B (NMB) upon activation. NMB in turn activates NMBR-expressing neurons in the spinal trigeminal nucleus which then synapse onto neurons in the caudal ventral respiratory group to drive the sneeze reflex[21,22] (Fig 1). Whether MrgprC11-expressing nasal nociceptors, which drive itch sensation in the skin[53,54], contribute to nose rubbing or wiping behaviors remains an open question.

In contrast, the mechanisms that mediate rhinorrhea (runny nose) remain less clearly defined. Human studies suggest a role for acetylcholine and the neuropeptides Substance P and vasoactive intestinal peptide[55–58] (VIP), but this remains to be casually demonstrated. It is hypothesized that parasympathetic neurons release acetylcholine, which activates muscarinic acetylcholine receptors on nasal epithelial cells to stimulate fluid and mucus secretion[59]. However, recent work in the gut suggests that Tuft cells, rare chemosensory epithelial cells, release acetylcholine to drive mucus production[60,61]. Whether nasal Tuft cells contribute to rhinorrhea and how their responses are coordinated with nociceptive signaling remains an exciting area for future research.

II. Larygneal and tracheal nociceptors

The larynx and trachea are innervated by neurons from the jugular and nodose ganglia. These neurons project centrally to the brainstem, where the jugular neurons project to the paratrigeminal nucleus and spinal trigeminal complex and the nodose predominately to the nucleus of the solitary tract (NTS) in the brainstem, a major integrative hub for autonomic sensory input[62] (Fig. 1). Recent studies deepen our understanding of how specialized vagal sensory neurons and their circuits, in concert with epithelial cells, mediate airway-guarding reflexes such as apnea, glottic closure, bronchoconstriction, coughing, and gasping. These reflexes serve to rapidly restrict airflow and initiate protective behaviors in response to noxious mechanical or chemical stimuli.

Recent studies on airway-guarding reflexes suggest an organizational logic such that epithelial cells act as frontline detectors, releasing signaling molecules such as ATP in response to environmental threats, which in turn activate molecularly distinct vagal sensory neurons. For instance, laryngeal P2RY1-expressing neurons coordinate an airway defense program including apnea, vocal fold adduction, swallowing, and expiratory reflexes when stimulated by epithelial ATP signals. These neurons form corpuscular endings that lie near laryngeal taste buds and detect irritants like acid or water[26]. Similarly, a recent study identified Ascl1-lineage neuroendocrine (NE) cells in the larynx and trachea also respond to similar stimuli and release ATP to activate laryngeal nerve afferents. The resulting reflexes include apnea, post-swallow expiratory efforts, and cough-like responses[25]. Notably, laryngeal taste cells appear to trigger an abrupt, forceful exhalation (an “expiratory reflex”) without a preceding inhalation, a mechanism for preventing irritants from descending further into the airway. In contrast, NE cell activation drives a more classic cough-like event, featuring a robust exhalation after a preparatory inhalation, that forcefully expels substances already in the airway.

Recent work has aimed to define the specific neural populations responsible for cough, a particularly challenging reflex to characterize in rodents. Jiang et al. identified a population of somatostatin-expressing (SST^+) sensory neurons with central projects in the NTS that selectively mediate coughing but not sneezing[22]. Another recent study identified downstream of these, Tac1-expressing neurons in the NTS receive input from vagal afferents and generate coordinated cough-like motor patterns[23]. Notably, these cough reflexes are evoked by a range of chemical irritants, including capsaicin, citric acid, and ammonia. Whether these neurons correspond to the P2X-responsive populations activated by ATP released from epithelial cells, described by Seeholzer et al.[25] remains to be determined. However, a major limitation across current studies is the lack of standardized definitions or behavioral criteria for identifying cough in mice. Each study employs different experimental approaches and classification criteria, making cross-comparison difficult and highlighting the need for unified standards for sneeze and cough in mice in the field.

III. Lung nociceptors

Distinct subsets of vagal sensory neurons, particularly those from the nodose ganglia, innervate the bronchi and lung parenchyma, modulate breathing and contribute to reflexes such as cough and bronchoconstriction, often acting in coordination with central pattern generators for breathing[63,64]. and contribute to reflexes such as cough,

bronchoconstriction, often in coordination with central pattern generators for breathing. Thoracic DRG neurons innervate the airways[62,65], including the lung; however, their role in airway nociception is not well understood, and further work is needed to clarify their functional relevance in respiratory reflexes. Beyond their roles in controlling respiratory function, airway nociceptors also contribute to neurogenic inflammation and immune modulation, particularly in disease contexts, which will be discussed in later sections.

Airway Nociceptors in Allergy and Asthma

Sensing Allergens

Nociceptors detect allergens both directly and indirectly through immune mediators released during the allergic response, as extensively reviewed elsewhere[66,67]. While these interactions have been well characterized in the skin, and many of the same molecules are expressed in the airways, the mechanisms underlying nociceptor activation in the allergic lung remain less well defined and are not covered in detail here.

Role During Allergy and Asthma

Upper Airway Symptoms

Airway nociceptors drive acute allergen-evoked reflexes such as sneezing, coughing, and rhinorrhea. In allergic models, mast cell-dependent sneezing requires TRPV1 and TRPV1+, MrgprC11^{+} neurons, which act via neuromedin B (NMB) signaling in the brainstem to trigger sneeze circuits[21]. However, the mechanisms driving allergic rhinorrhea remain less well understood. Human studies implicate neuropeptides like substance P and vasoactive intestinal peptide (VIP) in promoting allergen-triggered nasal secretions[55,58], but more mechanistic studies are needed to understand the cells and molecules that mediate this response. Whether the same neuronal subsets and molecular mediators that drive allergic itch in the skin also contribute to irritation and itch in the nose and upper airways remains to be tested.

Airway Hyperreactivity

While airway hyperreactivity (AHR) has traditionally been attributed to smooth muscle sensitivity and immune cell activation, recent studies demonstrate that airway-innervating nociceptors play a central role in both driving and modulating this response. TRPA1 activation enhances bronchoconstriction, and both genetic deletion and pharmacological inhibition of TRPA1 significantly reduce AHR in ovalbumin-sensitized mice[45]. In this same model, TRPV1+ and MrgprC11+ neurons have been demonstrated to mediate allergen-induced bronchoconstriction[49,68]. Notably, ablation of TRPV1- and MrgprC11-expressing neurons reduces methacholine-induced airway constriction

without affecting immune cell infiltration or cytokine production in the lung, supporting the existence of a neural component of AHR that operates independently of classical inflammatory pathways. Interestingly, this role appears to be model-dependent, as MrgprC11+ neurons are dispensable in certain dust mite-induced asthma models[69].

A recently identified population of neurons in the NTS marked by Dbh, has been shown to be both required and sufficient to drive bronchoconstriction[70]. These Dbh+ neurons are activated in a mast cell-, IL-4-, and vagal nerve-dependent manner and exert their effects on the lungs via parasympathetic neurons. Allergen exposure increases synaptic connectivity between vagal nociceptors and these Dbh+ NTS neurons, suggesting that ongoing inflammation induces synaptic plasticity within brainstem circuits. Such changes could underlie the chronicity of symptoms in allergic asthma. Together, these findings link TRPV1+ and TRPA1+ vagal nociceptors to Dbh+ brainstem neurons, outlining a complete neural circuit that shapes airway reactivity over time.

Allergic Inflammation

Emerging evidence, however, shows that airway nociceptors do more than drive allergic symptoms; they actively shape immune responses. By releasing neuropeptides and engaging in bidirectional crosstalk with epithelial and immune cells, these nociceptors can amplify or mitigate allergic inflammation. Recent work highlights that airway nociceptors govern immune cell recruitment and cytokine signaling, indicating they are key modulators rather than passive sensors of allergic responses.

Several key studies have highlighted the significant roles of TRPV1+ and TRPA1+ nociceptors in mediating allergic airway inflammation. TRPA1-expressing nociceptors have been shown to actively drive allergic inflammation by promoting leukocyte infiltration, cytokine release, mucus overproduction, in addition to AHR, positioning TRPA1 as a key mediator in airway hypersensitivity and inflammation[45]. Similarly, TRPV1-expressing vagal sensory neurons have been shown to amplify allergic responses by interacting with immune cells, particularly type 2 innate lymphoid cells (ILC2s) and CD4+ T-cells[71]. However, recent findings also suggest a counter-regulatory role, as TRPV1+ neurons can express CGRPβ in a JAK1-dependent manner, which suppresses ILC2 activation and allergic inflammation[72]. This dual role of TRPV1+ nociceptors highlights their complex contribution to airway immune modulation and opens avenues for therapeutic strategies that could either inhibit or harness their regulatory functions.

Nociceptors are key modulators of allergic immunity

Nociceptors function as dynamic sensors and modulators of the immune environment in allergic airway disease. Some of these seemingly contradictory findings in the field may be explained by the inherent diversity of nociceptors, as distinct subsets may exert opposing effects depending on the context. These subsets express different combinations of sensory receptors and neuropeptides that exert pleiotropic effects of various immune cells. Thus, how nociceptors modulate airway immunity depends on which neurons are activated, how they are activated, and who they signal to peripherally

and centrally. This diversity enables highly context-specific signaling that can either amplify or suppress allergic inflammation. Future studies will need to delineate the precise molecular signals and cellular interactions that govern the initiation, maintenance, and resolution of allergic airway disease.

Roles for Airway Nociceptors in Respiratory Infection

The course of infection is a dynamic landscape shaped by simultaneous and interacting host and pathogen responses. While the pathogen seeks to replicate and spread, the host mounts defenses to contain the invader. Pathogens evolve strategies to evade the immune system, and the host, in turn, evolves mechanisms to overcome them, an ongoing evolutionary tug-of-war. Every pathogen elicits a distinct immune response, and even the same pathogen can trigger different outcomes across individuals or within the same individual at different times. The context of the infection, including the type of pathogen, the timing, and the host's immune status, critically shapes disease progression. This complex interplay has profound consequences for human health, as starkly illustrated by the COVID-19 pandemic and its lasting impact on society.

Nociceptors are increasingly recognized as active participants in the host response to respiratory infection. These sensory neurons work in concert with airway epithelial cells, which serve as a physical barrier and as immunologically active sentinels, and immune cells that initiate inflammation to eliminate pathogens and infected cells. Upon infection, epithelial cells release signals that trigger inflammatory cascades and recruit immune cells to the airway. In parallel, nociceptors detect both pathogen- and host-derived signals, initiating protective reflexes such as sneezing and coughing, as well as pain sensations associated with tissue injury and infection. While these responses contribute to acute defense, excessive or prolonged nociceptor activation can drive persistent symptoms, including chronic cough, pain, and altered respiration. In some cases, infection-induced maladaptive plasticity may alter neuronal function in ways that contribute to long-term post-infectious sequelae.

Sensing infection

Understanding how nociceptors respond to infection requires dissecting the specific signals that engage them during disease. It has been proposed that infections modulate nociceptor activity both indirectly through inflammatory mediators produced during infection and directly, via neuronal infection. Recent studies suggest three non-mutually exclusive mechanisms by which airway nociceptors are activated during infection:

I. Activation by Inflammatory Mediators

A wide range of host-derived inflammatory signals can directly stimulate sensory neurons during infection (extensively reviewed elsewhere[73,74]). Among the best characterized are prostaglandins, bradykinin, and pro-inflammatory cytokines such as TNF-α and IL-1β, which can activate and sensitize nociceptors to drive pain[75–78]. Prostaglandins have been long shown to activate and sensitize nociceptors[78], and

recent studies have demonstrated that during influenza infection, airway nociceptor activation are activated by prostaglandin E2 to promote sickness behaviors[79]. Type I interferons (IFN-α and IFN-γ), typically associated with antiviral defense, can also directly activate dorsal root ganglion (DRG) neurons and elicit pain-like behaviors in mice[80]. Additional host-derived molecules associated with infection, including hemoglobin breakdown products (HMB)[81,82] and vascular endothelial growth factor A (VEGF-A)[83] have also been shown to modulate nociceptors.

II. Direct Infection of Neurons

Several viruses, including herpes simplex virus (HSV) and coronaviruses such as SARS-CoV-2 and murine coronaviruses, have been shown to directly infect sensory neurons[84–88]. Respiratory syncytial virus (RSV) has also been observed to co-localize with sensory nerve endings in the lung[89]. Because nociceptors consist of single cytoplasmic extensions linking the periphery to the central nervous system, they may serve both as potential reservoirs for latent infection and as conduits to the brain. These findings suggest that sensory neurons may, by necessity, actively participate in antiviral responses, with direct infection potentially modulating their sensory functions in ways that remain poorly understood. In animal models and in vitro systems, SARS-CoV-2 infection of sensory ganglia has been shown to induce changes in gene expression that may promote hypersensitivity[24,90] and human trigeminal neurons infected with HSV display gene expression signatures suggesting they are primed for hyperreactivity[85]. Additionally, the expression of viral proteins—such as virally encoded ion channels like SARS-CoV-2 ORF3a, which shares biophysical properties with nociceptive channels including TRPV1, OSCA, and P2X receptors[91]—may represent another mechanism by which infection alters neuronal physiology. How direct infections affect neuronal output or contribute to persistent symptoms remains an exciting and open area of investigation.

III. Direct Activation by Microbial Products

Airway pathogens can directly stimulate nociceptors through pathogen-associated molecular patterns (PAMPs) or secreted virulence factors. This mechanism has been more extensively characterized in bacterial infections, with well-established examples including LPS activation of TLR4[92–94],pore-forming toxins[95,96] and an expanding array of other bacterial molecules (extensively reviewed elsewhere[74,97]). In contrast, direct activation of nociceptors by viruses remains less well understood. One earlier study showed that polyinosinic:polycytidylic acid (Poly I:C), a synthetic analog of viral double-stranded RNA, activates dorsal root ganglion (DRG) neurons via TLR3 and induces itch[98]. More recent work has demonstrated that viral proteins such as the SARS-CoV-2 spike protein and papain-like protease can directly activate airway nociceptors[24,99]. A few studies have also shown that components of the fungal cell wall can activate sensory neurons, partly via TLR2[100,101]; however, little is known about how respiratory fungal pathogens interact with nociceptors. Compared to bacterial pathogens, the molecular mechanisms by which viruses and fungi activate nociceptors are only beginning to be defined.

Role during infection

As outlined above, infection can modulate nociceptors through multiple pathways, creating a dynamic landscape with many possibilities for how neuronal function may be altered. A major challenge for the field is to mechanistically define the roles that nociceptors play across the course of infection. Here, I consider their contribution in three key contexts of respiratory infection: (1) the acute symptoms during infection, (2) post-infectious sequelae, and (3) modulation of host immunity.

I. Acute symptoms of infection

Recent studies have shed light on the cells and molecules that drive sneezing and coughing, hallmark symptoms of respiratory infection. Mice exhibit sneezing during influenza infection, a response mediated by trigeminal MrgprC11^{+} nociceptors, the same neuronal population implicated in allergic sneezing[22]. Similarly, other pathogens have evolved mechanisms to directly engage sensory neurons: the Mycobacterium tuberculosis surface lipid SL-1 can activate nociceptors to induce cough[102], while the SARS-CoV-2 papain-like protease triggers both sneezing and coughing through direct nociceptor activation[24]. These findings raise the question of whether similar neuronal mechanisms underlie sneeze and cough responses in other respiratory infections, such as viral illnesses like the common cold or bacterial infections like pertussis (whooping cough). Do host signals also trigger sneeze or cough? Sneezing and coughing are highly efficient mechanisms for aerosolizing and spreading pathogens, raising the possibility that certain microbes have evolved to exploit host defense reflexes to enhance their own transmission. While the cells and molecules that mediate sneeze and cough are only beginning to be uncovered, a key question emerges: do these reflexes serve the host, the pathogen, or both?

Beyond these acute reflexes, nociceptors contribute to broader physiological responses during respiratory infection, including complex sickness behaviors such as pain, lethargy, and dyspnea. These sickness behaviors may not only support recovery by conserving energy and reducing activity but also act as social signals that trigger adaptive responses in others to prevent transmission. For instance, airway nociceptor activation by prostaglandin E2 (PGE2) during influenza infection promotes early-stage decreases in food intake, water intake, and mobility, while loss of these neurons improves survival[79]. Similarly, activation of TLR4 by lipopolysaccharide (LPS) on vagal sensory neurons drives sickness behaviors during Pseudomonas infection[103], suggesting that nociceptors can drive both acute reflexes and sickness behaviors during respiratory infection. Further studies are needed to identify the specific peripheral neurons and circuits that mediate these distinct behavioral outputs.

II. Post-infectious sequelae

Post-infectious sequelae refer to persistent symptoms that continue or newly emerge after the resolution of an acute infection. In the context of respiratory illness, these may include chronic cough, airway hypersensitivity, ongoing pain or discomfort, altered breathing patterns, fatigue, and sensory disturbances such as throat irritation or heightened sensitivity to environmental triggers. These symptoms can persist for weeks

to months and may occur even in the absence of detectable inflammation or ongoing infection, suggesting underlying changes in neural function.

While the mechanisms by which nociceptors contribute to post-infectious sequelae remain unclear, studies from chronic pain and itch disorders offer useful insights. First, persistent inflammatory signals can maintain neuronal activation and drive ongoing symptoms[104]. Second, infection-induced changes in gene expression, such as those triggered by SARS-CoV-2 infection[24,90], may increase neuronal sensitivity to otherwise innocuous stimuli or exacerbate responses to noxious stimuli[105]. Third, circuit-level plasticity may allow low-threshold inputs to elicit nociceptive responses that persist beyond the resolution of infection[106]. These mechanisms may underlie chronic post-infectious symptoms such as persistent cough and airway discomfort, which are commonly reported after respiratory infections, including in cases of long COVID[107,108].

III. Modulation of host immunity

Studies in various mouse models of respiratory infection have revealed that nociceptors can play both protective and detrimental roles in shaping antibacterial and antiviral immunity. During *Staphylococcus aureus* pneumonia[109] and Carbapenem-resistant *Klebsiella pneumoniae* [110] infection, sensory neurons exacerbate disease and suppress host immunity, while during *Streptococcus pneumoniae*[111] and influenza[112,113], neurons appear to play protective roles during infection by promoting host immunity. These contrasting outcomes likely reflect the diversity of nociceptor subtypes and pathogen-specific differences in their activation. Pathogens differ in many ways, including the site of infection, virulence, and the host immune response they elicit, that can lead to differences in nociceptor activation and their effects on host defense. Current genetic loss-of-function studies, while informative, may obscure this nuance by broadly silencing heterogeneous neuronal populations. More refined mechanistic studies are needed to dissect the specific molecular pathways and neuronal subsets that shape host responses over the course of infection.

Nociceptors: caught in the host-pathogen arms race?

Respiratory pathogens may exploit nociceptor pathways to enhance their own transmission. Highly infectious agents such as Mycobacterium tuberculosis (Mtb) and SARS-CoV-2 activate nociceptors to trigger coughing and sneezing, facilitating spread. While the study of host-pathogen interactions has traditionally focused on how microbes manipulate innate immune pathways, exploring how airway pathogens engage nociceptive circuits presents an exciting direction for future research.

In summary, airway-innervating nociceptors play multifaceted roles in respiratory health and disease. They initiate essential defensive reflexes, detect and respond to both environmental and internal signals, and shape immune responses during allergy and infection. These neurons act not only as sensors, but also as effectors and modulators, capable of amplifying or resolving inflammation through context-specific signaling. The emerging view of nociceptors as integral players in airway immunity has important

implications for understanding chronic respiratory diseases and developing novel therapeutic strategies.

Chapter II: Drosophila Epidermal Cells Are Intrinsically Mechanosensitive and Modulate Nociceptive Behavioral Outputs

This chapter is a reproduction of the paper by the same name (Yoshino, J. *et al.* Drosophila epidermal cells are intrinsically mechanosensitive and modulate nociceptive behavioral outputs**.** *Elife*, 2025). I performed ex vivo calcium imaging experiments to demonstrate stretch sensitivity of Drosophila epidermal cells, used genetic and pharmacological approaches to identify candidate mechanotransducers, and characterized store-operated calcium signaling in this cell type. I also prepared Figure 5a-d, Figure 5- Supplement 1a-f, Figure 6c-l, and Figure 6- Supplement 2a-f, and wrote the manuscript with Jiro Yoshino, Claire Williams, Diana Bautista, and Jay Parrish.

Summary

Somatosensory neurons (SSNs) that detect and transduce mechanical, thermal, and chemical stimuli densely innervate an animal's skin. However, although epidermal cells provide the first point of contact for sensory stimuli. our understanding of roles that epidermal cells play in SSN function, particularly nociception, remains limited. Here, we show that stimulating Drosophila epidermal cells elicits activation of SSNs including nociceptors and triggers a variety of behavior outputs, including avoidance and escape. Further, we find that epidermal cells are intrinsically mechanosensitive and that epidermal mechanically evoked calcium responses require the store-operated calcium channel Orai. Epidermal cell stimulation augments larval responses to acute nociceptive stimuli and promotes prolonged hypersensitivity to subsequent mechanical stimuli. Hence, epidermal cells are key determinants of nociceptive sensitivity and sensitization, acting as primary sensors of noxious stimuli that tune nociceptor output and drive protective behaviors.

Introduction

The ability to detect tissue-damaging noxious stimuli and mount an escape response is essential for survival. Likewise, prolonged hypersensitivity following injury is an important form of plasticity that protects an animal from further damage. In *Drosophila*, a single class of identified somatosensory neurons (SSNs), class IV dendrite arborization (C4da) neurons, are necessary and sufficient for nociception; inactivating C4da neurons renders larvae insensitive to noxious stimuli whereas activating these neurons drives nocifensive behavior responses[114–116]. A variety of agents that cause tissue damage including UV irradiation and chemical toxins induce long-lasting allodynia and hyperalgesia[117,118], but this damage-induced hypersensitivity develops on a timescale of hours. *Drosophila* also display acute hypersensitivity noxious mechanical stimuli[115]. However, the cellular and molecular mechanisms underlying mechanical pain hypersensitivity remain enigmatic.

Recent studies demonstrate that epidermal cells work in concert with SSNs to transduce noxious and innocuous physical stimuli. For example, epidermal Merkel cells are mechanosensory cells that signal to sensory neurons to mediate touch transduction[28,119]. Similarly, keratinocytes are directly activated by noxious thermal and mechanical stimuli

and release molecules that modulate nociceptor functions[120–125]. Furthermore, epidermal cells in invertebrates and vertebrates ensheath nociceptors in mesaxon-like structures[126–131], and these sheaths may serve as sites of epidermis-nociceptor signaling[132]. Indeed, epidermal ensheathment is required for normal responses to noxious mechanical stimuli in *Drosophila*[131]. However, whether epidermal cells are directly activated by noxious stimuli and modulate C4da neuronal activity has not been studied.

Here, we examined the capacity of *Drosophila* epidermal cells to drive nociceptor activation and modulate mechanical nociceptive responses. We found that stimulation of epidermal cells, but no other non-neuronal cell types in the larval body wall evokes activity in a variety of SSNs neurons and triggers nocifensive behavioral responses. Our *in vitro* and *ex vivo* calcium imaging experiments demonstrate that epidermal cells are intrinsically mechanosensitive. Using an unbiased genetic screen, we discovered a role for the store-operated calcium channel Orai, and its activator Stim in epidermal mechanotransduction and mechanical sensitization. Downstream of Stim/Orai activation, epidermal cells evoke nociceptor activation and mechanical hypersensitivity via epidermal vesicular release. Overall, we demonstrate that *Drosophila* epidermis-neuron signaling mediates both the acute detection of noxious mechanical stimuli and a form of prolonged mechanical hypersensitivity.

Results

Stimulation of epidermal cells evokes nocifensive behavior

To identify peripheral non-neuronal cell types that contribute to nociception, we conducted an optogenetic screen for light-evoked nocifensive behavior. First, as a benchmark for comparison we used the light-activated cation channel CsChrimson[133] to optogenetically activate nociceptive C4da neurons. Consistent with prior reports[114,115], C4da activation triggered nocifensive behaviors including c-bending and rolling in 100% of larvae (Fig. 1A, Fig. 1S1A, Movie S1). Next, we selectively expressed CsChrimson using GAL4 drivers in combination with *elav-GAL80*, which effectively siliences GAL4 expression in larval sensory neurons (Fig. 1S2), to target the six principle non-neuronal cell types within the larval body wall: epidermis, trachea, muscle, hemocytes, oenocytes, and glia (Fig. 1S3, Table S1). We then monitored light-evoked behavioral outputs associated with stimulation of each cell type. We found that optogenetic stimulation of epidermal cells, like C4da neurons, elicited nocifensive c-bending and/or rolling behaviors in 73% of larvae (Fig. 1A, 1S1B), without significantly altering nociceptor morphogenesis (Fig. 1S4). In contrast, stimulation of other body wall cell types elicited a variety of non-nociceptive behavior outputs: for example, muscle stimulation triggered hunching behavior followed by prolonged freezing, whereas glia stimulation reproducibly induced only hunching behavior (Fig. 1S1C-I) [134]. Thus, epidermal cells are the only non-neuronal body wall cell type that triggers robust nocifensive behavioral responses.

To further validate the selective ability of body wall epidermal cells to drive nocifensive behaviors, we examined eight other epidermal drivers in addition to *R38F11-GAL4*, which displays no expression in sensory neurons and limited non-epidermal cell expression

overall (Fig. 1S5). We found that optogenetic stimulation evoked nocifensive behaviors with each of the eight epidermal driver lines we tested: seven of the lines displayed rolling behavior while all eight displayed c-bending (Fig. 1B, Fig. 1S6). Although the previously described pan-epidermal *A58-GAL4* driver[135] drove robust nocifensive rolling responses (Fig. 1B, 1S6), *A58-GAL4* is expressed broadly in the larval CNS (Fig. 1S7) and stocchastically expressed in sensory neurons (Jiang et al 2014). In contrast, the remaining seven drivers including *R38F11-GAL4* exhibited limited expression aside from epidermal cells, with no detectable expression in nociceptors, other larval SSNs, or peripheral glia, and highly restricted or undetectable expression in the CNS (Fig. 1S7). Further underscoring the connection between epidermal stimulation and nocifensive responses, the nocifensive behavioral response with these epidermal drivers correlated with the proportion of epidermal expression (Fig 1B).

We next used thermogenetic stimuluation with the warmth-activated TRP channel dTRPA1[136] as an independent method of probing nociceptive responses triggered by epidermal cell activation. On its own, the thermal stimulus (35° C) rarely induced rolling behavior in control larvae bearing *UAS-TRPA1* alone. In contrast, we found that >75% of larvae expressing TRPA1 in all nociceptors exhibited rolling behavior in response to a thermal stimulus (Fig. 1C). Likewise, thermogenetic activation of epidermal cells induced robust rolling responses in >75% of larvae, and addition of GAL80 transgenes (*tsh-GAL80 elav-GAL80*) that silenced the sparse *R38F11-GAL4* VNC expression (Fig. 1S5) had no effect on the rolling frequency (Fig. 1C, Fig. 1S3). Altogether, these results demonstrate that epidermal stimulation evokes nocifensive responses in *Drosophila*. Of note, prior studies demonstrated that sparse thermogenetic activation of nociceptors (<5 cells) yielded no significant increase in nocifensive rolling whereas activation of >10 cells was required to elicit rolling responses in a majority of larvae[137]. Hence, epidermal stimulation likely engages numerous C4da neurons to elicit these behavioral responses.

In addition to C4da nociceptors, the epidermis is innervated by a variety of other SSNs including mechanosensory C3da and chordotonal (Cho) neurons and proprioceptive C1da neurons. Whereas direct stimulation of C4da nociceptors principally elicited nocifensive behavioral outputs, epidermal stimulation elicited an array of behaviors in addition to nocifensive responses, including freezing and hunching (Fig. 2A, 2B), behaviors associated with stimulation of C3da and Cho neurons[138,139]. These data suggest that epidermal cells may broadly modulate SSN activity in *Drosophila*.

To examine whether different epidermis-evoked behaviors were associated with activation of distinct classes of SSNs, we compared epidermis-evoked and SSN-evoked behaviors. Stimulation of C4da, C3da and Cho neurons elicited distinct behavioral motifs: only C4da neurons elicited rolling behavior; stimulation of C3da and Cho neurons together elicited hunching, C-bending, and backing; stimulation of Cho neurons alone principally elicited hunching and freezing responses (Fig. 2A-2C, 2F). In contrast, optogenetic epidermal stimulation elicited all of these behaviors in a stereotyped sequence, with nocifensive behaviors (c-bending, rolling) preceding non-nociceptive behaviors (backing, freezing) (Fig. 2D, 2F, 2S1). We note that neither the behavioral motifs induced by epidermal or SSN stimulation nor the behavioral sequence induced by

epidermal stimulation was recapitulated in effector-only controls (*UAS-CsChrimson* ATR+; Fig. 2S1E), demonstrating that the observed responses were driven by activation of the respective cell types.

We observed three striking differences in behavior evoked by stimulation of epidermal cells versus individual SSNs. First, although rapid, latency to rolling was significantly longer following epidermal stimulation compared to stimulation of C4da (Fig. 2F). Second, the duration of rolling, bending, and backing responses was significantly longer for epidermis versus SSN stimulation (Fig. 2G). Third, backing and freezing behaviors persisted beyond the duration of the light stimulus for epidermis but not SSN stimulation (Fig. 2H). In summary, we find that epidermal stimulation triggers more robust, varied and prolonged behaviors compared to responses from direct stimulation of discrete SSN subtypes.

Somatosensory neurons are activated by epidermal stimulation

We next asked whether epidermal stimulation activates larval SSNs including C4da, C3da, C1da, and Cho neurons. To test this possibility, we developed a semi-intact larval preparation in which we optogenetically stimulated epidermal cells while simultaneously monitoring calcium responses in axon terminals of SSNs (Fig. 3A). We found that epidermal stimulation triggered rapid and robust calcium transients in nociceptive C4da neurons, responses that were not observed in the absence of ATR or in effector-only controls (Fig. 3B). Epidermal stimulation likewise evoked calcium transients in mechanosensory C3da and Cho neurons, and in proprioceptive C1da neurons (Fig. 3C-3E, 3S1). Hence, epidermal stimulation can broadly modulate activity of larval SSNs.

We next tested the requirement for SSN synaptic transmission in epidermis-evoked behaviors. We stimulated epidermal cells with CsChrimson while blocking SSN neurotransmitter release using tetanus toxin light chain (TnT)[140]. We found that inhibiting C4da or C3da + Cho neurotransmission significantly reduced the frequency and duration of epidermal-evoked rolling and backing behaviors, respectively (Fig. 3E, 3F, 3S2). These data suggest that C4da and C3da/Cho neurons act downstream of epidermal cells to drive behaviors. We note that TnT expression in C4da neurons did not completely block epidermis-evoked nocifensive behaviors, and this likely reflects both incomplete C4da neuron silencing and epidermal activation of other SSNs that promote nociceptive outputs including C3da neurons, C2da neurons, and Cho neurons[115,116,141]. Further, silencing C4da or C3da/Cho neurons while stimulating epidermal cells led to an increase in the non-nocifensive behaviors hunching and freezing (Fig. 3E, 3F). These results, along with the observation that rolling behaviors predominate the early behavioral responses to epidermal stimulation (Fig. 2B), suggest that the nervous system prioritizes nocifensive behavioral outputs following epidermal stimulation. These data support a model in which epidermal cells and SSNs are functionally coupled.

Epidermal stimulation potentiates nociceptive neurons and behaviors

What is the physiological relevance of this functional coupling of epidermal cells and SSNs? To address this question, we compared calcium responses in C4da neurons to either simultaneous epidermal and C4da stimulation or C4da stimulation alone. Simultaneous stimulation significantly enhanced the magnitude and duration of calcium responses in C4da axons (Fig. 4A-4D, 4S1). Based on this prolonged calcium response, we hypothesized that simultaneous epidermis and C4da neuron stimulation would yield enhanced nocifensive behavior output. To test this, we optogenetically stimulated C4da neurons and epidermal cells individually or in combination using low intensity CsChrimson activation and monitored larval behavior responses. In this stimulation paradigm, simultaneous epidermal cell and C4da neuron stimulation resulted in rolling in 100% of larvae whereas selective stimulation of C4da neurons or epidermal cells induced rolling in only 63% or 18% of larvae, respectively (Fig. 4E, 4F). Furthermore, simultaneous stimulation elicited a significantly higher number of rolls among responders than stimulation of nociceptors or epidermal cells alone (26.9 rolls for C4da + Epi, 4.9 for C4da, and 5.3 for Epi stimulation; Fig 4G, 4H). Likewise, simultaneous stimulation significantly reduced the latency to the first roll (Fig. 4I) and increased the duration of rolling behaviors (Fig. 4J). We next tested whether this functional coupling extends to mechanical stimuli. We simultaneously presented larvae with a noxious mechanical stimulus and a low intensity optogenetic epidermal stimulus that was insufficient to trigger rolling on its own (0% response rate, n = 200). This concurrent epidermal stimulation significantly increased touch-evoked nocifensive responses, yielding a 91% or 49% increase in rolling responses to 20 mN or 50 mN Von Frey stimulus, respectively (Fig. 4K). We next probed the kinetics of this epidermis-induced mechanical sensitization.

When *Drosophila* larvae are presented with two nociceptive mechanical stimuli in succession, they exhibit enhanced behavioral responses to the second stimulus[115]. We hypothesized that selective epidermal stimulation would sensitize larvae to subsequent nociceptive mechanical stimuli. To test this hypothesis, larvae expressing the warmth-activated calcium-permeable channel dTRPA1 in epidermal cells were presented with a thermal stimulus, 32º C to activate dTRPA1, followed by a 40 mN mechanical stimulus 10 sec later (Fig. 4L). Indeed, we found that dTRPA1-mediated epidermal stimulation significantly sensitized larvae to a subsequent mechanical stimulus, increasing the roll probability more than two-fold. In contrast, dTRPA1-mediated stimulation of C4da neurons did not induce mechanical sensitization, and we confirmed this result with two independent C4da neuron drivers (Fig. 4L). Thus, activation of epidermal cells but not C4da nociceptors alone induces prolonged sensitization to noxious mechanical stimuli. We next assessed the duration of sensitization following transient epidermal activation. Thermogenetic epidermal stimulation yielded persistent sensitization that recovered over a timescale of minutes (τ = 337 sec, Fig. 4M, 4N). The magnitude and duration of mechanical sensitization by thermogenetic epidermal stimulation was remarkably similar to the sensitization evoked by a prior mechanical stimulus (63% roll probability in response to a second stimulus, τ = 334 sec, Fig. 4N, 4S1B). Altogether our data support a model whereby epidermal cells are mechanosensitive cells that signal to SSNs to drive acute nocifensive behaviors and prolong mechanical sensitization.

Epidermal cells are intrinsically mechanosensitive

Prior studies have shown that vertebrate epidermal cells directly respond to mechanical stimuli[121,142–146]. Therefore, we next assessed whether *Drosophila* epidermal cells are intrinsically mechanosensitive. We developed a protocol to acutely dissociate epidermal cells and measure the responses of individual GCaMP6s-expressing epidermal cells to mechanical stimuli (Fig. 5A). We found that radial stretch elicits calcium responses in epidermal cells in a dose-dependent manner. For example, a low 0.5% stretch activated 18% of cells and a subsequent 1% stretch recruited an additional 10% of stretch-responding cells (Fig. 5B-5D). Overall, 51% of epidermal cells displayed stretch sensitivity (Fig. 5C, 5D). We also found that 43% of epidermal cells responded to hypoosmotic challenge and 35% responded to laminar flow; 19% of epidermal cells responded to both hypoosmotic challenge and laminar flow (Fig. 5S1). Given that dissociated epidermal cells were intrinsically mechanosensitive, we next assessed mechanically evoked responses in a semi-intact body wall preparation (Fig. 5E). We found that 50% of epidermal cells exhibited a robust calcium transient in response to a 25 µm membrane displacement using a glass probe (Fig. 5E-5G, 5S1G). Altogether, these results indicate that *Drosophila* larval epidermal cells are intrinsically mechanosensitive.

Mechanically evoked epidermal responses rely on store-operated calcium entry

Our studies demonstrate that, like vertebrate keratinocytes, *Drosophila* epidermal cells exhibit mechanically evoked calcium transients. What is the mechanism of mechanotransduction in these cells? RNA-seq analysis of acutely dissociated epidermal cells revealed expression of more than 20 cation channels, including the mechanosensitive ion channels Piezo, TMEM63, and TMCO (Fig. 6S1). We assessed the epidermal requirements of these channels in mechanical nociception using available RNAi transgenes (Fig. 6A). Our behavioral screen identified one channel, *Orai*, the sole *Drosophila* pore-forming subunit of the Ca^{2+} release-activated Ca^{2+} (CRAC) channel[147], that blocked mechanically-evoked nociceptive sensitization without impacting behavioral responses to the first stimulus (Fig. 6A, 6B, 6S2A) or altering nociceptor morphogenesis (Fig. 1S4). Interestingly, our screen uncovered an epidermal role for *Task6*, an orthologue of stretch-sensitive 2-pore potassium channels [148], in mechanonociception, as *Task6* RNAi increased nocifensive rolling responses to the initial mechanical stimulus (Fig. 6S2B). Finally, although our RNAi studies did not reveal epidermal requirement for other known mechanosensitive cation channels in mechanonociceptive behaviors, it is possible that multiple channels function redundantly, or that RNAi knockdown was incomplete.

To gain insight into mechanically evoked nociceptive sensitization, we focused on probing the role of Orai in epidermal mechanosensory responses. We first asked whether Orai is functional in *Drosophila* epidermal cells. Orai is a store-operated calcium (SOC) channel that is activated by the endoplasmic reticulum (ER)-calcium sensitive molecule, Stim, upon calcium release from ER calcium stores. Thapsigargin (TG) induces calcium release from intracellular stores and thus triggers activation of Orai channels. Indeed, *Drosophila* epidermal cells displayed TG-induced calcium release in the absence of extracellular calcium, followed by calcium influx upon re-addition of extracellular calcium (Fig. 6C). Calcium influx was significantly inhibited by the addition of low nanomolar lanthanum,

consistent with the high sensitivity of Orai channels to lanthanides (Fig. 6S2C). This characteristic store operated calcium entry (SOCE) response was significantly reduced by epidermis-specific *Stim* or *Orai* RNAi knockdown (Fig. 6S2D-F). Consistent with a key role for SOCE in mechanotransduction, we found that radial stretch induced both calcium release from intracellular stores in the absense of extracellular calcium and influx upon calcium re-addition. While both store release and calcium influx constitute the calcium response to stretch, in 69% of cells, calcium due to store release exceeded that of calcium re-entry (Fig. 6E). Consistent with this observation, depletion of intracellular stores and inhibition of calcium re-entry reduced the number of stretch sensitve cells by 61% (stretch non-responsive cells in WT = 49% vs. store depleted = 80%) and 30% (stretch non-responsive cells in WT = 49% vs. La^{3+} = 64%; Fig. 6F-G), respectively. Given that Stim and Orai mediate SOCE, we investigated requirements for epidermal Stim and Orai in mechanically evoked calcium responses. RNAi knockdown of either *Stim* or *Orai* significantly reduced the fraction of stretch-responsive epidermal cells (RNAi control = 48%, *Stim* RNAi = 22%, *Orai* RNAi = 24%; Fig. 6H-I), with *Stim* or *Orai* RNAi preferentially attenuating stretch evoked responses to larger magnitude stretch stimuli. We also found that human keratinocytes display dose-dependent stretch evoked calcium responses, though they respond to higher magnitudes of stretch than *Drosophila* epidermal cells (Fig. 6J). Like *Drosophila*, both store release and calcium influx contribute to stretch evoked calcium responses in human keratinocytes (Fig. 6K).

Two hallmarks of Stim and Orai-mediated SOCE are steep inward rectification, with larger currents at hyperpolarizing potentials, and highly cooperative Orai activation by Stim[149]. Since Stim and Orai mediate mechanical responses of epidermal cells *in vitro*, we predicted that increasing the calcium driving force through Orai activity by either hyperpolarizing epidermal cells or by activating additional Orai channels via *Stim* overexpression would enhance behavioral responses to mechanical stimuli. Indeed, we found that hyperpolarizing epidermal cells with the light-activated anion channelrhodopsin GtACR1[150] increased behavioral responses to mechanical stimuli (Fig. 6L). In addition, overexpressing *Stim* in epidermal cells significantly enhanced nocifensive behavioral responses to mechanical stimuli (Fig. 6M). Altogether, these results demonstrate that mechanically evoked responses of epidermal cells and the resulting nocifensive behavior outputs require store-operated calcium entry.

How might mechanically evoked calcium entry in epidermal cells drive nociceptor activation and behavior? Stim/Orai-mediated calcium entry contributes to exocytosis in a variety of cell types, including neurons and immune cells[151–155]. Therefore, we investigated the contribution of epidermal exocytosis in nociceptive sensitization with the temperature-sensitive dynamin mutant *shibire^{ts}* (*shi^{ts}*) to inducibly block vesicle recycling, as this treatment rapidly and potently blocks neurotransmitter release [156] and we found that acute epidermal dynamin inactivation using *UAS-shi^{ts}* had no discernable effect on nociceptor morphogenesis (Fig. 1S4). In this paradigm, larvae expressing *shi^{ts}* in epidermal cells, but not control larvae, exhibited significant attenuation of mechanically evoked nociceptive sensitization following pre-incubation at the non-permissive temperature (Fig. 6N). In contrast, both genotypes exhibited comparable responses to a mechanical stimulus at the permissive temperature (25° C) and to the first mechanical

stimulus following pre-incubation at the non-permissive temperature (30° C). Taken together, these results are consistent with a model in which mechanical stimuli induce calcium influx and vesicular release from epidermal cells, which in turn activates nociceptors to induce acute nocifensive behaviors and prolonged sensitization (Fig. 6O). Although our RNA-seq analysis of epidermal cells did not reveal expression of neurotransmitter biosynthesis genes, epidermal cells express a large repertoire of genes involved in vesicular release as well as several neuropeptide genes, providing an entrypoint to defining the molecules involved in epidermis-SSN communication (Fig. 6S3).

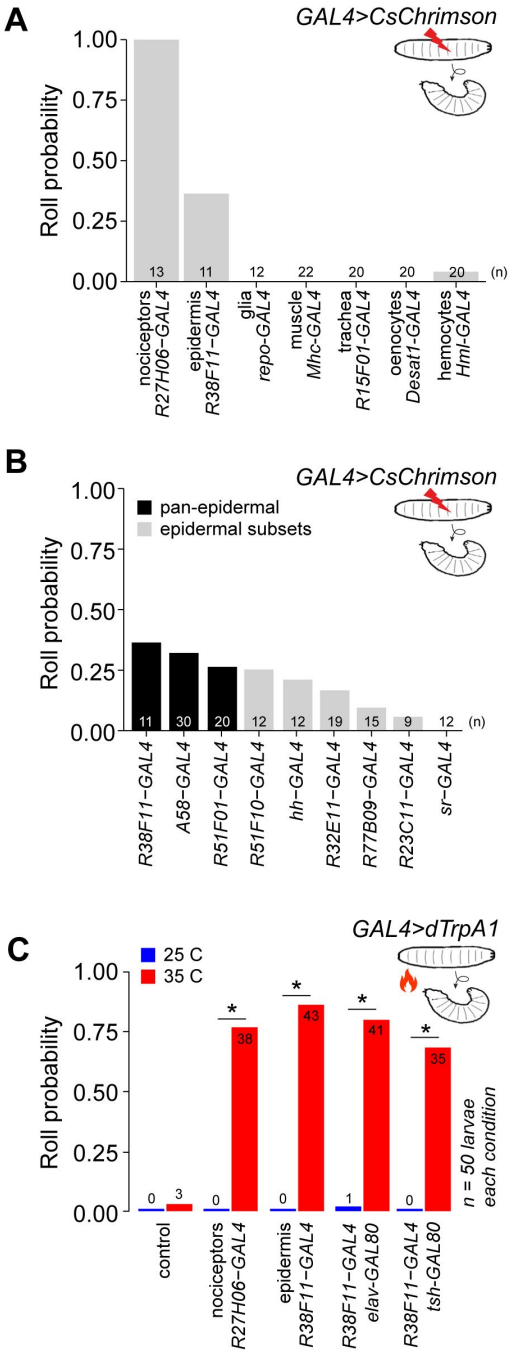

Figure 1. Stimulation of epidermal cells elicits nociceptive behaviors. (A) Fraction of larvae that exhibited optogenetic-induced rolling (roll probability) using the indicated GAL4 lines to drive UAS-CsChrimson expression. All experimental genotypes, except for larvae expressing UAS-CsChrimson in C4da neurons, included elav-GAL80 to suppress neuronal GAL4 activity. Genotypes: GAL4, UAS-CsChrimson, elav-GAL80/+. (B) Roll probability of larvae following optogenetic stimulation using the indicated GAL4 lines in combination with elav-GAL80 (or tsh-GAL80 + cha-GAL80 in the case of A58-GAL4) to

drive UAS-CsChrimson expression in epidermal cells. All epidermal drivers except for sr-GAL4, which is expressed in apodemes but no other epidermal cells, elicited rolling responses. Genotypes: GAL4, UAS-CsChrimson, elav-GAL80/+. (C) Roll probability of larvae following thermogenetic stimulation using the indicated GAL4 line to express the warmth (35°C) -activated UAS-TrpA1. The number of rolling larvae (out of 50) is indicated for each group. Genotypes: GAL4, UAS-TrpA1, GAL80 (as indicated)/+. Control, UAS-TrpA1/+. Sample sizes are indicated in each panel. Asterisk (*) indicates $p<0.05$ in this and subsequent figures. Details of statistical analyses, including tests performed, p-values, and q-values are provided in the supplemental materials.

Figure 1 - Figure supplement 1

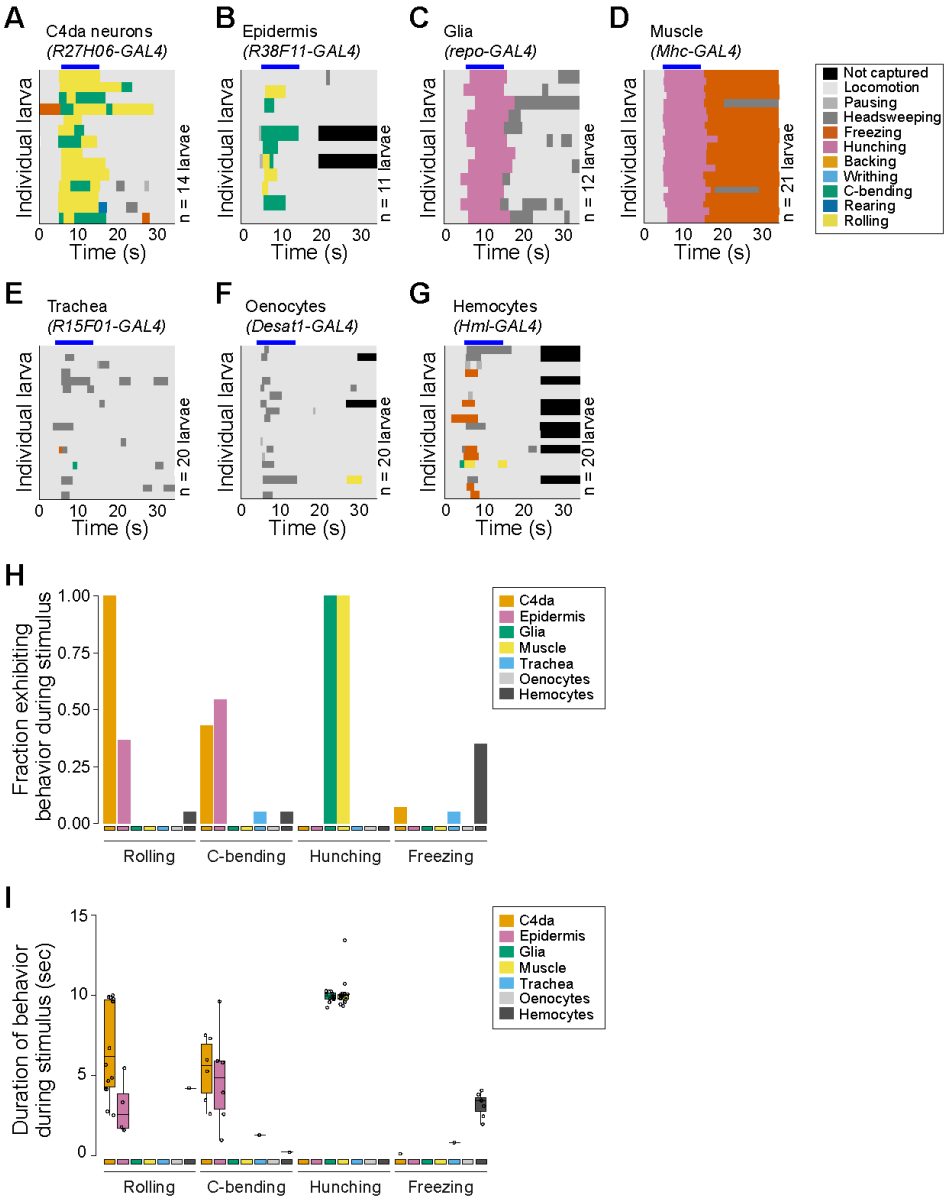

Figure 1 – figure supplement 1. Related to Figure 1A. Detailed behavior analyses of larvae following optogenetic stimulation using the indicated GAL4 lines to express *UAS-CsChrimson*. (A-G) Behavior ethograms show behaviors of individual larvae (rows) prior to, during, and after application of the light stimulus (indicated by the blue bar above the ethogram). (H) Fraction of larvae exhibiting indicated behaviors and (I) duration of indicated behaviors during light stimulus.

Figure 1 - Figure supplement 2

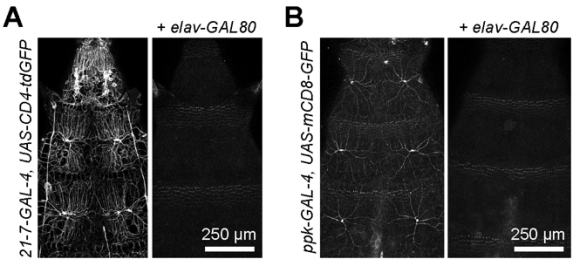

Figure 1 – figure supplement 2. Related to Figure 1A. Efficacy of *GAL80* transgenes. Maximum intensity projections show body wall expression patterns of (A) the pan-da neuron driver *GAL4*$^{21\text{-}7}$ and (B) the nociceptor-specific driver *ppk-GAL4* with or without *elav-GAL80* to silence neuronal GAL4 expression. Note that *elav-GAL80* completely suppresses GFP reporter expression from each of the drivers. Genotypes: (A) *GAL4*$^{21\text{-}7}$ *UAS-CD4-tdGFP/+* and *GAL4*$^{21\text{-}7}$ *UAS-CD4-tdGFP/+, elav-GAL-80/+*, (B) *ppk-GAL4, UAS-CD4-tdGFP/+* and *ppk-GAL4, UAS-CD4-tdGFP/+, elav-GAL-80/+*.

Figure 1 - Figure supplement 3

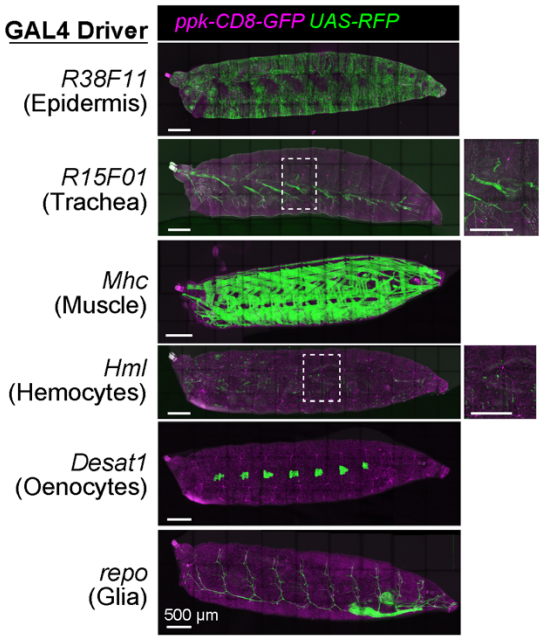

Figure 1 – figure supplement 3. Related to Figures 1A and 1C. Expression analysis of the pan-epidermal *R38F11-GAL4* driver. (A-B) Maximum intensity projections of confocal stacks show larval expression of a red fluorescent protein (*UAS-tdTomato*) under control of *R38F11-GAL4* in larvae additionally expressing *Nrg167-GFP*, an exon trap line that labels epidermal and glial membranes [157,158]. (A) Low-magnification view showing stereotyped expression in dorsal epidermis across multiple larval segments. Larvae are oriented dorsal-up. *R38F11-GAL4* is likewise expressed throughout the ventral and lateral epidermis. Compared to other epidermal drivers (see Fig. 1S5), *R38F11-GAL4* exhibited more uniform expression from segment to segment and among epidermal subpopulations within a given segment. (B) *R38F11-GAL4* expression in the dorsal epidermis of a single abdominal segment, A2. (C) High-resolution images of *R38F11-GAL4* expression visualized using a nuclear localized red fluorescent protein (*UAS-NLS-RFP*). Images depict expression in larval skin territory containing dorsal cluster of SSNs (visualized by HRP immunoreactivity), which includes the nociceptive neuron ddaC (outlined by dashed lines). Note that although *R38F11-GAL4* is expressed in epidermal cells, expression is undetectable in da neurons. The *R38F11-GAL4* expression domain likewise excludes SSNs throughout the body wall. (D) *R38F11-GAL4* expression of *UAS-NLS-RFP* in the larval CNS. *R38F11-GAL4* is expressed in a single motor neuron in each segment of the ventral ganglion, ~10 VNC interneurons, and <50 additional neurons in each brain hemisphere. (E-H) GAL80-mediated refinement of *R38F11-GAL4* expression. (E) *Tsh-GAL80* induced variegation in epidermal *R38F11-GAL4* expression and (F) suppressed VNC expression while expanding brain expression domains of *R38F11-GAL4*. (G) *Elav-GAL80* likewise induced epidermal variegation in *R38F11-GAL4* expression but (H)

completely attenuated CNS expression. Dashed lines in (D, G, and H) outline the larval brain and ventral ganglion. Genotypes: (A-B) *Nrg^{G00305}/+; UAS-tdTomato/+; GAL4^{GMR38F11}/+*, (C) *GAL4^{GMR38F11}/+, UAS-NLS-RedStinger/+*, (E-F) *Nrg^{G00305}/+; UAS-tdTomato/tsh-GAL80; GAL4^{GMR38F11}/+*, (G-H) *Nrg^{G00305}/+; UAS-NLS-RedStinger/+; GAL4^{GMR38F11}/elav-GAL80*.

Figure 1 - Figure supplement 4

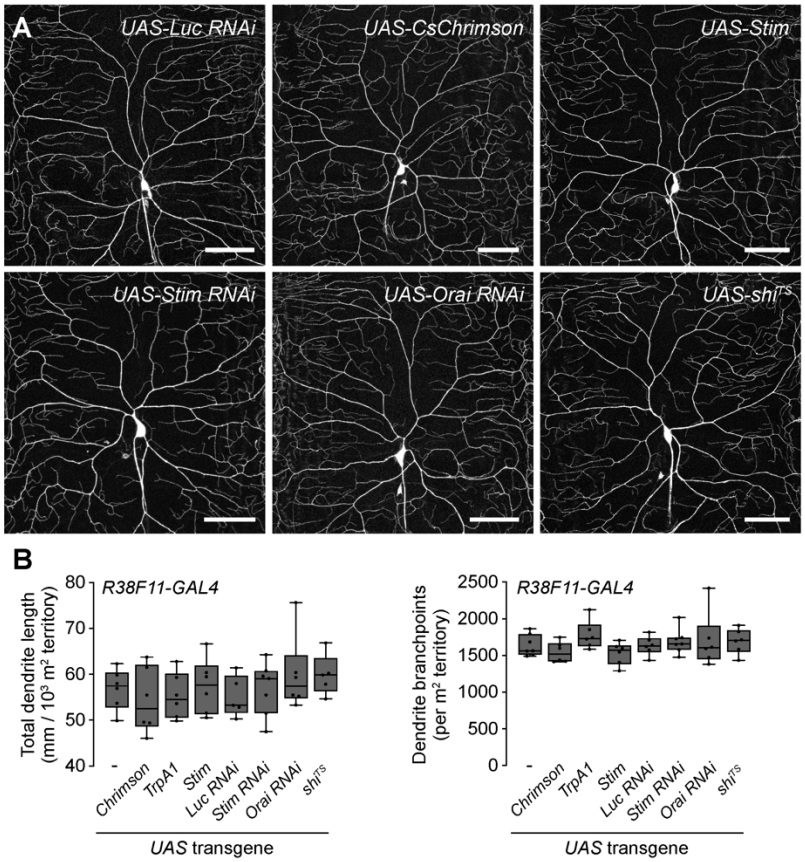

Figure 1 – figure supplement 4. Related to Figure 1A. Epidermal manipulations have no effect on C4da neuron dendrte morphogeness. (A) Maximum intensity projections show dendrites of representative C4da neurons labeled with *ppk-CD4-tdGFP* in the indicated treatment groups. (B) Morphometric analysis of C4da dendrites. Box plots depict the total dendrite length (left) and the number of dendrite branchpoints (right) normalized to larval segmental area in larvae containing the pan-epidermal driver *R38F11-GAL4* and the indicated *UAS*-transgenes at 120 h AEL. Prior to imaging, *ppk-CD4-tdGFP/+, R38F11-GAL4/UAS-shi^{TS}* larvae were incubated for 10 min at 30° C, as in Fig. 6N. N $\geq$ 6 neurons for each genotype, points represent measurements from individual neurons, boxes display the first and third quartiles, hatches mark medians, and whiskers mark maximum and minimum values. ANOVA with post-hoc Tukey's test revealed no significant difference between control and treatment groups for both metrics. Genotypes: *ppk-CD4-tdGFP/+; R38F11-GAL4/+* without (-) or with a single copy of the indicated *UAS*-transgenes.

Figure 1 - Figure supplement 5

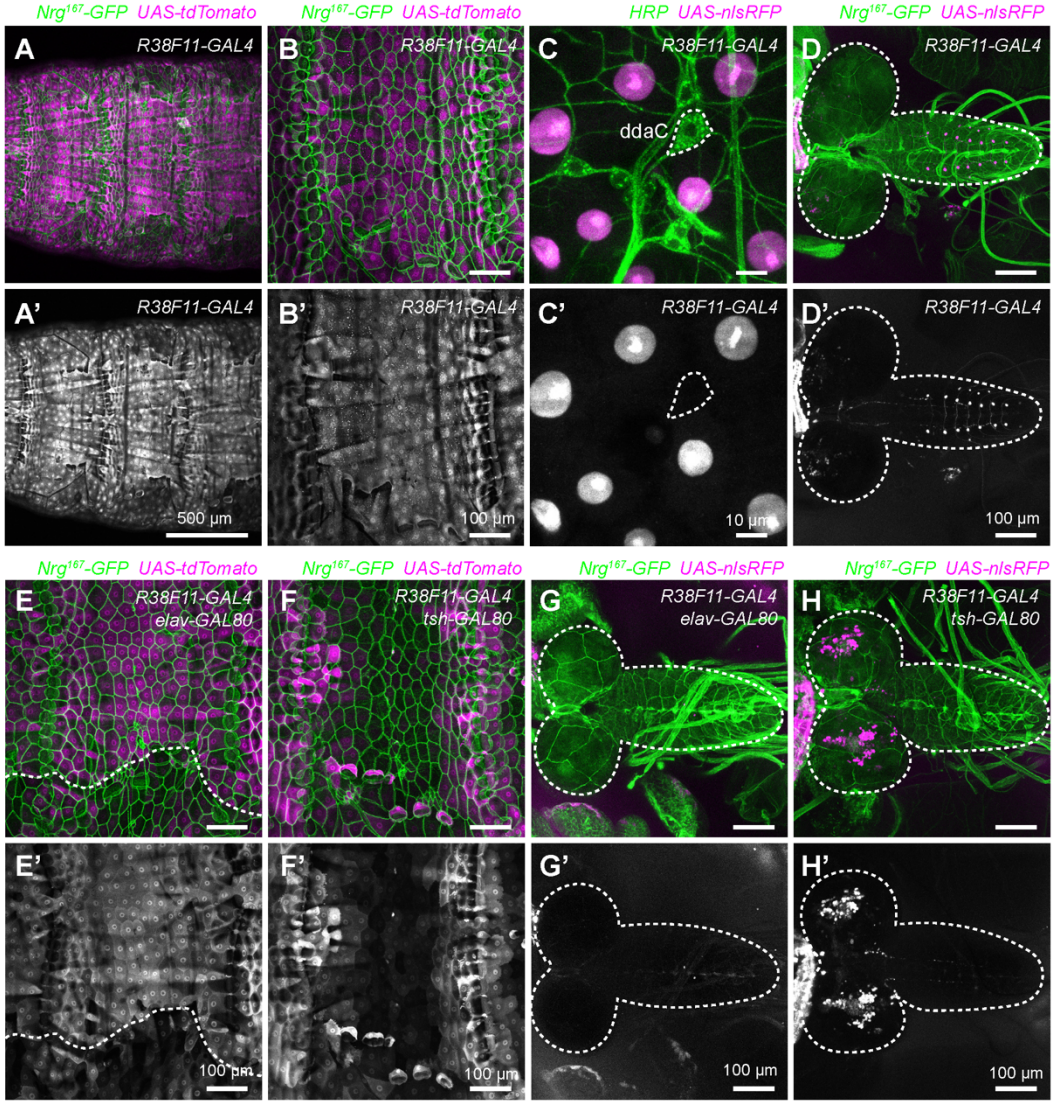

Figure 1 – figure supplement 5. Related to Figures 1A and 1C. Expression patterns of body wall *GAL4* drivers. Maximum intensity projections of tiled confocal stacks show larval expression of membrane-targeted RFP (*UAS-mCD2-Cherry*) by the indicated drivers in larvae additionally expressing the C4da neuron-specific marker *ppk-CD8-GFP*. Scale bars, 500 µm. Genotypes: *ppk-mCD8-GFP/+; UAS-mCD2-Cherry/+; GAL4/+*

Figure 1 - Figure supplement 7

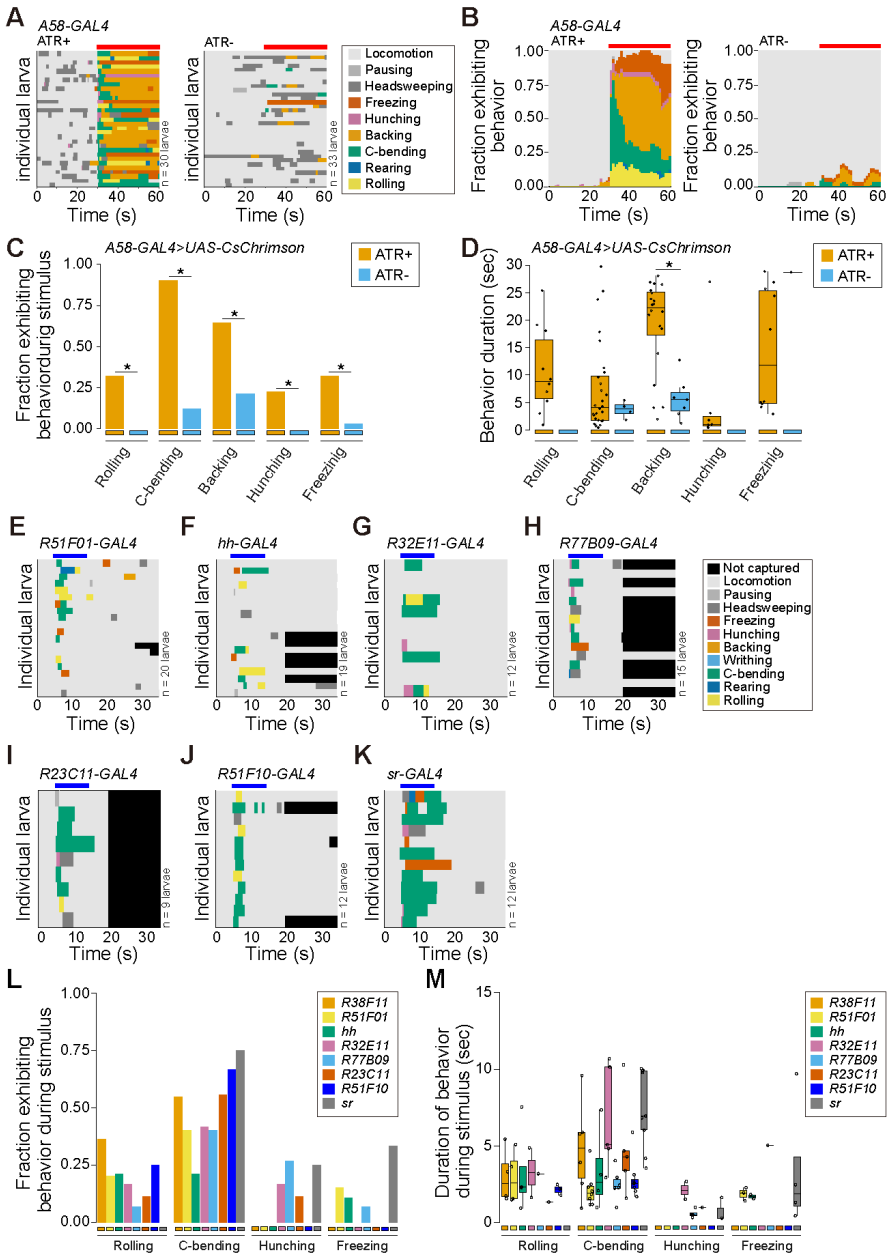

Figure 1 – figure supplement 6. Related to Figure 1B.
(A-B) Behaivior ethograms of larvae following pan-epidermal stimulation (denoted with a red bar) mediated by *A58-GAL4*. (C) Fraction of larvae exhibiting indicated behaviors and (I) duration of indicated behaviors during optogenetic stimulation. (Genotype: *A58-GAL4, UAS-CsChrimson, tsh-GAL80, cha-GAL80/+*). (E-K) Behavioral ethograms of larvae following optogenetic stimulation (denoted with a blue bar) with a panel of epidermal GAL4 drivers. (L) Fraction of larvae exhibiting indicated behaviors and (M) duration of indicated behaviors during light stimulus. Genotype: *GAL4, UAS-CsChrimson, elav-GAL80/+*.

Figure 1 - Figure supplement 7

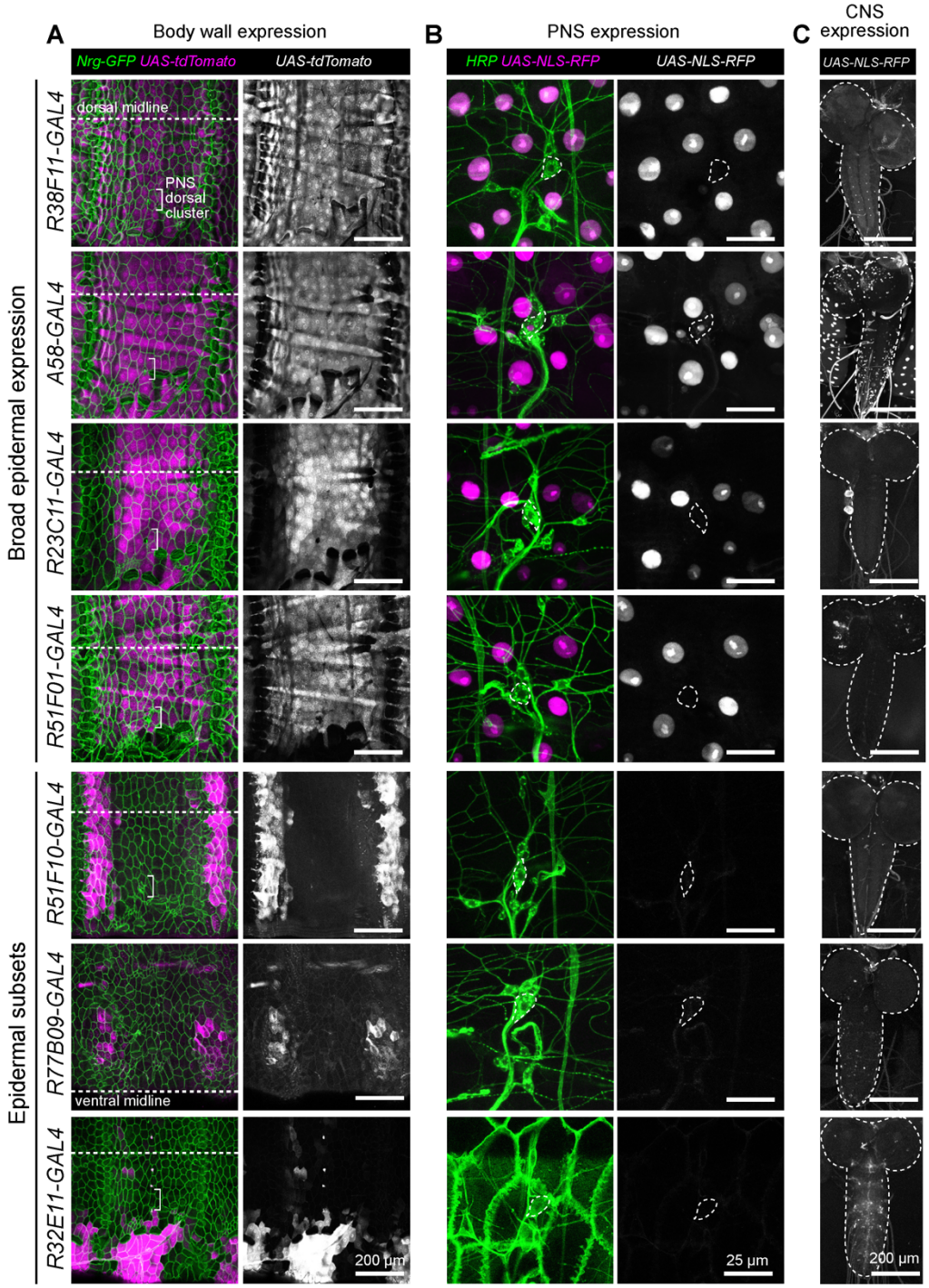

Figure 1 – figure supplement 7. Related to Figure 1B. Expression patterns of epidermal GAL4 drivers in the larval body wall and CNS. (A) Maximum intensity projections of confocal stacks show larval expression of a red fluorescent protein (*UAS-tdTomato*) under control of the indicated epidermal drivers in larvae additionally expressing *Nrg167-GFP*, an exon trap line that labels epidermal and glial membranes [157,158]. White brackets

mark the location of the dorsal cluster of SSNs, which are visualized at high resolution in (B). (B) Maximum intensity projections of confocal stacks show larval expression of a nuclear-localized form of RFP (*UAS-RedStinger*) under control of the indicated *GAL4* drivers in larval fillets stained with fluorescently conjugated anti-HRP antibody to label sensory neurons. The nociceptive C4da neuron soma is outlined with a white hatched line in composite images and the outline is superimposed on images depicting *UAS-RedStinger* signal. Sensory neuron expression is undetectable for all epidermal drivers except for *A58-GAL4*, for which stochhastic sensory neuron expression has been previously described [159]. (C) Maximum intensity projections show CNS expression epidermal drivers used in this study. Aside from *A58-GAL4*, each driver exhibits sparse nervous system expression. Genotypes: (A) Nrg^{G00305}/+; *UAS-tdTomato/+; GAL4/+*, (B-C) *UAS-NLS-RFP/+; GAL4/+*.

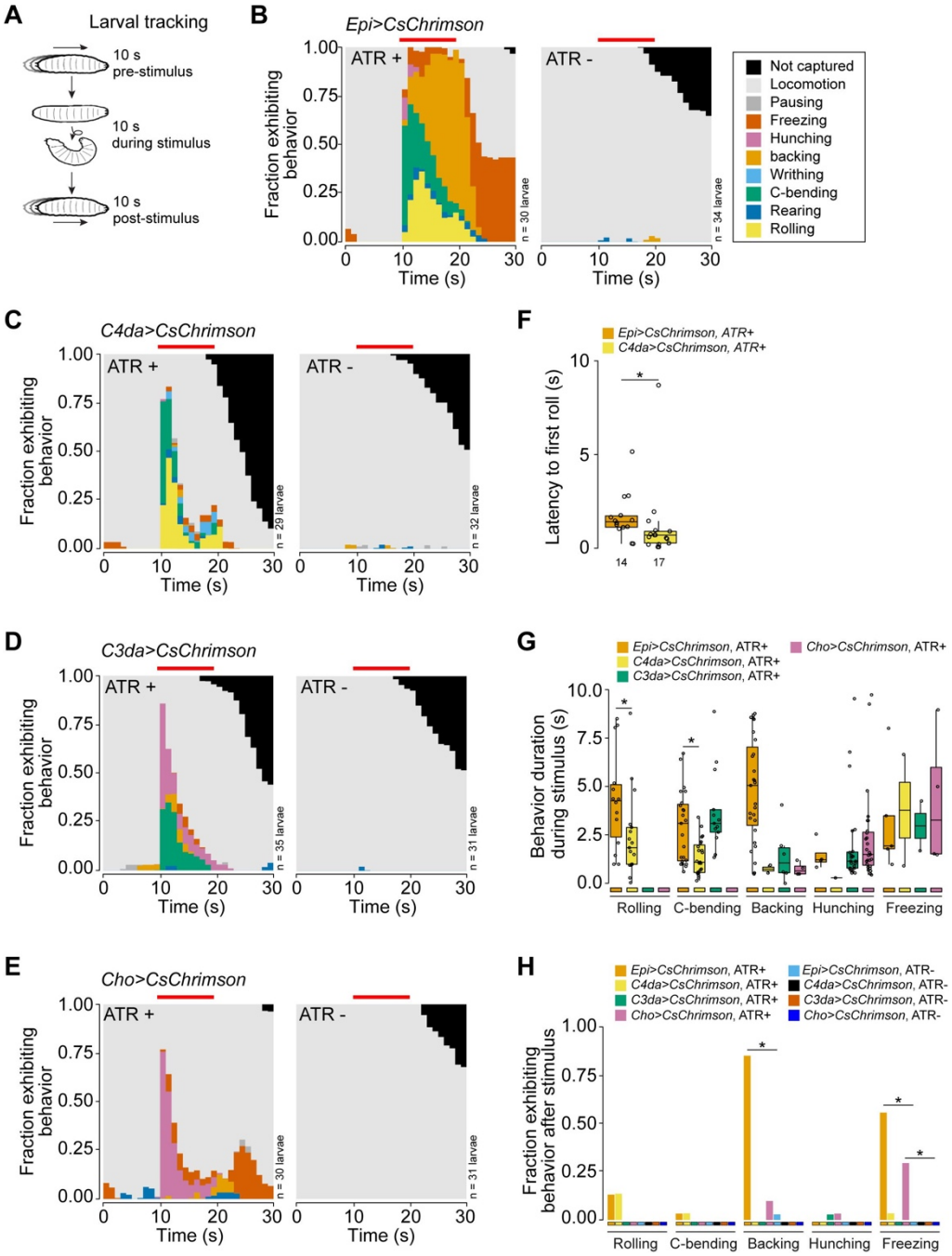

Figure 2. Stimulation of epidermal cells evokes multimodal behavioral responses.
(A) Larval behaviors were scored for 10 sec before, during, and after optogenetic stimulation. (B-E) Fraction of larvae exhibiting indicated behaviors over time in one second bins expressing CsChrimson in (B) epidermal cells, (C) C4da neurons, (D) C3da neurons, and (E) Cho neurons in the presence and absence of all-trans retinal (ATR). Red line indicates the presence of light stimulation. (F) The latency to the first roll of the larvae that rolled from *Epi>Chrimson* ATR+ and *C4da>Chrimson* ATR+ treatment groups (n = 14, 17, respectively). (G) The duration of indicated behaviors of the larvae that displayed those behaviors during optogenetic stimulation. (H) The fraction of larvae that

exhibited indicated behaviors following removal of the light stimulus of all larvae from panels (B-E). Genotypes: *GAL4, UAS-CsChrimson/+*.

Figure 2 - Figure supplement 1

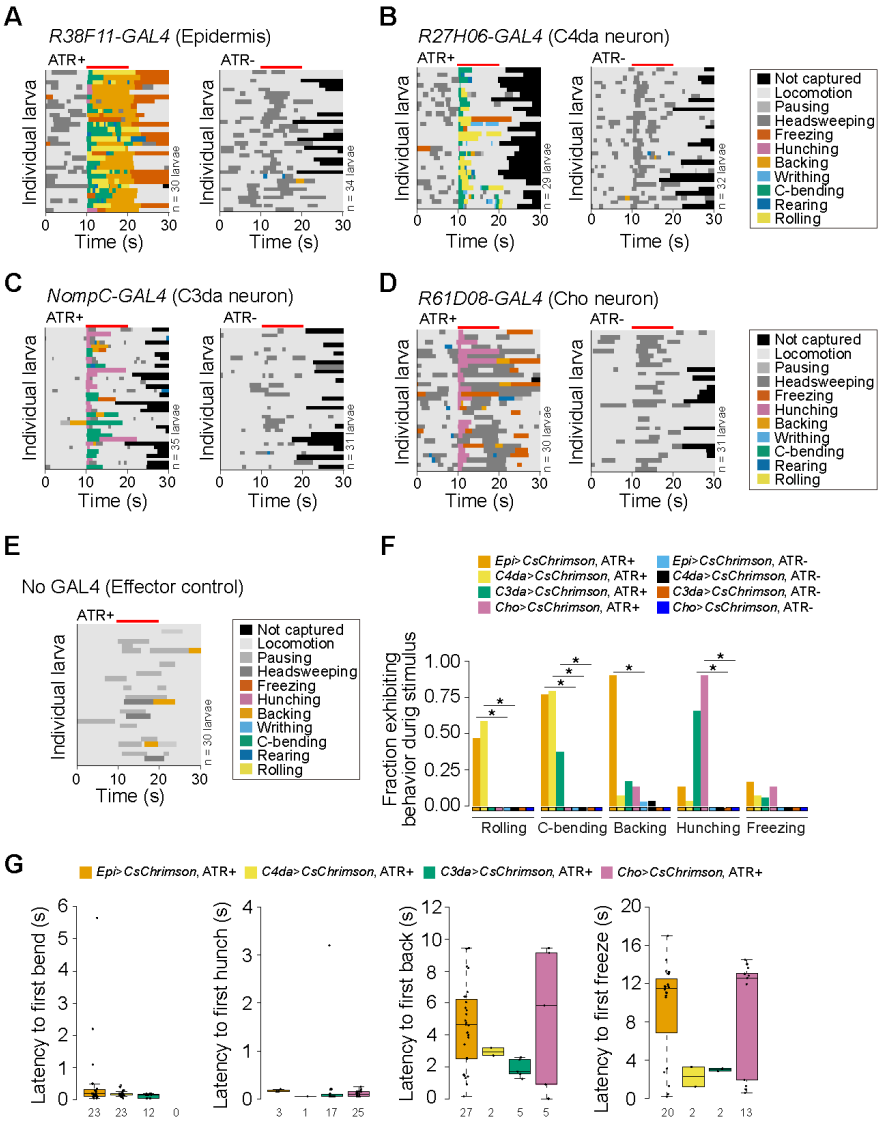

Figure 2 – figure supplement 1. (A-E) Behavior ethograms depict behaviors of individual larvae displayed in one second bins, scored for 10 sec before, during, and after optical stimulus. Plots depict responses of larvae which contain a single copy of *UAS-CsChrimson* together with the indicated *GAL4* driver in the absence and presence of ATR (A-D), or responses of effector-only (*UAS-CsChrimson*/+, ATR+) controls (E). (F) Plot depicts the fraction of larvae exhibiting indicated behaviors during light stimulus. (G) Latency to the first bend, hunch, back and freeze behaviors following optogenetic stimulation. Genotypes: *GAL4, UAS-CsChrimson/+*.

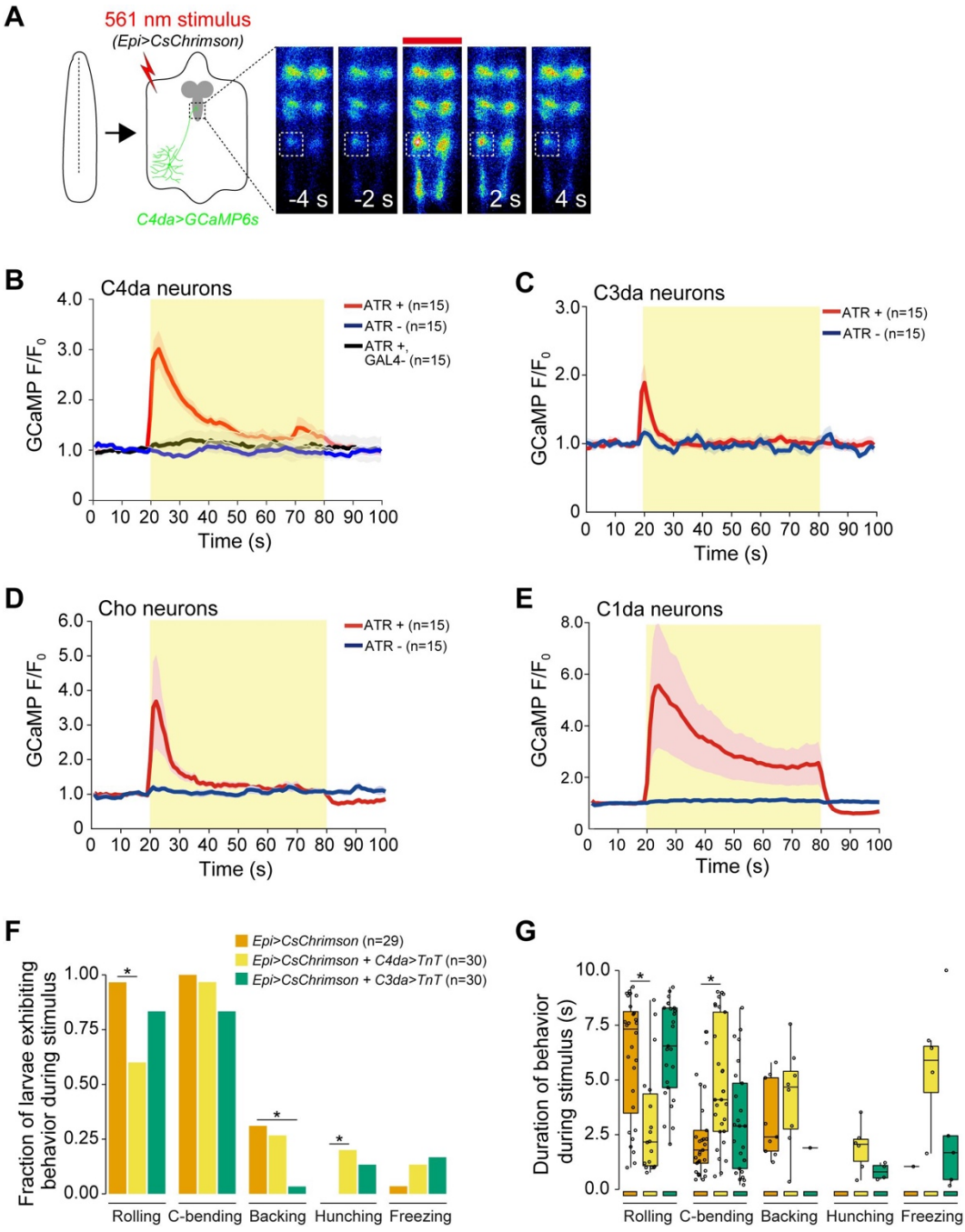

Figure 3. (A) Optogentic activation of CsChrimson-expressing epidermal cells in the body wall triggers calcium transients in the axon terminal of GCaMP6s-expressing nociceptive SSNs. Images show responses from one representative animal. Plots depict mean GCaMP6s fluorescence intensity of the axon terminals of (B) C4da, (C) C3da, (D) Cho, and (E) C1da neurons following optogenetic activation (light stimulus, yellow box) of epidermal cells over time. Solid lines depict mean GCaMP6s fluorescence across replicates (n=15 larval fillet preparations), shading indicates SEM, red traces are *GAL4+* ATR+, blue traces are *GAL4+* ATR-, black trace is *GAL4-* ATR+. (F) The fraction of larvae exhibiting indicated behaviors during optogenetic epidermal stimulation in combination with SSN silencing via Tetanus Toxin (TnT) expression. We note that although baseline

rolling probability is elevated in all genetic backgrounds containing the *AOP-LexA-TnT* insertion, silencing C4da and C3da neurons significantly attenuates responses to epidermal stimuluation. (G) The duration of the behavioral responses during optogenetic epidermal stimulation with neuronal TnT expression. Genotypes: (A-B) *R27H06-LexA* (C4da neurons), *AOP-GCaMP6s, UAS-CsChrimson/+; R38F11-GAL4/+* or *R27H06-LexA* (C4da neurons), *AOP-GCaMP6s, UAS-CsChrimson/+* (*GAL4*-ATR- effector-only control); (C) *AOP-GCaMP6s, UAS-CsChrimson/+; R38F11-GAL4/NompC-LexA* (C3da neurons); (D) *UAS-GCaMP6s, AOP-CsChrimson, R61D08-GAL4* (Cho neurons)*/R38F11-LexA*; (E) *UAS-GCaMP6s, AOP-CsChrimson, R11F05-GAL4* (C1da neurons)*/R38F11-LexA*; (F-G) *R38F11-GAL4, UAS-CsChrimson, AOP-LexA-TnT/+* (*Epi>CsChrimson*); *R38F11-GAL4, UAS-CsChrimson, AOP-LexA-TnT/ppk-LexA* (*Epi>CsChrimson + C4da>TnT*); *R38F11-GAL4, UAS-CsChrimson, AOP-LexA-TnT/NompC-LexA* (*Epi>CsChrimson + C3da>TnT*).

Figure 3 - Figure supplement 1

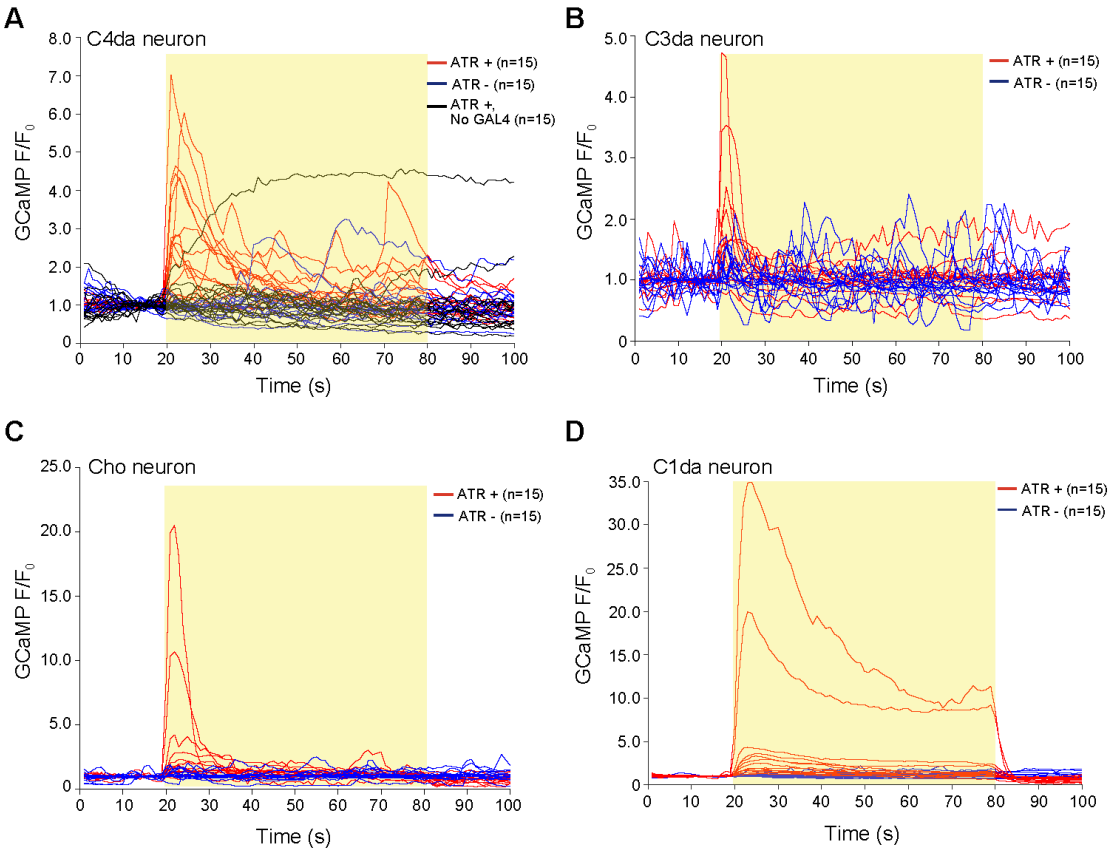

Figure 3 – figure supplement 1. Related to Figure 3A-3D. GCaMP6s responses in axon terminals of (B) C4da, (C) C3da, (D) Cho and (E) C1da neurons following optogenetic activation (light stimulus, yellow box) of epidermal cells over time. Each trace represents the GCaMP6s fluorescence of an individual larval fillet. Red traces are *GAL4+* ATR+, blue traces are *GAL4+* ATR-, black trace is *GAL4-* ATR+. Genotypes: (A) *R27H06-LexA*, *AOP-GCaMP6s, UAS-CsChrimson/+; R38F11-GAL4/+* or *R27H06-LexA*, *AOP-GCaMP6s, UAS-CsChrimson/+* (*GAL4*-ATR- effector-only control); (B) *AOP-GCaMP6s, UAS-CsChrimson/+; R38F11-GAL4/NompC-LexA*; (C) *UAS-GCaMP6s, AOP-CsChrimson, R61D08-GAL4 /R38F11-LexA*; (D) *UAS-GCaMP6s, AOP-CsChrimson, R11F05-GAL4/R38F11-LexA*.

Figure 3 - Figure supplement 2

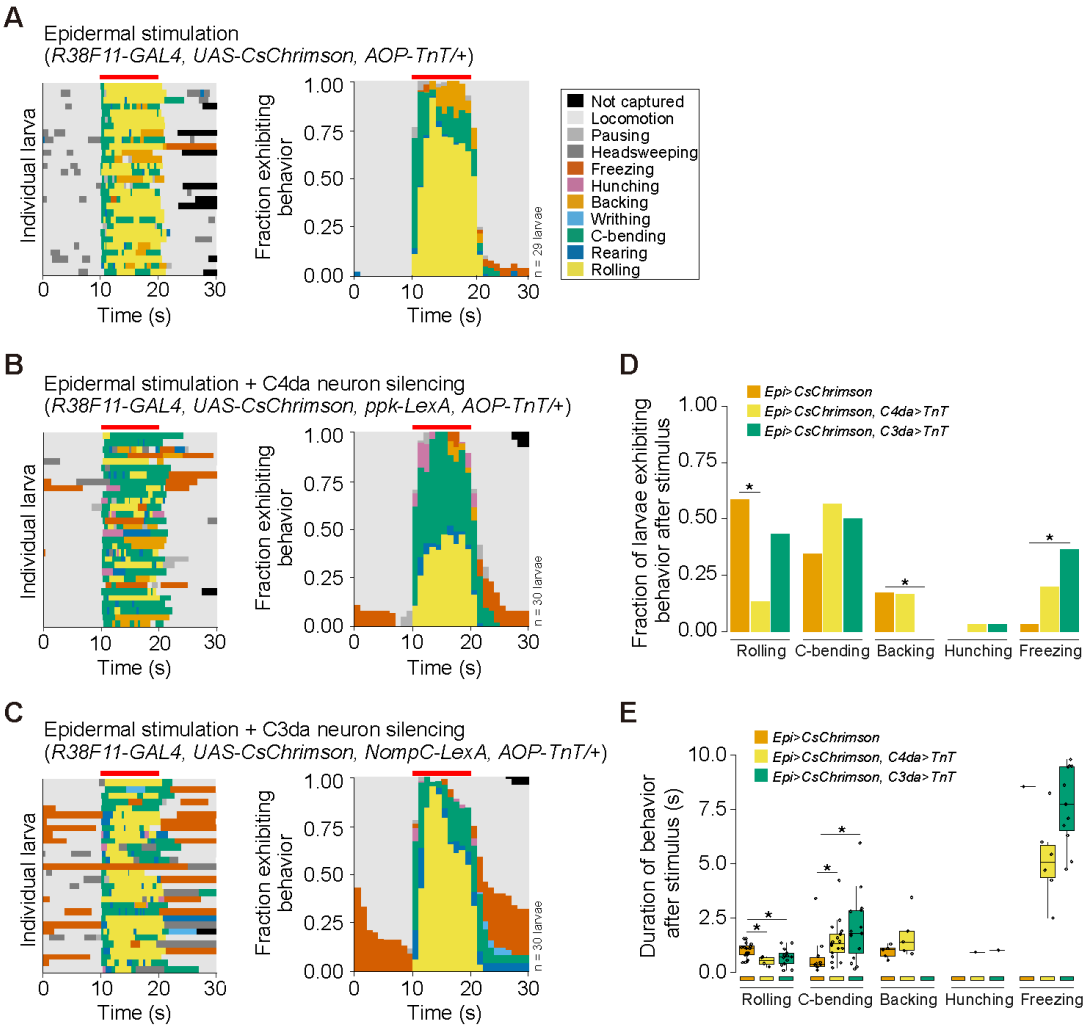

Figure 3 – figure supplement 2. Related to Figure 3E-3F. (A-C) Behavior ethograms (left) and fraction of larvae (right) exhibiting indicated behaviors to optogenetic epidermal stimulation in combination with (A) an *AOP-TNT* transgene (control lacking LexA driver), (B) C4da neuron silencing via Tetanus Toxin (TnT), and (C) C3da neuron silencing via TnT. (D) Fraction of larvae exhibiting each behavior and (E) the duration of behavior responses after removal of the light stimulus. Genotypes are indicated in (A-C).

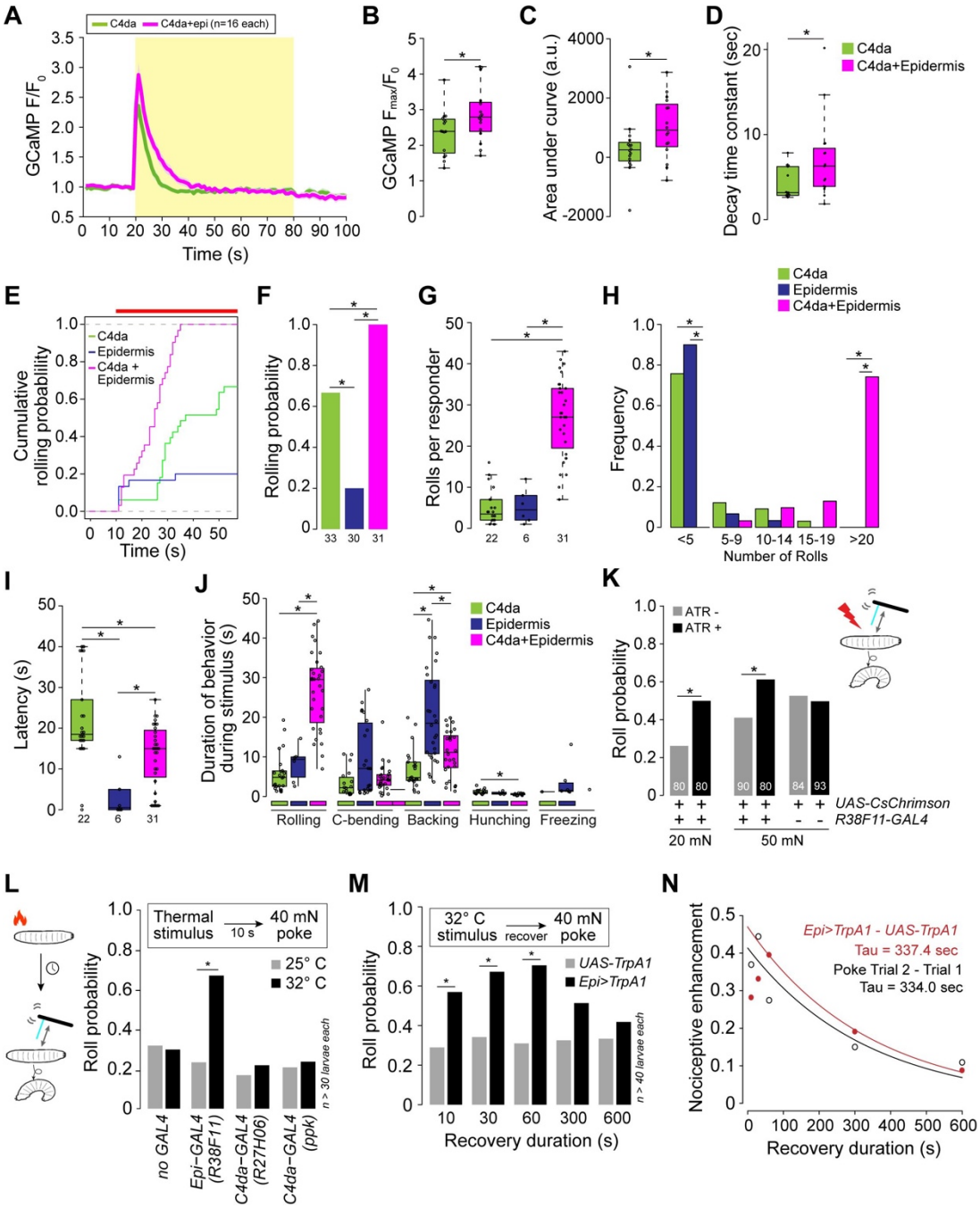

Figure 4. Epidermal stimulation augments nociceptive responses. (A) Mean GCaMP6s responses (F/F_0) in C4da axons during optogenetic stimulation (yellow box) of C4da neurons alone (green) or of C4da neurons and epidermal cells (magenta), shading indicates SEM. (B) Simultaneous epidermal stimulation increased the peak calcium response (F_{max}/F_0), (C) total calcium influx (area under the curve), and (D) duration of C4da neuron calcium responses compared to stimulation of C4da neurons alone. Genotypes: *ppk-LexA, AOP-GCAMP6s/+; R27H06-GAL4/UAS-CsChrimson* (C4da) and *ppk-LexA, AOP-GCAMP6s/+; R27H06-GAL4/R38F11-GAL4, UAS-CsChrimson* (C4da+epi). (E-J) Characterization of the behavioral responses to low-intensity optogenetic stimulation of C4da neurons, epidermal cells, or simulteanous C4da neurons

and epidermal cells. (E) Cumulative and (F) total roll probability during optogenetic stimulation (indicated by the red bar). n = 33 (*C4da>CsChrimson*), 30 (*Epi>CsChrimson*), and 31 (*C4da* + *Epi>CsChrimson*) larvae. (G, H) Number and frequency distribution of rolls, (I) latency to the first roll observed for larvae of the indicated genotypes, and (J) the duration of the indicated behaviors during light stimulus. Genotypes: *UAS-CsChrimson/+; R27H06-GAL4/+* (C4da), *UAS-CsChrimson/+; R38F11-GAL4/+* (Epidermis), *UAS-CsChrimson/+; R27H06-GAL4/R38F11-GAL4* (C4da+Epidermis). (K) Roll probability of larvae to a 20 mN or 50 mN von Frey mechanical stimulus and epidermal optogenetic activation (a light stimulus, 30mW/cm^2 that was insufficient on its own to induce nocifensive rolling). Larvae were reared in the presence or absence of ATR, as indicated. Genotypes: *UAS-CsChrimson/+; R38F11-GAL4/+*. (L-N) Prior epidermal but not nociceptor stimulus potentiates mechanical nociceptive responses. (L) Roll probability of control larvae (*UAS-TrpA1/+*) or larvae expressing TrpA1 in the epidermis (*Epi-GAL4: R38F11-GAL4)* or C4da neurons (*UAS-TrpA1/+*; *C4da-GAL4 #1: R27H06-GAL4, UAS-TrpA1/+*; *C4da-GAL4 #2: ppk-GAL4, UAS-TrpA1/+*), or control larvae (*no GAL4: UAS-TrpA1/+*;) in response to 40 mN mechanical stimulus 10 sec following 10 sec of a thermal stimulus (25º or 32º C). To control for effects of genetic background, we confirmed that each of the experimental genotypes exhibited mechanically induced nociceptive sensitization (Fig. 4S1C). (M) Roll probability of control larvae (*UAS-TrpA1/+*) or larvae expressing TrpA1 in the epidermis (*Epi>TrpA1*: *R38F11-GAL4, UAS-TrpA1/+*) in response to a 40 mN mechanical stimulus delivered at the indicated time interval following a 32º C thermal stimulus. (N) Nociceptive enhancement (difference in the roll probablity to the first and second stimulus) is plotted against the recovery duration and results were fit to an exponential curve to derive the decay time constant. The red line indicates nociceptive enhancement of a mechanical stimulus by a prior epidermal thermogenetic stimulus; the black line indicates nociceptive enhancement by a prior mechanical stimulus.

Figure 4 - Figure supplement 1

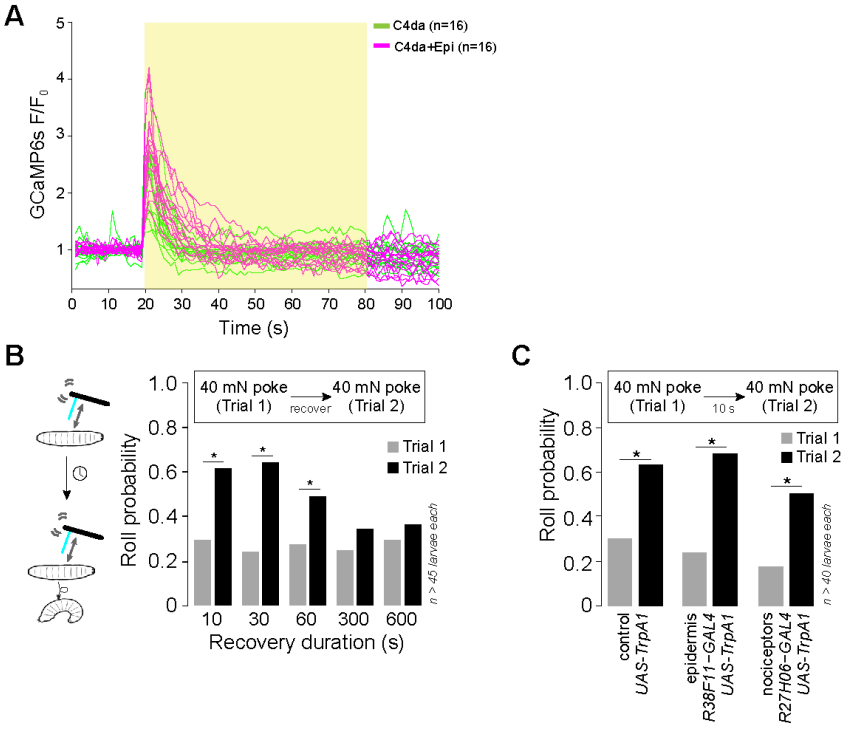

Figure 4 – figure supplement 1. (A) GCaMP6s responses (F/F_0) of individual replicates during optogenetic stimulation (yellow box) of C4da neurons alone (green) or C4da neurons and epidermal cells (magenta), yellow box indicates presence of light stimulus. Genotypes: *ppk-LexA, AOP-GCAMP6s/+; R27H06-GAL4/UAS-CsChrimson* (C4da) and *ppk-LexA, AOP-GCAMP6s/+; R27H06-GAL4/R38F11-GAL4, UAS-CsChrimson* (C4da+epi). (B) Roll probability of larvae in response to two successive 40 mN mechanical stimuli spaced by the indicated amount of time (recovery duration). Genotype: *R38F11-GAL4/+*. (C) Roll probability of larvae expressing *UAS-TrpA1* in nociceptors exhibited levels of mechanically induced nociceptive potentiation comparable to other experimental genotypes used in the study (control*: UAS-TrpA1/+*; epidermis*: R38F11-GAL4, UAS-TrpA1/+*; nociceptors*: R27H06-GAL4, UAS-TrpA1/+*).

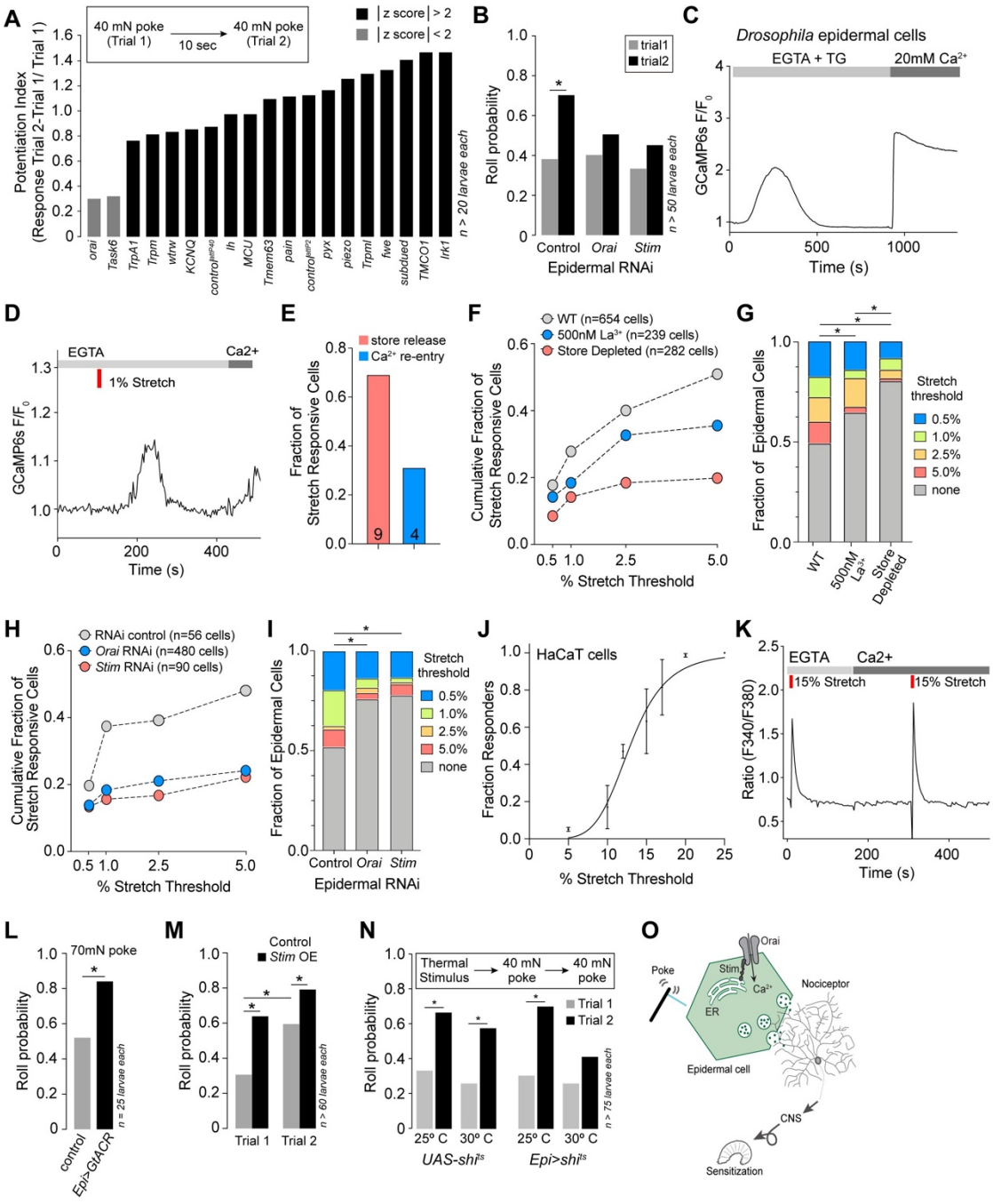

Figure 5. Epidermal cells are intrinsically mechanosensitive. (A) Schematic of preparation to measure radial stretch evoked calcium responses of dissociated epidermal cells. (B) Representative calcium responses of a dissociated epidermal cell to 0.5% and 1% radial stretch (successive stimuli), 2.5% radial stretch, and 5% radial stretch. (C) Dose response curve displaying the fraction of epidermal cells activated by increasing magnitudes of stretch. Red trace displays the mean ± SEM across six independent dissociated cell preparations, obtained from a minimum of 6 larvae. Gray traces display fraction responding in each dissociated cell preparation replicate. (D) Subsets of epidermal cells display varying stretch thresholds, n = 6 dissociated cell preparations, for a total of 654

epidermal cells. (E) Representative mechanically induced epidermal calcium responses in the larval body wall. Images show GCaMP6s fluorescence intensity 100 msec prior to (i) and 20 sec following (ii) a 25 μm membrane displacement (poke). (F) Distribution of the peak calcium response (F_{max}/F_0) to a 25 μm membrane displacement (poke) of 24 cells from 24 independent larval fillets. Cells were classified as responders (>10% increase in normalized GCaMP6s fluorescence). (G) Mean calcium responses (F/F_0) of poke responders and non-responders (n = 12 cells each). Solid lines depict mean normalized GCaMP6s fluorescence and shading indicates SEM. Genotype: *R38F11-GAL4, UAS-GCaMP6s*.

Figure 5 - Figure supplement 1

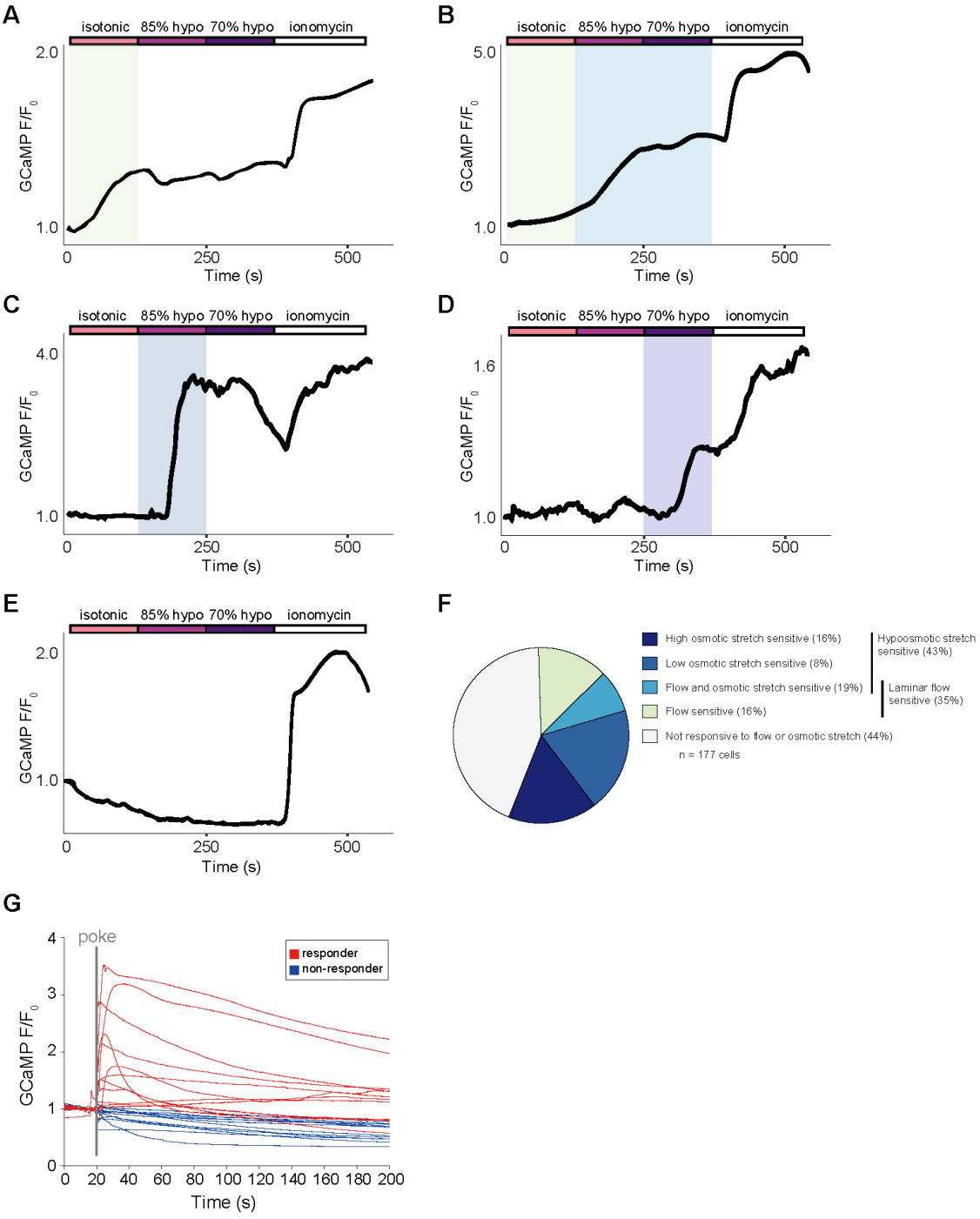

Figure 5 – figure supplement 1. Subsets of epidermal cells display calcium responses to diverse mechanical stimuli. Representative calcium traces of epidermal cells that respond to: (A) laminar flow via perfusion, (B) laminar flow and osmotic stretch, (C) 15% hypo-osmotic stretch, and (D) 30% hypo-osmotic stretch, or (E) do not respond to either

flow or stretch. (F) Proportion of epidermal cells that are sensitive to mechanical stimuli. n = three distinct cell preparations, 6 larvae per preparation, for a total of 177 cells. (G) Related to Figure 5G. GCaMP6s responses (F/F_0) of individual epidermal cells to a 25 μm membrane displacement. Genotype: *R38F11-GAL4, UAS-GCaMP6s*.

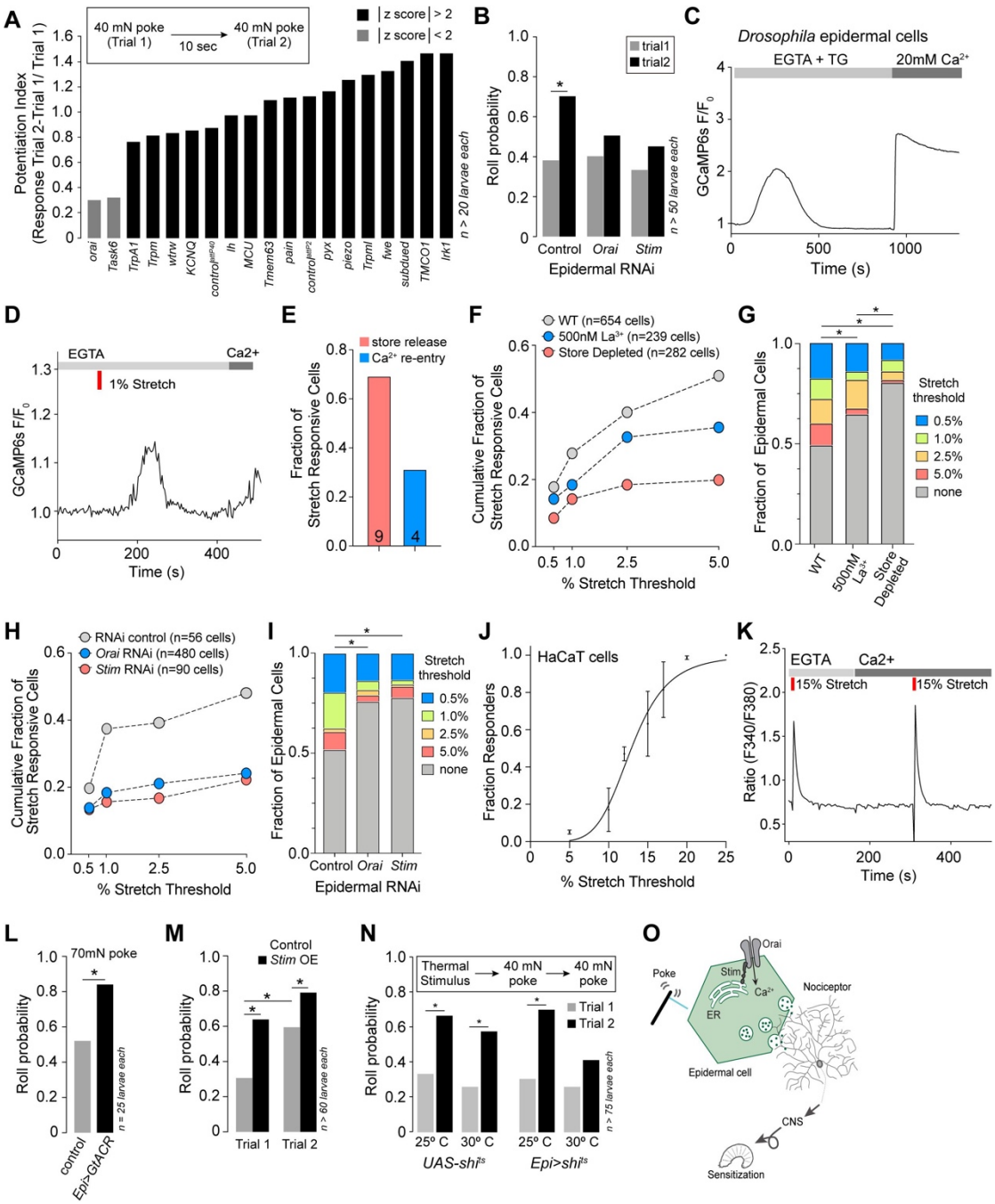

Figure 6. CRAC channels are required for epidermal mechanosensory responses and epidermal nociceptive potentiation. (A) RNAi screen for epidermal ion channels required for mechanically induced nociceptive potentiation. Bars depict nociceptive potentiation index (difference in the larval roll probability to the first and second mechanical stimuli divided by roll probability to the first mechanical stimulus). Candidate channels were chosen for further analysis if they had a a z-score greater than 2 (absolute value). (B) The CRAC channels Orai and Stim are required in epidermal cells for mechanically evoked nociceptive potentiation. Roll probability of larvae of the indicated genotypes (Control

RNAi, *R38F11-GAL4, UAS-RFP-RNAi/+*; *Stim* RNAi, *R38F11-GAL4, UAS-Stim-RNAi/+*; *Orai* RNAi, *R38F11-GAL4, UAS-Orai-RNAi/+*) to a 40 mN mechanical stimulus followed by a second 40mN mechanical stimulus 10 sec later. (C) *Drosophila* epidermal cells display classical store-operated calcium entry (SOCE). Treatment with the drug thapsigargin (TG) in the absence of extracellular calcium promoted depletion of intracellular calcium stores and calcium influx, following extracellular calcium re-addition. (D) Like TG, 1% stretch in the absence of extracellular calcium induced depletion of intracellular calcium stores and calcium influx, following extracellular calcium re-entry. (E) 69% of stretch responsive cells displayed greater calcium influx during intracellular calcium stores release than during the calcium re-entry phase. (F-G) The Orai blocker, lanthanum chloride (500 nM) or the depletion of intracellular stores by thapsigargin (1 μM) reduces the fraction of stretch-sensitive epidermal cells. (H-I) The fraction of stretch-sensitive epidermal cells is significantly decreased in cells isolated from larvae expressing *Stim* RNAi, or *Orai* RNAi, as compared to control RNAi. (J) Stretch stimuli evoke dose-dependent calcium signals in the human keratinocyte HaCaT cell line. (K) Representative stretch-evoked SOCE calcium response in HaCaT cells. Stretch induces calcium release from stores in the absence of extracellular calcium and a greater calcium influx in the presence of extracellular calcium. (L) Epidermal hyperpolarization enhances mechanical nocifensive responses. Roll probability of larvae expressing GtACR in epidermal cells (*R38F11-GAL4, UAS-GtACR/+*) or control larvae (*R38F11-GAL4/+*) to a single 70 mN mechanical stimulus. (M) Epidermal *Stim* overexpression enhances mechanical nocifensive responses. Roll probability of *Stim*-overexpressing larvae (*R38F11-GAL4, UAS-Stim/+*) and control larvae (*R38F11-GAL4/+*) to two successive 40 mN mechanical stimuli delivered 10 sec apart. (N) Epidermal potentiation of mechanical nociceptive responses requires exocytosis. Roll probability of control larvae (*UAS-shi^{ts}/+*) or larvae expressing temperature-sensitive dominant-negative shibire in epidermal cells (*R38F11-GAL4, UAS-shi^{ts}/+*) in response to two successive mechanical stimuli that followed 10 min of conditioning at the permissive (25º C) or non-permissive (30º C) temperature. (O) Model of epidermal-neuronal signaling. Mechanically evoked Stim/Orai calcium signaling in epidermal cells drives calcium influx and vesicle release that drives nociceptor activation and mechanical sensitization via activation of C4da nociceptors.

Figure 6 - Figure supplement 1

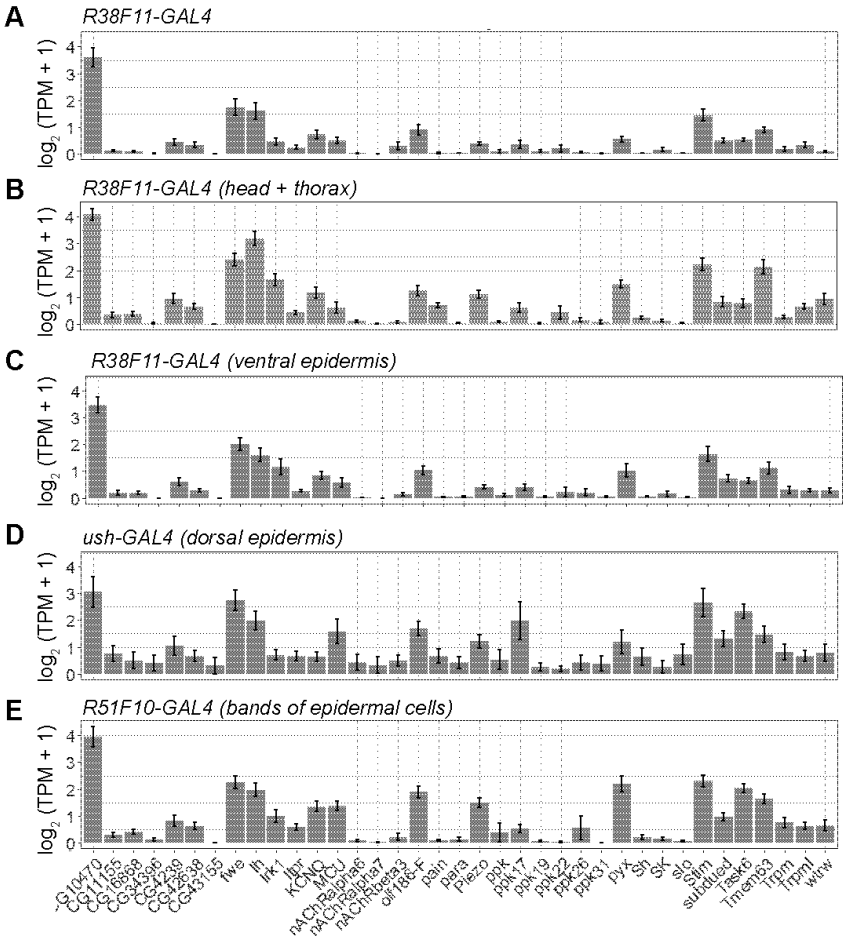

Figure 6 – figure supplement 1. Related to Figure 6A. Ion channel expression in epidermal cells. Five populations of *UAS-GFP*-expressing epidermal cells were selected for RNA-seq analysis. GFP-positive epidermal cells were dissociated into single cell suspensions, manually picked, and subjected to RNA-Seq analysis. Plots depict expression levels (mean +/- standard deviation) of the indicated ion channels (log_2(TPM+1)) from n > 6 independent libraries for each sample type.
(A) Expression in epidermal cells collected from *R38F11-GAL4* which labels all epidermal cells. (B) Anatomically defined subsets of epidermal cells were profiled by removing posterior segments from *R38F11-GAL4, UAS-GFP* larvae (*R38F11-GAL4* head and thorax) or (C) dissecting the ventral epidermis (*R38F11-GAL4* ventral epidermis). (D) Expression in the dorsal epidermis (*ush-GAL4*) and or (E) bands of epidermal cells (*R51F10-GAL4).*

Figure 6 - Figure supplement 2

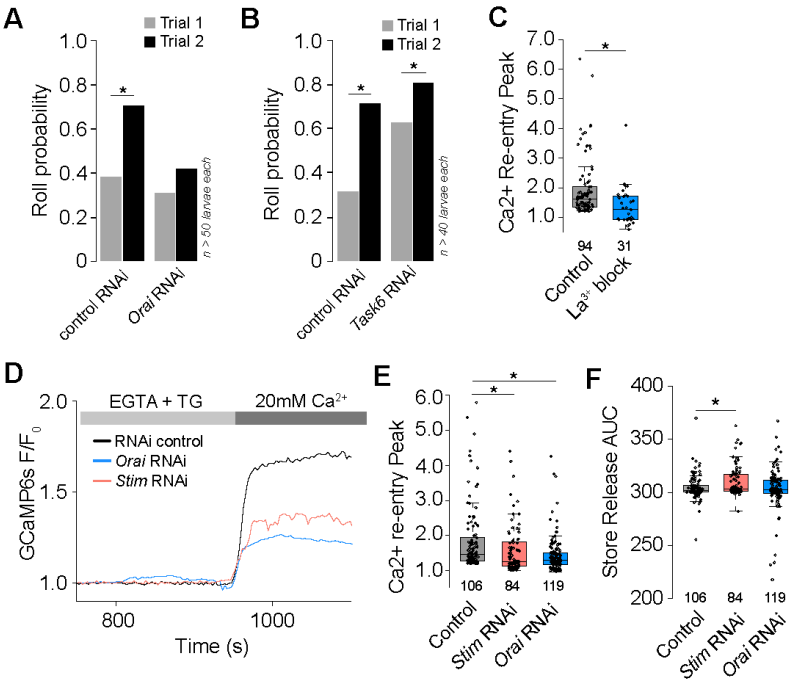

Figure 6 – figure supplement 2. (A-B) Epidermal knockdown of ion channels affects larval mechanical nociceptive responses. Roll probability in response to the first and second mechanical stimulus for larvae expressing RNAi transgenes to (A) *Orai* or *attP40* RNAi control transgene and (B) *Task6* or *attP2* RNAi control transgene. (C) Epidermal cell SOCE is attenuated by pre-treatment with the Orai blocker, lanthanum chloride (100 nM). (D) Representative SOCE after treatment with TG (1 μM) in epidermal cells isolated from larvae treated with control RNAi, *Stim* RNAi (red), or *Orai* RNAi, (blue). (E) Peak calcium response following SOCE in epidermal cells isolated from larvae treated with control RNAi, *Stim* RNAi (red), or *Orai* RNAi, (blue). (F) *Stim* RNAi decreases calcium store content of epidermal cells. Calcium store content was measured as the area under the curve of the cytosolic calcium response to TG (1 μM) in the absence of extracellular calcium.

Discussion

In this study, we have shown an essential role for Drosophila epidermal cells in escape responses to noxious mechanical stimuli. Activation of epidermal cells acutely activates SSNs to induce an array of behavioral outputs and mechanical sensitization. This epidermal potentiation persists for minutes to promote a prolonged, but reversible, mechanical hypersensitivity that may protect from further insult. This is distinct from previously described forms of neuropathic thermal and mechanical hypersensitivity in Drosophila which are induced by tissue damage and chemotherapuetic agents, respectively, emerge on a timescale of hours, and are long-lasting[117,118,160]. In the mammalian somatosensory system, a variety of inflammatory mediators have been shown to activate TRPA1 in neurons to promote mechanical hypersensitivity[161]; however, the molecular force transducers that mediate mechanical pain are unknown. In contrast, in the *Drosophila* somatosensory system, Ppk1/Ppk26, Piezo, and Trpa1 are key transducers of mechanonociception[162–166]. Prolonged sensitization to noxious mechanical stimuli plays an important protective role in an organism's survival; yet the mechanisms of mechanical sensitization of Drosophila nociceptors were unknown.

We demonstrate a new role for SOC signaling in both Drosophila and human epidermal cell mechanotransduction. While short-term sensitization is beneficial to survival, a key hallmark of pathological pain is prolonged and persistent mechanical hypersensitivity; whether deregulation of this mechanism of epidermis-evoked short-term sensitization contributes to pathological pain remains to be determined. Overall, we identified a mechanism that does not impact acute nociception but selectively regulates mechanical sensitization. These findings highlight Stim/Orai signaling as a new avenue for understanding mechanical pain.

This work has opened several new directions for future studies. First, how does radial and osmotic stretch lead to the activation of store-operated calcium signaling? Although Orai has not previously been shown to be mechanosensitive, our studies revealed a requirement for Orai and its activator Stim in mechanically-evoked calcium flux in Drosophila epidermal cells. We also showed that radial stretch of human keratinocytes triggered calcium release from stores and SOCE; our previous studies showed that Stim and Orai are required for SOCE in human keratinocytes[36]. These data in combination with previous findings that showed mechanical stimulation of human mesenchymal stem cells also triggers SOCE[167] suggests that Stim/Orai signaling may represent a conserved pathway for mechanotransduction in non-neuronal cells.

Second, how is Stim/Orai function linked to mechanotransduction? Stim/Orai signaling is activated downstream of G-protein coupled receptors (GPCRs) and receptor tyrosine kinases (RTKs) through phospholipase C. Studies have shown that a number GPCRs are mechanosensitive[168–172], though this has not been studied in epidermal cells. Alternatively, plasma membrane deformation has been shown to induce ER-plasma membrane junctions[173,174], where Stim and Orai clusters accumulate and interact to drive calcium influx[175].

Third, how does mechanically-induced singaling in epidermal cells lead to modulation of SSNs? Our data support a model whereby epidermal cells and multiple classes of SSNs are functionally coupled. Epidermal stimulation modulates activity of nociceptive C4da neurons, mechanosensory C3da and Cho neurons, and proprioceptive C1da neurons, and the output of neuronal activity is required for epidermis-evoked behaviors. We demonstrated a requirement for dynamin-dependent vesicle release from epidermal cells in mechanical sensitization, providing a potential link between Stim/Orai signaling in epidermal cells and downstream neuronal activity. However, the mediators that are released by epidermal cells and the signaling molecules in the nociceptors remain unknown. Furthermore, whether different types of SSNs are coupled to epidermal cells by distinct mechanisms remains to be determined. At least in the case of Cho neurons which are wrapped by ensheathing glial cells and scolopale cells, signaling from epidermal cells likely involves at least one additional cell type.

Epidermal cells ensheath peripheral arbors of some SSNs, including Drosophila nociceptive C4da neurons and, to a lesser extent, mechanosensory C3da neurons[131]. Hence, epidermal sheaths could facilitate transduction of epidermal signals that modulate nociceptor function. Consistent with this possibility, blocking ensheathment attenuates Drosophila larval responses to noxious mechanical stimuli[131] and likewise impairs function of some *C. elegans* mechanosensory neurons[176]. However, our finding that epidermal stimulation evokes calcium responses from SSNs that are not ensheathed by epidermal cells (C1da, Cho neurons) argues that epidermal sheaths are unlikely to play an essential function in epidermis-SSN functional copuling. Instead, ensheathment may facilitate nociceptor activation by increasing the efficiency of vesicular exchange or, alternatively, may modulate nociceptor activity through through enhanced ionic coupling to epidermal cells.

Which epidermal-derived molecules might modulate neuronal activity? There are several mechanisms by which mammalian epidermal cells activate SSNs. Vesicular release of norepinephrine from mouse epidermal Merkel cells is required for sustained touch-evoked firing of mechanosensory neurons[177]. Additionally, mechanical stimuli trigger ATP release from mouse keratinocytes that activates nociceptors via purinergic (P2X4) receptors [121,143,146]. Finally, Stim/Orai-dependent SOCE mediates the release of the cytokine thymic stromal lymphopoietin (TSLP) from keratinocytes that directly activates a subset of TRPA1-expressing SSNs to induce itch[36]. Similar to these mammalian models, UV-damage has been shown to induce the release of the cytokine Eiger to promote nociceptor sensitization[117]; though this occurred on a slower timescale than the epidermal-evoked mechanical sensitization we describe here (8 hrs vs. ~ 10 sec, Fig. 4L). Likewise, epidermal platelet-derived growth factor (PDGF) ligands regulate mechanonociceptive responses in Drosophila[178] and intrathecal delivery of PDGF or the closely related growth factor EGFR yields mechanical hypersensitivity in rats[179,180], but it remains to be determined whether growth factor signaling can yield rapid sensitization. Hence, future studies will address which neurotransmitters, neuropeptides, or inflammatory mediators underly epidermal cell-mediated mechanical sensitization.

Our data support a model whereby epidermal cells and multiple classes of SSNs are functionally coupled. Future studies will address which neurotransmitters, neuropeptides, or inflammatory mediators underly epidermal cell-mediated mechanical sensitization. An additional key next step is understanding whether the neuronal plasticity underlying mechanical sensitization results from the direct modulation of mechanosensitive channels or rapid insertion of new mechanosensitive channels into the plasma membrane, or from changes in the signaling pathways or channels that regulate neuronal excitability. Overall, we performed an unbiased genetic screen that for the first time establishes a key role for mechanically-evoked Stim/Orai calcium signaling in epidermal cells that drive nociceptor modulation and mechanical hypersensitivity.

Methods

Drosophila strains

Flies were maintained on standard cornmeal-molasses-agar media and reared at 25° C under 12 h alternating light-dark cycles. For all experiments involving optogenetic manipulations, larvae were raised in the constant dark at 25 °C on Nutri-Fly Instant Food (Genesee Scientific #66-117), supplemented with 1 mM all-trans retinal (ATR; Sigma #R2500). See Table S1 for a complete list of alleles used in this study. Experimental genotypes are listed in figure legends.

Behavior analysis

Optogenetic behavior screen

Individual larvae were rinsed in ddH2O, transferred to an agarose substrate (1% agarose, 100 mM dish) in a darkened arena, and habituated for 30 sec. Larvae were stimulated with a top-mounted 488 nM LED illuminator (PE-300, CoolLED) and images were captured with a sCMOS camera (Orca Flash 3.0, Hamamatsu) at frame acquisition rate of 20 fps and behaviors were scored before, during and after optogenetic stimulation.

High resolution video tracking of optogenetic-gated larval behavior

Following 5 min of light deprivation including 15 sec of habituation in the behavioral arena, larvae were tracked before, during and after optical stimulus (10 sec each, 30 sec total) (Fig. 2A). For these studies we modified our stimulation paradigm in two key ways: to avoid potential contributions of nociceptor light evoked responses [181], we stimulated larvae using yellow-shifted light; and to facilitate kinetic analysis of behavior outputs, we used an automated shutter. Larvae were stimulated with a top-mounted 585 nm LED illuminator (SPECTRA X, Lumencor) equipped with a filter (FF01 585/40-25, Semrock), and images were captured with a sCMOS camera (Zyla4.2, Andor) at a frame rate of 20Hz. Larvae were constantly illuminated with an infrared (940 nm) light source (LDR2-132IR2-940-LA, CSS) for visualization. Larvae were fed (ATR+) or vehicle alone (ATR-) as indicated.

Thermogenetic behavior assays

Larvae for thermogenetic assays were reared at room temperature (20° C) to limit TRPA1 activation during development. Third instar larvae were isolated from their food, washed in distilled water, and recovered to damp agar plates for several min, and transferred individually to a Peltier plate held at 25° C or 35° C. Behavior responses were recorded under infrared light with a computer-controlled GigE camera (FLIR) at an acquisition rate of 20 fps for 20 sec. Responses were analyzed post-hoc blind to genotype and were plotted as the proportion of larvae that exhibited at least one complete nocifensive roll during stimulus application.

Mechanonociception assays

Third instar larvae were isolated from their food, washed in distilled water, and placed on a scored 35 mm petri dish with a thin film of water such that larvae stayed moist but did not float. Larvae were stimulated dorsally between segments A4 and A7 with calibrated Von Frey filaments that delivered the indicated force upon buckling, and nocifensive rolling responses were scored during the 10 sec following stimulus removal. For assays involving multiple stimuli, larvae were stimulated individually, allowed to freely locomote in the arena for up to 1 min (for longer recoveries larvae were recovered onto 2% agar to prevent desiccation), and subsequently presented with the second stimulus. For assays involving thermal and mechanical stimuli, larvae were individually transferred to a pre-warmed Peltier plate containing a thin layer of water, incubated for the indicated time, and transferred to the behavior arena (or a 2% agar plate for recoveries > 1 min) with a paint brush for subsequent mechanical stimulation. All assays were conducted in ambient light except for experiments with GtACR (Fig. S72), which were conducted under broad-spectrum (500-700 nm) LED illumination (CoolLED PE-300, green). Our illumination setup for these experiments provided limited working distance, therefore larvae were restrained with forceps and given only a single stimulus.

Video annotations

Videos of individual larvae responding to light stimuli were scored on a frame-by-frame basis using the annotation software BORIS[182]. Behaviors scored, along with descriptions of the criteria for each behavior, are detailed in Table S2. Video analysts were blind to the genotype and treatment during scoring. Scoring on a training set was compared across all analysts to calibrate, and any behaviors for which the primary analyst was uncertain were reviewed by an additional analyst. Additionally, 10% of videos were scored independently by two analysts and there was at least 80% concordance in behaviors annotated in these comparisons.

Microscopy

Calcium imaging: ventral nerve cords

Third-instar larvae were dissected along the dorsal midline and pinned on a sylgard-coated dish (Silpot 184, Dow Corning Toray). The internal organs except for neural tissues were removed. Larvae were bathed in HL3.1 (Feng et al, 2004) modified to remove calcium (Table S3) to minimize larval movement. The ventral nerve cord was imaged using an Olympus BX51WI microscope, equipped with a spinning-disk confocal unit Yokogawa CSU10 (Yokogawa) and an EM-CCD digital camera (Evolve, Photometrics). For activation of epidermal cells with the light gated CsChrimson, red light was delivered by a pE-300 (CoolLED) equipped with a filter (ET645/30x, Chroma). Obtained images were analyzed using Metamorph (https://www.moleculardevices.com/systems/metamorph-research-imaging) and ImageJ (Schneider *et al.*, 2012). Baseline fluorescence was calculated as the mean fluorescence intensity of an ROI over the ten frames prior to light stimulus delivery. The trapezoidal method was used to calculate area under the curve, utilizing the trapz function of MATLAB. Data points from the onset of stimulation to the end of stimulation were used for the calculation.

Calcium imaging: fillet preparations

Third-instar larvae were dissected along the ventral midline and pinned on sylgard (Dow Corning) dishes with the internal surface facing towards the microscope. All internal organs, including the central nervous system, were removed. Larvae were bathed in calcium-containing HL3.1[183] (Table S3) except where indicated and images of the dorsal midline between abdominal segments A2 and A4 were captured with a Zeiss Axio Zoom V16 microscope. Captured images were analyzed using ImageJ[184]. Mechanical stimulus: fillets were poked with a tapered borosilicate capillary with a rounded tip, using a micromanipulator to induce a deflection of 25 µm. The decay time constant was calculated by fitting the data points from the peak response to the end of the experiment into an exponential curve $f(x) = a*\exp(b*x)$ using MATLAB with $R^2>0.9$ used as a threshold for reliable fitting.

Calcium imaging: dissociated epidermal cells

Six to eight larval fillets were dissociated in 400 µL of 50% Saline (modified Ringer's recipe) / 50% Schneider's media with 200 U/mL collagenase type I (Fisher 17-100-017), with mixing at 1000 RPM at 33°C for 16 min, with trituration every 8 min. Undigested fillets were removed and the remaining suspension was spun at 500 g for 3 min, followed by aspiration of the supernatant down to a 10 µL cell suspension. Cells were resuspended in 30 µL fresh PBS / Schneider's solution and plated onto poly-D-lysine (1 mg/ml, Sigma P7886) coated No. 1 coverslips, with 10 µL cell solution per coverslip. Cells were cultured at least 30 min and up to 2 hr at 25° C prior to imaging. Cells were imaged using a a 10x objective at a frame rate of 0.33 Hz. Solutions are indicated in figure legends (see Table S3 for recipes). Obtained Images were analyzed using MetaFluor and Python and baseline fluorescence was calculated as the mean fluorescence intensity of an ROI over 5 frames prior to stimulus delivery. For stretch stimulation, circular membranes were cut with an arch punch from sheets of glossy silicone of 0.01–0.02 inch thickness (Specialty Manufacturing, Inc.) and coated with 1 mg/ml poly-D-lysine for 1 h before plating cells.

Membranes were mounted onto the StageFlexer system and vacuum pressure was applied through the FX-3000 system (Flexcell). Calibrations were performed using fluorescent beads attached to the membranes, and images were taken before and during a static stretch. To stimulate cells, a 2 sec square wave of vacuum pressure was applied. Cells were imaged with an Olympus BX61WI upright microscope. For store-operated calcium entry measurements and osmotic stimulation, cells were imaged using a Zeiss Observer inverted microscope and solutions were perfused using the Automate Scientific ValveLink 8.2 perfusion system. At the end of each imaging session, 1uM ionomycin was perfused and only cells that showed a calcium response, as defined by a 10% increase from baseline fluorescence, were used in analysis. Flow, osmotic and radial stretch responders were defined by a 5% increase from baseline fluorescence.

Calcium imaging: human keratinocytes

Immortalized human keratinocytes (HaCaT) cells were plated on silicone membranes one day prior to stretch experiments. Prior to the radial stretch experiments, cells were loaded with 1 μm Fura-2AM supplemented with 0.01% Pluronic F-127 (w/v, Life Technologies) in a physiological Ringer's solution containing the following (in mm): 140 NaCl, 5 KCl, 10 HEPES, 2 CaCl2, 2 MgCl2, and 10 d-(+)-glucose, pH 7.4. Acquired images were displayed as the ratio of 340 nm/380 nm. Cells that had a response 10 standard deviations above baseline to ionomycin were included in the analysis and stretch responses were defined by a 15% increase in Fura-2 340/380 ratio.

Confocal Microscopy

For peripheral imaging of cellular morphology, live single larvae were mounted in 90% glycerol under a coverslip and imaged on a Leica SP5 confocal microscope using a 40x 1.25 NA lens. To image the larval CNS, larvae were dissected on sylgard plates, briefly fixed in 4% paraformaldehyde (PFA) in PBS for 15 min at room temperature, washed 3 x 5 min in PBS, and mounted for imaging.

<u>RNA-Seq analysis of epidermal cells</u>

RNA isolation for RNA-Seq

Larvae with cytoplasmic GFP expressed in different epidermal subsets were microdissected and dissociated in collagenase type I (Fisher 17-100-017) into single cell suspensions, largely as previously described[185], with the addition of 1% BSA to the dissociation mix. After dissociation, cells were transferred to a new 35 mm petri dish with 1 mL 50% Schneider’s media, 50% PBS supplemented with 1% BSA. Under a fluorescent stereoscope, individual fluorescent cells were manually aspirated with a glass pipette into PBS with 0.5% BSA, and then serially transferred until isolated without any additional cellular debris present. Ten cells per sample were aspirated together, transferred to a mini-well containing 3ul lysis solution (0.2 % Triton X-100 in water with 2 U / μL RNAse Inhibitor), lysed by pipetting up and down several times, transferred to a microtube, and

stored at -80º C. For the picked cells, 2.3 µL of lysis solution was used as input for library preparation.

RNA-Seq library preparation

RNA-Seq libraries were prepared from the picked cells following the Smart-Seq2 protocol for full length transcriptomes [186]. To minimize batch effects, primers, enzymes, and buffers were all used from the same lots for all libraries. Libraries were multiplexed, pooled, and purified using AMPure XP beads, quality was checked on an Agilent TapeStation, and libraries were sequenced as 51-bp single end reads on a HiSeq4000 at the UCSF Center for Advanced Technology.

RNA-Seq data analysis
Reads were demultiplexed with CASAVA (Illumina) and read quality was assessed using FastQC (https://www.bioinformatics.babraham.ac.uk/) and MultiQC [187]. Reads containing adapters were removed using Cutadapt version 2.4 (Martin, 2011) and reads were mapped to the *D. melanogaster* transcriptome, FlyBase genome release 6.29, using Kallisto version 0.46.0[188] with default parameters. AA samples were removed from further analysis for poor quality, including low read depth (< 500,000 reads), and low mapping rates (< 80%). Raw sequencing reads and gene expression estimates are available in the NCBI Sequence Read Archive (SRA) and in the Gene Expression Omnibus (GEO) under accession number SUB11489996.

Statistical analysis

For each experimental assay control populations were sampled to estimate appropriate sample numbers to allow detection of ~33% differences in means with 80% power over a 95% confidence interval. Details of statistical tests including treatment groups, sample numbers, statistical tests, p-values and q-values are provided in the experimental supplement.

Supplementary File 1: Details of Statistical Analysis

Figure 1C: Fisher's exact test with BH correction

UAS-TRPA1 groups (25 C vs 32 C)	p-value	q-value	Significance (q<0.05)
Control (no *GAL4* driver)	0.2424	2.424000e-01	F
R27H06-GAL4	2.2e-16	3.666667e-16	T
R38F11-GAL4	2.2e-16	3.666667e-16	T
R38F11-GAL4 + elav-GAL80	2.2e-16	3.666667e-16	T
R38F11-GAL4 + tshGAL80	4.111e-15	5.138750e-15	T

Figure 1S4: ANOVA with post-hoc Tukey's test

Dendrite length	p-value	Significance
R38 vs. UAS-luc RNAi	>0.9999	F
R38 vs. UAS-CsChrimson	0.9659	F
R38 vs. UAS-TRPA1	0.9982	F
R38 vs. UAS-orai RNAi	0.9009	F
R38 vs. UAS-Stim RNAi	0.9219	F
R38 vs. UAS-Stim	>0.9999	F
R38 vs. UAS-shi^TS	0.9974	F

Dendrite branchpoints	p-value	Significance
R38 vs. UAS-luc RNAi	0.9945	F
R38 vs. UAS-CsChrimson	0.9269	F
R38 vs. UAS-TRPA1	0.6859	F
R38 vs. UAS-orai RNAi	0.9896	F
R38 vs. UAS-Stim RNAi	0.9949	F
R38 vs. UAS-Stim	0.8654	F
R38 vs. UAS-shi^TS	>0.9999	F

Figure 1S6C: Fisher's exact test

	p-value	Significance
rolling	0.0002928	T
c-bend	2.035e-10	T
backing	0.0008424	T
hunch	0.004233	T
freeze	0.002342	T

Figure 1S6D: Wilcoxon rank sum test

	p-value	Significance
rolling	Cannot compare	
c-bend	0.8907	F
backing	0.00127	T
hunch	Cannot compare	
freeze	Cannot compare	

Figure 2F: Wilcoxon Rank-Sum test

	p-value	Significance
C4da vs Epi	0.0067	T

Figure 2G: Kruskal-Wallis test followed by Wilcoxon rank sum test with BH correction

	p-value	q-value	Significance (q<0.05)

Kruskal-Wallis test, rolling	N/A (only epi + C4da have values)		
rolling C4da vs Epi	0.03124		T
Kruskal-Wallis test, c-bend	0.0001652		T
c-bend C4da vs Epi	0.001468	0.002936	T
c-bend C3da vs Epi	0.3237	0.323700	F

Figure 2H Fisher's exact test with a BH correction

	p-value	q-value	Significance (q<0.05)
rolling Epi ATR+ vs ATR-	0.04313	0.09102	F
rolling C4da ATR+ vs ATR-	0.04551	0.09102	F
rolling C3da ATR+ vs ATR-	1	1	F
rolling Cho ATR+ vs ATR	1	1	F
c-bend Epi ATR+ vs ATR-	0.4687	0.9508	F
c-bend C4da ATR+ vs ATR-	0.4754	0.9508	F
c-bend C3da ATR+ vs ATR	1	1	F
c-bend Cho ATR+ vs ATR	1	1	F
back Epi ATR+ vs ATR-	0.00000000000004556	0.00000000000018224	T
back C4da ATR+ vs ATR	1	1	F
back C3da ATR+ vs ATR	1	1	F
back Cho ATR+ vs ATR-	0.1128	0.2256	F
hunch Epi ATR+ vs ATR	1	1	F
hunch C4da ATR+ vs ATR	1	1	F
hunch C3da ATR+ vs ATR-	1	1	F
hunch Cho ATR+ vs ATR-	0.4918	1	F
freeze Epi ATR+ vs ATR-	0.00000008682	0.00000034728	T
freeze C4da ATR+ vs ATR-	0.4754	0.6338667	F
freeze C3da ATR+ vs ATR-	1	1	F
freeze Cho ATR+ vs ATR-	0.000825	0.00165	T

Figure 2S1E: Fisher's exact test with BH correction

	p-value	q-value	Significance (q<0.05)
rolling Epi ATR+ vs ATR-	3.039e-06	6.0780e-06	T
rolling C4da ATR+ vs ATR-	9.667e-08	3.8668e-07	T
rolling C3da ATR+ vs ATR-	1	1.0000e+00	F
rolling Cho ATR+ vs ATR-	1	1.0000e+00	F
c-bend Epi ATR+ vs ATR-	1.388e-11	2.776e-11	T
c-bend C4da ATR+ vs ATR-	1.265e-11	2.776e-11	T
c-bend C3da ATR+ vs ATR-	0.00192	2.560e-03	T
c-bend Cho ATR+ vs ATR-	1	1.000e+00	F
back Epi ATR+ vs ATR-	1.238e-13	4.952000e-13	T
back C4da ATR+ vs ATR-	0.6003	6.003000e-01	F
back C3da ATR+ vs ATR-	0.02597	5.194000e-02	F
back Cho ATR+ vs ATR-	0.05251	7.001333e-02	F
hunch Epi ATR+ vs ATR-	0.04313	5.750667e-02	F
hunch C4da ATR+ vs ATR-	0.4754	4.754000e-01	F
hunch C3da ATR+ vs ATR-	1.03e-06	2.060000e-06	T
hunch Cho ATR+ vs ATR-	2.571e-14	1.028400e-13	T
freeze Epi ATR+ vs ATR-	0.01869	0.0747600	F
freeze C4da ATR+ vs ATR-	0.2219	0.2958667	F
freeze C3da ATR+ vs ATR-	0.5353	0.5353000	F
freeze Cho ATR+ vs ATR-	0.05251	0.1050200	F

Figure 3E Fisher's exact test with BH correction

	p-value	q-value	Significance (q<0.05)
rolling control vs *C4da>TNT*	0.001051	0.002102	T
rolling control vs *C3da>TNT*	0.1945	0.194500	F
c-bend control vs *C4da>TNT*	1	1.00000	F
c-bend control vs *C3da>TNT*	0.05219	0.10438	F
back control vs *C4da>TNT*	0.7787	0.778700	F
back control vs *C3da>TNT*	0.005579	0.011158	T
hunch control vs *C4da>TNT*	0.02372	0.04744	T
hunch control vs *C3da>TNT*	0.1124	0.11240	F
freeze control vs *C4da>TNT*	0.3533	0.3533	F
freeze control vs *C3da>TNT*	0.1945	0.3533	F

Figure 3F Kruskal-Wallis test followed by Wilcoxon rank sum test with BH correction

	p-value	q-value	Significance (q<0.05)
Kruskal-Wallis test, rolling	0.0004424		
rolling control vs *C4da>TNT*	0.001122	0.002244	T
rolling control vs *C3da>TNT*	0.7007	0.700700	F
Kruskal-Wallis test, c-bend	0.001948		
c-bend control vs *C4da>TNT*	0.0004278	0.0008556	T
c-bend control vs *C3da>TNT*	0.433	0.4330000	F
Kruskal-Wallis test, back	0.4203		
back control vs *C4da>TNT*	N/A		
back control vs *C3da>TNT*	N/A		
hunch control vs *C4da>TNT*	No Hunch in control		
hunch control vs C3da TNT	No Hunch in control (p=0.4127 C4vsC3)		
Kruskal-Wallis test, freeze	0.3808		
freeze control vs *C4da>TNT*	N/A		
freeze control vs *C3da>TNT*	N/A		

Figure 3S2 D: Fisher's exact test with BH correction

	p-value	q-value	Significance (q<0.05)
Control vs C4da silence, roll	0.0003682	0.0007364	T
Control vs C3da silence, roll	0.3015	0.3015000	F
Control vs C4da silence, c-bend	0.1188	0.2376	F
Control vs C3da silence, c-bend	0.2949	0.2949	F
Control vs C4da silence, backward	1	1.00000	F
Control vs C3da silence, backward	0.02372	0.04744	T
Control vs C4da silence, hunch	1	1	F
Control vs C3da silence, hunch	1	1	F
Control vs C4da silence, freeze	0.1028	0.102800	F
Control vs C3da silence, freeze	0.002466	0.004932	T

Figure 3S2 E: Kruskal-Wallis test followed by Wilcoxon rank sum test

	p-value	q-value	Significance
Kruskal-Wallis test, Roll	0.02471		T
Control vs C4da silence Roll	0.01604	0.03208	T
Control vs C3da silence Roll	0.04658	0.04658	T
Kruskal-Wallis test, c-bend	0.01971		T
Control vs C4da silence c-bend	0.008927	0.017854	T
Control vs C3da silence c-bend	0.02334	0.023340	T

Control vs C4da silence back	0.2222		F
Control vs C3da silence back	N/A		
Control vs C3da silence back	N/A		
Control vs C4da silence hunch	N/A		
Control vs C3da silence hunch	N/A		
Control vs C4da silene freeze	N/A		
Control vs C3da silence freeze	N/A		

Figure 4B: Wilcoxon Rank-Sum test

	p-value	Significance
Fmax/F0 C4da vs C4da +Epi	0.0288	T

Figure 4C: Wilcoxon Rank Sum test

	p-value	q-value	Significance (q<0.05)
C4da vs C4da+Epi	0.03184		T

Figure 4D: Wilcoxon Rank-Sum test

	p-value	Significance
C4da vs C4da+Epi	0.03277	T

Figure 4F: Fisher's exact test with BH correction

	p-value	q-value	Significance (q<0.05)
C4da vs Epi	0.0003136	3.741e-04	T
C4da vs Epi+C4da	0.7541	3.741e-04	T
Epi vs Epi+C4da	0.000005162	2.997e-11	T

Figure 4G: Kruskal-Wallis test followed by Wilcoxon rank sum test with BH correction

	p-value	q-value	Significance (q<0.05)
Kruskal-Wallis test	0.000000001544		
C4da vs Epi	0.7541	0.7541	F
C4da vs Epi+C4da	0.000000000001072	0.000000000003216	T
Epi vs Epi+C4da	0.000005162	0.000007743	T

Figure 4H: Fisher's exact test with BH correction

	p-value	q-value	Significance (q<0.05)
<5 C4da vs Epi	0.1894	1.894e-01	F
<5 C4da vs C4da+Epi	3.646e-11	5.469e-11	T
<5 Epi vs C4da+Epi	2.571e-14	7.713e-14	T
5-9 C4da vs Epi	0.674	0.674	F
5-9 C4da vs C4da+Epi	0.356	0.674	F
5-9 Epi vs C4da+Epi	0.6124	0.674	F
10 -14 C4da vs Epi	0.6144	0.9216	F
10 -14 C4da vs C4da+Epi	1	1.0000	F
10 -14 Epi vs C4da+Epi	0.6124	0.9216	F
15 -19 C4da vs Epi	1	1.0000	F
15-19 C4da vs C4da+Epi	0.1896	0.2844	F
15 -19 Epi vs C4da+Epi	0.1128	0.2844	F
>20 C4da vs Epi	1	1.0000	F
>20 C4da vs C4da+Epi	5.377e-11	1.6131e-10	T
>20 Epi vs C4da+Epi	2.644e-10	3.9660e-10	T

Figure 4I: Kruskal-Wallis test followed by Wilcoxon rank sum test with BH correction

	p-value	q-value	Significance (q<0.05)
Kruskal-Wallis test	5.993e-15		
C4da vs Epi	0.0009667	9.6670e-04	T
C4da vs Epi+C4da	4.97e-15	7.4550e-15	T
Epi vs Epi+C4da	5.028e-16	1.5084e-15	T

Figure 4J: Kruskal-Wallis test followed by Wilcoxon rank sum test with BH correction

	p-value	q-value	Significance (q<0.05)
Kruskal-Wallis test, rolling	4.024e-09		T
roll C4da vs Epi	0.1937	1.9370e-01	F
roll C4da vs C4da+Epi	9.024e-12	2.7072e-11	T
roll Epi vs C4da + Epi	5.506e-05	8.2590e-05	T
Kruskal-Wallis test, c-bend	0.06175		F
c-bend C4da vs Epi	N/A		
c-bend C4da vs C4da+Epi	N/A		
c-bend Epi vs C4da +Epi	N/A		
Kruskal-Wallis test, backing	9.145e-06		T
back C4da vs Epi	9.574e-07	2.8722e-06	T
back C4da vs C4da+Epi	0.02662	2.6620e-02	T
back Epi vs C4da+Epi	0.001987	2.9805e-03	T
Kruskal-Wallis test, hunching	0.006437		T
hunch C4da vs Epi	0.2706	0.270600	F
hunch C4da vs C4da+Epi	0.001252	0.003756	T
hunch Epi vs C4da+Epi	0.1836	0.270600	F
Kruskal-Wallis test, freezing	0.4857		F
freeze C4da vs Epi	N/A		
freeze C4da vs C4da+Epi	N/A		
freeze Epi vs C4da+Epi	N/A		

Figure 4K: Fisher's exact test with a BH correction

Epi-GAL4, UAS-CsChrimson treatment groups	p-value	q-value	Significance
20 mN ATR- vs ATR+ Epi>CsChrimson	0.003234	0.0097020	T
50 mN ATR- vs ATR+ Epi>CsChrimson	0.008797	0.0131955	T
50mN ATR- vs ATR+ CsChrimson	0.7639	0.7639000	F

Figure 4L: Fisher's exact test with BH correction

	p-value	q-value	Significance (q<0.05)
No *GAL4* 25 vs 32	0.6798	0.7806000	F
Epi-GAL4 25 vs 32	0.0005454	0.0021816	T
27H06-GAL4 25 vs 32	0.7806	0.7806000	F
ppk-GAL4 25 vs 32	0.7735	0.7806000	F

Figure 4M: Fisher's exact test with BH correction

UAS-TRPA1 comparisons	p-value	q-value	Significance (q<0.05)
10sec control vs 10sec *Epi-GAL4*	0.006108	0.01018000	T
30sec control vs 30sec *Epi-GAL4*	0.001265	0.00316250	T
60sec control vs 60sec *Epi-GAL4*	0.00007129	0.00035645	T
300sec control vs 300sec *Epi-GAL4*	0.07531	0.09413750	F
600sec control vs 600sec *Epi-GAL4*	0.4351	0.43510000	F

Figure 4N: Curve fitting

	fit curve	Decay time constant
Mechano (Fig 4S1B)	f(x) = 0.4139*exp(-0.002994*x)	334.001336
Epidermal activation (Fig 4L)	f(x) = 0.47*exp(-0.002964*x)	337.3819163

Figure 4S1B: Fisher's exact test with BH correction

	p-value	q-value	Significance (q<0.05)
10sec 1st vs 2nd	0.0007546	0.0018865	T
30sec 1st vs 2nd	0.000006865	0.000034325	T
60sec 1st vs 2nd	0.008544	0.01424	T
300sec 1st vs 2nd	0.131	0.16375	F
600sec 1st vs 2nd	0.3217	0.3217	F

Figure 4S1C: Fisher's exact test with BH correction

	p-value	q-value	Significance (q<0.1)
Control 1st vs 2nd	0.006746	0.00674600	T
Epi-GAL4 1st vs 2nd	6.336e-05	0.00019008	T
Nociceptor-GAL4 1st vs 2nd	0.005186	0.00674600	T

Figure 6B Fisher's exact test with BH correction

	p-value	q-value	Significance (q<0.1)
Control 1st vs 2nd	4.94E-05	0.0002472	T
Orai RNAi 1st vs 2nd	0.1329	0.3236667	F
Stim RNAi 1st vs 2nd	0.1942	0.3236667	F
Control 1st vs *Orai* RNAi 1st	0.8788	0.6660000	F
Control 1st vs *Stim* RNAi 1st	0.5328	0.8788000	F

Figure 6E: Chi-square comparing distribution of stretch sensitive cells

	Chi-square value	DF	p-value
Control vs *Stim* RNAi	33	4	<0.0001
Control vs *Orai* RNAi	150.6	4	<0.0001
Stim RNAi vs *Orai* RNAi	3.689	4	0.4497

Figure 6G: Chi-square comparing distribution of stretch sensitive cells

	Chi-square value	DF	p-value
Control vs La3+	36.09	4	<0.0001
Control vs Store Depleted	112.1	4	<0.0001
Store Depleted vs La3+	40.69	4	<0.0001

Figure 6J: Fisher's exact test

	p-value		
control vs *GtACR*	0.03216		

Figure 6K Fisher's exact test with BH correction

	p-value	q-value	Significance (q<0.1)
Control 1st vs 2nd	0.00037	0.00148000	T
Stim OE 1st vs 2nd	0.02386	0.03181333	T
Control 1st vs *Stim OE* 1st	0.002115	0.00423000	T

Figure 6L: Fisher's exact test with BH correction

	p-value	q-value	Significance
Control 25C 1st vs Control 25C 2nd	5.425e-05	7.233333e-05	T
Control 30C 1st vs Control 30C 2nd	1.033e-06	2.066000e-06	T
Epi>shi 25C 1st vs *Epi>shi* 25C 2nd	4.912e-07	1.964800e-06	T
Epi>shi 30C 1st vs *Epi>shi* 30C 2nd	0.05076	5.076000e-02	F

Figure 6S2A Fisher's exact test with BH correction

	p-value	q-value	significance
Control Trial 1 vs Trial 2	0.002438	0.004876	T
Orai RNAi Trial 1 vs Trial 2	0.4076	0.4076	F

Figure 6S2B Fisher's exact test with BH correction

	p-value	q-value	significance
Control Trial 1 vs Trial 2	0.00157	0.003140	T
Task6 RNAi Trial 1 vs Trial 2	0.004795	0.004795	T

Figure 6S2C Wilcoxon Rank-Sum test

	p-value	significance
Control vs La^{3+} block	0.0003377	T

Figure 6S2E: Kruskal-Wallis test followed by Wilcoxon rank sum test with BH correction

	p-value	q-value	Significance (q<0.05)
Kruskal-Wallis test	0.00001332		T
Control vs *Stim* RNAi	0.0009161	0.001374150	T
Control vs *Orai* RNAi	0.000005094	0.000015282	T
Stim RNAi vs *Orai* RNAi	0.3759	0.375900000	F

Figure 6S2F: Kruskal-Wallis test followed by Wilcoxon rank sum test with BH correction

	p-value	q-value	Significance (q<0.05)
Kruskal-Wallis test	0.004105		T
Control vs *Stim* RNAi	0.001296	0.002592	T
Control vs *Orai* RNAi	0.8294	0.829400	F

Table S1. Larval behaviors scored in this study

Behavior	Description / Criteria
Locomotion	Continuous forward movement with smooth, regular peristalsis
Pausing	Break in locomotion, lasting less than 1 second
Freezing	Break in locomotion that persists for longer than 1 second
Hunching	Contraction along the anterior-posterior axis; no forward / backward motion or curling
Backward locomotion	Anterior-to-posterior peristalsis accompanied by movement in reverse
Writhing crawl	Forward movement with anterior and posterior sweeping of the body, tilting onto the side axis
C-bending	Bending into a c-shape, with both head and tail bending in the same direction; includes incomplete rolls
Rearing	Upwards bending or arching of anterior part of the body, with posterior part largely stationary
Rolling	Larva completes a full 360-degree rotation of its body

Table S2. Solutions used in calcium imaging studies.

HL3.1, *Drosophila* saline			
Compound	**M.W. (g/mol)**	**1X Concentration (mM)**	**For 1L (1X)**
NaCl	58.44	120	7.013 g
KCl	74.55	5	0.373 g
Proline	115.13	5	0.576 g
HEPES	238.30	10	2.383 g
Trehalose	378.33	5	3.78 g
Sucrose	342.30	32.5	11.125 g
CaCl2	1M stock	1.5	1.5 ml from 1M stock
MgCl2	1M stock	1	1 ml from 1M tock
		pH (with NaOH)	7.15
		Osmolarity (mOsm/L)	310

Zero Ca2+ / EGTA HL3.1			
Compound	**M.W. (g/mol)**	**1X Concentration (mM)**	**For 1L (1X)**
NaCl	58.44	120	7.013 g
KCl	74.55	5	0.373 g
Proline	115.13	5	0.576 g
HEPES	238.30	10	2.383 g
Trehalose	378.33	5	3.78 g
Sucrose	342.30	32.5	11.125 g
EGTA	380.35	1.5	0.571 g
MgCl2	1M stock	1	1 ml from 1M tock
		pH (with NaOH)	7.15
		Osmolarity (mOsm/L)	310

20mM Ca2+ HL3.1			
Compound	**M.W. (g/mol)**	**1X Concentration (mM)**	**For 1L (1X)**
NaCl	58.44	101.5	5.932 g
KCl	74.55	5	0.373 g
Proline	115.13	5	0.576 g
HEPES	238.30	10	2.383 g
Trehalose	378.33	5	3.78 g
Sucrose	342.30	32.5	11.125 g
CaCl2	1M stock	20	20 ml from 1M stock
MgCl2	1M stock	1	1 ml from 1M tock
		pH (with NaOH)	7.15
		Osmolarity (mOsm/L)	310

Isotonic (modified from *Drosophila* saline to maintain ionic balance across osmolarities)			
Compound	**M.W. (g/mol)**	**1X Concentration (mM)**	**For 1L (1X)**
NaCl	58.44	90	5.260 g
KCl	74.55	5	0.373 g
Proline	115.13	5	0.576 g
HEPES	238.30	10	2.383 g
Trehalose	378.33	5	3.78 g
Sucrose	342.30	92.5	31.663 g
CaCl2	1M stock	1.5	1.5 ml from 1M stock
MgCl2	1M stock	1	1 ml from 1M tock
		pH (with NaOH)	7.15
		Osmolarity (mOsm/L)	310

85% Hypoosmotic			
Compound	**M.W. (g/mol)**	**1X Concentration (mM)**	**For 1L (1X)**
NaCl	58.44	90	5.260 g
KCl	74.55	5	0.373 g
Proline	115.13	5	0.576 g
HEPES	238.30	10	2.383 g
Trehalose	378.33	5	3.78 g
Sucrose	342.30	46.5	15.917 g
CaCl2	1M stock	1.5	1.5 ml from 1M stock
MgCl2	1M stock	1	1 ml from 1M tock
		pH (with NaOH)	7.15
		Osmolarity (mOsm/L)	

70% Hypoosmotic			
Compound	**M.W. (g/mol)**	**1X Concentration (mM)**	**For 1L (1X)**
NaCl	58.44	90	5.260 g
KCl	74.55	5	0.373 g
Proline	115.13	5	0.576 g
HEPES	238.30	10	2.383 g
Trehalose	378.33	5	3.78 g
Sucrose	342.30	0	15.917 g
CaCl2	1M stock	1.5	1.5 ml from 1M stock
MgCl2	1M stock	1	1 ml from 1M tock
		pH (with NaOH)	7.15
		Osmolarity (mOsm/L)	

Chapter III: SARS-Cov-2 Papain-Like Protease Activates Nociceptors to Drive Sneeze, Cough, and Pain

This chapter is revised reproduction of the preprint by a similar name (Mali, S.S. *et al.* SARS-CoV-2 Papain-like protease activates nociceptors to drive sneeze and pain. *bioRxiv*, 2024). I co-conceived the project with Diana Bautista and designed all experiments. I led and performed the majority of experiments, analyzed all data presented in the manuscript, prepared all figures, and wrote the manuscript with Diana Bautista.

Summary

SARS-CoV-2, the virus responsible for COVID-19, triggers symptoms such as sneezing, coughing, and pain[189,190]. These symptoms are mediated by a subset of sensory neurons, known as nociceptors, that detect noxious stimuli, densely innervate the airway epithelium, and interact with airway resident epithelial and immune cells[21,26,109,191,192]. However, the mechanisms by which viral infection activates these neurons to trigger pain and airway reflexes are unknown. Here, we show that the coronavirus papain-like protease (PLpro) directly activates airway-innervating trigeminal and vagal nociceptors in mice and human iPSC-derived nociceptors. PLpro elicits sneezing, coughing, and acute pain in mice and triggers the release of the neuropeptide calcitonin gene-related peptide (CGRP) from airway afferents. We demonstrate the proteolytic activity of PLpro is required for neuronal activation and sneeze and that this PLpro-dependent activation requires the host TRPA1 ion channel, a key mediator of pain, cough and inflammation[41,46]. SARS-CoV-2 infection of sensory neurons induces transcriptional changes that selectively impact nociception, upregulating the same TRPA1-CGRP signaling pathway directly activated by PLpro. Our findings are the first demonstration of a viral product that directly activates sensory neurons to trigger pain and airway reflexes and highlight a new role for PLpro as a therapeutic target in COVID-19.

Introduction

Common symptoms of viral infections including SARS-CoV-2, the virus responsible for COVID-19, include sneezing, coughing, headache, and other aches and pain. Sneezing and coughing are common host responses to SARS-CoV-2 infection that promote transmission by generating and dispersing airborne droplets that contain the virus. Somatosensory and vagal sensory neurons drive protective reflexes, such as sneezing, and initiate pain sensations during injury or infection[192,26,23,22,193]. Yet, little is known about how these neurons are activated by SARS-CoV-2 infection to drive symptoms.

When epithelial cells are infected, they release cytokines and other inflammatory mediators that activate surrounding epithelial and immune cells, as well as the sensory neurons that innervate the epithelia. Studies to date have focused on endogenous inflammatory mediators released during viral infection that activate sensory neurons[79,80,194,195]. However, infection also generates viral proteins that may be released and modulate host physiology. Viral products are known to activate airway epithelial and

immune cells to drive inflammation, but little is known about the direct actions of viral molecules on sensory neurons[97,196]. Among viral proteins, proteases have been of much interest as therapeutic targets for COVID-19 due to their critical role in viral replication. While proteases from plants, insects, bacteria, and immune cells have been demonstrated to activate sensory neurons to trigger itch, pain and inflammation [197–206]; viral proteases in this context have been unexplored. SARS-CoV-2 papain-like protease (PLpro) plays an essential role in viral replication by processing viral polyproteins and suppresses the host immune response of infected cells[207,208]. Here, we show a new role for PLpro in the activation of airway-innervating sensory neurons to drive airway reflexes and pain behaviors.

Introduction

Common symptoms of viral infections including SARS-CoV-2, the virus responsible for COVID-19, include sneezing, coughing, headache, and other aches and pain. Sneezing and coughing are common host responses to SARS-CoV-2 infection that promote transmission by generating and dispersing airborne droplets that contain the virus. Somatosensory and vagal sensory neurons drive protective reflexes, such as sneezing, and initiate pain sensations during injury or infection[192,26,23,22,193]. Yet, little is known about how these neurons are activated by SARS-CoV-2 infection to drive symptoms.

When epithelial cells are infected, they release cytokines and other inflammatory mediators that activate surrounding epithelial and immune cells, as well as the sensory neurons that innervate the epithelia. Studies to date have focused on endogenous inflammatory mediators released during viral infection that activate sensory neurons[79,80,194,195]. However, infection also generates viral proteins that may be released and modulate host physiology. Viral products are known to activate airway epithelial and immune cells to drive inflammation, but little is known about the direct actions of viral molecules on sensory neurons[97,196]. Among viral proteins, proteases have been of much interest as therapeutic targets for COVID-19 due to their critical role in viral replication. While proteases from plants, insects, bacteria, and immune cells have been demonstrated to activate sensory neurons to trigger itch, pain and inflammation [197–206]; viral proteases in this context have been unexplored. SARS-CoV-2 papain-like protease (PLpro) plays an essential role in viral replication by processing viral polyproteins and suppresses the host immune response of infected cells[207,208]. Here, we show a new role for PLpro in the activation of airway-innervating sensory neurons to drive airway reflexes and pain behaviors.

Results

SARS-CoV-2 PLpro activates airway-innervating neurons to drive sneeze, cough, and pain

Functional PLpro is well positioned to act on sensory neurons that densely innervate the airways. PLpro activity is detected in human throat swabs[209] and saliva[210] collected from individuals with active SARS-CoV-2 infection. We also detected PLpro activity in the

supernatant of infected human airway epithelial cells 48 hours post-infection at a concentration (29.8 ± 5.9 nM; Supplemental Fig.1d) comparable to concentrations detected in human samples.

Thus, we set out to test whether PLpro activates sensory neurons of the nasal mucosa and airways. We performed intravital calcium imaging of the trigeminal ganglion (TG) sensory neurons in mice (Fig.1a). Intranasal perfusion with PLpro elicited a transient increase in calcium in a subset of sensory neurons (Fig.1b). Perfusion with 1 nM PLpro elicited calcium transients in 21.2% of vehicle-insensitive neurons, and subsequent perfusion with 100 nM and 10 μM PLpro activated an additional 15.3% and 14.3% of neurons, respectively (Fig.1c). Perfusion with vehicle alone activated a subset of neurons (28.4%; Fig. 1b), likely representing a mechanosensitive population of neurons; these mechanosensitive neurons did not exhibit dose-dependent activation in response to PLpro (Fig. 1c). Neurons that express the ion channels TRPV1, known as nociceptors, trigger pain and defensive airway reflexes in response to a variety of noxious stimuli, including chemical irritants and inflammatory mediators. Perfusion with the TRPV1 agonist, capsaicin, a potent airway irritant, revealed that PLpro activates 45% of nociceptors, defined by capsaicin sensitivity (Fig. 1d). Taken together, these data demonstrate that PLpro activates a subset of airway-innervating nociceptors in vivo.

Trigeminal nociceptors mediate sneezing[21], nasal secretion[211], and head pain[212], common symptoms of viral infection. Which, if any, of these behaviors does PLpro trigger? We used high speed video and audio recordings to quantify behavioral responses to intranasal treatment of vehicle or PLpro (10 μM). Sneezing and coughing generate distinct auditory and respiratory patterns in mice and other animals[20–23,213,214]. PLpro elicited rapid high frequency auditory events (latency: 11.6 ± 2.5 s; Fig. 1e, Supplemental Fig. 2a, Supplemental Fig. 3e), typical of a sneeze, over two minutes in mice (Fig. 1f, g). In contrast, vehicle-treated mice sneezed less and were slower to sneeze (latency: 25.9 ± 7.5 s; Supplemental Fig. 3e and Fig. 1f, g). The sneeze reflex is a convulsive expulsion of air that helps clear the airways of irritants and pathogens. To validate and visualize nasal expulsion, we applied PLpro or vehicle combined with blue dye. The number of sneezes correlated with the presence of dye at the bottom of the chamber (Supplemental Figure 2b). We also observed dye expelled onto the sides and floor of the chamber during audible sneeze events (Fig. 1e, Supplemental Figure 2a).

To further characterize the respiratory reflexes triggered by PLpro, we employed whole body plethysmography and identified specific respiratory patterns that correlated with dye expulsion events (Supplemental Figure 2c). We observed two stereotypical waveforms: one consisting of a rapid inspiration followed by a sharp expiration, characteristic of a sneeze; and another featuring an extended inspiration followed by a sharp expiration, indicative of a cough (Fig. 1h). These findings demonstrate that PLpro triggers rapid sneezing, coughing, and nasal secretion which could promote expulsion of virus from the nasal cavity and airways.

Capsaicin is well known to trigger airway irritation, as well as sneezing and coughing. Intranasal treatment with capsaicin triggered robust airway reflexes and nose rubbing and

a cessation of face wiping (Supplemental Fig. 4a-d). In comparison, PLpro primarily induced airway reflexes accompanied by a rapid nose rub (latency: 24.9 ± 3.5 s), a behavior not observed with vehicle treatment (latency: 39.4 ± 5.2 s; Supplemental Fig. 3e and Fig. 1i). Thus, our assay effectively captures a range of behavioral and physiological responses to intranasal treatments. Previous studies have shown that irritants and inflammatory mediators such as allergens, histamine, and serotonin, can drive sneezing in mice[21,215,216]. This data demonstrates for the first time that a viral molecule, PLpro, is alone sufficient to trigger sneezing and coughing, key symptoms of viral infection and mechanisms for viral spread.

In addition to triggering airway reflexes, activation of skin-innervating trigeminal nociceptors can drive itch or pain behaviors. We examined the consequences of intradermal injection of PLpro in the cheek, where painful stimuli promote wiping with the forelimbs and itch stimuli evoke scratching with the hindlimb. Mice injected with PLpro displayed rapid wiping, indicative of pain, compared to vehicle-injected mice (Supplemental Fig. 5a, b). However, PLpro did not elicit itch-evoked scratching behaviors (Supplemental Fig. 5c, d). Overall, these data show that PLpro drives acute behaviors in the skin and airways associated with pain and irritation.

PLpro directly activates nociceptors via proteolytic activity

To elucidate the mechanisms by which PLpro activates nociceptors, we tested if the protease could directly activate sensory neurons in vitro. The airways are innervated by somatosensory neurons from the TG and dorsal root ganglia (DRG), and vagal sensory neurons from the nodose and jugular ganglia (NJG). We found that PLpro induced calcium transients in neurons cultured from all three ganglia from mice (Fig. 2a-e and Supplemental Fig. 6a, b). We observed rapid and robust calcium transients and a dose-dependent increase in percentage of neurons responding to PLpro in DRG cultures with a maximum of 15.2% activation (Fig. 2b). We observed similar proportions of responses in TG cultures (Supplemental Fig. 6a). Interestingly, we observed a greater fraction of neurons that responded to PLpro in cultures of NJG neurons across all PLpro concentrations (33.9% at 100nM; Fig. 2d). Consistent with the activation of nociceptors, PLpro-responsive neurons were of small diameter (Supplemental Fig. 6c-e) and responded to capsaicin (TG: 63.3%; DRG: 85.7%; NJG: 100%, Supplemental Fig. 6b and Fig. 2c, e). A subset of TRPV1+ nociceptors also express the TRPA1 ion channel, a key driver of pain and airway inflammation. PLpro responsive neurons in the DRG and NJG also responded to the TRPA1 agonist, Allyl isothiocyante (AITC; TG: 32.9%, DRG: 33.3%, NJG: 50%; Supplemental Fig. 6b and Fig. 2c, e). As observed in mouse nociceptors, PLpro also evoked calcium transients in a subset of human iPSC-derived nociceptors and elicited significantly more calcium influx than vehicle (Fig. 2f, g). Taken together, we demonstrate that PLpro directly activates a subset of human and mouse nociceptors.

How does PLpro activate neurons? Proteolytic activity of PLpro is required for both viral protein processing and inhibition of anti-viral immunity[208]. Is proteolytic activity also required for neuronal activation? Studies have shown that a point mutation of the key catalytic cysteine to a serine ($PLpro_{C111S}$) results in a catalytically inactive mutant PLpro

(Fig. 3a, b). The $PLpro_{C111S}$ mutant activated significantly fewer DRG neurons than active $PLpro_{WT}$, comparable to activation by vehicle perfusion (Fig. 3c, d and Fig. 2b). Likewise, co-application of PLpro with PLpro inhibitor 19[217] that blocks catalytic activity significantly decreased the percentage of DRG neurons that are activated (Supplemental Fig. 6f). Together, this demonstrates that neuronal activation by PLpro is dependent on its cysteine protease activity. Thus, we asked whether catalytic activity is also required for PLpro-evoked sneezing. Indeed, unlike treatment with PLpro, intranasal treatment with the $PLpro_{C111S}$ mutant elicited few sneezes, similar to vehicle treatment (Fig. 3e,f). These data show that both neuronal activation and sneeze reflexes are mediated directly by the proteolytic activity of PLpro.

PLpro is expressed by all coronaviruses including the pathogenic betacoronaviruses. SARS-CoV (SARS) and MERS-CoV (MERS) share 89% and 51% sequence similarity to SARS-CoV-2 PLpro, respectively, and each of these proteases display different substrate specificity and efficiency[208,218,219]. Nonetheless, all three proteases share an identical cleavage sequence motif (L-x-G-G). Thus, we assessed whether the SARS and MERS PLpro also activate mouse neurons. We observed nearly identical dose-dependent responses to SARS, MERS, and SARS-CoV-2 PLpro (Fig. 3g), further suggesting that cleavage of this amino acid sequence is sufficient to drive neuronal activation. Overall, these data demonstrate a new mechanism by which pathogenic betacoronaviruses target the nervous system raising interesting questions about the evolution of PLpro to drive host responses that promote viral transmission.

PLpro-induced sneeze and pain require the host TRPA1 ion channel

We thus set out to probe the mechanism by which PLpro activates nociceptors in mice. PLpro opens a calcium-permeable ion channel in the plasma membrane, as calcium responses were eliminated when extracellular calcium was chelated (Supplemental Fig. 6g). Airway irritants and inflammatory mediators, including proteases, activate nociceptors via the calcium-permeable ion channels, TRPV1 or TRPA1[41,47,95,220,221]. To test the requirement for these channels, we examined PLpro responses in TRPV1 or TRPA1 deficient mice and found that the percent of PLpro responders was reduced (WT: 6.8%, TRPV1 KO: 4.3%, TRPA1 KO: 2.7%; Fig. 4a, Supplemental Fig. 6g). The acute blockade of TRPA1 with the antagonist HC-030031 (HC) but not blockade of TRPV1 with the antagonist AMG 517 (AMG), also reduced PLpro responders (WT: 4.4%, AMG: 7.4%, TRPA1 KO: 2.5%; Fig. 4b, Supplemental Fig. 6g) comparable to responses observed in TRPA1 KO neurons. These data demonstrate that PLpro activates sensory neurons via the TRPA1 ion channel.

Pain is a common symptom of acute COVID-19 infection and animal models of SARS-CoV-2 infection display mechanical allodynia both during and after infection[87,90,108,189]. A wide variety of irritants and inflammatory mediators induce mechanical or thermal sensitization via TRPV1 and TRPA1[41,222]. Thus, we tested if, in addition to acute pain behaviors (Supplemental Fig. 5a, b), PLpro could also drive pain hypersensitivity. We found that PLpro promotes mechanical hypersensitivity following intradermal injection into the hindpaw. PLpro significantly reduced the von Frey paw withdrawal threshold three

hours after injection and reversed by 24 hours (Fig. 4c). TRPA1-deficient mice failed to develop the PLpro-induced mechanical sensitization observed in wild-type and TRPV1-deficient mice (Fig. 4d, Supplemental Fig. 7a-c). Interestingly, we observed no difference in heat sensitivity between vehicle-and PLpro-injected paws (Fig. 4e), consistent with TRPA1's role in promoting mechanical, but not thermal sensitization(Bautista et al., 2006; Lennertz et al., 2012). We also found that TRPA1 is required for PLpro-induced sneezing. PLpro triggers robust sneezing in wild-type and TRPV1-deficient mice but not in TRPA1-deficient mice (Fig, 4f-i). Altogether, these data demonstrate that PLpro activates nociceptors via TRPA1 to drive sneezing and pain behaviors. While TRPA1 is well known to mediate pain and cough[41,46], we now also demonstrate a role for TRPA1 in viral-associated sneezing and pain.

SARS-CoV-2 infection targets a key nociceptive signaling pathway via divergent mechanisms

A key hallmark of TRPA1- and TRPV1-expressing neurons is the release of the neuropeptides calcitonin gene-related peptide (CGRP) and Substance P that can drive neurogenic inflammation(Basbaum et al., 2009) and immunomodulation(Pinho-Ribeiro et al., 2017; Tamari et al., 2024). We tested if PLpro was sufficient to elicit release of CGRP and Substance P from trigeminal ganglia cells in vitro. PLpro triggered acute release of CGRP (Fig. 5a). However, surprisingly, unlike allergen proteases, we did not observe the release of Substance P (Supplemental Fig. 8a)[203,206]. Using an ex vivo mouse tracheal preparation, we found that PLpro induced significant release of CGRP above baseline from tracheal nerve endings (Fig. 5b). These data demonstrate that activation of neurons by PLpro is sufficient to induce acute release of CGRP both in vitro and into the airways. CGRP has been detected in bronchoalveolar lavage fluid of SARS-CoV-2 infected patients and correlates with viral load and disease severity[223]. Our data demonstrating PLpro-evoked neuronal release of CGRP now provides a potential mechanism for this clinical finding.

Direct infection of SARS-CoV-2 is observed in human, hamster, and mouse sensory ganglia[86,87,90,224]. While these neurons are susceptible to infection, unlike in epithelial cells, the virus does not replicate[86,87,224] . Despite this lack of replication, infection drives gene expression changes in hamster sensory ganglia that are related to neuronal signaling and neuroinflammation[90], which could reflect consequences of the systemic response to infection or direct infection of the ganglia. Thus, we assessed the consequences of direct SARS-CoV-2 infection on cultured mouse trigeminal ganglia. SARS-CoV-2 infection significantly upregulated 789 genes and downregulated 1664 genes with the most differentially expressed genes being related to inflammation (Supplemental Fig. 8b, c). We then assessed how infection and this infection-induced inflammatory response alters the transcriptional signatures associated with functional neuronal subtypes within the sensory ganglia. Nociceptor-associated gene sets were significantly altered, including those corresponding to both non-peptidergic and peptidergic nociceptors, while gene sets associated with mechanoreceptors, proprioceptors, and itch were not significantly changed (Fig. 5c). This suggests that infection drives transcriptional changes that may selectively impact nociception. More so,

several of the most upregulated nociceptive genes encode ion channels (*P2rx3, Scn9a, Trpa1, Trpv1, Cacna1b, Cacna1a, Chrnb2,* and *Grin1*) that can increase the excitability of nociceptors to promote pain (Fig. 5d). SARS-CoV-2 infection also upregulated *Calca* and *Calcb,* the genes that encode CGRP-α and -β, but not *Tac1,* the gene that encodes Substance P (Supplemental Fig. 8e). The same TRPA1-CGRP signaling pathway that is directly activated by PLpro is also transcriptionally upregulated by SARS-CoV-2 infection. We found that treatment with PLpro alone did not induce any significantly differentially expressed genes (Supplemental Fig. 8f) suggesting that SARS-CoV-2 has evolved convergent mechanisms to target nociceptor function to promote sneeze, cough, and pain.

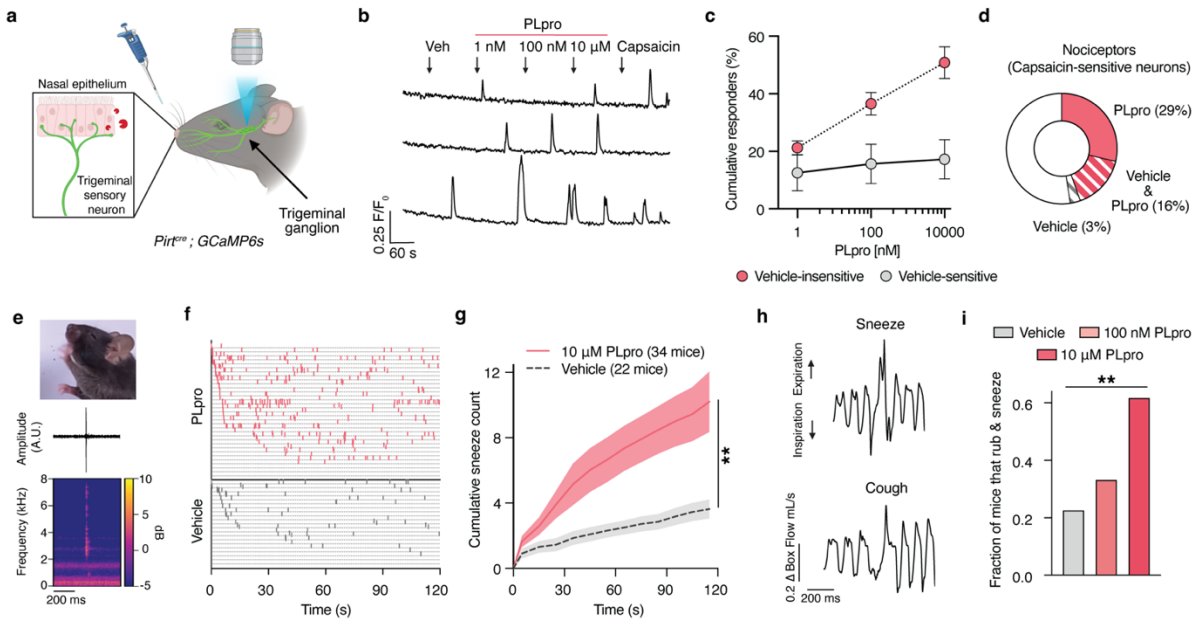

Figure 1: PLpro activates upper airway-innervating neurons to trigger sneeze and cough.

a, Schematic of in vivo imaging of trigeminal ganglion neurons during intranasal perfusion. **b**, Representative calcium transients of trigeminal neurons following intranasal perfusion of vehicle (Veh), 1 nM, 100 nM, 10 µM PLpro, and 100 µM capsaicin; arrowheads indicate time of intranasal perfusion. **c**, Percentage of PLpro-responsive neurons among vehicle-sensitive and vehicle-insensitive neurons, *n* = 6 mice. **d**, PLpro activates a subset (45 of 101) of nociceptors, defined by capsaicin sensitivity; data of 101 neurons from 6 mice. **e**, Intranasal PLpro triggers high-frequency audio events (bottom) and nasal expulsions (top). **f**, Raster plot of sneeze events, identified by audio recordings, in mice treated intranasally with 10 µM PLpro (*n* = 34 mice) or vehicle (*n* = 22 mice). **g**, Average cumulative sneeze counts following intranasal treatment of 10 µM PLpro and vehicle-treated mice. Two-way repeated measures ANOVA: $F(1,54) = 7.34$, p (Vehicle vs. PLpro) = 0.0090. **h**, Representative PLpro-evoked sneeze and cough waveforms recorded using whole-body plethysmography. **i**, Fraction of mice exhibiting rubbing and sneezing behaviors within 30 seconds of intranasal treatment of vehicle (*n* = 22 mice), 100 nM PLpro (*n* = 18 mice), and 10 µM PLpro (*n* = 34 mice). Fisher's exact test: p (Veh vs. 100 nM PLpro) = 0.2972, p (Veh vs. 10 µM PLpro) = 0.0142. Error bars and shading represent mean ± SEM. Illustration in **a** was created using BioRender (https://www.biorender.com).

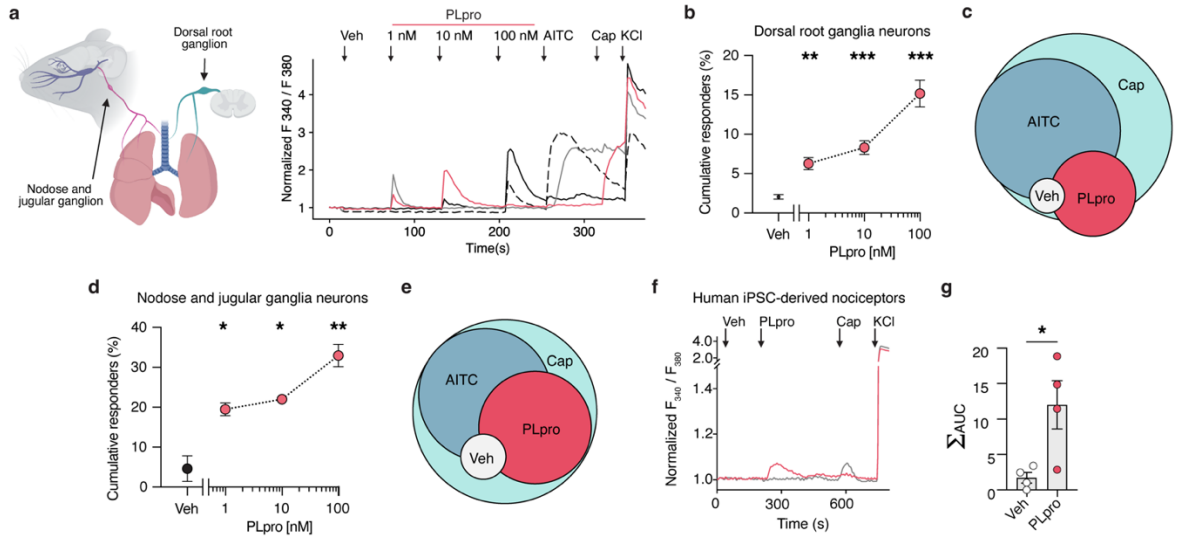

Figure 2: PLpro directly activates nociceptors.

a, Left, schematic illustrating airway-innervating sensory ganglia; Right, representative calcium transients from dorsal root ganglia (DRG) neurons following perfusion of vehicle (Veh), 1 nM, 10 nM, 100 nM PLpro, 100 µM allyl isothiocyanate (AITC), 1 µM capsaicin (Cap), and high potassium solution (KCl), arrowheads indicate time of stimulus perfusion. **b**, PLpro induces dose-dependent activation of DRG neurons: 1 nM (6.3%), 10 nM (8.3%), and 100 nM (15.2%), significantly greater than vehicle (2.1%). One-way ANOVA: $F(3, 32) = 27.04$, $p < 0.0001$; Dunnett's post hoc test: p (Veh vs. 1 nM) = 0.0216, p (Veh vs. 10 nM) = 0.0006, p (Veh vs. 100 nM) < 0.0001, n = 9 mice. **c**, Venn diagram of PLpro-, Veh-, AITC-, and Cap-responsive DRG neurons (n = 154 neurons). **d**, PLpro induces dose-dependent activation of NJG neurons: 1 nM (19.49%), 10 nM (22.01%), and 100 nM (32.96%), significantly greater than vehicle (4.60%). One-way ANOVA: $F(3, 4) = 25.50$, $p = 0.0046$; Dunnett's post hoc test: p (Veh vs. 1 nM) = 0.0235, p (Veh vs. 10 nM) = 0.0134, p (Veh vs. 100 nM) = 0.0022, n = 2 biological replicates, each containing NJG from two mice. **e,** Venn diagram of PLpro-, Veh-, AITC-, and CAP-responsive NJG neurons (n = 220 neurons). **f**, Representative calcium transients evoked by 500 nM PLpro and 1 µM Cap in human iPSC-derived neurons. **g**, PLpro induces significantly greater calcium influx (area under the curve, AUC) than vehicle perfusion (t-test: $t = 2.953$, $df = 6$, $p = 0.026$, n = 4 wells per condition). Error bars represent mean ± SEM. Illustration in **a** was created using BioRender (https://www.biorender.com).

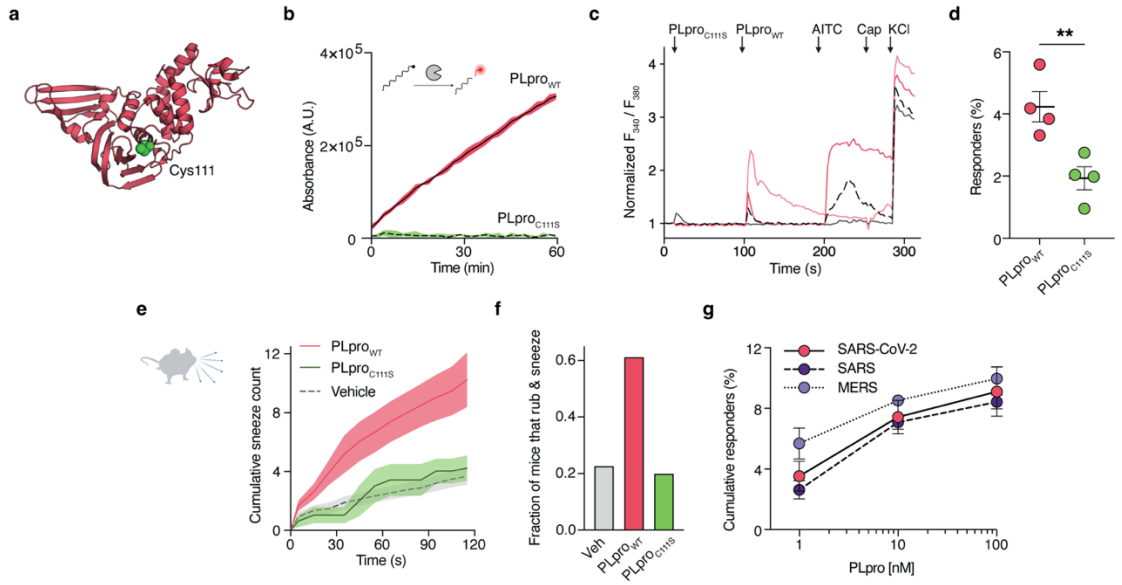

Figure 3: PLpro catalytic activity is required to activate sensory neurons and induce sneeze.

a, Structure of PLpro (PDB id: 7JIW) highlighting the active site residue Cys111 (represented as spheres). **b**, Proteolytic activity measured by fluorescence from cleaved substrate for wild-type PLpro ($PLpro_{WT}$) and catalytically inactive mutant PLpro ($PLpro_{C111S}$). **c**, Representative calcium transients from DRG neurons following perfusion of 100 nM $PLpro_{C111S}$, 100 nM $PLpro_{WT}$, 100 µM AITC, 1 µM capsaicin, and high potassium solution (KCl), arrowheads indicate time of perfusion. **d**, $PLpro_{C111S}$ activates significantly fewer neurons compared to $PLpro_{WT}$ (*t*-test: t = 3.755, df = 6, $p = 0.0095$, n = 4 mice). **e**, Average cumulative sneeze counts following intranasal treatment of vehicle (n = 22 mice), 10 µM $PLpro_{WT}$ (n = 34 mice), and $PLpro_{C111S}$ (n = 5 mice). **f**, Fraction of mice exhibiting rubbing and sneezing behaviors within 30 seconds of intranasal treatment of vehicle, 10 µM $PLpro_{WT}$, and 10 µM $PLpro_{C111s}$. **g**, PLpro from SARS-CoV-2 (n = 4 mice), SARS (n = 3 mice), and MERS (n = 2 mice) induces nearly identical dose-dependent activation of DRG neurons. Error bars and shading represent mean ± SEM. Illustration in **e** was created using BioRender (https://www.biorender.com).

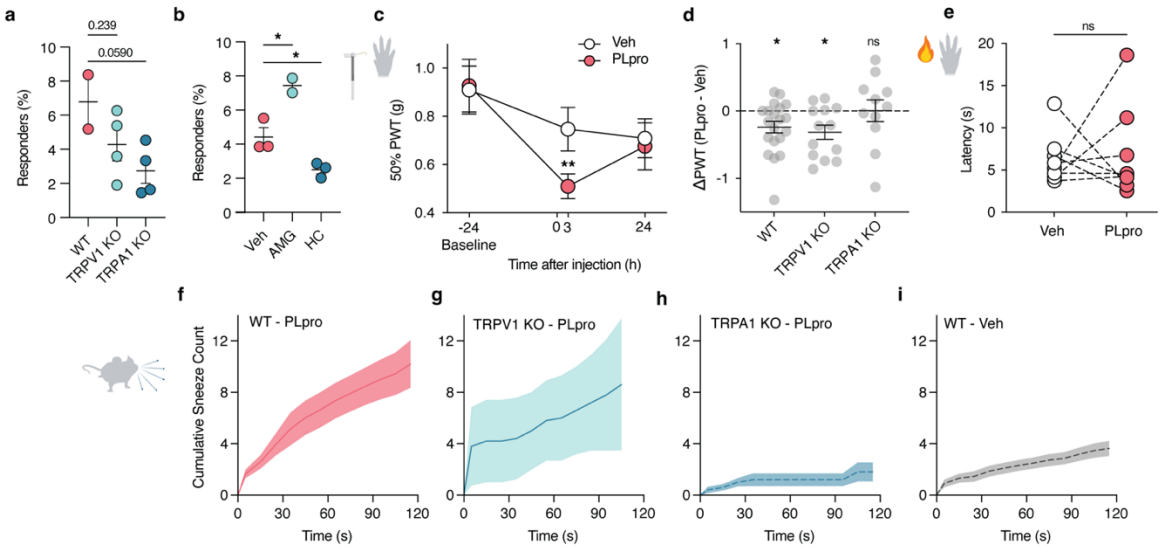

Figure 4: PLpro-evoked pain and sneeze require the host ion channel TRPA1
a, Percentage of DRG neurons responding to 100 nM PLpro in wild-type C57BL/6J (WT) mice (n = 2 mice), TRPV1 KO mice (n = 4 mice), and TRPA1 KO mice (n = 4 mice). One-way ANOVA: F(2, 7) = 3.367, p = 0.0945; Dunnett's post hoc test: p (WT vs. TRPV1 KO) = 0.2386, p (WT vs. TRPA1 KO) = 0.0590. **b**, Percentage of DRG neurons from WT mice responding to 100 nM PLpro in the presence of vehicle (0.1% DMSO, n = 3 mice), a TRPV1 antagonist (AMG, n = 2 mice), or a TRPA1 antagonist (HC, n = 3 mice). One-way ANOVA: F(2, 5) = 28.48, p = 0.0019; Dunnett's post hoc test: p (Veh vs. AMG) = 0.0102, p (Veh vs. AMG) = 0.0389. **c**, Intradermal injection of 50 µM PLpro reduces the paw withdrawal threshold (PWT) at 3 hours post-injection but not at 24 hours, compared to baseline (24 hours pre-injection). Two-way repeated measures ANOVA: F(1.793, 64.56) = 5.477, p (time) = 0.008; Dunnett's multiple comparisons: Vehicle-injected paws: p (Baseline vs. 3 h) = 0.5550, p (Baseline vs. 24 h) = 0.0729; PLpro-injected paws: p (Baseline vs. 3 h) = 0.0077, p (Baseline vs. 24 h) = 0.2007; n = 19 mice per group. **d**, WT and TRPV1 KO mice, but not TRPA1 KO mice, develop mechanical hypersensitivity 3 hours post-injection. WT: one-sample t-test, t = 2.746, df = 19, p = 0.013, n = 11 mice; TRPV1 KO: one-sample t-test, t = 3.001, df = 20, p = 0.011, n = 13 mice; TRPA1 KO: one-sample t-test, t = 0.039, df = 10, p = 0.970, n = 11 mice. **e**, Intradermal PLpro injection does not alter response latency to radiant heat (paired t-test: t = 0.233, df = 7, p = 0.822, n = 8 mice). **f-i**, Intranasal treatment of 10 µM PLpro triggers more sneezing in **f,** WT (n = 34 mice) and **g**, TRPV1 KO mice (n = 5 mice) compared to **h**, TRPA1 KO mice (n = 5 mice) or **i**, vehicle-treated WT mice (n = 11 mice). Error bars and shading represent mean ± SEM. Illustrations in **c,e,f** were created using BioRender (https://www.biorender.com).

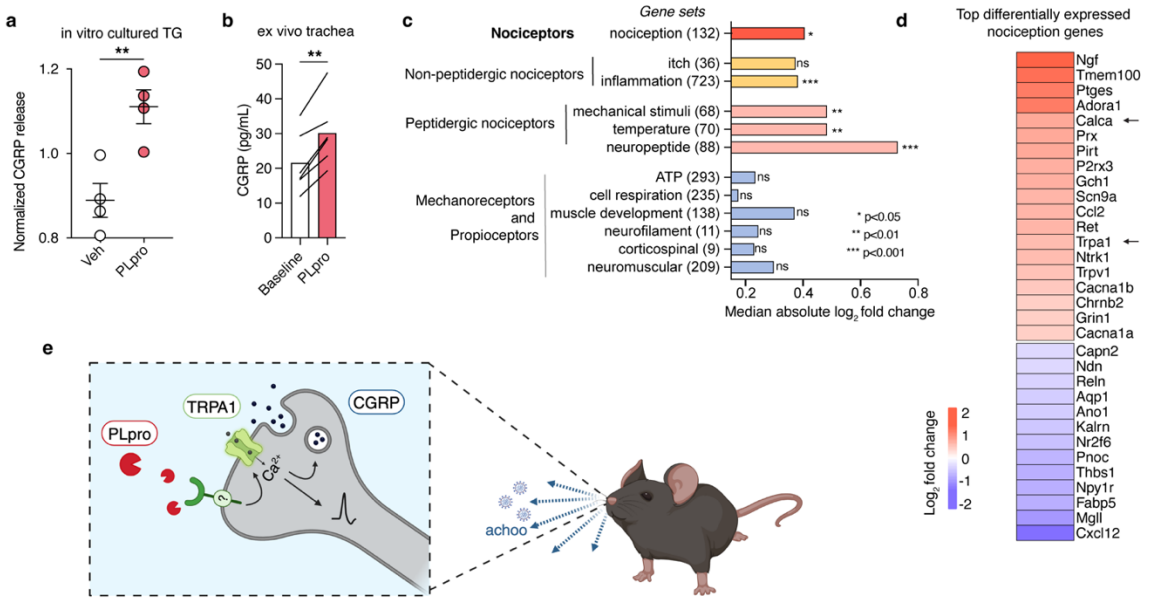

Figure 5: SARS-CoV-2 infection and PLpro activation share a key nociceptive signature.

a, PLpro induces CGRP release from cultured TG (*t*-test: $t = 3.928$, df = 6, $p = 0.008$, n = 4 animals) **b**, PLpro significantly increases CGRP release compared to baseline in an ex vivo tracheal preparation (one sample *t*-test: $t = 6.80$, $df = 5$, $p = 0.001$, $n = 6$ tracheas (one per mouse). **c**, SARS-CoV-2 infection significantly alters gene sets associated with nociceptors but not mechanoreceptors and proprioceptors. Median absolute $\log_2$ fold changes for each custom gene set were tested against 100,000 random permutations of identically sized gene sets (gene set sizes listed in parenthesis). Mock infected: $n = 4$ wells, SARS-CoV-2 infected: $n = 3$ wells. *p <0.05, **p<0.01, ***p<0.001. **d**, Heatmap of the most significantly differentially expressed nociception-associated transcripts ($\log_2$ fold change: infection vs mock). **e**, Model: PLpro activates nociceptors through its proteolytic activity, triggering TRPA1-dependent sneezing, coughing, and pain behaviors. Illustration in **e** was created using BioRender (https://www.biorender.com).

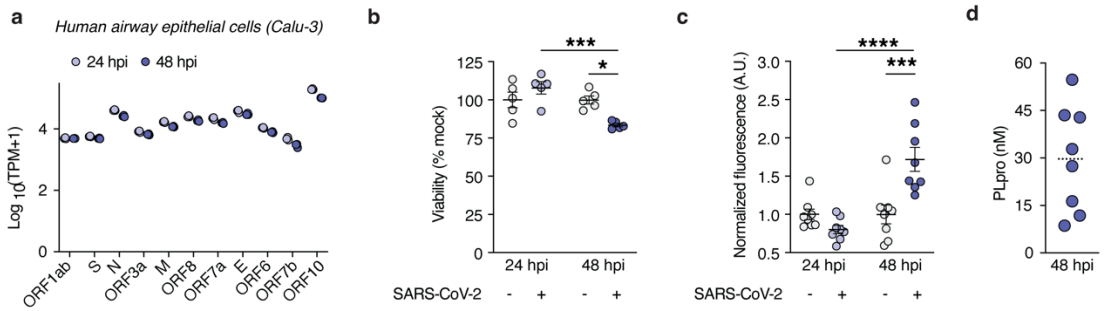

Supplemental Figure 1: SARS-CoV-2 PLpro is released from infected airway epithelial cells.

a, SARS-CoV-2 transcript expression (transcripts per million, TPM) in Calu-3 cells infected at a multiplicity of infection (MOI) of 1, measured at 24 and 48 hours post-infection (hpi). *n* = 3 wells per condition. **b**, Infection induces cell death at 48 hpi measured as the percentage of viable cells relative to mock-infected controls. Two-way ANOVA**:** F(1,16) = 11.69, *p* (Interaction of time and infection) = 0.0035; Šídák's multiple comparisons**:** *p* (mock vs. infected 24hpi) = 0.3628, *p* (mock vs. infected 48 hpi) = 0.0140, *p* (24hpi vs. 48 hpi infected) = 0.0005, n = 5 wells per group. **c**, Proteolytic activity of PLpro in culture media from SARS-CoV-2- or mock-infected Calu-3 cells at 24 and 48 hpi, measured by fluorescence of cleaved substrate and normalized to same-day controls. Two-way ANOVA**:** F(1,28) = 18.01, *p* (Interaction of time and infection) = 0.0002; Šídák's multiple comparisons**:** *p* (mock vs. infected 24hpi) = 0.5022, *p* (mock vs. infected 48 hpi) = 0.0002, *p* (24hpi vs. 48 hpi infected) < 0.0001, *n* = 8 wells per group. Data from two independent experiments. Error bars represent mean ± SEM**.** **d**, Interpolated concentration of PLpro in the supernatant of Calu-3 cells at 48 hpi, n = 8 wells; line represents the mean.

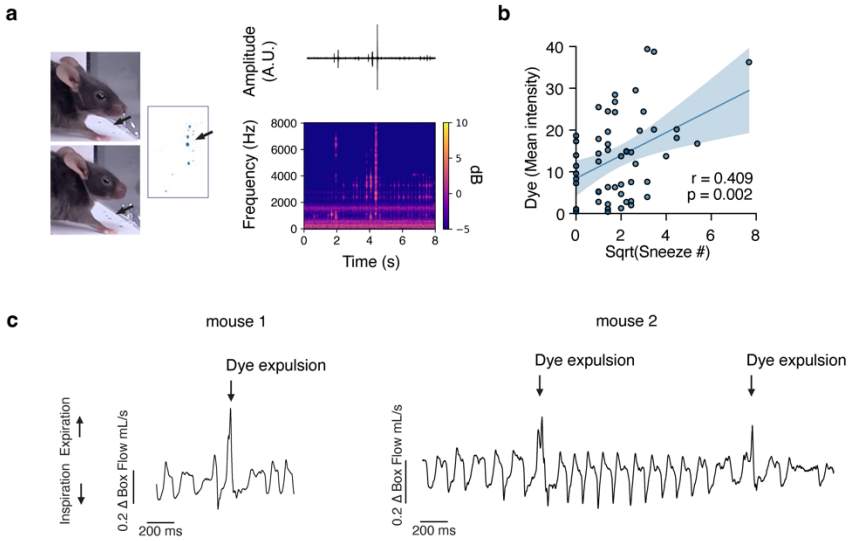

Supplemental Figure 2: Nasal dye expulsions correlate with high-frequency audible events and respiratory waveforms.
a, Sneeze events are identified by audio waveforms and correlate to dye droplets on the bottom of the chamber. Left, images before and after a dye expulsive event, arrow indicates dye from this sneeze on the bottom of the chamber; Right, audio waveform during this dye expulsive event. **b**, The number of sneezes over 2 minutes correlates with the amount of dye at the bottom of the chamber. The square root-transformed sneeze count is significantly correlated with the mean dye intensity (Pearson's r = 0.4094, *p* = 0.0023) **c**, Dye expulsive events correlate to distinct respiratory patterns. Left, images before and after a dye expulsive event, arrow indicate expelled dye droplet with corresponding respiratory waveform during this dye expulsive event. Two consecutive dye expulsive events captured in another mouse correlate to respiratory waveforms that resemble sneeze (first event) and cough (second event).

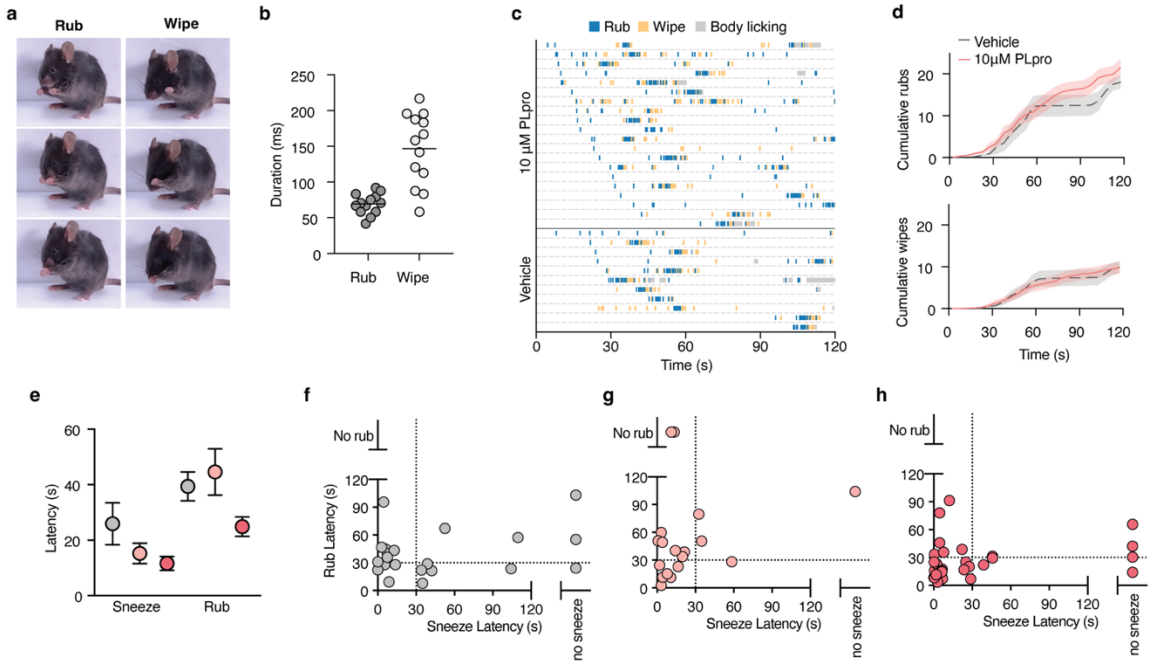

Supplemental Figure 3: Characterization of behaviors elicited by intranasal PLpro treatment.

a, Image sequence of a nose rub and face wipe. **b**, Duration (milliseconds) of the behavioral sequence for a nose rub and face wipe. **c**, Raster plot of rubs, wipes, and body-licking events for intranasal 10 µM PLpro and vehicle-treated mice. **d**, Average cumulative rub and wipe counts from individual mice treated with 10 µM PLpro (*n* = 20) or vehicle (*n* = 11). **e**, Mean and standard error of the mean of the sneeze and rub latency for mice treated with **f**, vehicle (*n* = 22 mice), **g**, 100 nM PLpro (*n* = 18 mice), and **h**, 10 µM PLpro (*n* = 34 mice). Error bars and shading represent mean ± SEM.

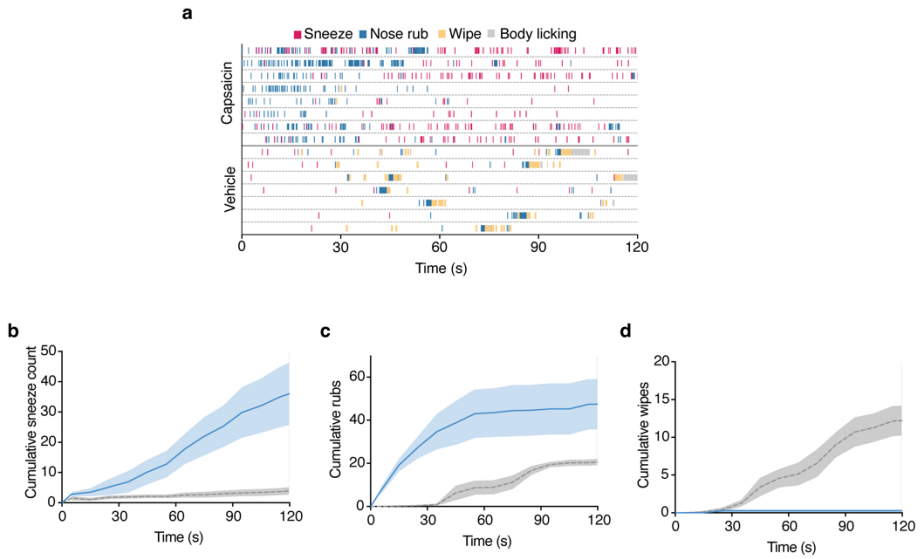

Supplemental Figure 4: Capsaicin triggers a variety of intranasal behaviors.
a, Raster plot of sneeze, rub, wipe, and body-licking events for mice intranasally treated with 100 μM capsaicin or vehicle (0.1% DMSO). **b,** Cumulative sneeze count, **c**, rub count and **d**, wipe counts from mice treated with 100 μM capsaicin (*n* = 8) or vehicle (*n* = 7). Shading represents mean ± SEM.

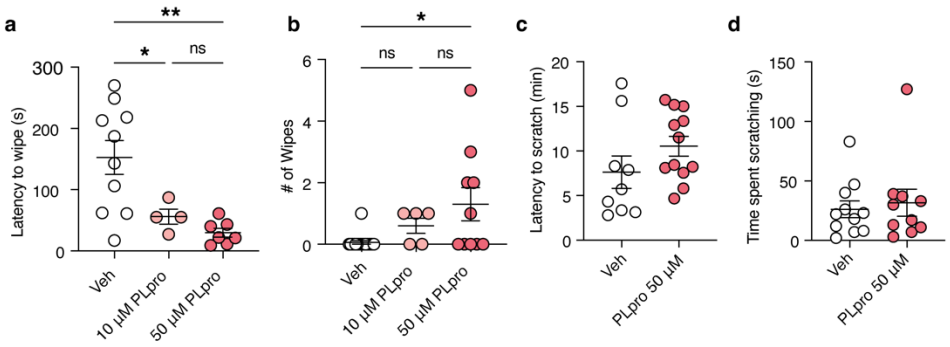

Supplemental Figure 5: PLpro triggers pain but not itch-associated behaviors. **a**, PLpro elicited a significantly shorter latency to the first wipe. One-way ANOVA: $F(2,18) = 9.983$, $p = 0.003$; Tukey's multiple comparisons test: p (Veh vs. 10 µM) = 0.0495, p (Veh vs. 50 µM) = 0.0028, p (10 µM vs. 50 µM) = 0.7890. **b**, PLpro induced a dose-dependent increase in the number of wipes in the first minute. Kruskal-Wallis test: $\chi^2 = 8.920$, $p = 0.0116$; Dunn's multiple comparisons test: p (Veh vs. 10 µM) = 0.1340, p (Veh vs. 50 µM) = 0.0209, p (10 µM vs. 50 µM) > 0.9999. Vehicle (n = 17 mice), 10 µM PLpro (n = 5 mice), 50 µM PLpro (n = 10 mice). **c**, PLpro did not significantly affect the latency or **d**, frequency of scratching behavior compared to vehicle. Vehicle (n = 11 mice), 50 µM PLpro (n = 10 mice). Error bars represent mean ± SEM.

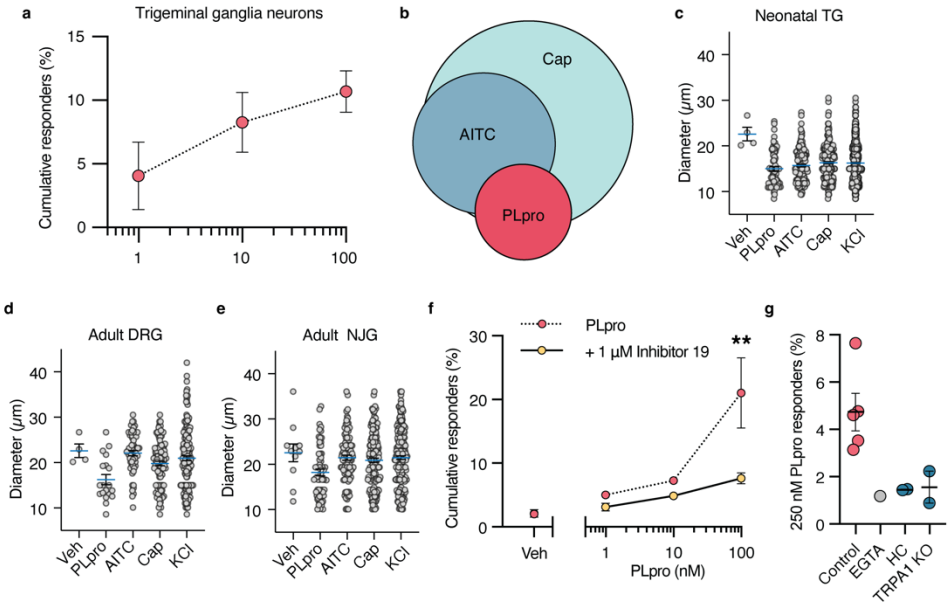

Supplemental Figure 6: PLpro activates nociceptors.
a, PLpro induces dose-dependent activation of TG neurons: 1 nM (4.1%), 10 nM (8.3%), and 100 nM (10.7%). **b**, Venn diagram of PLpro-, Veh-, AITC-, and CAP-responsive TG neurons (*n* = 744 neurons). **c**, PLpro responders are of smaller diameter compared to vehicle responders and the population overall in **c**, neonatal mouse trigeminal ganglia (Veh: 22.6 µm, PLpro: 15.0 µm, AITC: 15.7 µm, Cap: 16.3 µm, KCl: 16.3 µm) **d**, adult DRG (Veh: 22.6 µm, PLpro: 16.2 µm, AITC: 22.1 µm, Cap: 19.8 µm, KCl: 21.0 µm) and **e**, adult NJG neurons (Veh: 22.5 µm, PLpro: 18.2 µm, AITC: 21.4 µm, Cap: 20.9 µm, KCl: 21.5 µm). **f,** Co-application of 1 uM PLpro activity inhibitor 19 significantly reduces the dose-dependent activation of DRG neurons observed with PLpro alone. Two-way repeated measures ANOVA: F(3,6) = 4.891, *p* (Interaction of stimulus and inhibitor) = 0.0473; Šídák's multiple comparisons**:** *p* (Veh ± inhibitor) > 0.0999, *p* (1 nM ± inhibitor) = 0.9500, *p* (10 nM ± inhibitor) = 0.8920, *p* (100 nM ± inhibitor) = 0.0060, *n* = 2 mice per group. **g**, Percentage of mouse TG neurons that respond to 250nM PLpro in control neurons from wild-type C57BL/6N mice in physiological extracellular calcium (2 mM Ca2+, 4.7%, *n* = 5) is greater than in the absence of extracellular calcium (EGTA, 1.2%, *n* = 1), in the presence of a TRPA1 antagonist (HC, 1.4%, *n* = 2), and in neurons from TRPA1 KO (1.6%, *n* = 2). Error bars represent the mean ± SEM, *n* = biological replicates (animals), with 3-4 wells per animal containing ~100–300 neurons per well.

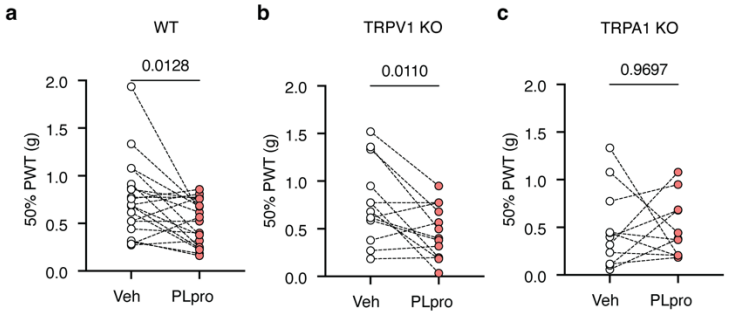

Supplemental Figure 7: TRPA1 KO mice do not develop PLpro-induced mechanical hypersensitivity.

a, WT and **b**, TRPV1 KO mice, but not **c**, TRPA1 KO mice develop mechanical hypersensitivity in the PLpro-injected paw compared to the contralateral vehicle-injected paw 3 hours post-injection. **a**, WT; Paired *t*-test, $t = 2.746$, $df = 19$, $p = 0.013$, $n = 11$ mice. **b**, TRPV1 KO; Paired *t*-test, $t = 3.001$, $df = 20$, $p = 0.011$, $n = 13$ mice. **c**, TRPA1 KO; paired *t*-test, $t = 0.039$, $df = 10$, $p = 0.970$, $n = 11$ mice.

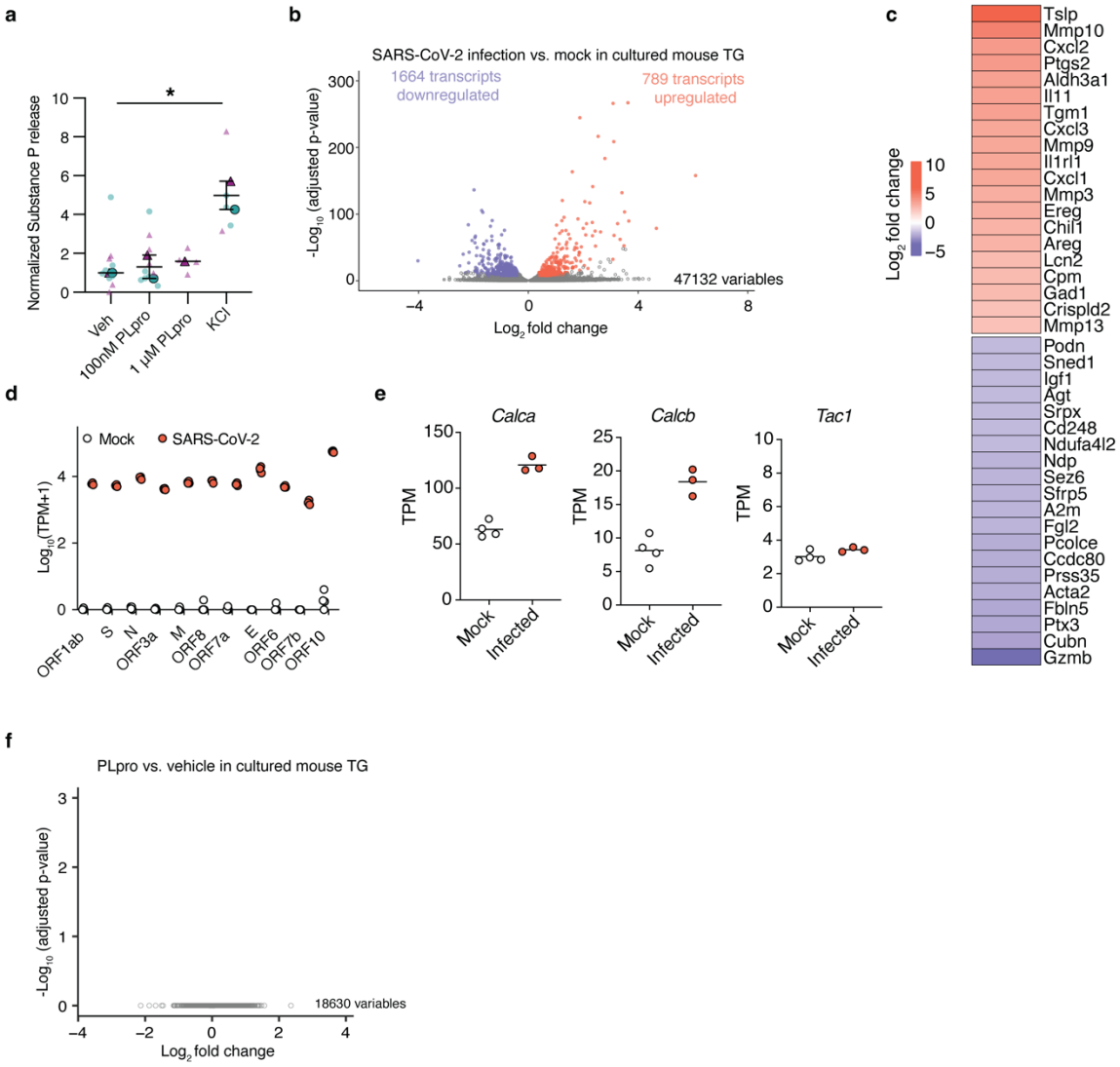

Supplemental Figure 8: SARS-CoV-2 infection drives gene expression changes in cultured primary mouse trigeminal ganglia.

a, PLpro does not elicit the release of Substance P from cultured adult trigeminal ganglia (TG). One-way ANOVA: F(3,3) = 11.44, p = 0.00377; Dunnett's post hoc test: *p* (Veh vs. 100 nM PLpro) = 0.9577, *p* (Veh vs. 1 µM PLpro) = 0.8682, *p* (Veh vs. KCl) =.0303, Vehicle (*n* = 2 biological replicate), 100 nM PLpro (*n* = 2 biological replicate), 1 µM PLpro (*n* = 1 biological replicate), KCl (*n* = 2 biological replicate). Each biological replicate contains pooled TG, with 2-6 wells per biological replicate. **b**, SARS-CoV-2 infection for 48 hours upregulates 789 transcripts and downregulates 1,664 transcripts compared to mock infection in cultured TG. Differentially expressed genes were identified using the following criteria: base mean > 152, $\log_2$ fold change > 0.37, and adjusted p-value < 0.01. SARS-CoV-2-infected (*n* = 3 wells) and mock-infected (*n* = 4 wells), *n* represents wells from pooled TG from 4 mice. **c**, Heatmap of the 20 most highly upregulated and downregulated transcripts ($\log_2$ fold change of SARS-CoV-2 infection vs. mock). **d**, SARS-CoV-2 viral transcript (transcript per million [TPM]) expression in cultured TG 48

hours post-infection. **e**, *Calca* and *Calcb* but not *Tac1* transcripts are significantly upregulated by SARS-CoV-2 infection. Adjusted *p* (*Calca)* = 9.05 x 10^{-21}, adjusted *p* (*Calcb)* = 5.52 × 10^{-9}; adjusted *p* (*Tac1)* = 0.991. **f**, Treatment with 2 μM PLpro (14-16 hours) does not alter transcript expression in cultured TG neurons compared to vehicle treatment PLpro (*n* = 6 biological replicates) and vehicle (*n* = 5 biological replicates), each biological replicate contains TG pooled from 4 mice.

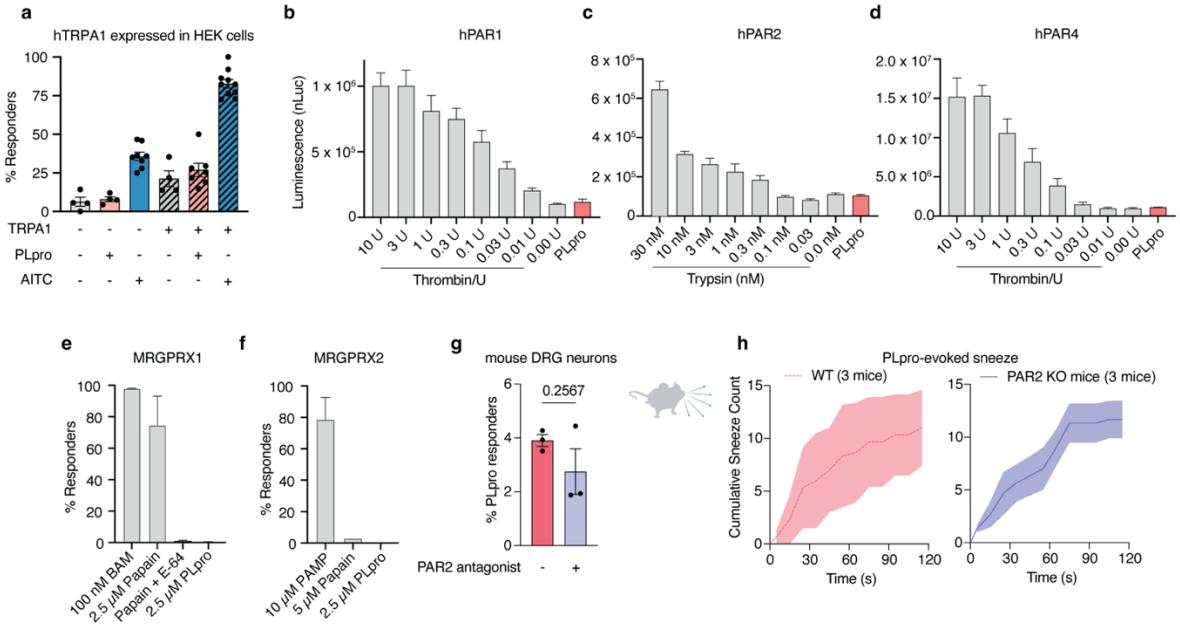

Supplemental Figure 9: PLpro does not activate heterologously expressed TRPA1, PARs, or MRGPRs, nor does it require mPAR2 for neuronal activation or sneezing. **a-f**, PLpro does not activate heterologously expressed TRPA1 or other candidate receptors. **a**, Percentage of HEK293 cells transfected with human TRPA1 that respond to PLpro, assessed by calcium responses. HEK293 cells transfected with human TRPA1. **b-d**, PAR cleavage assays using nLuc-PAR-eYFP-CHO cells. Cleavage data for human **b**, PAR1, **c**, PAR2, and **d**, PAR4 following treatment with PLpro, thrombin (for PAR1 and PAR4), or trypsin (for PAR2). **e-f**, Percentage of Chem-1 cells stably expressing MRGPRX1 or MRGPRX2 that respond to PLpro, assessed by calcium responses. **g**, Percentage of mouse DRG neurons that respond to 100 nM PLpro in the presence of the PAR2 antagonist, AZ3451, compared to controls (*t*-test: t = 1.322, df = 4, $p = 0.2567$, $n = 3$ mice). **h**, PAR2 KO mice exhibit comparable PLpro-evoked sneezing to WT mice, $n = 3$ mice per group. Illustration in **h** was created using BioRender (https://www.biorender.com).

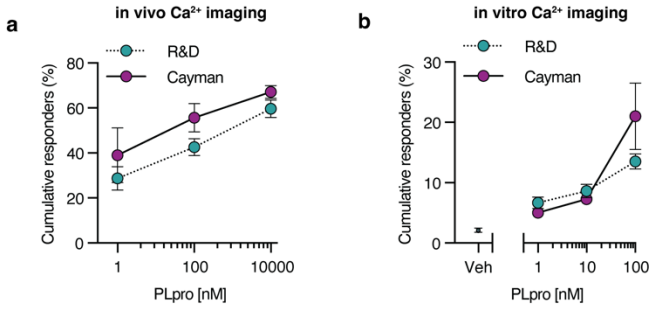

Supplemental Fig. 10: PLpro from two suppliers induces comparable neuronal activation.

a, Cumulative percentage of trigeminal neurons responding to PLpro from R&D and Cayman in vivo. Two-way ANOVA**:** F(2,8) = 10.18, *p* (R&D vs. Cayman) = 0.2451; Šídák's multiple comparisons**:** *p* (1 nM) = 0.6320, *p* (100 nM) = 0.4480, *p* (10 µM) = 0.8183, *n* = 3 mice per group. **b**, PLpro from both suppliers induces dose-dependent activation of DRG neurons in vitro. Two-way ANOVA**:** F(1,7) = 7.140, *p* (R&D vs. Cayman) = 0.5455; Šídák's multiple comparisons**:** *p* (veh) = 0.9951, *p* (1 nM) = 0.5219, *p* (10 nM) = 0.6979, *p* (100 nM) = 0.8668, R&D (*n* = 7 mice), Cayman (*n* = 2 mice). Error bars represent the mean ± SEM, *n* = biological replicates (animals), with 3-4 wells per animal containing ~100–300 neurons per well.

Discussion

Common symptoms of viral infection, such as sneezing, coughing, and headache, result from activation of somatosensory and vagal sensory neurons. Previously, viral infections, including SARS-CoV-2, were proposed to indirectly activate sensory neurons through inflammatory mediators released by infected epithelial and immune cells. Here, we demonstrate that SARS-CoV-2 directly activates sensory neurons independently of inflammation via PLpro, revealing a new mechanism whereby viral proteins stimulate neuronal reflexes such as sneezing and coughing. Together with previous findings demonstrating that bacteria directly target neurons to trigger cough (e.g., *Mycobacterium tuberculosis*)[102] or suppress immunity (e.g., *Staphylococcus aureus*)[109], our data suggest that peripheral neurons may be a pervasive yet underappreciated target among respiratory pathogens. By demonstrating that a virus, SARS-CoV-2, can also directly activate sensory neurons, these findings further our understanding of the diverse mechanisms by which pathogens manipulate host physiology.

We show that PLpro activates sensory neurons via the calcium-permeable ion channel TRPA1, a key mediator of irritation and inflammation. However, TRPA1 does not contain the canonical PLpro cleavage sequence nor is it activated directly by PLpro when heterologously expressed, suggesting an intermediate receptor or signaling pathway (Supplemental Fig. 9a). Although protease-activated receptors (PARs) and Mas-related G protein-coupled receptors (MRGPRs) are potential targets, like TRPA1, these receptors do not contain the PLpro cleavage motif nor are activated by PLpro (Supplemental Fig. 9b-h). Future work is necessary to identify the receptor and signaling pathway coupling PLpro activity to TRPA1-mediated neuronal activation.

Critically, our findings demonstrate that the proteolytic activity of PLpro is essential for neuronal activation, highlighting a conserved molecular mechanism for processing viral polyproteins, antagonizing interferon-stimulated immune responses, and promoting viral transmission via the induction of host symptoms. This multifunctional mechanism appears to be evolutionarily conserved among pathogenic betacoronaviruses, including SARS-CoV and MERS-CoV. While sneezing and coughing helps clear pathogens from the host, they also promote airborne viral dissemination, demonstrating a viral strategy that simultaneously drives immune evasion and enhances transmission. Thus, PLpro represents an attractive therapeutic target for COVID-19, as PLpro inhibitors could suppress viral replication and alleviate virus-induced symptoms such as sneezing, coughing, and pain.

Methods

Mouse studies

All mice were housed in standard conditions in accordance with standards approved by the Animal Care and Use Committee of the University of California Berkeley (14 hour light: 10 hour dark cycle, 21 °C). Wild-type C57BL/6N mice were obtained from Charles River for neonatal trigeminal cultures and C57BL/6J from Jackson Laboratories and were used for all other mouse experiments. All experiments were performed under the policies and recommendations of the International Association for the Study of Pain and approved by the University of California Berkeley Animal Care and Use Committee. Where appropriate, genotyping was performed by Transnetyx using real-time PCR. Mouse lines used in this study included Pirt-Cre (Pirttm3.1(cre)Xzd) gift from Dr Xinzhong Dong (Johns Hopkins University, Baltimore, MD) and Ai96 (B6J.Cg-Gt(ROSA)26Sortm96$^{(CAG-GCaMP6s)Hze}$/MwarJ), Trpv1 KO; Trpv1tm1Jul RRID:MGI:4417977, and Trpa1 / (A1 KO; Trpa1tm1Jul, RRID:MGI:3696956) originally from Jackson Laboratories and bred in-house.

Calcium imaging

In vivo calcium imaging of trigeminal ganglion

In vivo calcium imaging of trigeminal neurons was conducted in anesthetized mice as previously described[225]. In brief, Pirt-Cre;GCaMP6s mice were anesthetized with ketamine and xylazine (100 and 10 mg/kg intraperitoneal) and body temperature was maintained at 36°C throughout surgery and imaging. Mice were head-fixed on a custom chamber and tracheotomized to allow normal breathing and restrict intranasal perfusion to the upper airways. A unilateral craniotomy and hemispherectomy was performed to expose the dorsal surface of the right trigeminal ganglion. Hemostasis was achieved using Surgifoam gel sponge (Ethicon 1972). Images were collected at 5 Hz using a Sutter Movable Objective Microscope (MOM) equipped with an Olympus XL-Fluor 4X/340 (NA 0.28) lens, ORCA-Fusion BT Digital CMOS camera. 480nM illumination was provided by Lambda 721 (Sutter). Stimuli were applied via intranasal perfusion of 10 µL of solution applied evenly between both nostrils using a P20 pipette. Stimuli were applied at 2-minute intervals.

In vivo imaging analysis

Motion correction and source extraction were performed using Suite2p[226]. Suite2p-generated regions of interest (ROIs) were manually inspected and additional ROIs were manually identified. Neuropil was subtracted with a coefficient of 0.7. F_0 is defined as the median fluorescence 150 frames prior to stimulus treatment and used to calculate dF/F_0. Normalized traces were Gaussian filtered (sigma =2). Stimulus responders were identified if the peak dF/F_0 response during the 2-minute stimulation period was > 10%. Cells were identified as spontaneously active if their peak fluorescence was 5% greater

than the median fluorescence during the baseline window. The percentage of responsive cells were quantified by pooling all cells that respond to any of the applied stimuli.

Neuronal cultures

TG, DRG and NJG were cultured as previously described[47,227]. In brief, sensory ganglia were dissected and incubated in warmed Collagenase P (Roche) in Hanks calcium-free balanced salt solution (HBSS) followed by incubation in 0.25% trypsin with gentle agitation. Cells were washed, triturated, and plated in Minimum Essential Medium (MEM, Gibco) supplemented with 10% horse serum (v/v), MEM vitamins, penicillin/streptomycin and L-glutamine. Neonatal TG cultures were plated on poly-D-Lysine coated eight-well chambers for calcium imaging. Adult TG, DRG, and NJG were plated on poly-D-Lysine and laminin-coated eight-well chambers for calcium imaging or 96-well plates for infection and ELISA experiments. Age-matched WT controls were prepared on the same day for experiments on neurons from knockout mice. Human iPSC-derived neurons were differentiated per manufacturer's instructions and used in calcium imaging 21- and 39-days post differentiation (Axol Bioscience, ax0555).

In vitro calcium imaging

Neuronal Ca^{2+} imaging experiments were carried out as previously described[227]. Neuronal cultures were loaded for 45 min at room temperature with 10 μM Fura-2AM supplemented with 0.01% Pluronic F-127 (wt/vol, Life Technologies) in a physiological Ringer's solution containing (in mM) 140 NaCl, 5 KCl, 10 HEPES, 2 CaCl2, 2 MgCl2 and 10 D-(+)-glucose, pH 7.4. Cells were identified as neurons by eliciting depolarization with high potassium Ringer's solution (75 mM) at the end of each experiment. Acquired images were displayed as the ratio of 340 nm / 380 nm. Fura-2 rations were normalized to baseline ratio. Responding neurons were defined as those having a > 10% increase from baseline ratio. Human iPSC-derived neurons were defined as responding to > 5% increase from baseline ratio. All calcium imaging analyses were performed using custom python scripts. Neurons were stimulated with SARS-CoV-2 PLpro (R&D #E-611), SARS-CoV-2 PLpro C111S mutant (R&D custom order), SARS-CoV PLpro (R&D #E-610), MERS-CoV PLpro (R&D #E-609), SARS-CoV-2 PLpro (Cayman #31817) diluted in Ringer's to the appropriate concentration. The vehicle (50 mM HEPES, 300 mM NaCl, 1 mM TCEP, 10% (v/v) glycerol, pH 8.0) was matched to the dilution buffer for PLpro (R&D #E-611). For PLpro (Cayman #31817), Ringer's solution served as the vehicle. No differences in neuronal activation were observed between the two PLpro preparations or their respective vehicles, so data were combined (Supplemental Fig. 10). Each biological replicate (mice unless noted otherwise) represents an average of 3-4 wells with ~100-300 neurons per well.

Heterologous receptor expression and calcium imaging

Chem-1 cells stably expressing MRGPRX1 (Eurofins Discoverx HTS122RTA) and MRGPRX2 (Eurofins Discoverx HTS058RTA) were thawed as per manufacturer's instructions. HEK-293 cells were transfected with 300 ng human TRPA1 as described

previously[227]. Chem-1 cells were loaded with 1 μM Fura-2AM and HEK cells with 1 μM Fluo-4AM supplemented with 0.01% Pluronic F-127 (wt/vol, Life Technologies) in a physiological Ringer's solution containing (in mM) 140 NaCl, 5 KCl, 10 HEPES, 2 CaCl2, 2 MgCl2 and 10 D-(+)-glucose, pH 7.4 and calcium imaging was performed as described above. Responding cells were defined as those having a > 10% increase from baseline ratio.

PAR cleavage assay

Luciferase-based PAR cleavage assays were performed as previously described[197,228]. Chinese Hamster Ovary (CHO-K1) cells stably expressing hPAR1, 2, or 4 tagged with nano-luciferase (nLuc) at the N-terminus and enhanced yellow fluorescent protein (eYFP) at the C-terminus were grown. For the cleavage assay, cells were washed with sterile HBSS, and supernatant was collected to measure background luminescence. Cells were incubated for 15 minutes with 100 nM SARS-CoV-2 PLpro, or different concentrations of standard proteases (thrombin 0.001:10 U/ml for PAR1 and 4, and trypsin 0.03:30 nM for PAR2), after which supernatant was collected, mixed with 2 μL/mL Nano-Glo Luciferase Assay Substrate Fumarizine (Promega, N113A). Luminescence was measured on a Mithras LB 940 Berthold Technologies plate reader with 1 second/well integration time.

Neuropeptide release

TG from 7-8 week old mice were cultured overnight as described above and supplemented with 50 ng/mL of nerve growth factor. Cultured neurons were incubated with vehicle or PLpro for 15 min in Ringer's solution at room temperature. For ex vivo trachea stimulation, tracheas were dissected and washed in HBSS for 30 min at 37°C. Tracheas were then incubated in DMEM for 30 min at 37° with gentle rotation for baseline measurement and in DMEM with PLpro or vehicle for 1 hour at 37°C with gentle rotation. After incubation, the supernatant (from in vitro experiments) and medium (from ex vivo experiments) was collected and used to quantify the concentration of neuropeptide using an enzyme linked immunosorbent kit (CGRP: Cayman Chemicals #589001, Substance P: Cayman Chemicals #583751) according to the manufacturer's instructions.

SARS-CoV-2 infection

Human airway epithelial cell and primary mouse neuron infection

Human adenocarcinoma lung epithelial (Calu-3) cells (ATCC, HTB-55) were maintained with RPMI (Fisher Scientific) supplemented with fetal bovine serum (FBS), L-glutamine, penicillin/streptomycin. 4-5 x 10^5 Calu-3 cells were incubated with SARS-CoV-2 (WA1) in medium (10% heat-inactivated FBS, sodium pyruvate, HEPES, L-glutamine, penicillin/streptomycin) diluted in phenol-red free RPMI to an MOI of 1 for 24 or 48 hours. Mouse TG were cultured as described above and plated in a 96-well plate. TGs (2 each) across 4 animals were pooled and plated across 8 wells. TG cultures were infected with 5 x 10^5 SARS-CoV-2 virions or medium (mock infection) for 48 hours.

Protease activity

Supernatant from SARS-CoV-2- and mock-infected Calu-3 cells was mixed with the PLpro substrate Ubiquitin-Rh110 (R&D Systems, #U-555) at a concentration of 670 nM or 1 µM in phenol-free RPMI. Fluorescence (excitation 485nm, emission 535nm) was read on a Spectramax L (Molecular Devices). Samples were run in duplicate. A standard curve was generated by assessing protease activity from a dose-response curve of recombinant SARS-CoV-2 PLpro (R&D), diluted in mock infection medium and measured in parallel.

Cell viability

Cell viability was measured using the CellTiter-Glo 2.0 reagent (Promega), prepared according to the manufacturer's instructions. After removing the supernatant, the reagent was added to the cells, and luminescence was measured on a Spectramax L. Cell viability was determined by comparing ATP levels to those in mock-infected cells.

RNA sequencing and analysis

After removing supernatant from infected cells, RNA was isolated with DNA/RNA Shield (Zymo Research) according to the manufacturer's instructions. RNA library preparation (lnc-RNA library with rRNA removal) and sequencing on an Illumina NovaSeq 6000 were performed by Novogene. For quantification of viral transcripts, reads were mapped to the appropriate host (human or mouse) transcriptome concatenated with the SARS-CoV-2 transcriptome using *Kallisto (0.44.0)*. For analysis of infected mouse TG, reads were mapped to the mouse genome concatenated with the SARS-CoV-2 genome using *STAR (2.7.10a)*. Gene counts were extracted using featureCounts in *Subread (2.0.1).* All but one sample contained more than 80% mapped features; one sample contained 68% mapped reads and was excluded based on the robust principal component analysis method[229]. The uniquely aligned features were used for differential expression analysis using *DESeq2.* Gene sets associated with functional neuronal subtypes were generated from previous study[230]. As done in the paper, we pooled the same Gene Ontology terms Mouse Genome Informatics (MGI) (updated as of November 2023) except for the itch gene list, which we used from the paper. We tested if these custom gene sets were significantly differentially expressed above chance. In brief, we established a null distribution by sampling random sets of genes (of the same size) from all transcripts expressed across our samples 100,000 times. We then compare the median absolute Log_2 fold change for our custom gene sets to the null distribution to identify the empirical p-value.

Behavioral studies

Intranasal behavior and scoring

For intranasal behavioral experiments, mice were acclimated for 10 minutes in a custom behavioral chamber (4" x 2" x 6") with a filter paper bottom (VWR #28321-113) prior to

treatment. Mice were treated intranasally with vehicle or PLpro with 10mg/mL Evan's blue dye in phosphate-buffered solution administered 5μL/nostril (10uL total) with a P20 pipette. Mice were then placed back in the chamber for recording. A GoPro Hero 11 (recording at 2.7 megapixels, 240Hz) was used to record video and ambient audio. An audio recorder (aTTo digital, 16 kHz) placed inside the chambers. Experimenters were blinded to genotype or treatment. Behavior was scored for 2 minutes by individuals blinded to both genotype and treatment. A nose rub was defined as a singular elliptical stroke made by both forepaws simultaneously, directed to the nose. A face wipe was also a singular elliptical stroke of the forelimbs but contacted the face above the nose and below the ears, making a circular motion. The time of each individual nose rub and face wipe was recorded. A bout of body licking was defined as an uninterrupted series of licking the flank, chest, stomach, and tail. The filter paper that was on the bottom of the chamber was scanned and quantified using *Fiji* by measuring the mean intensity. This mean intensity was inverted (subtracted from 255) and scaled (by 10^8).

Sneeze audio analysis

Sneeze events were identified from peaks in the audio recordings. Audio recordings were cropped to the start of the experiment and a 2-3 second recording of background sound from the recording was used for noise reduction in Audacity (Noise reduction: 30dB, sensitivity: 6, frequency of smoothing: 6 bands). Denoised audio recordings were then analyzed using a custom python script. Audio peaks were identified using the SciPy "find_peaks" function (peak prominence > 1000 and a minimum distance of 0.2s between peaks). The audio recordings from inside the chamber were aligned to the video and audio recordings from the GoPro (outside the chamber). Audio peaks recorded both inside and outside the chamber were excluded as background noise. Audio peaks that correlated with other behaviors such as biting the chamber and body licking were excluded.

Whole body plethysmography

Respiratory traces were recorded using Buxco Small Animal Whole Body Plethysmography (WBP) System (DSI, 601-1400-001) and data were collected on the FinePointe Software (DSI). Mice were acclimated in the chambers 10 minutes prior to intranasal treatment. Mice were treated intranasally as described above and returned to the WBP chambers for recording. Box flow was exported and analyzed using custom python scripts and aligned to video recordings and to identify instances of dye expulsion.

Cheek behavior

Itch and acute pain behavioral measurements were performed as described previously[227]. In brief, mice were shaved and singly housed one week prior to the experiment. Mice were acclimated to the chamber for an hour on both the day prior and day of injection. Compounds were injected intradermally (20 μL) into the cheek. Behavior was videotaped for one hour and scored for either the first 30 min (scratching) or the first 5 min (wiping) as previously described[231].

Von Frey and radiant heat behavior

Mice were lightly anesthetized with isoflurane (2.5%) and received intradermal injections (15 µL) of PLpro or vehicle into the plantar surface of the hind paw. For von Frey, both hind paws were injected, one with treatment and the other with vehicle solution. For radiant heat, only the left hind paw was injected with either treatment or vehicle solution. Mice were acclimated in behavioral chambers for two consecutive days for at least one hour each day, followed by an additional 30-minutes acclimation with the investigator in the room. Mechanical threshold was measured using calibrated von Frey monofilaments (Touch Test) on a metal grate platform (IITC). Von Frey was performed as previously described[232,233] using the up-down method[234]. Measurements were taken one day prior to injection, the 3, 27, and 52 hours following injection. Radiant heat assay was performed using the Hargreaves test system (IITC Life Science) as previously described[233,235]. A glass platform was set at 30°C during the acclimation and throughout the experiment and the radiant heat source raised the platform temperature to 41.5°C within 5 s and to 44.9°C within 10 s, as measured by a fast temperature probe (Physitemp). Valid responses for both von Frey and radiant heat included fast paw withdrawal, licking/biting/shaking of the affected paw, or flinching. Experimenter was blind to treatment and genotype.

Statistical reporting

Unless otherwise noted, data are expressed as mean ± standard error of the mean (SEM). Statistical tests were performed using Prism (Graphpad) and were two-tailed.

Chapter IV: Cryo-EM Structure of SARS-CoV-2 ORF3a in Lipid Nanodiscs

This chapter is a reproduction of the paper by the same name (Kern, D. M. et al. Cryo-EM structure of SARS-CoV-2 ORF3a in lipid nanodiscs. *Nat. Struct. Mol. Biol.* **28**, 573–582, 2021). For this study, I developed and optimized fluorescent ion flux assays for 3a-reconstituted liposomes, which I used to demonstrate that ORF3a is permeable to calcium and large cations. I performed an inhibitor screen that identified ruthenium red as a blocker of ORF3a-mediated ion flux. I generated Figures 4e and 5a–f, and, and wrote the manuscript with David Kern, Ben Sorum, Christopher Hoel, Diana Bautista, and Stephen Brohawn.

Summary

SARS-CoV-2 ORF3a is a putative viral ion channel implicated in autophagy inhibition, inflammasome activation and apoptosis. 3a protein and anti-3a antibodies are found in infected patient tissues and plasma. Deletion of 3a in SARS-CoV-1 reduces viral titer and morbidity in mice, suggesting it could be an effective target for vaccines or therapeutics. Here, we present structures of SARS-CoV-2 3a determined by cryo-EM to 2.1-Å resolution. 3a adopts a new fold with a polar cavity that opens to the cytosol and membrane through separate water- and lipid-filled openings. Hydrophilic grooves along outer helices could form ion-conduction paths. Using electrophysiology and fluorescent ion imaging of 3a-reconstituted liposomes, we observe Ca^{2+}-permeable, nonselective cation channel activity, identify mutations that alter ion permeability and discover polycationic inhibitors of 3a activity. 3a-like proteins are found across coronavirus lineages that infect bats and humans, suggesting that 3a-targeted approaches could treat COVID-19 and other coronavirus diseases.

Introduction

Coronavirus disease 2019 (COVID-19), caused by the SARS-CoV-2 virus, is an ongoing global pandemic. Vaccine and therapeutic development are predominantly focused on the essential virus-encoded Spike, main protease and RNA-dependent RNA polymerase proteins. High-resolution structures of these targets, some in complex with drug candidates or neutralizing antibodies, have yielded mechanistic insight into their function and have provided a platform for successful structure-guided vaccine and drug design[236–241]. Still, expanding our knowledge of SARS-CoV-2 target proteins remains important both for understanding SARS-CoV-2 virology and developing alternative treatments to mitigate against potential resistance that evolves, or new viruses that emerge, in the future[242].

Virally encoded open reading frame 3a (ORF3a, 3a for short) has been considered a potential target for vaccines or therapeutics[243,244]. Amino terminus of the SARS coronavirus protein 3a elicits strong, potentially protective humoral responses in infected patients[245]. Biopsies from SARS-CoV-1 patients show 3a expression in infected tissue and SARS-CoV-1 and SARS-CoV-2 patient plasma contain anti-3a antibodies[243,246–248]. SARS-CoV-1 3a has been implicated in inflammasome activation[249] and both apoptotic[250] and necrotic cell death[251] while SARS-CoV-2 3a has been implicated in

apoptosis and inhibition of autophagy in vitro[252]. In mouse models of both SARS-CoV-1 and 2 infection, genomic deletion of 3a reduces viral titer and morbidity[253,254,254].

3a has been proposed to form an ion channel and is one of two putative viroporins encoded by the SARS-CoV-2 genome together with the envelope protein E (SARS-CoV-1 encodes an additional putative viroporin, ORF8a). SARS-CoV-1 3a has been reported to form an emodin- and Ba^{2+}-sensitive cation channel[255,256]. Viroporins from other viruses have been shown to modify host membrane permeability to promote viral assembly and release[257–259]. However, the precise roles of 3a in disease pathogenesis are unknown, precluded in part by the lack of a mechanistic understanding of 3a. Here, we determine structures of SARS-CoV-2 3a by cryo-electron microscopy (cryo-EM) and assess putative ion channel activity in vitro using electrophysiology and fluorescent ion flux assays.

Results

Structure determination

We determined structures of dimeric and tetrameric SARS-CoV-2 3a in lipid nanodiscs. Full length SARS-CoV-2 3a was heterologously expressed in *Spodoptera frugiperda* (Sf9) cells with a cleavable C-terminal green fluorescent protein (GFP) tag. Purification of 3a in detergent resulted in two species separable by gel filtration (Supplemental Fig. 2). Most 3a runs at a position consistent with a 62-kDa dimer (Supplemental Fig. 2a, c, and e) and roughly 10–30% runs as a 124-kDa tetramer (Supplemental Fig. 2). A similar degree of tetramer formation was observed at low concentrations of 3a by fluorescence size-exclusion chromatography, indicative of a biochemically stable species rather than concentration-dependent nonspecific aggregation (Supplemental Fig. 2e). These data are consistent with previous reports of dimeric and tetrameric SARS-CoV-1 3a observed by western blot[251,255].

We separately reconstituted dimeric and tetrameric SARS-CoV-2 3a into nanodiscs made from the scaffold protein MSP1E3D1 and a mixture of DOPE, POPC and POPS lipids, and determined their structures by cryo-EM to 2.9- and 6.5-Å resolution (Supplemental Figs. 3–5). Based on a report of improved resolution of apoferritin and $GABA_A$ structures using new cryo-EM instrumentation (including the electron source, energy filter and camera; see Methods for details[260], we asked whether similar improvements would be possible for the sub-100-kDa 3a. Indeed, a reconstruction generated from data collected on this instrumentation, using the same batch of grids, was improved to 2.1 Å (Fig. 1, Supplemental Figs. 3 and 6). We note we cannot exclude other differences including in accelerating voltage, pixel size or defocus range from potentially contributing to the improvement in resolution.

3a dimer structure

The 2.9-Å dimeric reconstruction (with C2 symmetry applied, PDB 6XDC) permitted de novo modeling of 195 of the 275 amino acids per protomer chain. The N terminus (amino acids 1–39), C terminus (amino acids 239–275) and a short cytoplasmic loop (amino acids 175–180) are weakly resolved in the density map due to conformational differences between particles or because they are disordered (Supplemental Fig. 6). The 2.1-Å dimeric reconstruction (with C2 symmetry applied, PDB 7KJR) allowed for improved rotamer assignments due to better defined side chain density throughout the protein, including visible holes in many aromatic residues (Fig. 1a–f). We additionally modeled a

portion of each MSP1E3D1 scaffold protein (amino acids 25–55, Fig. 1g,h), two DOPE lipids and 122 water molecules. We refer to the higher-resolution structure in the remainder of the paper unless otherwise indicated. The scaffold protein is partially well-resolved due to a specific interaction visible on each side of the 3a dimer (even in C1 reconstructions) between MSP1E3D1 W40 and the transmembrane region of 3a (Fig. 1g,h). The symmetric nature of this interaction means that the two MSPE3D1 protomers must twist around the lipid bilayer rather than adopting the canonical arrangement of two parallel stacked rings.

3a adopts a new fold that, to our knowledge, has not been observed in available protein structures. Querying the protein structure database for homologs with Dali returned only weak hits for fragments of 3a domains[261]. Viewed from the membrane plane, 3a is approximately 70 Å tall with a 40-Å high transmembrane region and a cytosolic domain (CD) extending 30 Å out of the membrane (Fig. 1a,b). The transmembrane region is composed of three helices per protomer with N termini oriented on the extracellular or lumenal side and C termini on the cytosolic side of the membrane. Viewed from the extracellular side, the transmembrane helices (TMs) trace the circumference of an ellipse with TM1–3 from one protomer followed by TM1–3 of the second protomer in a clockwise order (Fig. 1c). TM1s and TM2s pack against each other across the elliptical minor axis with TM3s positioned at the main axis vertices. TM1–TM2 and TM2–TM3 are joined by short intracellular and extracellular linkers, respectively.

The transmembrane region connects to the CD through a turn-helix-turn motif following TM3. Each protomer chain forms a pair of opposing β-sheets packed against one another in an eight stranded β-sandwich (Fig. 1b,d). The outer sheet is formed by strands β1, β2 and β6 and the N-terminal half of β7. The inner sheet is formed by strands β3, β4, β5 and β8 and the C-terminal half of β7. The inner sheets from each protomer interact through a large (roughly 940 $Å^2$ of buried surface area per chain) and highly complementary interface with residues V168, V225, F230 and I232 forming a continuous hydrophobic core (Fig. 1d). The interaction between β-sandwiches from each protomer thus forms a strong and stable link between monomers in the dimer.

Structural features of 3a tetramers

We next examined the structure of 3a tetramers. Two-dimensional (2D) class averages of tetrameric 3a show a side-by-side arrangement of two dimers with separated TMs and close juxtaposition of CDs (Fig. 2a). Tetrameric 3a reconstructions had lower final resolutions (roughly 6.5 Å) than dimeric 3a (Fig. 2a and Supplemental Fig. 2), which precluded detailed model building, but were sufficiently featured in the CDs for rigid-body docking of two copies of the 3a dimer to determine their approximate relative orientation (Fig. 2b and Supplemental Fig. 7a). The best fit model shows a continuous interface (roughly 300 $Å^2$ buried surface area per dimer) formed between TM3–CTD linkers and β1–β2 linkers from neighboring dimers. While the exact positions of side chains cannot be determined at this resolution, residues W131, R134, K136, H150, T151, N152, C153 and D155 are poised to mediate tetramerization through a network of hydrophobic, polar and electrostatic interactions (Fig. 2c). In SARS-CoV-1 3a, reducing agents and a C133A mutation resulted in loss of oligomerization, membrane localization and ion channel activity[255]. However, expression of the C133A mutant was dramatically reduced, suggesting these results might be a consequence of protein destabilization[255]. In SARS-CoV-2 3a, C133 is located in a notable cysteine-rich pocket adjacent to the

tetramerization interface (Supplemental Fig. 7b). At the base of TM3, C133 projects back toward the top faces of β1 and β2 in close proximity to solvent exposed C148 and buried C157. All three cysteines are reduced in the structure, although they are within potential disulfide-bonding distance (Cα distance 4.4–6.5 Å) (Supplemental Fig. 7b). While it is unlikely a disulfide involving C133 mediates tetramerization of 3a without substantial rearrangement of this region, it could be that disruption of this cysteine-rich pocket with cysteine modifying agents or mutations disfavors 3a oligomerization allosterically.

Potential ion permeation paths through 3a

Ion conduction pathways are required for ion channel function, so we analyzed the 3a structures to identify potential permeation routes. 3a forms a large polar cavity within the inner half of the TM region. The cavity is continuous with the cytosol and surrounding bilayer through three pairs of openings: the upper, lower and intersubunit tunnels (Fig. 3a–f). The upper tunnels are formed between TM2 and TM3 within each protomer, narrow to roughly 2.2 Å in radius, and likely open to the membrane (Fig. 3a–c). The lower tunnels run underneath the TM1–TM2 linker and above the CD, narrow to roughly 2 Å in radius, and open to the cytosol (Fig. 3a,d,e). The lower tunnels are open paths for ion and water movement between the cell interior and channel cavity. Consistently, a network of ordered water molecules extends through these openings, the cavity and the CD (Fig. 3b,d). The intersubunit tunnels run between TM1 and TM3 from opposing protomers, just above the CD, and open to the membrane–cytosol interface (Fig. 3a,f). Strong lipid-shaped density present within each intersubunit tunnel is modeled as DOPE (the most abundant lipid in these nanodiscs) with the ethanolamine head group pointed into the cavity. Lipid binding is stabilized by electrostatic interactions: the positively charged ethanolamine interacts with negatively charged D142 and the backbone carbonyls of I63 and D142 while the lipid phosphate interacts with R126, R122, Y206, N144 and the backbone amide of L65.

While the polar cavity reduces the energetic barrier to ion movement across the inner half of the low dielectric membrane, the current structures lack a central pore connecting the cavity to the lumenal or extracellular side. Instead, a hydrophobic seal is formed between TMs in the extracellular half of the membrane above the polar cavity (Fig. 3). The top of the cavity is formed by polar interactions between Q57, S58, N82 and Q116 side chains (Fig. 3a,g). Just extracellular to these interactions, the hydrophobic seal is formed by interactions between residues F43, L46, I47, V50, L95 and L96 (Fig. 3a,h,i). Opening a central pore would require substantial conformational rearrangement to break these hydrophobic interactions.

Most ion channels have central pores for conduction, but some, including those of the TMEM16 and OSCA families, have evolved ion pathways through external grooves or tunnels near membrane-facing surfaces[262–265]. 3a exhibits a distinctive membrane-facing, partially hydrophilic groove is observed between TM2 and TM3 (Fig. 3j). It is bounded by the upper tunnel and TM2–TM3 linker at the cytoplasmic and extracellular sides, respectively, and is lined by conserved polar residues N119, N82, S117, Q116, S58, T89, Y113, S92, Y109 and H93 (Fig. 3k). The hydrophilic character of this region would be expected to lower the energetic barrier for movement of ions across the outer half of the membrane and more subtle conformational changes would be required to permit permeation along this route relative to a central pore. 3a oligomerization could also be important for building a conduction path either through conformational changes or pore

assembly, as was proposed for SARS-CoV-1 3a[255]. While a pore is not formed in the context of the SARS-CoV-2 tetramer, we observe that one of the partially hydrophilic TM2–TM3 grooves from each dimeric unit face one another across a narrow membrane (Supplemental Fig. 6c).

Assessment of channel activity in 3a-reconstituted proteoliposomes

We next used electrophysiology and calcium imaging to assess whether SARS-Cov-2 3a is capable of permeating ions. We did not observe consistent currents in recordings from transfected cells and reasoned this could be due to most of 3a being localized to internal membranes (Supplemental Fig. 8), inactivation at the plasma membrane and/or 3a toxicity. We therefore purified 3a in detergent, reconstituted it into phosphatidylcholine-containing proteoliposomes, and recorded currents across excised patches pulled from proteoliposome blisters. Excised patches from 3a-containing liposomes exhibited currents that reversed at 0 mV and displayed modest outward rectification in symmetric $[K^+]$ (Fig. 4a and Supplemental Fig. 9). In contrast, channel-like activity was not observed in recordings from mock-reconstituted (empty) proteoliposomes (Supplemental Fig. 9g). We evaluated ion selectivity of 3a by replacing the K^+-containing bath solution with solutions containing Na^+, $NMDG^+$ or Ca^{2+}. Solution exchange resulted in reversal potential shifts from 0.3 ± 0.3 mV in K^+ to −8.2 ± 0.8 mV in Ca^{2+}, −13.5 ± 1.8 mV in Na^+ and −31.0 ± 1.1 mV in $NMDG^+$ (Fig. 4b,d). These shifts correspond to the following permeability ratios (P_X/P_{K+}): Ca^{2+} (1.88 ± 0.08) > K^+ (1.0 ± 0.01) > Na^+ (0.59 ± 0.04) > $NMDG^+$ (0.29 ± 0.01) (Fig. 4c). Alkaline or acidic pH had little effect on channel activity (Supplemental Fig. 9f). Consistent with the electrophysiological measurements, we also observed significant calcium influx in 3a proteoliposomes using Fluo-5N calcium imaging following the addition of 8 mM $[Ca^{2+}]_{ext}$ compared to empty liposomes (Fig. 4e).

We performed mass spectrometry of 3a samples to assess whether channel activity observed in vitro could be due to channel contaminants in purified 3a or lipids used for reconstitution. We analyzed samples of 3a in detergent before liposome incorporation, 3a-reconstituted proteoliposomes and mock-reconstituted liposomes, and searched a database consisting of the 3a construct, the *S. frugiperda* (expression system) proteome, the *Glycine max* (lipid source) proteome and common contaminants (Supplemental Fig. 10). We detected 3a peptides in both 3a-containing samples, with the detergent sample giving better sequence coverage and more matched peptides. The only other proteins identified were at low levels and from common contaminants; no peptides from known channels or transmembrane proteins other than 3a were observed in any sample. While we cannot definitively rule out the presence of an unannotated contaminant or one below the detection threshold for mass spectrometry, these results indicate that SARS-CoV-2 3a is responsible for the Ca^{2+}-permeable nonselective channel activity observed in vitro.

Polycations block 3a channel activity in vitro

We next asked whether blockers of nonselective cation channels inhibit 3a ion conduction in liposomes. We found that ruthenium red, a 786-Da polycationic dye, blocks 3a activity in current recordings (Fig. 4g,h) and Ca^{2+} influx measurements (Fig. 4e). Ruthenium red displays dose-dependent inhibition of 3a activity in proteoliposome recordings (IC_{50} = 90 ± 10 μM) with flickery block at negative potentials, similar to that observed with other large pore channels (Fig. 4g). In addition, we identified the polyamine spermidine, which showed near complete block at 10 mM, and the trivalent ions Gd^{3+}, Fe^{3+} and Tb^{3+}, which showed partial block at 1–10 mM, as 3a inhibitors in proteoliposome

recordings (Fig. 4g). ruthenium red, spermidine, Gd^{3+} and other trivalents are relatively nonselective inhibitors of cation channels including TRPs, RyRs, CALHMs, K2Ps and K_{IR}s[266–272], but the spectrum of 3a blockers and affinities observed here is, to our knowledge, distinct from those of other known channels. We further tested reported low-affinity blockers of SARS-CoV-1 3a channel activity[255,256], but found that neither Ba^{2+} nor the small molecule emodin inhibited SARS-CoV-2 3a activity (Supplemental Fig. 9d,e). Consistently, in a cryo-EM structure of dimeric 3a determined in the presence of 100 μM emodin to 3.7-Å resolution (Supplemental Figs. 2 and 5), we observed no evidence of emodin binding or structural changes compared to apo 3a.

3a permeates the large divalent ion YO-PRO-1

Given the ability of 3a channels to weakly conduct $NMDG^+$ (Fig. 4a–d), we next used a YO-PRO-1 fluorescence-based flux assay to assess the ability of 3a channels to conduct other large cations. YO-PRO-1, a 629-Da divalent cation, does not readily cross lipid bilayers and has been used to study the activity of other nonselective cation channels, including P2X7 and TRP channels, that can conduct large organic cations[266,267,273,274]. Robust YO-PRO-1 uptake was observed in a subset of 3a liposomes that was significantly higher than background fluorescence observed in empty liposomes (Fig. 5a–d). To compare YO-PRO-1 uptake across multiple experiments, we quantified a single value (area under the curve) to represent both the number of YO-PRO-1+ liposomes and the amount of YO-PRO-1 uptake (Fig. 5e). Using this analysis, we found 3a liposomes display significantly greater YO-PRO-1 uptake and accumulation as compared to empty liposomes (Fig. 5e). Uptake was dependent on 3a protein because liposomes containing the human K2P channel TRAAK displayed little uptake and accumulation of YO-PRO-1, similar to empty liposomes, as expected for a highly selective K^+ channel (Fig. 5a,c–e). Similar to current recordings (Fig. 4e,f), we observed a dose-dependent ruthenium red block of 3a activity in the YO-PRO-1 flux assay (IC_{50} = 175 ± 98 μM). These data indicate that 3a can form an ion channel that is capable of passing large cations. Ruthenium red (786 Da) block and YO-PRO-1 (629 Da) and $NMDG^+$ (406 Da) permeation sets limits on 3a pore size that are similar those observed for TRP and P2X channels.

3a mutants alter ion conduction

We speculate that, relative to the structures presented here, an open conformation of 3a involves substantial rearrangement of the hydrophobic seal to create a central pore or more subtle rearrangement of the partially hydrophilic membrane-facing grooves between TM2 and TM3 to create lateral conduction pathways. To probe the structural determinants for 3a ion conduction, we set out to identify 3a mutations that alter channel activity. To this end, we purified nine mutated or truncated 3a constructs, reconstituted each into proteoliposomes, and compared them to wild-type 3a in electrophysiological recordings (Fig. 6a and Supplemental Fig. 11). We find that two separate mutants alter channel activity, one at the top of the cavity (Q57E) and another and base of the TM2–TM3 grooves (S58L,Q116L). Both Q57E and S58L,Q116L mutants reduce Ca^{2+} and $NMDG^+$ permeability without altering Na^+ or K^+ permeability. These effects were specific to these mutations as seven additional mutations, including a common circulating variant Q57H[275], had no effect on relative ion permeability. These results are consistent with the hypothesis that 3a channel opening involves conformational changes of residues that form constrictions above the polar cavity or along the hydrophilic membrane-facing TM2–TM3 grooves.

Our structural analysis revealed an unassigned region of density in the cryo-EM maps stretching between subunits just above the extracellular side of the transmembrane region and near the top of the TM2–TM3 grooves that likely corresponds to a portion of the unmodeled N terminus (Supplemental Fig. 8). To investigate the potential role of the N terminus in channel function, we generated an N-terminal deletion construct lacking the first 41 amino acids (3aΔN). This mutant displayed reduced Ca^{2+} and $NMDG^{+}$ relative permeability in proteoliposome recordings, albeit to a lesser extent than Q57E and S58L,Q116L (Fig. 6b). The relative permeability changes observed in liposomes suggest that residues in the N terminus, such as those at the top of the polar cavity, mediate the ability of 3a to permeate large cations. In addition, the N terminus may be involved in 3a subcellular localization as 3aΔN channels displayed increased localization to the plasma membrane (Supplemental Fig. 8).

3a-like proteins in Alpha- and Betacoronavirus

While 3a is well conserved in the *Betacoronavirus* subgenus (Supplemental Fig. 1), related proteins have not yet been identified in other coronaviruses, including the other five species known to infect humans: MERS-CoV, HCoV-NL63, HCoV-229E, HCoV-HKU1 and HCoV-OC43. Thus, we asked whether we could identify more distant homologs using the 3a structure and structure prediction algorithms. 3a homologs were not detected in *Gammacoronavirus*, *Deltacoronavirus* or in the *Betacoronavirus* subgenus *Embecovirus* (which includes HCoV-HKU1 and HCoV-OC43). Distant homology to the CD was identified in the membrane protein ORF5 found in *Betacoronavirus* subgenus *Merbecovirus* species including MERS-CoV. We identified high confidence structural homologs in all remaining *Betacoronavirus* and *Alphacoronavirus* subgenera (including in HCoV-229E and HCoV-NL63 (Supplemental Fig.12)), several of which have also been reported to have ion channel activity[276–278]. Notably, coronaviruses with 3a homologs have been proposed to derive from viruses that circulate primarily in bats, while coronaviruses without 3a structural homologs have been proposed to derive from viruses that circulate primarily in rodents, birds or pigs. It may be that the presence of 3a in coronaviruses with bats as their principal reservoir reflects a unique aspect of bat coronavirus biology.

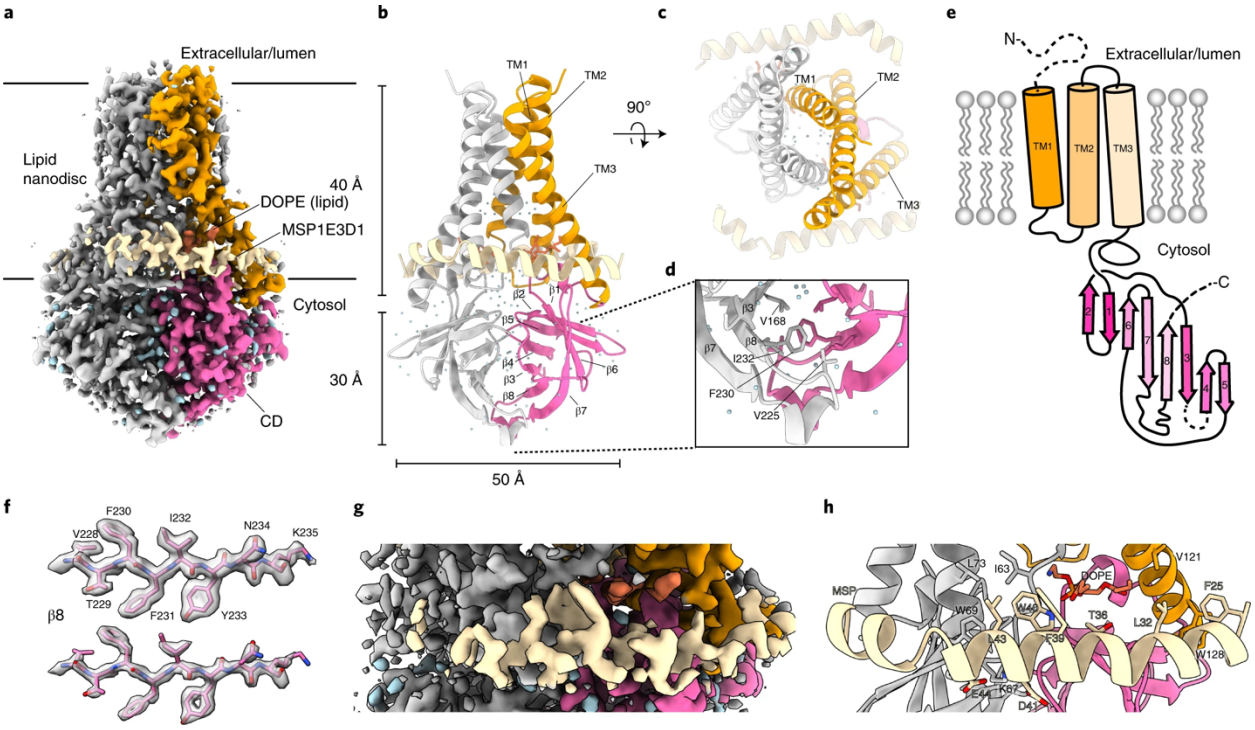

Figure 1: Structure of dimeric 3a in lipid nanodiscs.

a, Cryo-EM map of the 3a dimer in MSP1E3D1 nanodiscs at 2.1-Å nominal resolution, viewed from the membrane plane. One subunit is colored gray, and the second subunit is colored with transmembrane region in orange and the CD in pink. Density from the nanodisc MSP1E3D1 is colored tan, and the DOPE lipid is coral. **b**,**c**, Model of dimeric 3a viewed from the membrane (**b**) (as in **a**) and from the extracellular or lumenal side (**c**). **d**, Enlarged view of the interaction between subunits in the CD with residues forming the hydrophobic core indicated. **e**, Schematic of a 3a monomer. Secondary structure elements are indicated, and unmodeled termini and a five-amino-acid β3–β4 loop are shown with dashed lines. **f**, Cryo-EM density and model for a selected strand from the CD at two different thresholds. **g**, Enlarged view of density in the MSP1E3D1-interaction region. **h**, Model in the same region as **g** with key residues in the area displayed as sticks.

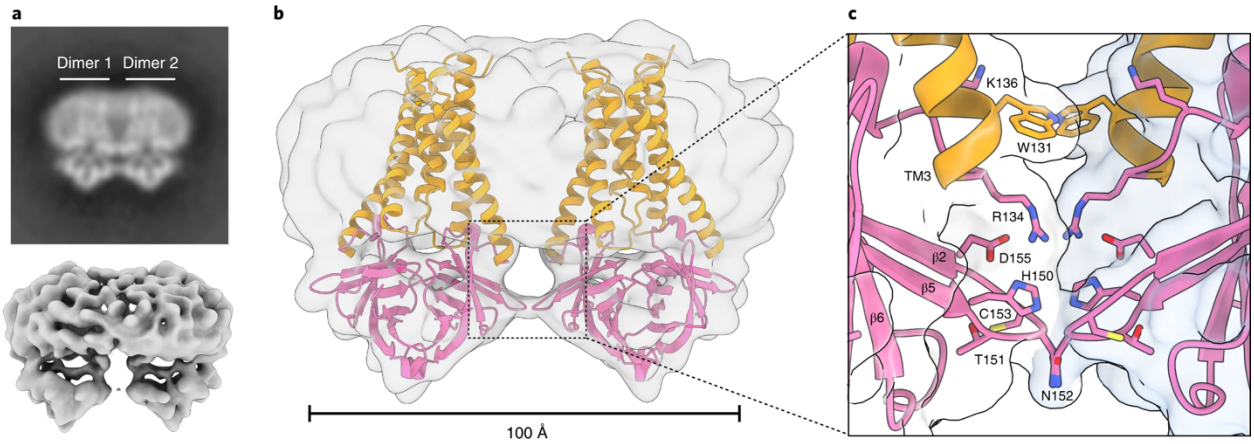

Figure 2: Structure of tetrameric 3a in lipid nanodiscs.
a, Two-dimensional class average of tetrameric 3a in MSP1E3D1 lipid nanodiscs (top) and cryo-EM map at 6.5-Å nominal resolution (bottom). **b**, Approximate assembly of 3a tetramers. Two 3a dimer structures are rigid-body fit into the tetrameric cryo-EM map. **c**, Enlarged view of the interface between 3a dimers observed after rigid-body fitting with residues potentially mediating the interaction displayed as sticks.

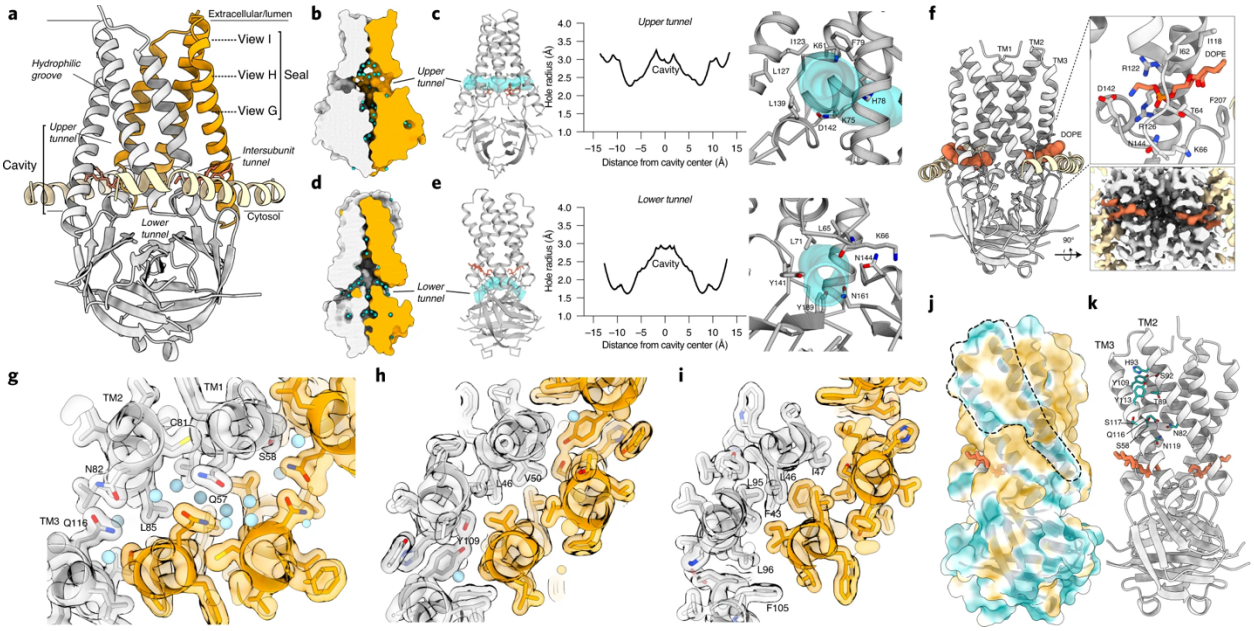

Figure 3: The 3a polar cavity and tunnels.
a, View of a 3a dimer from the membrane plane with key regions labeled and with planes (dotted lines) and viewing direction (arrow) for **g**–**i**) indicated. **b**, The 3a upper tunnel with solvent-excluded surface shown for each subunit and water molecules shown as light blue spheres. The approximate lipid bilayer region is marked by black lines. One 3a subunit is colored orange and the other in gray. **c**, Left, model of 3a (gray) with the HOLE path through the upper tunnel shown in transparent cyan. Lipid (coral) is displayed as sticks. Middle, the radius of the upper tunnel as a function of distance from the cavity center calculated with HOLE. Right, the view into the upper tunnel from the membrane with key residues shown as sticks. **d**, As in **b**, for a view of the lower tunnel. **e**, As in **c**, for the lower tunnel, with the view on the right into the tunnel from the cytosol. **f**, The intersubunit tunnel with bound DOPE lipid (coral) shown as space-filling spheres. Top right, an enlarged view of the lipid interaction with key residues shown as sticks. Bottom-right, a cut-through view of the cryo-EM density of the lipid interaction region viewed from the cytosolic side. **g**–**i**, Model and transparent surface of the viewing planes indicated in **a** (**g**, view **G**; **h**, view **H**; **i**, view **I**). Water molecules are shown as light blue spheres. One 3a subunit is colored orange and the other in gray. **j**, The solvent-excluded surface of 3a colored from hydrophilic (dark cyan) to most hydrophobic (dark orange). A membrane-facing hydrophilic groove is outlined. **k**, Key residues in the hydrophilic groove are depicted as sticks colored in dark cyan.

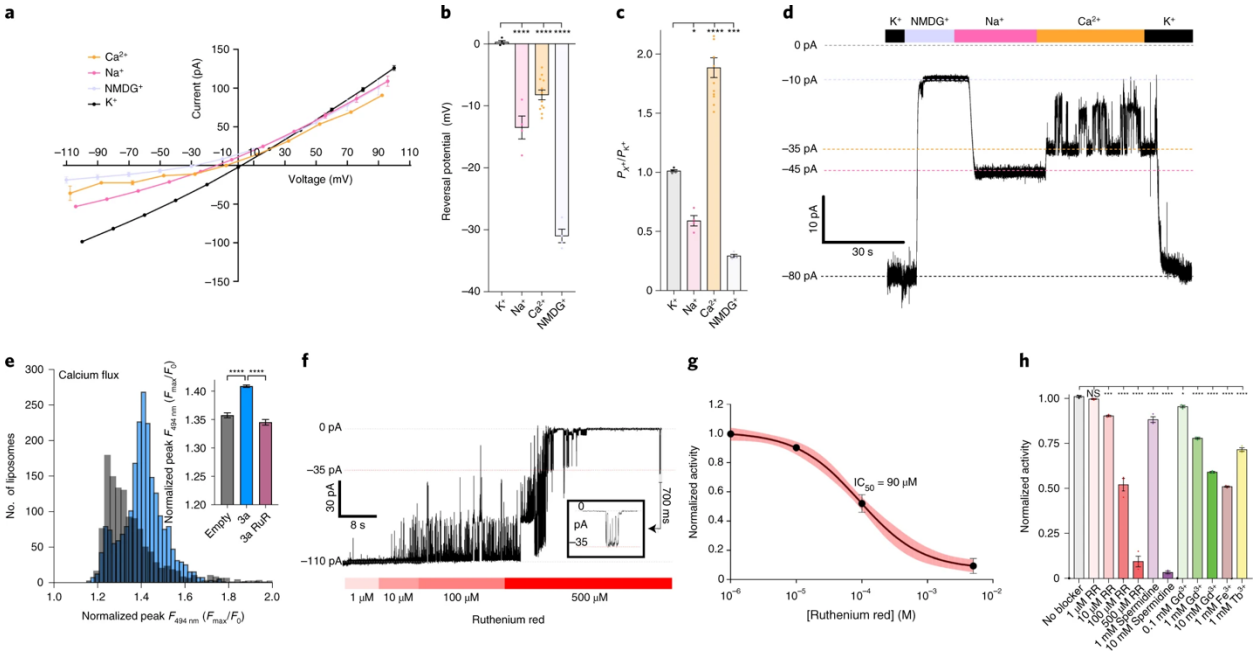

Figure 4: Function and inhibition of purified and reconstituted SARS-CoV-2 3a. **a**, Current–voltage relationship from a 3a-proteoliposome patch. Pipette solution was 150 mM K^+ and external solution was 150 mM K^+ (black), 150 mM Na^+ (pink), 75 mM Ca^{2+} (orange) or 150 mM $NMDG^+$ (blue) (mean ± s.e.m., $n = 3$ recordings from a representative patch). **b**, Reversal potential. Pipette solution was 150 mM K^+ and external solution was 150 mM K^+ (black), 150 mM Na^+ (pink), 75 mM Ca^{2+} (orange) or 150 mM $NMDG^+$ (blue) (mean ± s.e.m., $n = 4$, 4, 12 and 4 patches, respectively). One-way ANOVA with Dunnett correction, $^{****}P < 0.0001$). **c**, Permeability ratios (P_{X+}/P_{K+}) calculated from **b**. Pipette solution was 150 mM K^+ and external solution was 150 mM K^+ (black), 150 mM Na^+ (pink), 75 mM Ca^{2+} (orange) or 150 mM $NMDG^+$ (blue) (mean ± s.e.m., $n = 4$, 4, 12 and 4 patches, respectively). One-way ANOVA with Dunnett correction, $^{*}P < 0.05$, $^{***}P < 0.001$, $^{****}P < 0.0001$). **d**, Gap-free current recording held at −80 mV during bath solution exchanges indicated in the bar above the current trace. **e**, Histogram of peak calcium influx (F_{max}/F) measured by Fluo-5N fluorescence following the addition of 8 mM $[Ca^{2+}]_{ext}$ to 3a liposomes (blue) or empty liposomes (gray). For the inset graph, mean ± s.e.m. of peak calcium influx for 3a liposomes, empty liposomes and 3a liposomes incubated in 200 μM ruthenium red (one-way ANOVA ($F_{(2,4945)} = 99.01$); $n = 1{,}219$, 2,178 and 1,551 liposomes per group, respectively, with Dunnett's multiple-comparisons test, $^{****}P < 0.0001$). **f**, Gap-free current recording in symmetric 150 mM KCl held at −80 mV during bath solution exchanges of varying ruthenium red concentrations indicated in the bar below the current trace. The boxed inset shows magnified channel openings and closures selected from the region indicated. **g**, Normalized activity in symmetric 150 mM KCl at different concentrations of ruthenium red with fit (black line) and 95% confidence interval (red) shown (mean ± s.e.m., $n = 3$ patches, $IC_{50} = 90 \pm 10$ μM). **h**, Normalized 3a activity in symmetric 150 mM KCl and (from left to right) no blocker, 1 μM ruthenium red ($P = 0.9127$), 10 μM ruthenium red ($P < 0.001$), 100 μM ruthenium red ($P < 0.0001$), 500 μM ruthenium red ($P < 0.0001$), 1 mM spermidine ($P < 0.0001$),, 10 mM spermidine ($P < 0.0001$), 0.1 mM Gd^{3+} ($P = 0.0441$), 1 mM Gd^{3+} ($P < 0.0001$), 10 mM

Gd^{3+} ($P < 0.0001$), 1 mM Fe^{3+} ($P < 0.0001$) and 1 mM Tb^{3+} ($P < 0.0001$) (mean ± s.e.m., $n = 3$ patches for each, one-way ANOVA with Dunnett correction, *$P < 0.05$, ***$P < 0.001$, ****$P < 0.0001$). NS, not significant.

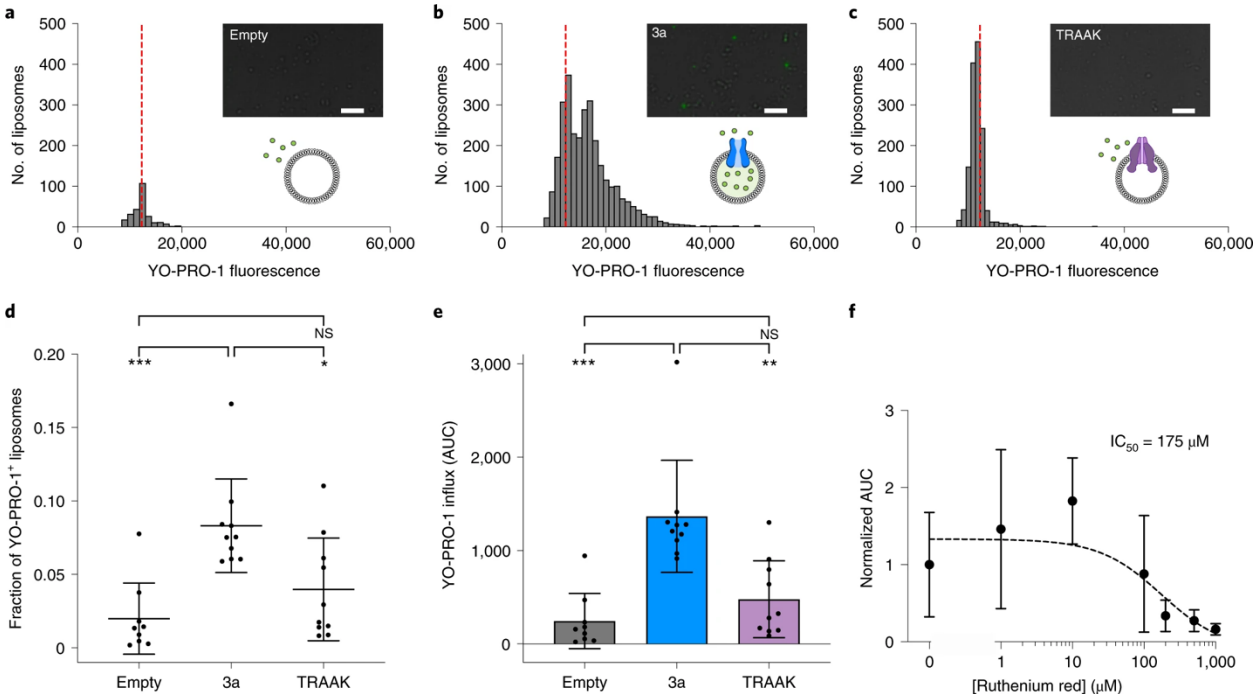

Figure 5: A flux assay of SARS-CoV-2 3a channel activity.
a–**c**, Histograms from quantified images following a 10-min incubation in 10 μM YO-PRO-1 for empty liposomes (**a**), 3a liposomes (**b**) or TRAAK liposomes (**c**) ($n = 255$, 3,046 and 1,408 for empty, 3a and TRAAK liposomes, respectively). Dotted red lines indicate the position of the mean fluorescence of empty liposomes. Insets, representative images with YO-PRO-1 fluorescence (green) overlaid on brightfield. Scale bars, 20 μm. **d**, Fraction of YO-PRO-1-positive liposomes (mean ± s.d., $n = 9$, 10 and 10 independent replicates for empty, 3a and TRAAK liposomes with 500–5,000 liposomes per replicate, $P = 0.0004$ (one-way ANOVA ($F_{(2,26)} = 10.52$)). Tukey's multiple-comparisons test $P_{\text{empty versus 3a}} = 0.0004$; $P_{\text{TRAAK versus 3a}} = 0.0113$ and $P_{\text{empty versus TRAAK}} = 0.3571$). **e**, Area under the curve (AUC) of YO-PRO-1 fluorescence histograms of the fraction of liposomes that took up YO-PRO-1 per well (mean ± s.d., $n = 9$, 10 and 10 independent replicates for empty, 3a and TRAAK liposomes with 500–5,000 liposomes per replicate, $P < 0.0001$ (Welch's ANOVA test ($W_{(2,16.68)} = 13.22$)), Dunnett's multiple-comparisons test: $P_{\text{empty versus 3a}} = 0.0005$; $P_{\text{TRAAK versus 3a}} = 0.0041$; $P_{\text{empty versus TRAAK}} = 0.4178$). **f**, YO-PRO-1 uptake in 3a liposomes is inhibited by ruthenium red. Mean ± s.d., sigmoidal fit (black dotted line) and IC_{50} are shown.

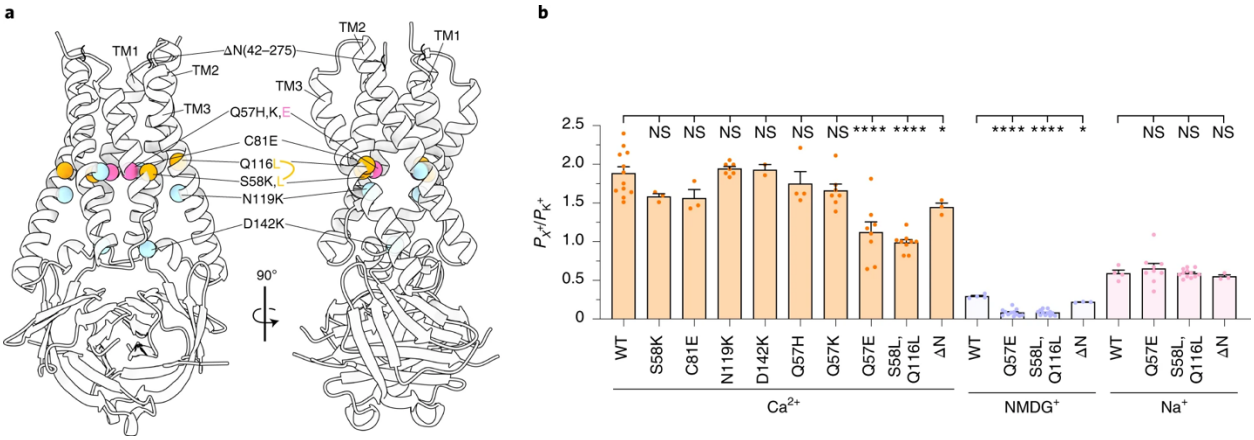

Figure 6: Modification of 3a alters channel activity.
a, Two views of 3a from the membrane plane with the positions of 3a mutations and truncation indicated. **b**, Permeability ratios (P_X/P_{K+}) calculated from reversal potential shifts for 3a mutations and ΔN truncation (mean ± s.e.m., $n = 8, 3, 3, 7, 2, 4, 7, 8, 9$ and 3 patches for wild-type (WT), S58K ($P = 0.2352$), C81E ($P = 0.1741$), N119K ($P = 0.9971$), D142K ($P = 0.9997$), Q57H ($P = 0.9005$), Q57K ($P = 0.2220$), Q57E ($P < 0.0001$), S58L,Q116L ($P < 0.0001$) and ΔN (for Ca^{2+} $P = 0.0251$ and for $NMDG^+$ $P = 0.0287$), respectively, $^*P < 0.05$, $^{****}P < 0.0001$, one-way ANOVA with Dunnett correction for multiple comparisons).

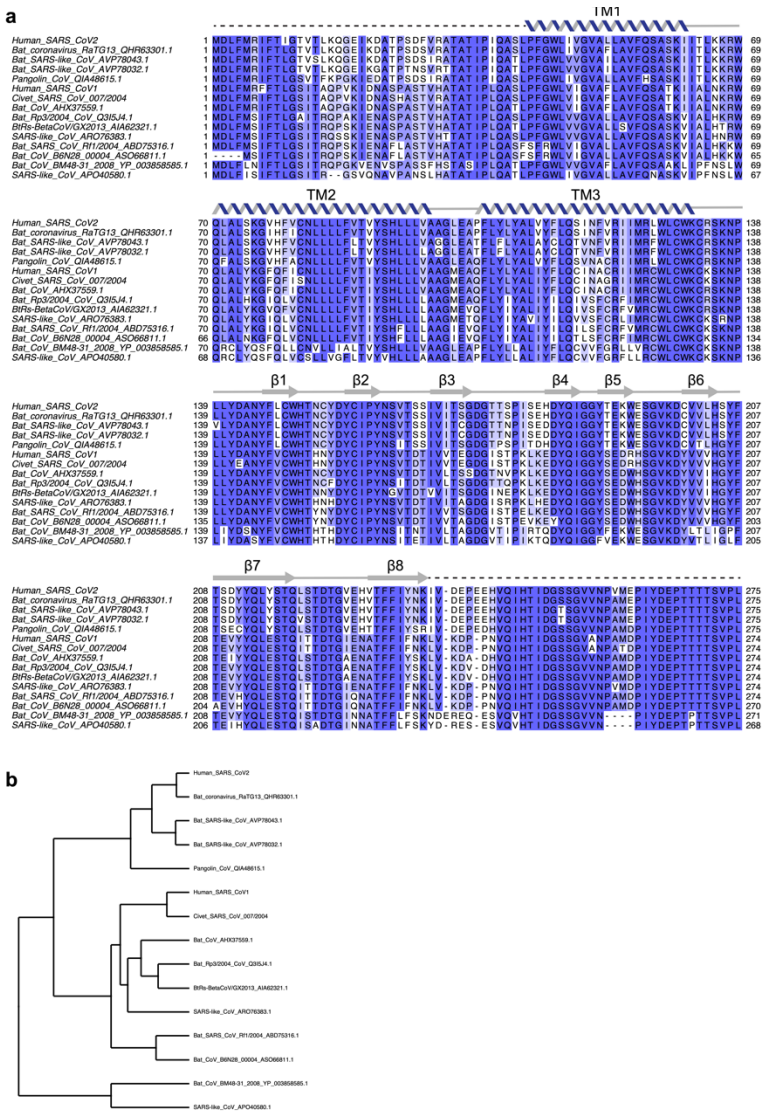

Supplemental Figure 1: Sequence alignment of 3a from Betacoronavirus Sarbecovirus.

a, Alignment of fifteen 3a protein sequences colored by conservation in a ramp from white (not conserved) to dark blue (highly conserved). Accession numbers are indicated. Sequences were selected to maximize diversity among annotated Sarbecovirus 3a proteins. Secondary structure for SARS-CoV-2 is drawn above the sequence with unmodeled sequence drawn as dashed lines. **b**, Neighbor-joining tree calculated from the alignment in (a).

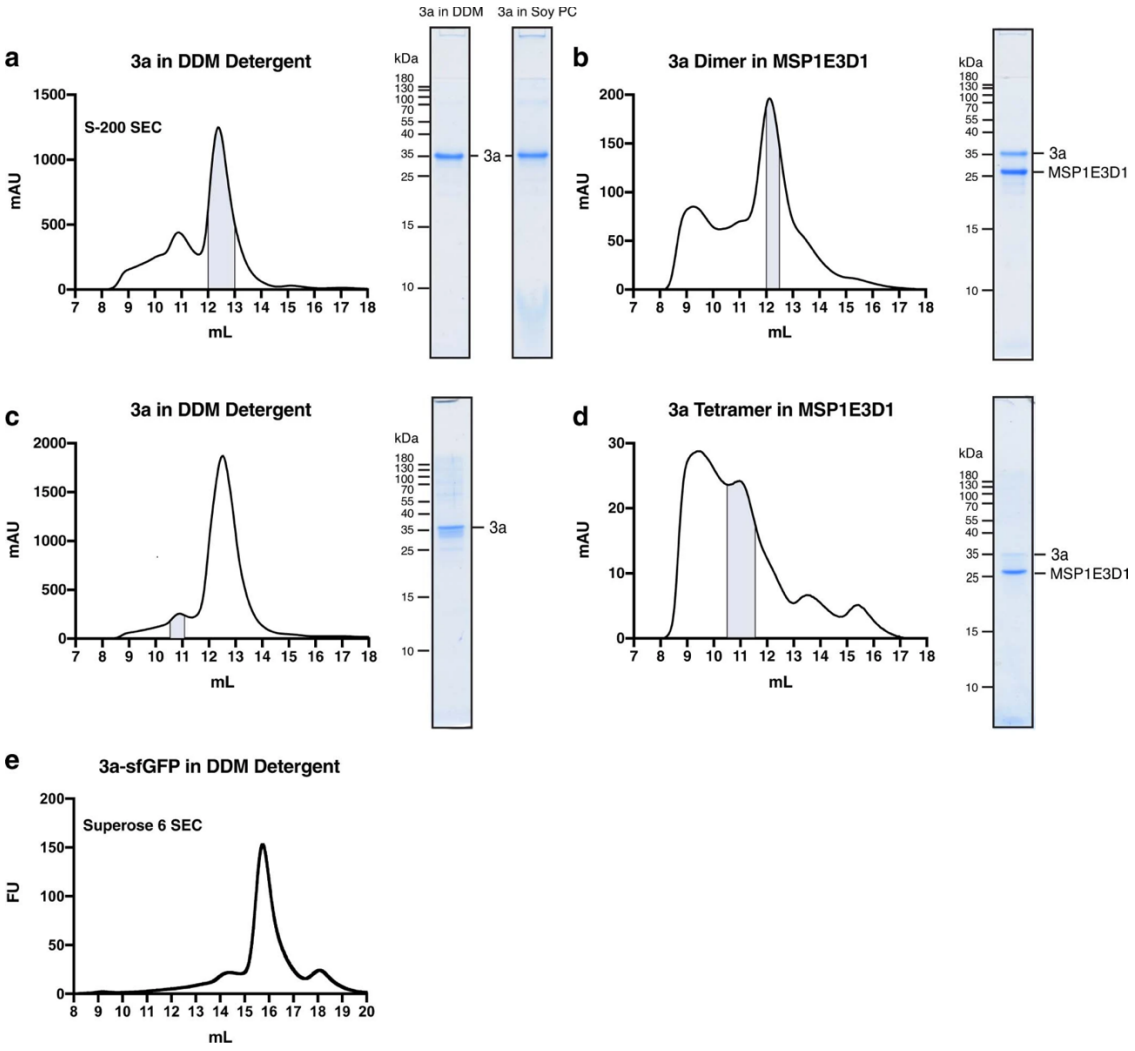

Supplemental Figure 2: Purification and reconstitution of 3a.
a, Size exclusion chromatogram of 3a expressed in insect cells and extracted and purified in DDM (left). Pooled fractions corresponding to dimeric 3a are highlighted in blue. Coomassie-stained SDS-PAGE of pooled dimeric 3a-containing fractions (center) and of 3a following reconstitution into PC lipids (right). This is a representative preparation used for 3a proteoliposome experiments. WT 3a was purified into DDM six times with similar biochemical behavior. Proteoliposomes from three Soy PC preparations were used for activity assays. **b**, Size exclusion chromatogram of dimeric 3a reconstituted into MSP1E3D1 lipid nanodiscs (left). Pooled fractions are highlighted blue. 3a was incorporated into nanodiscs three separate times with similar biochemical behavior, and this representative preparation was used for dimeric 3a cryo-EM data collection (**c**,**d**) Same as (**a**,**b**), but for tetrameric 3a. The tetrameric peak has been observed in all WT 3a preparations. This representative preparation was used for cryo-EM of tetrameric 3a. **e**, GFP fluorescence chromatogram of 3a expressed in SF9 cells and extracted in DDM detergent. Samples were run on a Superose 6 column.

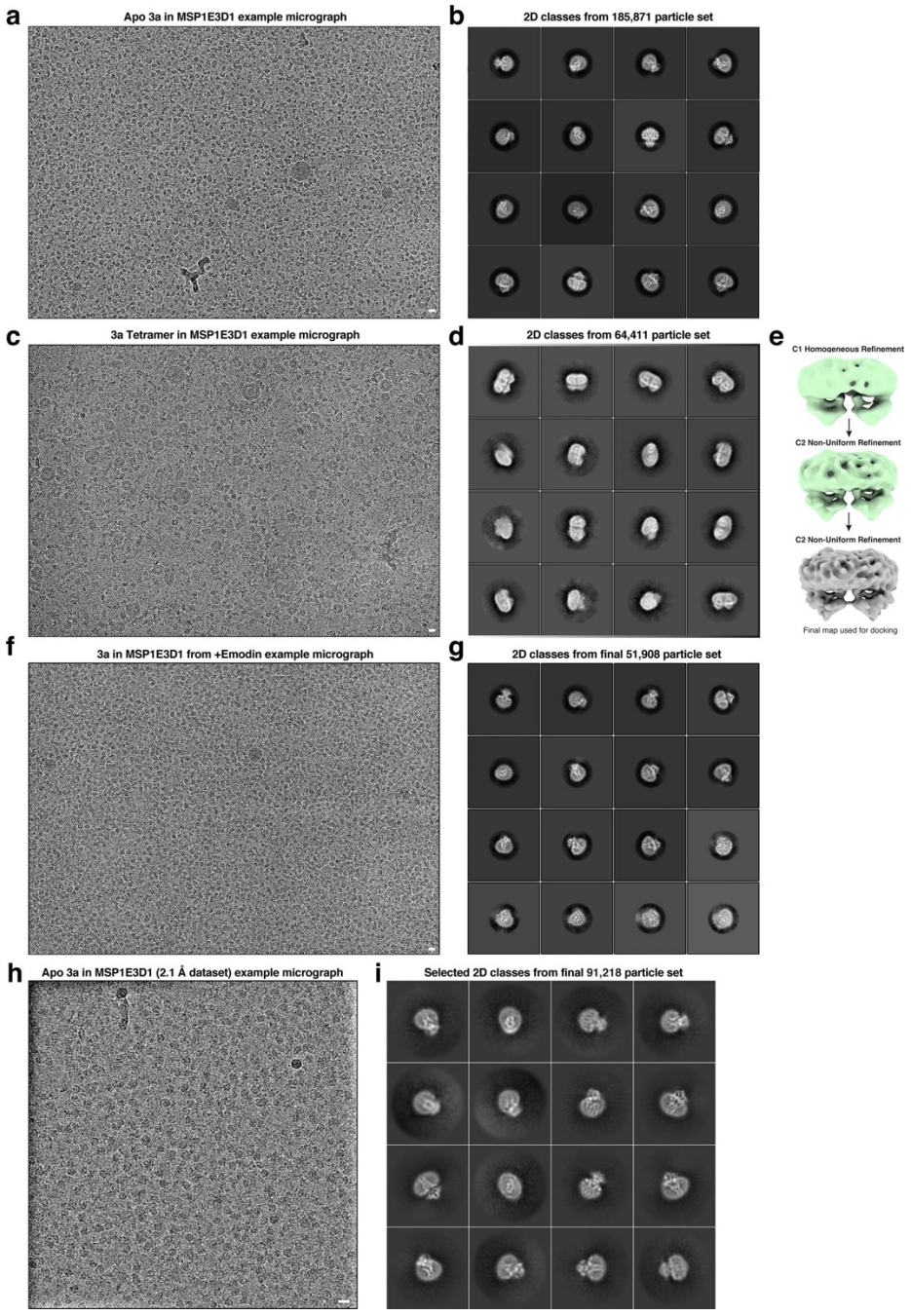

Supplemental Figure 3: Example micrographs and 2D class averages of 3a structures.

a, Representative micrograph and (**b**) 2D class averages of dimeric apo 3a in MSP1E3D1 lipid nanodiscs. **c**, Representative micrograph and (**d**) 2D class averages of tetrameric apo 3a in MSP1E3D1 lipid nanodiscs. **e**, Map overview pipeline for final steps of tetramer processing (Also see Methods) (**f**) Representative micrograph and (**g**) 2D class averages of dimeric 3a in MSP1E3D1 lipid nanodiscs with emodin added. **h**, Representative micrograph and (**i**) 2D class averages of the Krios/CFEG/Selectris

collected dimeric apo 3a in MSP1E3D1 lipid nanodiscs (from cryoSPARC). Micrograph scale bars, 100 Å.

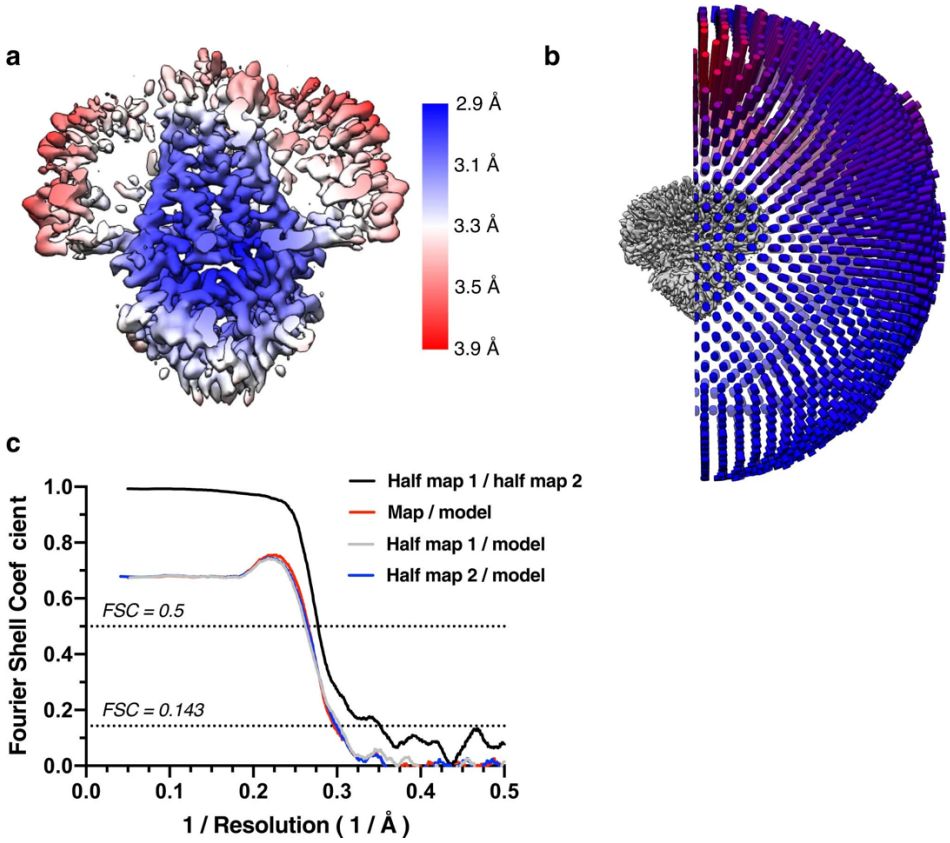

Supplemental Figure 4: Cryo-EM validation for dimeric apo 3a in MSP1E3D1 lipid nanodiscs.
a, Local resolution estimated in Relion colored as indicated on the final map. **b**, Angular distribution of particles used in final refinement with final map for reference. **c**, Fourier Shell Correlation (FSC) relationships (unmasked) between (black) the two unfiltered half-maps from refinement and used for calculating overall resolution at 0.143, (red) the final map and model, (gray) half-map one and model, and (blue) half-map and model.

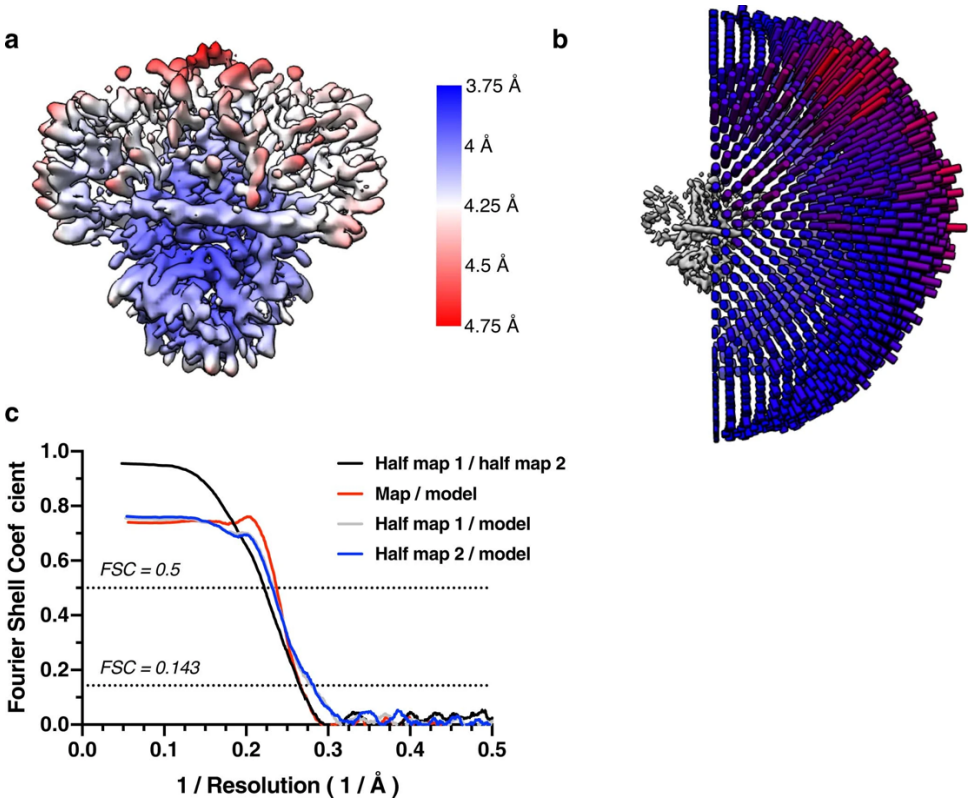

Supplemental Figure 5: Cryo-EM validation for dimeric 3a in MSP1E3D1 lipid nanodiscs with emodin added.

a, Local resolution estimated in Relion colored as indicated on the final map. **b**, Angular distribution of particles used in final refinement with final map for reference. **c**, Fourier Shell Correlation (FSC) relationships (masked) between (black) the two unfiltered half-maps from refinement and used for calculating overall resolution at 0.143, (red) the final map and model, (gray) half-map one and model, and (blue) half-map and model.

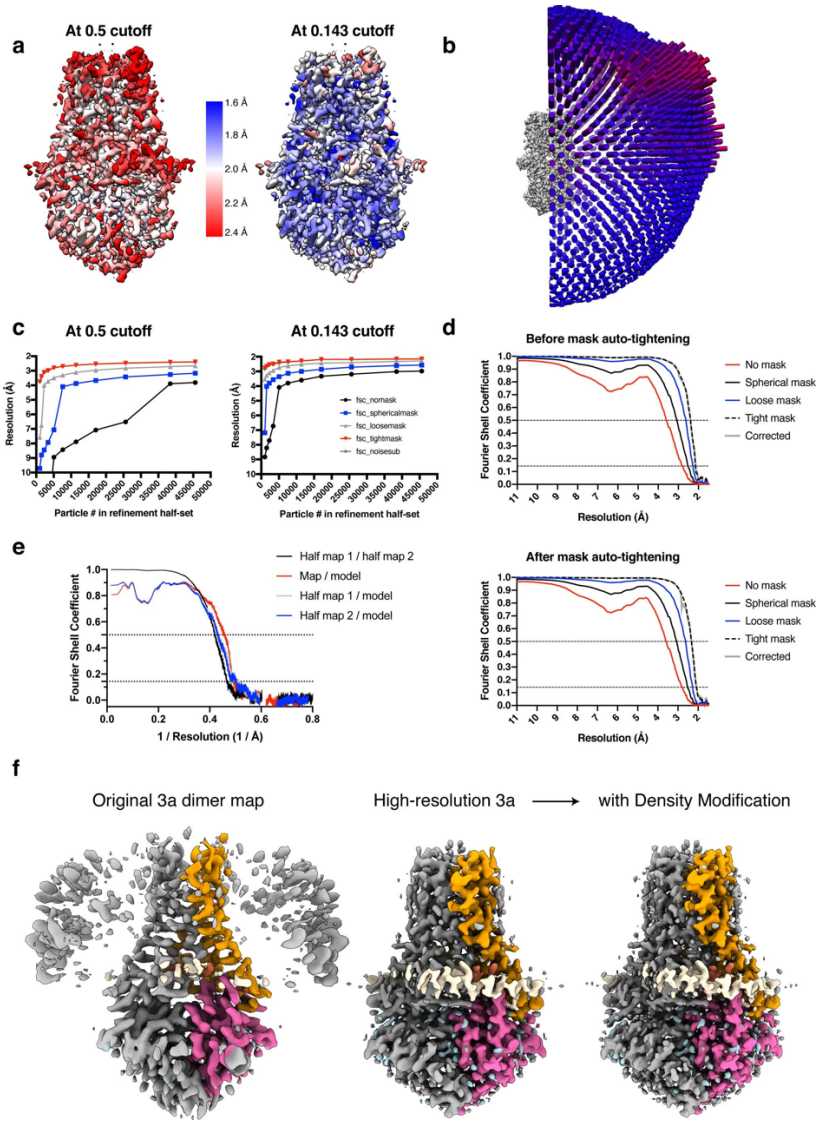

Supplemental Figure 6: Cryo-EM validation for 2.1 Å dimeric apo 3a in MSP1E3D1 lipid nanodiscs.

a, Local resolution estimated in cryoSPARC at the indicated FSC thresholds colored as indicated on the density modified map. **b**, Angular distribution of particles used in final refinement with map for reference. **c**, ResLog analysis conducted in cryoSPARC at the indicated FSC thresholds. **d**, Fourier Shell Correlation as calculated in cryoSPARC before (top) and after (bottom) mask auto-tightening in the final round of refinement. **e**, Fourier Shell Correlation (FSC) relationships (masked) calculated in Phenix between (black) the two unfiltered half-maps from refinement and used for calculating overall resolution at 0.143, (red) the final map and model, (gray) half-map one and model, and (blue) half-map and model. **f**, Comparison of the original (2.9 Å) 3a map left to the high-resolution (2.1 Å) map before (middle) and after (right) Phenix density modification.

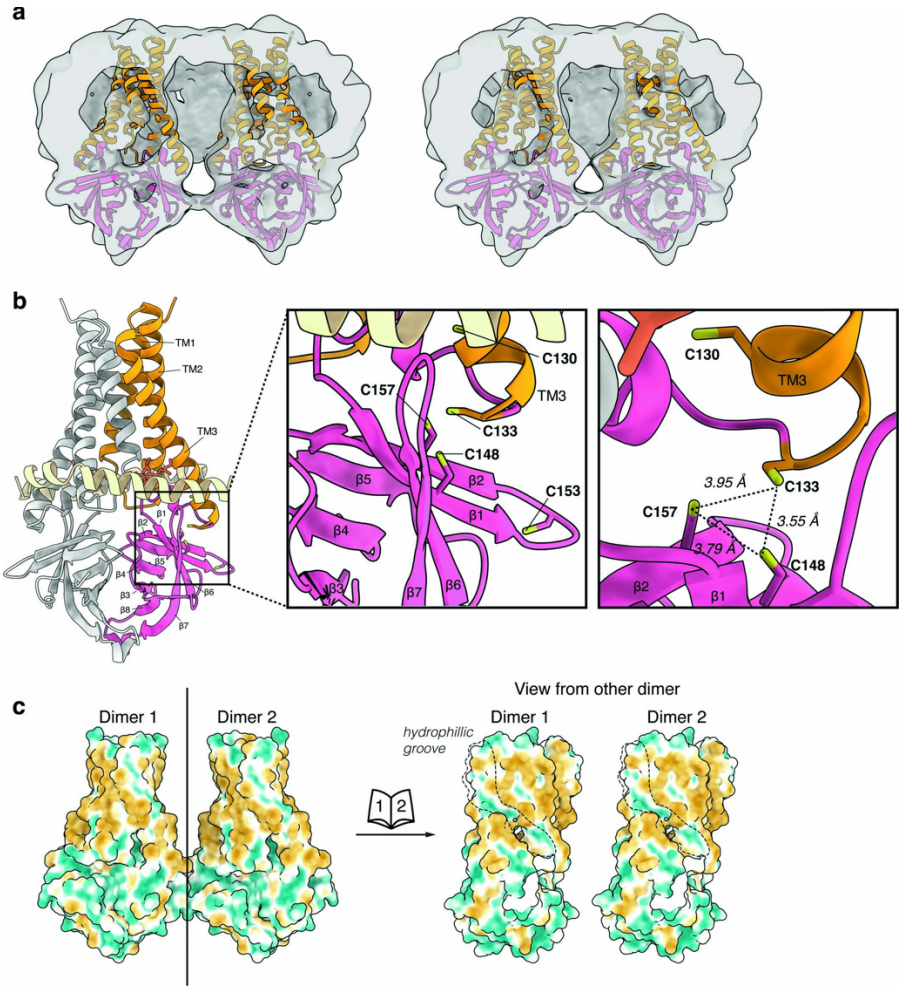

Supplemental Figure 7: The dimer-dimer interface and a cysteine rich pocket in 3a.

a, A slice through the tetramer map with docked dimer models to illustrate the rigid body fit of model to map. Left: Same threshold as in Fig. 2 (0.25). Right: At a lower threshold (0.21). **b**, Dimer model (left) with boxed region zoom-in (middle) and an alternate view (right) to show the cysteine¯rich region of 3a. Distances (dotted lines) between the reduced cysteines are displayed. **c**, Left: Dimers docked into the tetramer map with the solvent excluded surface of 3a colored from hydrophilic (dark cyan) to hydrophobic (dark orange). Right: 'Open book' view of each dimer from the perspective of the other dimer in the tetrameric assembly. The hydrophilic groove between TM2 and TM3 is outlined.

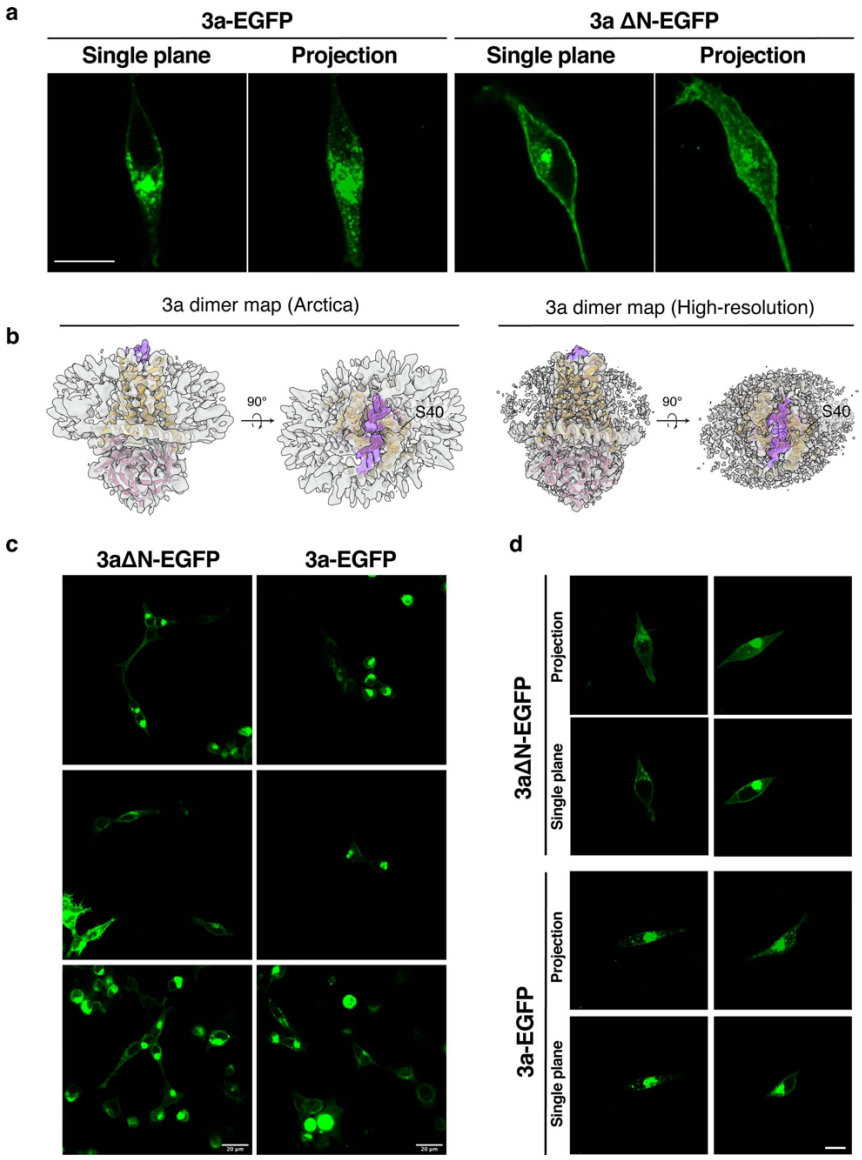

Supplemental Figure 8: Localization of 3a-EGFP and 3aΔN-EGFP expressed in HEK293 cells.

a, 3a-GFP fluorescence localization in HEK293 cells transfected with 3a-EGFP or 3aΔN-EGFP. Single plane and brightest-point projection are displayed for each. Scale bar, 10 µm. **b**, Side view and view from the extracellular/lumenal space for dimeric 3a cryo-EM density (gray) from the original (left) and high-resolution (right) maps with unmodeled extended density above the mouth of the pore that may correspond to the N-terminal regions colored in purple. A 3a dimer model is drawn orange (TMD) and pink (CD) inside the density. The position of the final modeled N-terminal residue (S40) is indicated. **c**, 3a-EGFP or 3aΔN-EGFP field of view with multiple cells imaged using a 20X objective. Scale bar, 20 µm. **d**, Additional images of cells imaged with the 63X objective with both single plane and brightest-point projections displayed. Scale bar, 10 µm.

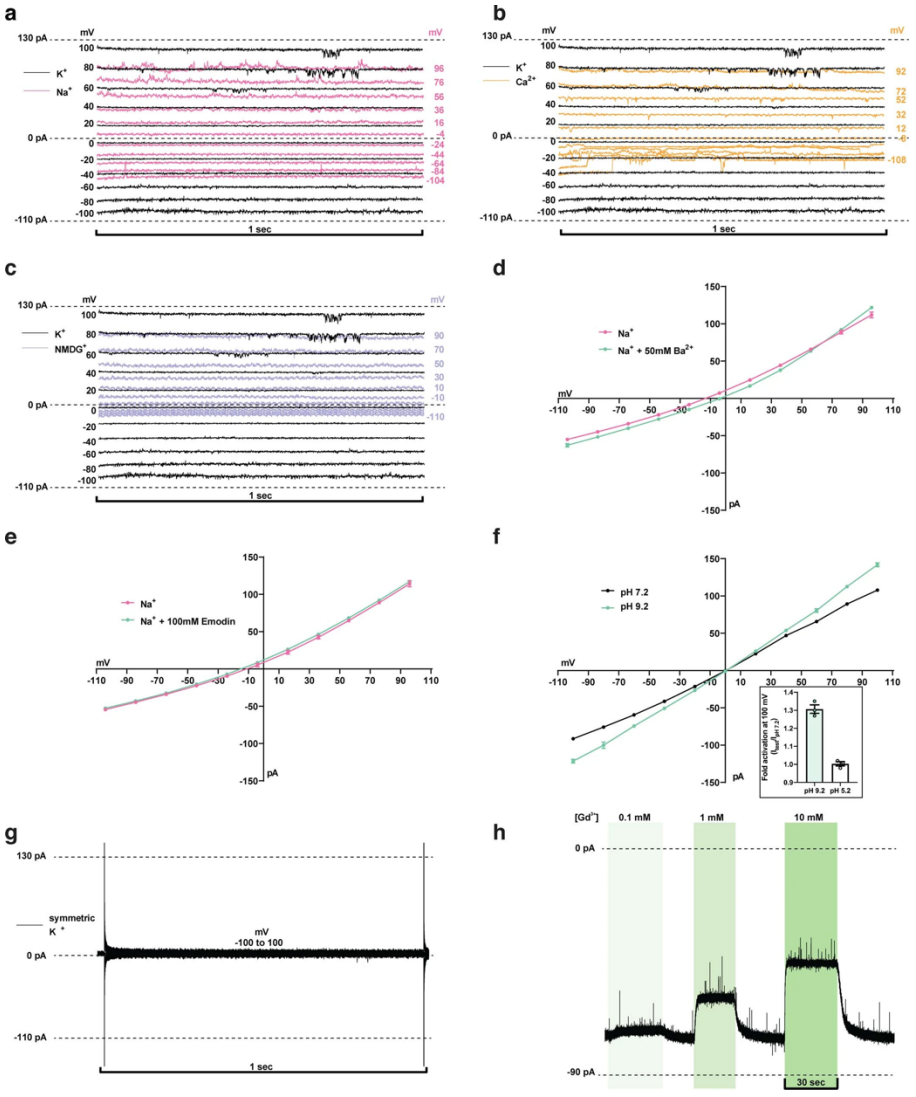

Supplemental Figure 9: Patch recordings from 3a-proteoliposomes.

(**a**-**c**,**g**) Representative current recordings from 3a-proteoliposome. Currents were recorded with the following protocol: V_{hold} = 0 mV, V_{test} = -100 to 100 mV, ΔV = 20 mV, t_{test} = 1 sec. Voltages indicated were corrected after recording for liquid junction potential. **a**, 150 mM K^+ (black) or 150 mM Na^+ (pink) bath solution. **b**, 150 mM K^+ (black) or 75 mM Ca^{2+} (orange) bath solution. **c**, K^+ (black) or 150 mM $NMDG^+$ (blue) bath solution. **d**, Ba^{2+} does not block 3a currents. Current-voltage relationship plotted from a recording in 150 mM Na^+ (pink) or 150 mM Na^+ with 50 mM Ba^{2+} (green) bath solution. **e**, Emodin does not block 3a currents. Current-voltage relationship plotted from a recording in 150 mM Na^+ (pink) or 150 mM Na^+ with 100 µM emodin (green) bath solution. **f**, pH sensitivity of 3a. Current-voltage relationship plotted from a recording in 150 mM K^+ pH 7.2 (black) and 150 mM K^+ pH 9.2 (green) bath solution. (inset) Fold activation at +100 mV at pH 9.2 (mean ± s.e.m., n = 3) or pH 5.2 compared to pH 7.2 (mean ± s.e.m., n = 3). **g**, Representative current recordings from mock reconstituted (empty) liposome patch. **h**, Gap-free current recording in symmetric 150 mM KCl held at

−80 mV during bath solution exchange and washout of varying Gd^{3+} concentrations represented by vertical green bars.

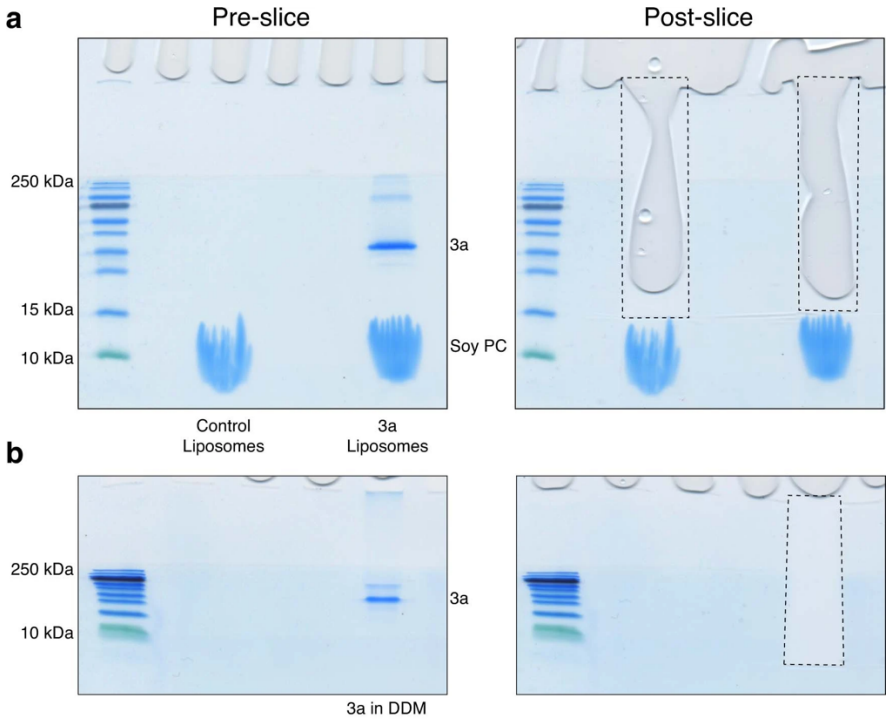

c

Protein	Source (search)	MW (kDa)	% Sequence Coverage (# Matched Peptides)		
			3a in DDM	3a in liposomes	Control liposomes
orf3a	SARS-CoV-2 (Recombinant)	32.1	30.6% (180)	8.8% (25)	0% (0)
cytochrome P450	*S. frugiperda*	55.9	7.3% (2)	0% (0)	0% (0)
vps28	*S. frugiperda*	24.8	0% (0)	0% (0)	7.6% (1)
ubiquitin	*S. frugiperda*	8.6	52.6% (22)	0% (0)	0% (0)
ubiquitin-activating enzyme 7	Contaminant	111.7	0% (0)	0% (0)	1% (1)

Supplemental Figure 10: Mass spectrometry analysis of 3a and control samples. **a**, SDS-PAGE gels with 3a and mock liposome samples prior to (left) and post (right) gel slice extraction for mass spectrometry. Approximate outline of the extracted region is shown with a dotted line. The control and 3a samples were from a liposome preparation used for both electrophysiological and fluorescence assays. **b**, Same as (**a**), but for 3a in DDM sample (prior to liposome incorporation). This sample was from a DDM prep used for both cryo-EM and proteoliposome preparations. **c**, Summary table of mass spectrometry analysis for the three analyzed samples. The only other hits were to human keratin proteins from the common contaminant library. No additional hits were detected from the *G. max* (soy) search.

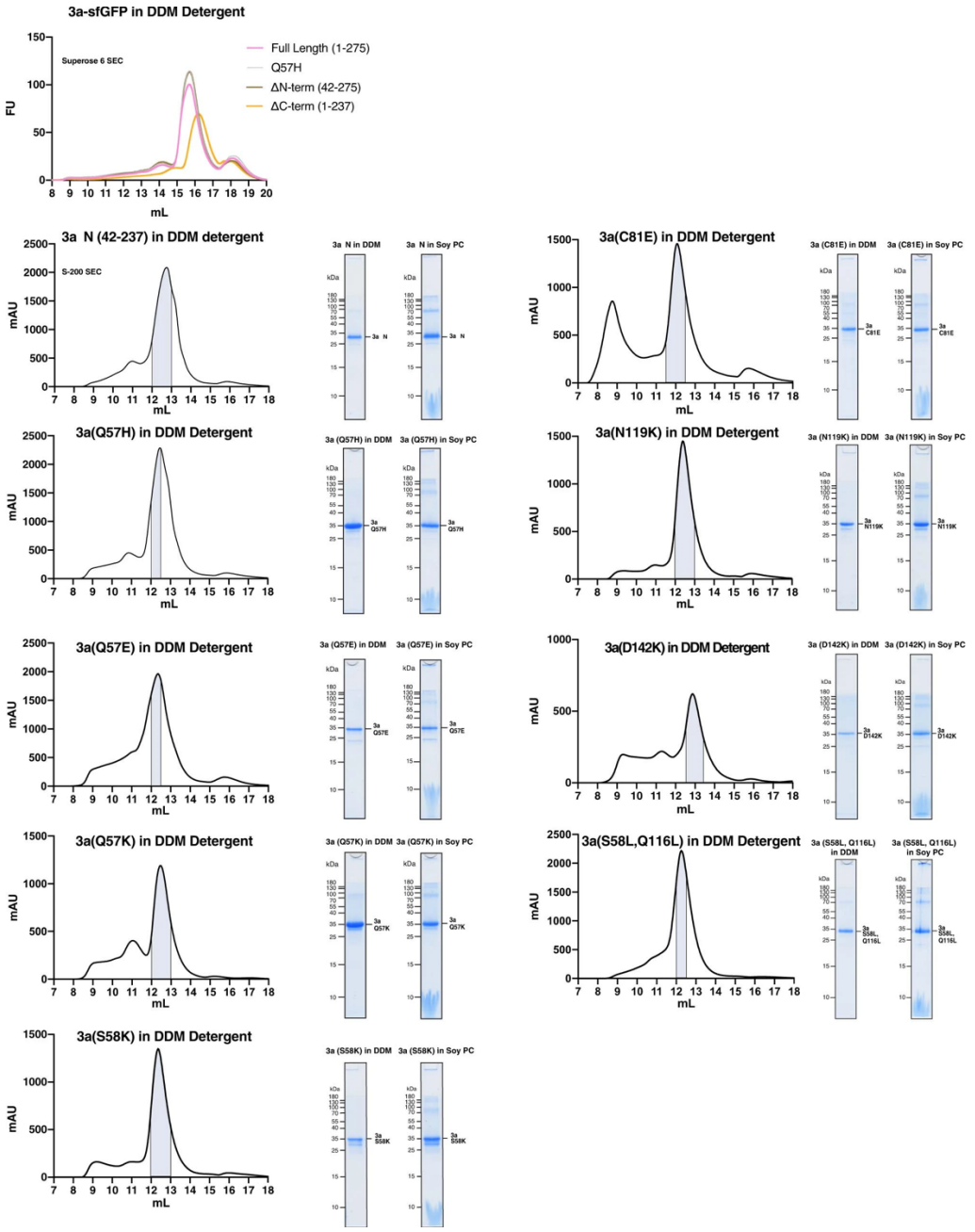

Supplemental Figure 11: Purification and liposome reconstitution of 3a mutants and truncation. Top: GFP fluorescence chromatogram (FSEC) of 3a, as well as indicated mutants and truncations, expressed in SF9 cells and extracted in DDM detergent. Samples were run on a Superose 6 column. For all other panels: Size exclusion chromatogram from a s200 column of indicated 3a constructs expressed in insect cells and extracted and purified in DDM (left), coomassie-stained SDS-PAGE of pooled dimeric 3a construct -containing fractions (center), and of 3a following reconstitution into PC lipids (right). These gels and chromatograms are from the preparations used for electrophysiological assays.

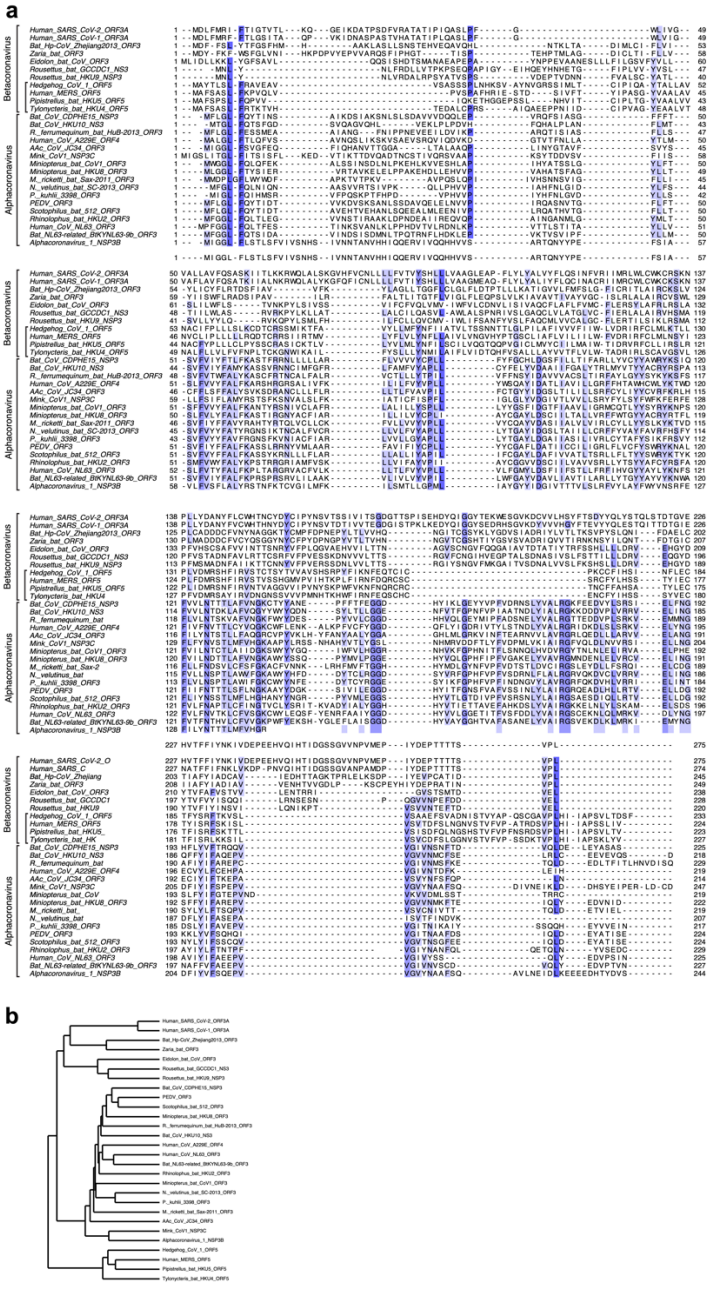

Supplemental Figure 12: Sequence alignment of 3a-like proteins across *Coronaviridae.*

a, Alignment of twenty-eight 3a-like protein sequences colored by conservation in a ramp from white (not conserved) to dark blue (highly conserved). Accession numbers are listed in Table 2. Sequences were selected from representative species from each Coronavirus subgenus. *Alphacoronavirus* and Betacoronavirus clades are indicated. Within Betacoronavirus the subgenus *Merbecovirus* is also indicated with a bar. **b,** Neighbor-joining tree calculated from the alignment in (a).

Discussion

Together, our data demonstrate that SARS-CoV-2 3a adopts a novel dimeric fold widely conserved across Coronaviridae and can form a nonselective Ca^{2+} permeable cation channel. These results provide a basis for further studies to determine mechanisms of 3a channel gating and conduction. A polar cytoplasmic cavity creates a low energy path for ions to traverse between the cytoplasm and halfway across the membrane. However, 3a lacks a central pore across the outer half of the membrane and conformational changes to open one would require breaking interactions that form a hydrophobic seal between TMs in the current structure. Alternatively, lateral conduction pathways could be formed along conserved hydrophilic membrane-facing grooves between TM2 and TM3. Similar lateral conduction paths have precedence among other channels including members of the TMEM16 and OSCA families[262–265].

Oligomeric 3a assemblies could also mediate 3a activation. 3a dimers associate into tetramers and assembly could feasibly be propagated further into higher-order oligomers. Consistently, we observe increased oligomeric 3a bands in SDS–PAGE gels after liposome incorporation (Supplemental Figs. 2 and 11). This observation, together with the lipid binding pocket within 3a and its localization to organellar membranes, suggests the membrane environment may be important for 3a structure and function.

In liposomes, SARS-CoV-2 3a exhibits permeability to large cations including $NMDG^{+}$ and YO-PRO-1 and sensitivity to ruthenium red and Gd^{3+}, broadly reminiscent of other Ca^{2+}-permeable channels including TRPV1, TRPA1 and P2X7[266,267] while displaying, to our knowledge, a unique functional fingerprint. We note that our data are only partially consistent with previously reported properties of SARS-CoV-1 3a. For example, we do not observe block by Ba^{2+} or emodin and while both proteins apparently form nonselective cation channels, their relative permeability for cations differs. This could be explained by sequence and functional divergence: 3a in the two viruses shares just 73% sequence identity. Alternatively, different recording and lipid environments might alter channel properties. SARS-CoV-1 3a activity was recorded in *Xenopus* oocytes or cultured cells, while SARS-CoV-2 3a activity was recorded in reconstituted membranes. Whether SARS-CoV-2 3a channel activity is observed in cells, perhaps in intracellular membranes where most heterologously expressed protein is localized, remains to be determined.

If 3a has channel activity in cells, it could be important for promoting viral maturation through inhibition of autophagy and disruption of lysosomes[279,280]. The unresolved N and C termini may also play important roles in determining 3a's localization and binding partners. The calcium permeability of 3a is of particular interest in the context of infection. SARS-CoV-2 3a has been recently shown to trigger programmed cell death in cultured cells[252] and calcium influx through 3a could serve as a switch that activates calcium-dependent caspases and apoptosis. Previous studies showed SARS-CoV-1 3a expression in infected lung pneumocytes, a key cell type also infected by SARS-CoV-2, and calcium signaling in type II pneumocytes plays an important role in maintaining airway homeostasis[281,282]. Thus, the expression of a calcium permeable channel, as for SARS-CoV-2 3a, could affect lung homeostasis and COVID-19 pathogenesis. Our data indicate that 3a could represent a target for treating COVID-19 and other coronavirus diseases and points the way to future experiments to elucidate the role of 3a in the viral life cycle and disease pathology.

Methods

Cloning and protein expression

The coding sequence for the 3a protein from SARS-Cov-2 was codon optimized for *S. frugiperda* (Sf9 cells) and synthesized (Integrated DNA Technologies). The sequence was then cloned into a custom vector based on the pACEBAC1 backbone (MultiBac, Geneva Biotech) with an added C-terminal PreScission protease (PPX) cleavage site, linker sequence, superfolder GFP (sfGFP) and 7×His tag, generating a construct for expression of 3a-SNS-LEVLFQGP-SRGGSGAAAGSGSGS-sfGFP-GSS-7×His. Mutants and truncation were also introduced into this construct using PCR. MultiBac cells were used to generate a Bacmid according to the manufacturer's instructions. Sf9 cells were cultured in ESF 921 medium (Expression Systems) and P1 virus was generated from cells transfected with Escort IV reagent (MillaporeSigma) according to the manufacturer's instructions. P2 virus was then generated by infecting cells at 2 million cells per ml with P1 virus at a multiplicity of infection of roughly 0.1, with infection monitored by fluorescence and harvested at 72 h. P3 virus was generated in a similar manner to expand the viral stock. The P2 or P3 viral stock was then used to infect Sf9 cells at 4 million cells per ml at a multiplicity of infection of around 2–5. At 72 h, infected cells containing expressed 3a-sfGFP protein were collected by centrifugation at 2,500*g* for 10 min and frozen at −80 °C.

Protein purification

For preparation of the 3a dimer and mutant constructs, infected Sf9 cells from 1 l of culture (roughly 15–20 ml of cell pellets) were thawed in 100 ml of lysis buffer containing 50 mM Tris, 150 mM KCl, 1 mM EDTA pH 8. Protease inhibitors (final concentrations E64 (1 μM), pepstatin A (1 μg ml^{-1}), soy trypsin inhibitor (10 μg ml^{-1}), benzamidine (1 mM), Aprotinin (1 μg ml^{-1}), leupeptin (1 μg ml^{-1}), AEBSF (1 mM) and phenylmethylsulfonyl fluoride (1 mM)) were added to the lysis buffer immediately before use. Benzonase (4 μl) was added after the cell pellet thawed. Cells were then lysed by sonication and centrifuged at 150,000*g* for 45 min. The supernatant was discarded and residual nucleic acid was removed from the top of the membrane pellet using Dulbecco's phosphate buffered saline (DPBS). Membrane pellets were scooped into a dounce homogenizer containing extraction buffer (50 mM tris, 150 mM KCl, 1 mM EDTA, 1% *n*-dodecyl-β-d-maltopyranoside (DDM) (Anatrace), pH 8). A 10% stock solution of DDM was dissolved and clarified by bath sonication in 200 mM tris pH 8 before addition to buffer to the indicated final concentration. Membrane pellets were then homogenized in extraction buffer and this mixture (150 ml of the final volume) was gently stirred at 4 °C for 1 h. The extraction mixture was centrifuged at 33,000*g* for 45 min and the supernatant, containing solubilized membrane protein, was bound to 4 ml of sepharose resin coupled to anti-GFP nanobody for 1 h at 4 °C. The resin was then collected in a column and washed with 10 ml of buffer 1 (20 mM HEPES, 150 mM KCl, 1 mM EDTA, 0.025% DDM, pH 7.4), 40 ml of buffer 2 (20 mM HEPES, 500 mM KCl, 1 mM EDTA, 0.025% DDM, pH 7.4) and 10 ml of buffer 1. The resin was then resuspended in 6 ml of Buffer 1 with 0.5 mg of PPX protease and rocked gently in the capped column for 2 h. Cleaved 3a protein was then eluted with an additional 8 ml of Wash Buffer, spin concentrated to roughly 500 μl with Amicon Ultra spin concentrator 10-kDa cutoff (Millipore), and then loaded onto a Superdex 200

increase column (GE Healthcare) on an NGC system (Bio-Rad) equilibrated in buffer 1. Peak fractions containing 3a channel were then collected and spin concentrated before incorporation into proteoliposomes or nanodiscs. For the tetramer, the preparation was carried out in a similar manner, except with overnight protease cleavage and collection of a peak of larger hydrodynamic radius (Supplemental Fig. 2). Traces for gel filtration were prepared using Chromlab 6.0 (Bio-Rad), Prism 8 and Adobe Illustrator.

Proteoliposome formation

For proteoliposome patching experiments, we incorporated protein into lipid and generated proteoliposome blisters for patch recordings using dehydration and rehydration as described previously with the following modifications[283]. The 3a dimer was first purified into buffer 1. Protein was then exchanged into lipid with the addition of Biobeads SM2 (Bio-Rad) and an overnight incubation at a protein:lipid ratio of 1:10 (corresponding to 0.5 mg purified 3a dimer and 5 mg of cleared soybean l-α-phosphatidylcholine, Soy PC, MillaporeSigma) in DR buffer (5 mM HEPES, 200 mM KCl, pH 7.2). For the YO-PRO-1 assay, 3a was incorporated at a ratio of 1:50. TRAAK control proteoliposomes were prepared at 1:50 as described previously[283]. Control liposomes were prepared from the same lipid mix and protocol with protein replaced with buffer 1.

Electrophysiology

All electrophysiology recordings were made from 3a-reconstituted Soy PC proteoliposomes. Patches formed in an inside-out configuration and were quickly (within 5–10 s) transferred to a solution exchange chamber. Recordings were made at room temperature using Clampex v.10.7 data acquisition software (as part of the pClamp v.10.7 suite) with an Axopatch 200B Patch Clamp amplifier and Digidata 1550B digitizer (Molecular Devices) at a bandwidth of 1 kHz and digitized at 500 kHz. A pressure clamp (ALA Scientific) was used to form seals. Potassium pipette and bath solution was 5 mM HEPES pH 7.2 and 150 mM KCl. Sodium bath solution was 5 mM HEPES pH 7.2 and 150 mM NaCl. NaCl in the bath solution was substituted for 150 mM NMDG-Cl or 75 mM $CaCl_2$ for permeability experiments. Borosilicate glass pipettes were pulled and polished to a resistance of 2–5 MΩ when filled with pipette solution. For cation permeability experiments, liquid junction potentials were calculated and data were corrected offline. For current–voltage plots, the following voltage protocol was applied: V_{hold} = 0 mV mV; V_{test} = −100 to +100 mV, Δ20 mV, t_{test} = 1 s. Currents from each patch correspond to mean values during the step to the indicated voltage.

Permeability ratios were calculated according to Goldman–Hodgkin–Katz relationship. For monovalent cations, permeability ratios were calculated as $P_{X+}/P_{K+} = \exp(\Delta V_{rev}F/RT)$. For divalent cations, permeability ratios were calculated as: $P_{X2+}/P_{K+} = \alpha_{K+}[K+]\exp(\Delta V_{rev}F/RT)(1 + \exp(\Delta V_{rev}F/RT))/ 4\alpha_{X2+}[X^{2+}]$ where V_{rev} is the reversal potential, F is Faraday's constant, R is the universal gas constant, T is absolute temperature (where RT/F = 25.2 mV at room temperature) and α is the ion activity coefficient (assumed to be 0.75 for K^+ and 0.25 for Ca^{2+}).

Mass spectrometry

Samples from 3a in DDM (before liposome incorporation), 3a in soy PC (1:50 ratio, and tested for activity in both electrophysiological and fluorescence-based assays) or control liposomes were run on SDS–PAGE gels and stained (Supplemental Fig. 9). For the DDM sample, the entire gel lane above the dye front was excised, including the stacking gel. For samples with lipid, to minimize lipid interference in sample digestion, the gel lane

above the stained lipid was then excised (which includes the region around 15 kDa and larger).

Mass spectrometry was performed by the Vincent J. Coates Proteomics/Mass Spectrometry Laboratory at UC Berkeley. The excised gel lanes were digested with trypsin in situ, and the resulting peptides extracted and concentrated. A nano liquid-chromatography column was packed in a 100-μm inner diameter glass capillary with an emitter tip. The column consisted of 10 cm of Polaris c18 5-μm packing material (Varian). The column was loaded by use of a pressure bomb and washed extensively with buffer A (5% acetonitrile/0.02% heptafluorobutyric acid). The column was then directly coupled to an electrospray ionization source mounted on a Thermo Fisher LTQ XL linear ion trap mass spectrometer. An Agilent 1200 HPLC equipped with a split line so as to deliver a flow rate of 300 nl min^{-1} was used for chromatography. Peptides were separated with a reverse phase elution using a gradient of 5 to 60% acetonitrile generated by a transition from buffer A to buffer B (60% acetonitrile/0.02% heptafluorobutyric acid) over 90 min.

Protein identification was done with Integrated Proteomics Pipeline (IP2, Integrated Proteomics Applications) using ProLuCID/Sequest, DTASelect2 and Census[284–286]. Tandem mass spectra were extracted into MS1 and MS2 files from raw files using RawExtractor[287]. Data were searched against a *S. frugiperda* protein database from Uniprot with the added amino acid sequence of purified 3a (including the cleavage site scar), supplemented with sequences of common contaminants and concatenated to form a decoy database[288]. Searches against soy (*G. max*) returned no hits for any sample. LTQ data were searched with 3000.0 milli-amu precursor tolerance and the fragment ions were restricted to a 600.0 ppm tolerance. All searches were parallelized and searched on the VJC proteomics cluster. Search space included all half tryptic peptide candidates with no missed cleavage restrictions. Carbamidomethylation (+57.02146) of cysteine was considered a static modification. To identify authentic termini, we required one tryptic terminus for each peptide identification. The ProLuCID search results were assembled and filtered using the DTASelect program with a peptide false discovery rate (FDR) of 0.001 for single peptides and a peptide FDR of 0.005 for additional peptides for the same protein. Under such filtering conditions, the estimated FDR was less than 1%.

Ca^{2+} uptake assay in proteoliposomes

Fluo-5N was incorporated into 3a-reconstituted proteoliposomes and control liposomes by first thawing frozen liposomes at a ratio of roughly 1:20 (v:v) into modified sucrose formation buffer[289] 25 mM HEPES pH 7.4, 150 mM KCl and 262 mM sucrose with a final concentration of 25 μM Fluo-5N (Stock concentration 5 mM in DMSO, AAT Bioquest). Next, the liposome mixtures in Eppendorf tubes were placed in a foam flotation in an ice bath and sonicated with a Branson Digital Sonifier 450 for 30 s in total (10% amplitude, 10 s pulse with 59-s wait time). Excess (unincorporated) Fluo-5N was then removed using microspin G-50 columns (Cytiva). The sample was then diluted into solution containing 50 mM HEPES, 300 mM KCl and 2 mM EGTA, pH 7.4, plated onto poly-d-lysine (Sigma-Aldrich, 1 mg ml^{-1}) coated 96-well plates and centrifuged (440*g* for 5 min) at room temperature. Ca^{2+} influx was measured on addition of a 50 mM HEPES, 285 mM KCl, 10 mM $CaCl_2$, pH 7.4 solution. Images were acquired every 3 s for a total of 150 s. Fluorescence intensity of each liposome was normalized to its average fluorescence before Ca^{2+} addition.

YO-PRO-1 flux assay

Liposomes were diluted in saline solution containing 300 mM KCl, 50 mM HEPES, pH 7.4 and plated onto poly-d-lysine (Sigma-Aldrich, 1 mg ml^{-1}) coated 96-well plates, centrifuged (5,000*g* for 5 min) and incubated in 10 μM YO-PRO-1 iodide (Invitrogen) for 10 min at room temperature. Liposomes were rinsed with saline solution to remove free YO-PRO-1. Images were acquired using an ImageXpress Micro XLS microscope with a solid-state light source and ×20 air objective. Images were analyzed using MetaXpress 6 software (Molecular Devices). Empty liposomes displayed low-level fluorescence in the 488/540-nm range. Thus, liposomes were defined as YO-PRO-1^+ if their fluorescence intensity was above the average intensity of unlabeled, empty liposomes. To calculate the total number of liposomes, we quantified the total number of liposomes using auto-segmentation on MetaXpress 6 from brightfield images. Stock solutions of ruthenium red (Tocris) were prepared in water, diluted in bath solution and applied to liposomes or cells 10 min before the start of the experiment. All statistical tests were performed using Prism (GraphPad). Values are reported as the mean ± s.d. or mean ± s.e.m as indicated. Mann–Whitney or a one-way or Welch's analysis of variance (ANOVA) followed by the Dunnett's, Sidak's or Tukey's post hoc tests (where appropriate) were used for statistical comparisons.

Nanodisc formation

Freshly purified 3a dimer in Buffer 1 was reconstituted into MSP1E3D1 nanodiscs with a mixture of lipids (DOPE:POPS:POPC at a 2:1:1 mass ratio, Avanti) at a final molar ratio of 1:4:400 (monomer ratio 3a, MSP1E3D1, lipid mixture). First, 20 mM solubilized lipid in Nanodisc formation buffer (20 mM HEPES, 150 mM KCl, 1 mM EDTA pH 7.4) was mixed with additional DDM detergent and 3a protein. This solution was mixed at 4 °C for 30 min before addition of purified MSP1E3D1. This addition brought the final concentrations to approximately 15 μM 3a, 60 μM MSP1E3D1, 6 mM lipid mix and 10 mM DDM in Nanodisc formation buffer. The solution with MSP1E3D1 was mixed at 4 °C for 10 min before addition of 200 mg of Biobeads SM2. Biobeads (washed into methanol, water, and then Nanodisc formation buffer) were weighed after liquid was removed by pipetting (damp weight). This mix was incubated at 4 °C for 30 min before addition of another 200 mg of Biobeads (for a total 400 mg of Biobeads per 0.5 ml of reaction). This final mixture was then gently tumbled at 4 °C overnight (roughly 12 h). Supernatant was cleared of beads by letting large beads settle and carefully removing liquid with a pipette. Sample was spun for 10 min at 21,000*g* before loading onto a Superdex 200 increase column in 20 mM HEPES, 150 mM KCl, pH 7.4. Peak fractions corresponding to 3a protein in MSP1E3D1 were collected, 10-kDa cutoff spin concentrated and used for grid preparation. MSP1E3D1 was prepared as described[290] without cleavage of the His-tag. Tetrameric 3a in nanodiscs was prepared similarly, except with a ratio of 1:2:200 (monomer ratio 3a, MSP1E3D1, lipid mixture).

Grid preparation

Dimeric 3a in MSP1E3D1 was prepared at final concentration of 1.1 mg ml^{-1}. For the sample with emodin (MillaporeSigma, cat. no. E7881), a stock solution of 50 mM emodin in DMSO added to protein sample for final concentrations of 1.1 mg ml^{-1} 3a and 100 μM emodin and 1% DMSO. Concentrated sample was cleared by a 10 min 21,000*g* spin at 4 °C before grid making. For freezing grids, a 3-μl drop of protein was applied to freshly glow discharged Holey Carbon, 300 mesh R 1.2/1.3 gold grids (Quantifoil). A FEI Vitrobot Mark IV (Thermo Fisher Scientific) was used with 4 °C, 100% humidity, 1 blot force, a wait

time of around 5 s and a 3 s blot time, before plunge freezing in liquid ethane. Grids were then clipped and used for data collection. Tetrameric 3a in MSP1E3D1 was frozen at 0.7 mg ml^{-1} with the same grid preparation. Unimaged grids from the same session were then shipped to the Netherlands for data collection on the 300 kV microscope with Falcon 4/CFEG/Selectris energy filter.

Cryo-EM data acquisition

For data collected on the Talos Arctica, grids were clipped and transferred to the microscope operated at 200 kV. Fifty frame videos were recorded on a Gatan K3 Summit direct electron detector in super-resolution counting mode with pixel size of 0.5685 Å. For the apo 3a dataset, the electron dose was 9.528 and 10.135 e^{-} $Å^2$ s^{-1} and total dose was 50.02 and 53.72 e^{-} $Å^2$ in the first set (1–2,007) and second set (2,008–6,309) of videos, respectively. The two different doses are the result of needing to restart the electron gun during collection. For the 3a with added emodin dataset, the electron dose was 8.991 e^{-} $Å^2$ s^{-1} and total dose was 47.21 e^{-} $Å^2$. For the 3a tetramer, the electron dose was 8.841 e^{-} $Å^2$ s^{-1} and total dose was 49.95 e^{-} $Å^2$. Nine videos were collected around a central hole position with image shift and defocus was varied from −0.6 to −2.0 µm through SerialEM[291].

For data collected for the high-resolution 3a dimer structure, clipped grids from the same batch used on Talos Artica were sent to Thermo Fisher Scientific RnD division in Eindhoven, Netherlands. Grids were loaded onto the Krios G4 microscope equipped cold field emission gun (CFEG) operated at 300 kV. Data were collected on a Falcon 4 detector that was mounted behind a Selectris X energy filter. The slit width of the energy filter was set to 10 eV. Then 5,599 video stacks containing 1,429 raw frames were collected with the electron event representation (EER) mode[292] of Falcon 4 detector at a magnification of ×165,000 corresponding to a pixel size of 0.727 Å. Each video stack was recorded with an exposure time of 6 s with a total dose of 50 e^{-} /$Å^2$ on sample and a defocus range between 0.5 and 1.2 µm.

Cryo-EM data processing

For the apo 3a dimer, motion correction and dose weighting were performed on all 6,309 videos using RELION 3.1's implementation of MotionCor2, and twice 'binned' to 1.137 Å per pixel[293–295]. CTFFIND-4.1 was used to estimate the contrast transfer function (CTF) parameters[296]. Micrographs were then manually sorted to eliminate subjectively bad micrographs, such as empty or contaminated holes, resulting in 3,611 good micrographs. Additionally, micrographs with a CTF maximum resolution lower than 4 Å were discarded, resulting in 2,595 remaining micrographs. Template-free auto-picking of particles was performed with RELION3.1's Laplacian-of-Gaussian filter yielding an initial set of particles. This initial set of particles were iteratively classified to generate templates, which were subsequently used to template-based auto-pick 1,750,730 particles.

Template-picked particles were iteratively two-dimensionally classified in RELION3.1 and then in cryoSPARC v.2[297], resulting in 820,543 particles. These particles were subsequently three-dimensionally classified in cryoSPARC v.2 with iterative ab initio and heterogeneous refinement jobs. The resulting maps were visually evaluated with regard to the transmembrane domain density. A set of 86,479 particles were identified, polished in RELION3.1 and refined in cryoSPARC v.2 with subsequent homogeneous and nonuniform refinement[298] jobs (maps were low-pass filtered to an initial resolution

where TM density was still visible (6–9 Å), and the dynamic mask was tightened with the near (2–5 Å) and far (3–9 Å) parameters), yielding a map with overall resolution of 3.6 Å. UCSF pyem tools were used to convert data from cryoSPARC to RELION format[299].

From this set of 86,479 particles, 2D classification was performed in RELION3.1 to identify a set of particles with subjectively equal view distribution. From the resulting set, 1,000 particles were randomly sampled and their coordinates used for training in the Topaz particle-picking pipeline[300]. Training, picking and extraction were performed independently on each subset of the micrographs. Then, 4,134,279 total particles were extracted in RELION3.1 with a box size of 256 pixels and 'binned' four times to 4.548 Å per pixel. These particles were then iteratively two-dimensionally classified in RELION3.1 resulting in 2,674,606 particles that were extracted at 2.274 Å per pixel. 2D classification was continued in both RELION3.1 and cryoSPARC v.2 resulting in 1,429,763 particles. Further classification was performed in cryoSPARC v.2 with subsequent ab initio (four classes, maximum resolution 8 Å) and heterogeneous refinement (8 Å initial resolution) jobs. The two best classes were selected and the particles pooled resulting in 743,800 particles, which were extracted in RELION3.1 at 1.137 Å per pixel.
Iterative three-dimensional (3D) classification was performed with subsequent ab initio and heterogeneous refinement jobs as described above. Following each round, 2D classification jobs were used to 'rescue' good particles from the worst classes before the next round. After three rounds, a final 2D classification job was used to identify 112,502 particles, which were subsequently pooled with the previous 86,479 RELION3.1 template-picked particles, resulting in 185,871 particles after duplicates (within 100 Å) were removed with RELION3.1.
These particles were then refined with subsequent homogeneous and nonuniform refinement jobs resulting in a map with overall resolution of 3.4 Å. This map was postprocessed in RELION3.1 using a mask with a soft edge (5-pixel extension, 7-pixel soft edge), the output of which was used for Bayesian particle polishing in RELION3.1 (training and polishing were each performed independently on each subset of the micrographs). The resulting 'shiny' particles were then refined in cryoSPARC v.2 with subsequent homogenous refinement (one extra pass, 7 Å initial resolution) and nonuniform refinement (C2, 1 extra pass, 9 Å initial resolution) to yield a map with 2.9-Å overall resolution.
For the 3a dimer with added 100 μM emodin, initial processing was similar to the dimer without the added drug . As with the apo 3a dimer, the critical steps included Topaz particle picking, particle clean-up with cryoSPARC v.2 ab initio and heterogeneous refinement, nonuniform refinement with tightened masking and RELION3.1 Bayesian particle polishing. However, in contrast to the apo dataset, we observed a set of particles that were included in <4-Å reconstructions that had discontinuous transmembrane domain density. Removal of these particles with RELION3.1 3D classification without angular sampling led to the best map from the emodin-added dataset. We did not see any evidence of bound emodin, but the 1% DMSO added with drug addition may have contributed to subtle map differences (Supplemental Fig. 5).
For the 3a tetramer, the initial 7,092 micrographs were first cleaned using manual inspection and removal of images with <4 Å CtfMaxResolution to obtain a set of 4,324 micrographs. Reference particles for Topaz particle picking were generated by first

template picking in RELION3.1, followed by 2D classification in both RELION3.1 and cryoSPARC v.2, and subsequent ab initio in cryoSPARC v.2. Particles from various views were then selected from iterative RELION3.1 2D classification to create a set of 6,843 particles. Using these coordinates for training, Topaz particle picking was then performed to generate a set of 1,282,913 initial particles. These particles were then cleaned using 2D classification in RELION3.1 and cryoSPARC v.2, followed by rounds of cryoSPARC v.2 ab initio and RELION3.1 3D classification. A major hurdle for tetramer processing was obtaining a reconstruction where most particles were properly oriented in the same direction (that is, intracellular domains on the same side of the nanodisc as seen in the 2D classes, Fig. 2f). Substantial, clean-up by 3D classification was needed to generate a correctly aligned reference map, but this map could then be used as a reference for refinements and classification for larger particle sets. Reconstructions with C1 or C2 symmetry looked similar (Supplemental Fig. 3e), although no tetramer reconstruction went to high enough resolution to determine symmetry with certainty. Therefore, it is possible that either the tetramer is pseudosymmetric or that different particles have heterogeneous orientations between dimer pairs. For the tetramer, the highest resolution reconstruction came from cryoSPARC v.2 nonuniform refinement with a tightened mask, which was subsequently used for dimer-docking and figure preparation.

For the apo 3a dimer imaged on a Krios with CFEG, Selectris X and Falcon 4, the EER video motion correction and subsequent polishing was performed in RELION3.1 using the devel-eer branch of Relion. Dose fractions consisting of 30 frames corresponding to 1.035 e^- /Å^2 per fraction were created. The initial 5,599 micrographs were pruned by selecting 4,495 micrographs with <3.5 Å CtfMaxResolution that also passed manual inspection. Similar to the Arctica datasets, an initial set of particles was generated with template-based picking and subsequent 2D classification, ab initio and heterogeneous refinement for clean-up was performed in cryoSPARC v.2. This particle set (44,944) was then used as training for the first round of Topaz particle picking. For initial particle clean-up, the most important step was heterogeneous refinement in cryoSPARC v.2, yielding a particle set (215,227) that gave a C2 nonuniform refinement at 2.69 Å. For final particle clean-up, using RELION3.1, polished particles were subjected to 3D classification with no angular sampling and high tau (40) during which we monitored the rounds of classification by looking for convergence in resolution and inspecting maps to check for quality of protein features or noise. This type of job reliably allowed us to select the best particles (61,531) for high-resolution reconstruction at 2.26 Å.

At this point, a second Topaz training and picking round was conducted using this set of particles. After merging the best particles from both rounds of Topaz picking, removing potential duplicate particles within a distance of 100 Å and subsequent processing, we obtained a set of particles (91,218) that achieved a nonuniform reconstruction at 2.17 Å. Finally, rounds of CtfRefine in cryoSPARC v.2 and a final nonuniform refinement (with higher-order CTF terms enabled) achieved a map with an estimated resolution of 2.1 Å. Depending on inputs into sharpening and local resolution jobs (Supplemental Fig. 6a), the map has regions that give resolution estimates below 2 Å, consistent with our observations of holes in aromatic side chain density.

We note that the merging of two Topaz picked particle sets likely allowed us to break a particle-limited barrier to achieve the final reconstruction based on ResLog[301] analysis performed in cryoSPARC (Supplemental Fig. 6c). Finally, we sampled various box sizes

during processing (as large as 416 pixels and as small as 256 pixels)[302]. The best reconstructions were consistently achieved with our final box size of 300 pixels (218.1 Å).

Modeling, refinement and analysis

Apo dimeric 3a cryo-EM maps were sharpened using cryoSPARC and were of sufficient quality for de novo model building in Coot[303]. Real space refinement of the models was carried out using Phenix.real_space_refine[304]. Molprobity[305] was used to evaluate the stereochemistry and geometry of the structure for subsequent rounds of manual adjustment in Coot and refinement in Phenix. For final sharpening and visualization of the high-resolution map we used Phenix Resolve Density Modification[306]. Docking of the apo dimeric 3a into the tetrameric 3a cryo-EM map was performed in Phenix using a map in which large empty regions of the nanodisc were erased in Chimera[307]. Similar results were found using maps with only the CDs present. Cavity measurements were made with HOLE[308] implemented in Coot. Comparisons to the structure database was performed with DALI[261]. Structure prediction was performed with Phyre2[309]. Figures were prepared using PyMOL, Chimera, ChimeraX[310], Fiji, Prism 8, GNU Image Manipulation Program and Adobe Photoshop and Illustrator software.

Fluorescence size-exclusion chromatography

Sf9 cells (roughly 4 million) from the third day of infection were pelleted, frozen and then thawed into extraction buffer (20 mM Tris pH 8, 150 mM KCl, all protease inhibitors used for protein purification, 1 mM EDTA, 1% DDM). Extraction was performed at 4 °C for 1 h and lysate was then pelleted at 21,000*g* at 4 °C for 1 h to clear supernatant. Supernatant was then run on a Superose 6 Increase column with fluorescence detection for GFP into 20 mM HEPES pH 7.4, 150 mM KCl and 0.025% DDM.

Transfection for confocal imaging

The constructs for full length 3a and 3aΔN were cloned into a vector with a CMV-promoter and C-terminal enhanced green fluorescent protein. Constructs (2 μg) were transfected into human embryonic kidney 293 cells on glass coverslips using Fugene HD (Promega) per the manufacturer's instructions. Two days after transfection, cells were washed with DPBS and then fixed in 4% formaldehyde in DPBS for 10 min. Cells were then washed with DPBS before mounting the coverslip with Prolong Glass Antifade with NucBlue (Thermo Fisher Scientific) per the manufacturer's instructions. Fluorescent images were collected using a Zeiss LSM 880 NLO AxioExaminer confocal microscope at either ×20 (numerical aperture 1.0) or ×63 oil immersion objective (numerical aperture 1.4). The samples were excited with 488 nm argon laser and we carried out image analysis using ImageJ (v.1.53a).

Conclusion

Life is full of danger. Accordingly, nociceptors have evolved to detect a remarkable array of stimuli, reflecting a tremendous evolutionary pressure (i.e. survival) to protect the organism from a similarly diverse array of threats. Their free nerve endings tile most of our skin and viscera, embedded among the epithelial cells at barrier surfaces like the airways. Despite their critical role in health and disease, the mechanisms of when and how nociceptors are activated remain incompletely understood.

In this dissertation, I describe two nociceptive epithelial-neuronal signaling axes: one in the context of mechanical force and the other during viral infection. Though both epithelial cells and sensory neurons can be activated by the same stimuli, be it stretch or the viral protease PLpro, these cells rely on distinct signaling pathways and operate on different timescales, with neurons responding much more rapidly. This principle has been first and elegantly described by the Merkel cell–neurite complex, where both Merkel cells and sensory neurons express Piezo2 and together enable the spatial and temporal precision of our sense of touch[27]. My findings demonstrate that this principle of epithelial and neuronal coordination extends beyond touch to other sensory modalities, including mechanonociception and the response to viral infection.

Given the diversity and heterogeneity of nociceptors themselves, and the added complexity introduced by signals from epithelial and other surrounding cells, much about nociceptor biology remains unresolved. Historically (albeit here I refer to a rather short history, marked by the advent of genetic tools in mice), the field has become reliant on ablation studies to infer nociceptor function. But the loss of such a heterogeneous and plastic cellular population leaves us with more questions than answers (perhaps, for the better). Some of the field's contradictory findings may reflect this underlying diversity, as different nociceptor subsets likely exert distinct, even opposing, effects depending on the physiological or pathological context. How nociceptors modulate physiology depends not only on which neurons are activated, but also on how they are activated, and to whom they signal, both peripherally and centrally. This diversity allows for highly context-specific signaling, and moving forward, mechanistic studies that carefully probe the timing, integration, and outputs of nociceptor activation will be essential for understanding the principles of nociceptor function.

Equally important is expanding how we think about nociceptive outputs, which are diverse, dynamic, and often multi-component. While pain-associated withdrawal and itch behaviors are the most studied, nocifensive responses vary significantly across species, tissues, and contexts. Recent work, including my own, has shown that even well-established behaviors, like Drosophila larval escape, contain layers of surprising cellular complexity. As the field of nociception moves beyond the skin, studies that carefully quantify and characterize these complex outputs will be key to uncovering principles of nociceptive encoding across tissues and organisms. In the airways, for example, nociceptive reflexes like sneezing and coughing remain poorly characterized. Readouts vary widely between labs, and in mice, there are no standardized definitions or respiratory waveforms for these responses. Advances in high-resolution, multidimensional

behavioral analysis (such as including measures of movement, facial features, vocalization, and plethysmography) will be critical for decoding airway reflexes with the same precision now being applied to somatic nociceptive behaviors.

Nonetheless, efforts to study sneeze and cough in mice, however imperfect, paved the way for uncovering the biology that underlies an observation public health has long understood: sneezes and coughs spread disease. The discovery that viruses, like SARS-CoV-2, target the nervous system to drive these reflexes offers a molecular basis for a century of epidemiological intuition, and reinforces the value of interventions like masking and ventilation as some of our most effective tools to curb viral spread. And yet, the rejection of these strategies, fueled by xenophobia, misinformation, and political failure, has burdened our society with an ongoing pandemic whose consequences we will bear for the rest of our lives. Pandemic preparedness is not a scientific challenge. It is a political, ethical, and global one. What use is understanding how viruses spread, if that knowledge does not compel serious and sustained efforts to implement protections, ones that are accessible to everyone, not just the wealthy or the countries enriched by imperial conquest?

And so, this search for biological mechanisms–of airway physiology, of disease transmission, of host defense–feels like one driven by my own hubris or desperation, or maybe both. Because no mechanism, however rigorous or elegant, can alone protect us from the present threats to airway health: the compounding effects of climate change, war, economic inequality, and systemic injustice. As the science in this thesis unfolded, so did the series of events that endow this very science and its scientist. What does it mean to study the biology of breathing while a virus surged through our world, armed police deployed military-grade tear gas on protestors demanding racial justice, wildfires blistered our state of California, and this country's tax dollars simultaneously funded my PhD and the bombs dropped on Gaza? The irony feels impossible to ignore; each of these crises filled our lungs with TRPA1 agonists, molecular signals of danger that our biology has evolved to detect and defend against. A mechanism we share not just with each other, but with nearly the entire animal kingdom. But then, why do we permit injustice to override the very biology that urges us to protect ourselves and one another?

As I look toward future directions, questions about the moral stakes, responsibilities, and obligations of scientific knowledge feel more urgent than those that might define the next frontier of biology. To keep repressing them, especially now, feels irresponsible, and even unscholarly.

I conclude this scholarship with the admission that neither hubris nor despair can inspire the curiosity or sustain the resilience discovery demands. What can, and what has, is an achingly deep hope that science, in its pursuit of truth, in its demand for humility, and in its commitment to integrity, can guide us toward justice.

References

1. Tobin, D. M. & Bargmann, C. I. Invertebrate nociception: Behaviors, neurons and molecules. *J. Neurobiol.* **61**, 161–174 (2004).
2. Basbaum, A. I., Bautista, D. M., Scherrer, G. & Julius, D. Cellular and Molecular Mechanisms of Pain. *Cell* **139**, 267–284 (2009).
3. Taylor-Clark, T. & Undem, B. J. Transduction mechanisms in airway sensory nerves. *J. Appl. Physiol.* **101**, 950–959 (2006).
4. Boivin, J.-C., Zhu, J. & Ohyama, T. Nociception in fruit fly larvae. *Front. Pain Res.* **4**, (2023).
5. Hwang, R. Y. *et al.* Nociceptive neurons protect Drosophila larvae from parasitoid wasps. *Curr Biol* **17**, 2105–2116 (2007).
6. Hu, C. Sensory integration and neuromodulatory feedback facilitate Drosophila mechanonociceptive behavior. *Nat Neurosci* **20**, 1085–1095 (2017).
7. Burgos, A. *et al.* Nociceptive interneurons control modular motor pathways to promote escape behavior in Drosophila. *eLife* **7**, e26016 (2018).
8. Tracey, W. D., Wilson, R. I., Laurent, G. & Benzer, S. painless, a Drosophila Gene Essential for Nociception. *Cell* **113**, 261–273 (2003).
9. Hamada, F. N. *et al.* An internal thermal sensor controlling temperature preference in Drosophila. *Nature* **454**, 217–220 (2008).
10. Kang, K. *et al.* Analysis of Drosophila TRPA1 reveals an ancient origin for human chemical nociception. *Nature* **464**, 597–600 (2010).
11. Hu, C. *et al.* Sensory integration and neuromodulatory feedback facilitate Drosophila mechanonociceptive behavior. *Nat. Neurosci.* **20**, 1085–1095 (2017).
12. Pan, G. *et al.* Cross-modal modulation gates nociceptive inputs in *Drosophila*. *Curr. Biol.* **33**, 1372-1380.e4 (2023).
13. Koch, S. C., Acton, D. & Goulding, M. Spinal Circuits for Touch, Pain, and Itch. *Annu. Rev. Physiol.* **80**, 189–217 (2018).
14. Cheng, L. *et al.* Identification of spinal circuits involved in touch-evoked dynamic mechanical pain. *Nat. Neurosci.* **20**, 804–814 (2017).
15. Undem, B. J. *et al.* Subtypes of vagal afferent C-fibres in guinea-pig lungs. *J. Physiol.* **556**, 905–917 (2004).
16. Canning, B. J. *et al.* Identification of the tracheal and laryngeal afferent neurones mediating cough in anaesthetized guinea-pigs. *J. Physiol.* **557**, 543–558 (2004).
17. Andrè, E. *et al.* Transient receptor potential ankyrin receptor 1 is a novel target for pro-tussive agents. *Br. J. Pharmacol.* **158**, 1621–1628 (2009).
18. Birrell, M. A. *et al.* TRPA1 Agonists Evoke Coughing in Guinea Pig and Human Volunteers. *Am. J. Respir. Crit. Care Med.* **180**, 1042–1047 (2009).
19. Brozmanova, M., Mazurova, L., Ru, F., Tatar, M. & Kollarik, M. Comparison of TRPA1-versus TRPV1-mediated cough in guinea pigs. *Eur. J. Pharmacol.* **689**, 211–218 (2012).
20. Zhang, C., Lin, R.-L., Hong, J., Khosravi, M. & Lee, L.-Y. Cough and expiration reflexes elicited by inhaled irritant gases are intensified in ovalbumin-sensitized mice. *Am. J. Physiol. Regul. Integr. Comp. Physiol.* **312**, 718–726 (2017).
21. Li, F. *et al.* Sneezing reflex is mediated by a peptidergic pathway from nose to brainstem. *Cell* **184**, 3762-3773 10 (2021).

22. Jiang, H. *et al.* Divergent sensory pathways of sneezing and coughing. *Cell* **187**, 5981-5997 14 (2024).
23. Gannot, N. *et al.* A vagal–brainstem interoceptive circuit for cough-like defensive behaviors in mice. *Nat. Neurosci.* **1–11**, (2024).
24. Mali, S. S. *et al.* SARS-CoV-2 papain-like protease activates nociceptors to drive sneeze and pain. 2024.01.10.575114 Preprint at https://doi.org/10.1101/2024.01.10.575114 (2024).
25. Seeholzer, L. F. & Julius, D. Neuroendocrine cells initiate protective upper airway reflexes. *Science* **384**, 295–301 (2024).
26. Prescott, S. L., Umans, B. D., Williams, E. K., Brust, R. D. & Liberles, S. D. An Airway Protection Program Revealed by Sweeping Genetic Control of Vagal Afferents. *Cell* **181**, 574-589.e14 (2020).
27. Maksimovic, S. Epidermal Merkel cells are mechanosensory cells that tune mammalian touch receptors. *Nature* **509**, 617–621 (2014).
28. Hoffman, B. U. *et al.* Merkel Cells Activate Sensory Neural Pathways through Adrenergic Synapses. *Neuron* **100**, 1401-1413.e6 (2018).
29. Woo, S.-H. *et al.* Piezo2 is required for Merkel-cell mechanotransduction. *Nature* **509**, 622–626 (2014).
30. Baumbauer, K. M. *et al.* Keratinocytes can modulate and directly initiate nociceptive responses. *eLife* **4**, e09674 (2015).
31. Moehring, F. *et al.* Keratinocytes mediate innocuous and noxious touch via ATP-P2X4 signaling. *Elife* **7**, (2018).
32. Mikesell, A. R. *et al.* Keratinocyte PIEZO1 modulates cutaneous mechanosensation. *eLife* **11**, e65987 (2022).
33. Yoshino, J. *et al.* Drosophila epidermal cells are intrinsically mechanosensitive and modulate nociceptive behavioral outputs. *eLife* **13**, (2025).
34. Chung, M.-K., Lee, H., Mizuno, A., Suzuki, M. & Caterina, M. J. TRPV3 and TRPV4 mediate warmth-evoked currents in primary mouse keratinocytes. *J Biol Chem* **279**, 21569–21575 (2004).
35. Sadler, K. E., Moehring, F. & Stucky, C. L. Keratinocytes contribute to normal cold and heat sensation. *Elife* **9**, 58625 (2020).
36. Wilson, S. R. *et al.* The epithelial cell-derived atopic dermatitis cytokine TSLP activates neurons to induce itch. *Cell* **155**, 285–295 (2013).
37. Bellono, N. W. *et al.* Enterochromaffin Cells Are Gut Chemosensors that Couple to Sensory Neural Pathways. *Cell* **170**, 185-198.e16 (2017).
38. Cole, E. C. & Cook, C. E. Characterization of infectious aerosols in health care facilities: An aid to effective engineering controls and preventive strategies. *Am. J. Infect. Control* **26**, 453–464 (1998).
39. Bessac, B. F. & Jordt, S.-E. Breathtaking TRP Channels: TRPA1 and TRPV1 in Airway Chemosensation and Reflex Control. *Physiology* **23**, 360–370 (2008).
40. Bessac, B. F. *et al.* Transient receptor potential ankyrin 1 antagonists block the noxious effects of toxic industrial isocyanates and tear gases. *FASEB J.* **23**, 1102–1114 (2009).
41. Bautista, D. M. *et al.* TRPA1 mediates the inflammatory actions of environmental irritants and proalgesic agents. *Cell* **124**, 1269–1282 (2006).

42. Bessac, B. F. *et al.* TRPA1 is a major oxidant sensor in murine airway sensory neurons. *J. Clin. Invest.* **118**, 1899–1910 (2008).
43. Macpherson, L. J. *et al.* An Ion Channel Essential for Sensing Chemical Damage. *J. Neurosci.* **27**, 11412–11415 (2007).
44. Andersson, D. A., Gentry, C., Moss, S. & Bevan, S. Transient Receptor Potential A1 Is a Sensory Receptor for Multiple Products of Oxidative Stress. *J. Neurosci.* **28**, 2485–2494 (2008).
45. Caceres, A. I. *et al.* A sensory neuronal ion channel essential for airway inflammation and hyperreactivity in asthma. *Proc. Natl. Acad. Sci.* **106**, 9099–9104 (2009).
46. Grace, M. S. & Belvisi, M. G. TRPA1 receptors in cough. *Pulm. Pharmacol. Ther.* **24**, 286–288 (2011).
47. Hill, R. Z., Morita, T., Brem, R. B. & Bautista, D. M. S1PR3 Mediates Itch and Pain via Distinct TRP Channel-Dependent Pathways. *J. Neurosci. Off. J. Soc. Neurosci.* **38**, 7833–7843 (2018).
48. Patil, M. J., Meeker, S., Bautista, D., Dong, X. & Undem, B. J. Sphingosine-1-phosphate activates mouse vagal airway afferent C-fibres via S1PR3 receptors. *J. Physiol.* **597**, 2007–2019 (2019).
49. Tränkner, D., Hahne, N., Sugino, K., Hoon, M. A. & Zuker, C. Population of sensory neurons essential for asthmatic hyperreactivity of inflamed airways. *Proc. Natl. Acad. Sci.* **111**, 11515–11520 (2014).
50. Imamachi, N. *et al.* TRPV1-expressing primary afferents generate behavioral responses to pruritogens via multiple mechanisms. *Proc. Natl. Acad. Sci.* **106**, 11330–11335 (2009).
51. Nassenstein, C. *et al.* Phenotypic distinctions between neural crest and placodal derived vagal C-fibres in mouse lungs. *J. Physiol.* **588**, 4769–4783 (2010).
52. Widdicombe, J. G. Reflexes from the Upper Respiratory Tract. in *Comprehensive Physiology* 363–394 (John Wiley & Sons, Ltd, 1986). doi:10.1002/cphy.cp030211.
53. Liu, Q. *et al.* The Distinct Roles of Two GPCRs, MrgprC11 and PAR2, in Itch and Hyperalgesia. *Sci. Signal.* **4**, ra45–ra45 (2011).
54. Wilson, S. R. *et al.* TRPA1 is required for histamine-independent, Mas-related G protein–coupled receptor–mediated itch. *Nat. Neurosci.* **14**, 595–602 (2011).
55. Mosimann, B. *et al.* Substance P, calcitonin gene-related peptide, and vasoactive intestinal peptide increase in nasal secretions after allergen challenge in atopic patients. *J. Allergy Clin. Immunol.* **92**, 95–104 (1993).
56. Baraniuk, J. N. *et al.* Vasoactive intestinal peptide in human nasal mucosa. *J. Clin. Invest.* **86**, 825–831 (1990).
57. Saunders, C. J., Christensen, M., Finger, T. E. & Tizzano, M. Cholinergic neurotransmission links solitary chemosensory cells to nasal inflammation. *Proc. Natl. Acad. Sci.* **111**, 6075–6080 (2014).
58. Devillier, P. *et al.* Nasal response to substance P and methacholine in subjects with and without allergic rhinitis. *Eur. Respir. J.* **1**, 356–361 (1988).
59. Sarin, S., Undem, B., Sanico, A. & Togias, A. The role of the nervous system in rhinitis. *J. Allergy Clin. Immunol.* **118**, 999–1014 (2006).
60. Ndjim, M. *et al.* Tuft cell acetylcholine is released into the gut lumen to promote anti-helminth immunity. *Immunity* **57**, 1260-1273.e7 (2024).

61. Billipp, T. E. *et al.* Tuft cell-derived acetylcholine promotes epithelial chloride secretion and intestinal helminth clearance. *Immunity* **57**, 1243-1259.e8 (2024).
62. Mazzone, S. B. & Undem, B. J. Vagal Afferent Innervation of the Airways in Health and Disease. *Physiol. Rev.* **96**, 975–1024 (2016).
63. Liu, Y., Arce, A. J. D. de & Krasnow, M. A. Molecular, anatomical, and functional organization of lung interoceptors. 2021.11.10.468116 Preprint at https://doi.org/10.1101/2021.11.10.468116 (2021).
64. Su, Y. *et al.* Identification of lung innervating sensory neurons and their target specificity. *Am. J. Physiol. - Lung Cell. Mol. Physiol.* **322**, L50–L63 (2022).
65. Kim, S.-H. *et al.* Mapping of the Sensory Innervation of the Mouse Lung by Specific Vagal and Dorsal Root Ganglion Neuronal Subsets. *eNeuro* **9**, (2022).
66. Han, C., Zhu, X. & Sokol, C. L. Neuroimmune Circuits in Allergic Diseases. (2025) doi:10.1146/annurev-immunol-082423-032154.
67. Hanč, P., Messou, M.-A., Ajit, J. & von Andrian, U. H. Setting the tone: nociceptors as conductors of immune responses. *Trends Immunol.* **45**, 783–798 (2024).
68. Xing, Y. *et al.* MrgprC11+ Jugular Neurons Control Airway Hyperresponsiveness in Allergic Airway Inflammation. *Am. J. Respir. Cell Mol. Biol.* **72**, 393–407 (2025).
69. Han, L. *et al.* Mrgprs on vagal sensory neurons contribute to bronchoconstriction and airway hyper-responsiveness. *Nat. Neurosci.* **21**, 324–328 (2018).
70. Su, Y. *et al.* Brainstem Dbh+ neurons control allergen-induced airway hyperreactivity. *Nature* **631**, 601–609 (2024).
71. Talbot, S. *et al.* Silencing Nociceptor Neurons Reduces Allergic Airway Inflammation. *Neuron* **87**, 341–354 (2015).
72. Tamari, M. *et al.* Sensory neurons promote immune homeostasis in the lung. *Cell* **187**, 44-61.e17 (2024).
73. Cook, A. D., Christensen, A. D., Tewari, D., McMahon, S. B. & Hamilton, J. A. Immune Cytokines and Their Receptors in Inflammatory Pain. *Trends Immunol.* **39**, 240–255 (2018).
74. Baral, P., Udit, S. & Chiu, I. M. Pain and immunity: implications for host defence. *Nat. Rev. Immunol.* **19**, 433–447 (2019).
75. Jin, X. & Gereau, R. W. Acute p38-Mediated Modulation of Tetrodotoxin-Resistant Sodium Channels in Mouse Sensory Neurons by Tumor Necrosis Factor-α. *J. Neurosci.* **26**, 246–255 (2006).
76. Binshtok, A. M. *et al.* Nociceptors Are Interleukin-1β Sensors. *J. Neurosci.* **28**, 14062–14073 (2008).
77. Cesare, P. & McNaughton, P. A novel heat-activated current in nociceptive neurons and its sensitization by bradykinin. *Proc. Natl. Acad. Sci.* **93**, 15435–15439 (1996).
78. Pitchford, S. & Levine, J. D. Prostaglandins sensitize nociceptors in cell culture. *Neurosci. Lett.* **132**, 105–108 (1991).
79. Bin, N.-R. *et al.* An airway-to-brain sensory pathway mediates influenza-induced sickness. *Nature* **615**, 660–667 (2023).
80. Barragán-Iglesias, P. *et al.* Type I Interferons Act Directly on Nociceptors to Produce Pain Sensitization: Implications for Viral Infection-Induced Pain. *J. Neurosci. Off. J. Soc. Neurosci.* **40**, 3517–3532 (2020).

81. Mazzone, S. B. *et al.* Modulation of Vagal Sensory Neurons via High Mobility Group Box-1 and Receptor for Advanced Glycation End Products: Implications for Respiratory Viral Infections. *Front. Physiol.* **12**, (2021).
82. Allette, Y. M. *et al.* Identification of a functional interaction of HMGB1 with Receptor for Advanced Glycation End-products in a model of neuropathic pain. *Brain. Behav. Immun.* **42**, 169–177 (2014).
83. Gomez, K. *et al.* Neuropilin-1 is essential for vascular endothelial growth factor A–mediated increase of sensory neuron activity and development of pain-like behaviors. *PAIN* **164**, 2696 (2023).
84. Gilden, D. H., Mahalingam, R., Cohrs, R. J. & Tyler, K. L. Herpesvirus infections of the nervous system. *Nat. Clin. Pract. Neurol.* **3**, 82–94 (2007).
85. Yang, L. *et al.* Human and mouse trigeminal ganglia cell atlas implicates multiple cell types in migraine. *Neuron* **110**, 1806-1821.e8 (2022).
86. Meinhardt, J. *et al.* Olfactory transmucosal SARS-CoV-2 invasion as a port of central nervous system entry in individuals with COVID-19. *Nat. Neurosci.* (2020) doi:10.1038/s41593-020-00758-5.
87. Joyce, J. D. *et al.* SARS-CoV-2 rapidly infects peripheral sensory and autonomic neurons, contributing to central nervous system neuroinvasion before viremia. *Int. J. Mol. Sci.* **25**, 8245 (2024).
88. Perlman, S., Jacobsen, G. & Afifi, A. Spread of a neurotropic murine coronavirus into the CNS via the trigeminal and olfactory nerves. *Virology* **170**, 556–560 (1989).
89. Li, X., Fu, Z. F., Alvarez, R., Henderson, C. & Tripp, R. A. Respiratory Syncytial Virus (RSV) Infects Neuronal Cells and Processes That Innervate the Lung by a Process Involving RSV G Protein. *J. Virol.* **80**, 537–540 (2006).
90. Serafini, R. A. *et al.* SARS-CoV-2 airway infection results in the development of somatosensory abnormalities in a hamster model. *Sci. Signal.* **16**, eade4984 (2023).
91. Kern, D. M. *et al.* Cryo-EM structure of SARS-CoV-2 ORF3a in lipid nanodiscs. *Nat. Struct. Mol. Biol.* **28**, 573–582 (2021).
92. Granton, E. *et al.* Biofilm exopolysaccharides alter sensory-neuron-mediated sickness during lung infection. *Cell* **187**, 1874-1888.e14 (2024).
93. Diogenes, A., Ferraz, C. C. R., Akopian, A. N., Henry, M. A. & Hargreaves, K. M. LPS sensitizes TRPV1 via activation of TLR4 in trigeminal sensory neurons. *J. Dent. Res.* **90**, 759–764 (2011).
94. Meseguer, V. *et al.* TRPA1 channels mediate acute neurogenic inflammation and pain produced by bacterial endotoxins. *Nat. Commun.* **5**, 3125 (2014).
95. Chiu, I. M. *et al.* Bacteria activate sensory neurons that modulate pain and inflammation. *Nature* **501**, 52–57 (2013).
96. Pinho-Ribeiro, F. A. *et al.* Blocking Neuronal Signaling to Immune Cells Treats Streptococcal Invasive Infection. *Cell* **173**, 1083-1097.e22 (2018).
97. Staurengo-Ferrari, L., Deng, L. & Chiu, I. M. Interactions between nociceptor sensory neurons and microbial pathogens in pain. *PAIN* **163**, S57 (2022).
98. Liu, T. *et al.* TLR3 deficiency impairs spinal cord synaptic transmission, central sensitization, and pruritus in mice. *J. Clin. Invest.* **122**, 2195–2207 (2012).
99. Kim, J. S., Ru, F., Meeker, S. & Undem, B. J. Direct activation of airway sensory C-fibers by SARS-CoV-2 S1 spike protein. *Physiol. Rep.* **11**, e15900 (2023).

100. Maruyama, K. *et al.* Nociceptors Boost the Resolution of Fungal Osteoinflammation via the TRP Channel-CGRP-Jdp2 Axis. *Cell Rep.* **19**, 2730–2742 (2017).
101. Kashem, S. W. *et al.* Nociceptive Sensory Fibers Drive Interleukin-23 Production from CD301b+ Dermal Dendritic Cells and Drive Protective Cutaneous Immunity. *Immunity* **43**, 515–526 (2015).
102. Ruhl, C. R. *et al.* Mycobacterium tuberculosis Sulfolipid-1 Activates Nociceptive Neurons and Induces Cough. *Cell* **181**, 293-305.e11 (2020).
103. Biofilm exopolysaccharides alter sensory-neuron-mediated sickness during lung infection: Cell. https://www-cell-com.libproxy.berkeley.edu/cell/fulltext/S0092-8674(24)00249-6?_returnURL=https%3A%2F%2Flinkinghub.elsevier.com%2Fretrieve%2Fpii%2FS0092867424002496%3Fshowall%3Dtrue#fig1.
104. Zheng, Q., Dong, X., Green, D. P. & Dong, X. Peripheral mechanisms of chronic pain. *Med. Rev.* **2**, 251–270 (2022).
105. Walsh, C. M. *et al.* Neutrophils promote CXCR3-dependent itch in the development of atopic dermatitis. *eLife* **8**, e48448 (2019).
106. Kuner, R. & Flor, H. Structural plasticity and reorganisation in chronic pain. *Nat. Rev. Neurosci.* **18**, 20–30 (2017).
107. Klein, J. *et al.* Distinguishing features of long COVID identified through immune profiling. *Nature* **623**, 139–148 (2023).
108. Sudre, C. H. *et al.* Attributes and predictors of long COVID. *Nat. Med.* **27**, 626–631 (2021).
109. Baral, P. *et al.* Nociceptor sensory neurons suppress neutrophil and γδ T cell responses in bacterial lung infections and lethal pneumonia. *Nat. Med.* **24**, 417–426 (2018).
110. Joshi, P. R. *et al.* Lung-innervating nociceptor sensory neurons promote pneumonic sepsis during carbapenem-resistant Klebsiella pneumoniae lung infection. *Sci. Adv.* **10**, eadl6162 (2024).
111. Aguilar, D. *et al.* Sensory neurons regulate stimulus-dependent humoral immunity in mouse models of bacterial infection and asthma. *Nat. Commun.* **15**, 8914 (2024).
112. Verzele, N. A. J. *et al.* Evidence for vagal sensory neural involvement in influenza pathogenesis and disease. *PLOS Pathog.* **20**, e1011635 (2024).
113. Yang, D. *et al.* Vagal TRPV1+ sensory neurons regulate myeloid cell dynamics and protect against influenza virus infection. 2024.08.21.609013 Preprint at https://doi.org/10.1101/2024.08.21.609013 (2024).
114. Hwang, R. Y. *et al.* Nociceptive neurons protect Drosophila larvae from parasitoid wasps. *Curr. Biol. CB* **17**, 2105–2116 (2007).
115. Hu, C. *et al.* Sensory integration and neuromodulatory feedback facilitate Drosophila mechanonociceptive behavior. *Nat. Neurosci.* **20**, 1085–1095 (2017).
116. Burgos, A. *et al.* Nociceptive interneurons control modular motor pathways to promote escape behavior in Drosophila. *eLife* **7**, (2018).
117. Babcock, D. T., Landry, C. & Galko, M. J. Cytokine signaling mediates UV-induced nociceptive sensitization in Drosophila larvae. *Curr. Biol. CB* **19**, 799–806 (2009).
118. Boiko, N. *et al.* TrpA1 activation in peripheral sensory neurons underlies the ionic basis of pain hypersensitivity in response to vinca alkaloids. *PloS One* **12**, e0186888 (2017).

119. Maksimovic, S. *et al.* Epidermal Merkel cells are mechanosensory cells that tune mammalian touch receptors. *Nature* **509**, 617–621 (2014).
120. Chung, M.-K., Lee, H., Mizuno, A., Suzuki, M. & Caterina, M. J. TRPV3 and TRPV4 mediate warmth-evoked currents in primary mouse keratinocytes. *J. Biol. Chem.* **279**, 21569–21575 (2004).
121. Koizumi, S. *et al.* Ca2+ waves in keratinocytes are transmitted to sensory neurons: the involvement of extracellular ATP and P2Y2 receptor activation. *Biochem. J.* **380**, 329–338 (2004).
122. Moqrich, A. *et al.* Impaired thermosensation in mice lacking TRPV3, a heat and camphor sensor in the skin. *Science* **307**, 1468–1472 (2005).
123. Mandadi, S. *et al.* TRPV3 in keratinocytes transmits temperature information to sensory neurons via ATP. *Pflugers Arch.* **458**, 1093–1102 (2009).
124. Liu, X. *et al.* STIM1 thermosensitivity defines the optimal preference temperature for warm sensation in mice. *Cell Res.* **29**, 95–109 (2019).
125. Sadler, K. E., Moehring, F. & Stucky, C. L. Keratinocytes contribute to normal cold and heat sensation. *eLife* **9**, e58625 (2020).
126. Cauna, N. The free penicillate nerve endings of the human hairy skin. *J. Anat.* **115**, 277–288 (1973).
127. Chalfie, M. & Sulston, J. Developmental genetics of the mechanosensory neurons of Caenorhabditis elegans. *Dev. Biol.* **82**, 358–370 (1981).
128. Han, C. *et al.* Integrins regulate repulsion-mediated dendritic patterning of drosophila sensory neurons by restricting dendrites in a 2D space. *Neuron* **73**, 64–78 (2012).
129. Kim, M. E., Shrestha, B. R., Blazeski, R., Mason, C. A. & Grueber, W. B. Integrins establish dendrite-substrate relationships that promote dendritic self-avoidance and patterning in drosophila sensory neurons. *Neuron* **73**, 79–91 (2012).
130. O'Brien, G. S. *et al.* Coordinate development of skin cells and cutaneous sensory axons in zebrafish. *J. Comp. Neurol.* **520**, 816–831 (2012).
131. Jiang, N. *et al.* A conserved morphogenetic mechanism for epidermal ensheathment of nociceptive sensory neurites. *eLife* **8**, (2019).
132. Yin, C., Peterman, E., Rasmussen, J. P. & Parrish, J. Z. Transparent Touch: Insights From Model Systems on Epidermal Control of Somatosensory Innervation. *Front. Cell. Neurosci.* **15**, 680345 (2021).
133. Klapoetke, N. C. *et al.* Independent optical excitation of distinct neural populations. *Nat. Methods* **11**, 338–346 (2014).
134. Zimmermann, G. *et al.* Manipulation of an innate escape response in Drosophila: photoexcitation of acj6 neurons induces the escape response. *PloS One* **4**, e5100 (2009).
135. Galko, M. J. & Krasnow, M. A. Cellular and genetic analysis of wound healing in Drosophila larvae. *PLoS Biol.* **2**, E239 (2004).
136. Hamada, F. N. *et al.* An internal thermal sensor controlling temperature preference in Drosophila. *Nature* **454**, 217–220 (2008).
137. Robertson, J. L., Tsubouchi, A. & Tracey, W. D. Larval defense against attack from parasitoid wasps requires nociceptive neurons. *PloS One* **8**, e78704 (2013).

138. Zhang, W., Yan, Z., Jan, L. Y. & Jan, Y. N. Sound response mediated by the TRP channels NOMPC, NANCHUNG, and INACTIVE in chordotonal organs of Drosophila larvae. *Proc. Natl. Acad. Sci. U. S. A.* **110**, 13612–13617 (2013).
139. Turner, H. N. *et al.* The TRP Channels Pkd2, NompC, and Trpm Act in Cold-Sensing Neurons to Mediate Unique Aversive Behaviors to Noxious Cold in Drosophila. *Curr. Biol. CB* **26**, 3116–3128 (2016).
140. Sweeney, S. T., Broadie, K., Keane, J., Niemann, H. & O'Kane, C. J. Targeted expression of tetanus toxin light chain in Drosophila specifically eliminates synaptic transmission and causes behavioral defects. *Neuron* **14**, 341–351 (1995).
141. Ohyama, T. *et al.* A multilevel multimodal circuit enhances action selection in Drosophila. *Nature* **520**, 633–639 (2015).
142. Haeberle, H., Bryan, L. A., Vadakkan, T. J., Dickinson, M. E. & Lumpkin, E. A. Swelling-activated Ca2+ channels trigger Ca2+ signals in Merkel cells. *PloS One* **3**, e1750 (2008).
143. Tsutsumi, M. *et al.* Mechanical-stimulation-evoked calcium waves in proliferating and differentiated human keratinocytes. *Cell Tissue Res.* **338**, 99–106 (2009).
144. Ranade, S. S. *et al.* Piezo2 is the major transducer of mechanical forces for touch sensation in mice. *Nature* **516**, 121–125 (2014).
145. Woo, S.-H. *et al.* Piezo2 is required for Merkel-cell mechanotransduction. *Nature* **509**, 622–626 (2014).
146. Moehring, F. *et al.* Keratinocytes mediate innocuous and noxious touch via ATP-P2X4 signaling. *eLife* **7**, (2018).
147. Feske, S. *et al.* A mutation in Orai1 causes immune deficiency by abrogating CRAC channel function. *Nature* **441**, 179–185 (2006).
148. Fink, M. *et al.* Cloning, functional expression and brain localization of a novel unconventional outward rectifier K+ channel. *EMBO J.* **15**, 6854–6862 (1996).
149. Hoover, P. J. & Lewis, R. S. Stoichiometric requirements for trapping and gating of Ca2+ release-activated Ca2+ (CRAC) channels by stromal interaction molecule 1 (STIM1). *Proc. Natl. Acad. Sci. U. S. A.* **108**, 13299–13304 (2011).
150. Mohammad, F. *et al.* Optogenetic inhibition of behavior with anion channelrhodopsins. *Nat. Methods* **14**, 271–274 (2017).
151. Pores-Fernando, A. T. & Zweifach, A. Calcium influx and signaling in cytotoxic T-lymphocyte lytic granule exocytosis. *Immunol. Rev.* **231**, 160–173 (2009).
152. Ashmole, I. *et al.* CRACM/Orai ion channel expression and function in human lung mast cells. *J. Allergy Clin. Immunol.* **129**, 1628-1635.e2 (2012).
153. Maneshi, M. M. *et al.* Orai1 Channels Are Essential for Amplification of Glutamate-Evoked Ca2+ Signals in Dendritic Spines to Regulate Working and Associative Memory. *Cell Rep.* **33**, 108464 (2020).
154. Chanaday, N. L. *et al.* Presynaptic store-operated Ca2+ entry drives excitatory spontaneous neurotransmission and augments endoplasmic reticulum stress. *Neuron* **109**, 1314-1332.e5 (2021).
155. Ramesh, G. *et al.* A short isoform of STIM1 confers frequency-dependent synaptic enhancement. *Cell Rep.* **34**, 108844 (2021).
156. Koenig, J. H., Saito, K. & Ikeda, K. Reversible control of synaptic transmission in a single gene mutant of Drosophila melanogaster. *J. Cell Biol.* **96**, 1517–1522 (1983).

157. Morin, X., Daneman, R., Zavortink, M. & Chia, W. A protein trap strategy to detect GFP-tagged proteins expressed from their endogenous loci in Drosophila. *Proc. Natl. Acad. Sci. U. S. A.* **98**, 15050–15055 (2001).
158. Yamamoto, M., Ueda, R., Takahashi, K., Saigo, K. & Uemura, T. Control of axonal sprouting and dendrite branching by the Nrg-Ank complex at the neuron-glia interface. *Curr. Biol. CB* **16**, 1678–1683 (2006).
159. Jiang, N., Soba, P., Parker, E., Kim, C. C. & Parrish, J. Z. The microRNA bantam regulates a developmental transition in epithelial cells that restricts sensory dendrite growth. *Dev. Camb. Engl.* **141**, 2657–2668 (2014).
160. Khuong, T. M. *et al.* Nerve injury drives a heightened state of vigilance and neuropathic sensitization in Drosophila. *Sci. Adv.* **5**, eaaw4099 (2019).
161. Bautista, D. M. *et al.* TRPA1 mediates the inflammatory actions of environmental irritants and proalgesic agents. *Cell* **124**, 1269–1282 (2006).
162. Zhong, L., Hwang, R. Y. & Tracey, W. D. Pickpocket is a DEG/ENaC protein required for mechanical nociception in Drosophila larvae. *Curr. Biol. CB* **20**, 429–434 (2010).
163. Kim, S. E., Coste, B., Chadha, A., Cook, B. & Patapoutian, A. The role of Drosophila Piezo in mechanical nociception. *Nature* **483**, 209–212 (2012).
164. Gorczyca, D. A. *et al.* Identification of Ppk26, a DEG/ENaC Channel Functioning with Ppk1 in a Mutually Dependent Manner to Guide Locomotion Behavior in Drosophila. *Cell Rep.* **9**, 1446–1458 (2014).
165. Guo, Y., Wang, Y., Wang, Q. & Wang, Z. The role of PPK26 in Drosophila larval mechanical nociception. *Cell Rep.* **9**, 1183–1190 (2014).
166. Mauthner, S. E. *et al.* Balboa binds to pickpocket in vivo and is required for mechanical nociception in Drosophila larvae. *Curr. Biol. CB* **24**, 2920–2925 (2014).
167. Kim, T.-J. *et al.* Distinct mechanisms regulating mechanical force-induced Ca^{2+} signals at the plasma membrane and the ER in human MSCs. *eLife* **4**, e04876 (2015).
168. Chachisvilis, M., Zhang, Y.-L. & Frangos, J. A. G protein-coupled receptors sense fluid shear stress in endothelial cells. *Proc. Natl. Acad. Sci. U. S. A.* **103**, 15463–15468 (2006).
169. Grosmaitre, X., Santarelli, L. C., Tan, J., Luo, M. & Ma, M. Dual functions of mammalian olfactory sensory neurons as odor detectors and mechanical sensors. *Nat. Neurosci.* **10**, 348–354 (2007).
170. Mederos y Schnitzler, M. *et al.* Gq-coupled receptors as mechanosensors mediating myogenic vasoconstriction. *EMBO J.* **27**, 3092–3103 (2008).
171. Connelly, T. *et al.* G protein-coupled odorant receptors underlie mechanosensitivity in mammalian olfactory sensory neurons. *Proc. Natl. Acad. Sci. U. S. A.* **112**, 590–595 (2015).
172. Xu, J. *et al.* GPR68 Senses Flow and Is Essential for Vascular Physiology. *Cell* **173**, 762-775.e16 (2018).
173. Venturini, V. *et al.* The nucleus measures shape changes for cellular proprioception to control dynamic cell behavior. *Science* **370**, eaba2644 (2020).
174. Aoki, K. *et al.* STIM-Orai1 signaling regulates fluidity of cytoplasm during membrane blebbing. *Nat. Commun.* **12**, 480 (2021).

175. Luik, R. M., Wang, B., Prakriya, M., Wu, M. M. & Lewis, R. S. Oligomerization of STIM1 couples ER calcium depletion to CRAC channel activation. *Nature* **454**, 538–542 (2008).
176. Chen, X. & Chalfie, M. Modulation of C. elegans touch sensitivity is integrated at multiple levels. *J. Neurosci. Off. J. Soc. Neurosci.* **34**, 6522–6536 (2014).
177. Hoffman, B. U. *et al.* Merkel Cells Activate Sensory Neural Pathways through Adrenergic Synapses. *Neuron* **100**, 1401-1413 6 (2018).
178. Lopez-Bellido, R. *et al.* Growth Factor Signaling Regulates Mechanical Nociception in Flies and Vertebrates. *J. Neurosci. Off. J. Soc. Neurosci.* **39**, 6012–6030 (2019).
179. Masuda, J., Tsuda, M., Tozaki-Saitoh, H. & Inoue, K. Intrathecal delivery of PDGF produces tactile allodynia through its receptors in spinal microglia. *Mol. Pain* **5**, 23 (2009).
180. Puig, S., Donica, C. L. & Gutstein, H. B. EGFR Signaling Causes Morphine Tolerance and Mechanical Sensitization in Rats. *eNeuro* **7**, ENEURO.0460-18.2020 (2020).
181. Xiang, Y. *et al.* Light-avoidance-mediating photoreceptors tile the Drosophila larval body wall. *Nature* **468**, 921–926 (2010).
182. Friard, O. & Gamba, M. BORIS: a free, versatile open-source event-logging software for video/audio coding and live observations. *Methods Ecol. Evol.* **7**, 1325–1330 (2016).
183. Feng, Y., Ueda, A. & Wu, C.-F. A modified minimal hemolymph-like solution, HL3.1, for physiological recordings at the neuromuscular junctions of normal and mutant Drosophila larvae. *J. Neurogenet.* **18**, 377–402 (2004).
184. Schneider, C. A., Rasband, W. S. & Eliceiri, K. W. NIH Image to ImageJ: 25 years of image analysis. *Nat. Methods* **9**, 671–675 (2012).
185. Williams, C. R., Baccarella, A., Parrish, J. Z. & Kim, C. C. Trimming of sequence reads alters RNA-Seq gene expression estimates. *BMC Bioinformatics* **17**, 103 (2016).
186. Picelli, S. *et al.* Full-length RNA-seq from single cells using Smart-seq2. *Nat. Protoc.* **9**, 171–181 (2014).
187. Ewels, P., Magnusson, M., Lundin, S. & Käller, M. MultiQC: summarize analysis results for multiple tools and samples in a single report. *Bioinforma. Oxf. Engl.* **32**, 3047–3048 (2016).
188. Bray, N. L., Pimentel, H., Melsted, P. & Pachter, L. Near-optimal probabilistic RNA-seq quantification. *Nat. Biotechnol.* **34**, 525–527 (2016).
189. Bliddal, S. *et al.* Acute and persistent symptoms in non-hospitalized PCR-confirmed COVID-19 patients. *Sci. Rep.* **11**, 13153 (2021).
190. Grant, M. C. *et al.* The prevalence of symptoms in 24,410 adults infected by the novel coronavirus (SARS-CoV-2; COVID-19): A systematic review and meta-analysis of 148 studies from 9 countries. *PloS One* **15**, (2020).
191. Finger, T. E., Jeor, V. L., Kinnamon, J. C. & Silver, W. L. Ultrastructure of substance P- and CGRP-immunoreactive nerve fibers in the nasal epithelium of rodents. *J. Comp. Neurol.* **294**, 293–305 (1990).
192. Pinho-Ribeiro, F. A., Verri, W. A. & Chiu, I. M. Nociceptor Sensory Neuron–Immune Interactions in Pain and Inflammation. *Trends Immunol.* **38**, 5–19 (2017).

193. Prescott, S. L. & Liberles, S. D. Internal senses of the vagus nerve. *Neuron* **110**, 579–599 (2022).
194. McFarland, A. J., Yousuf, M. S., Shiers, S. & Price, T. J. Neurobiology of SARS-CoV-2 interactions with the peripheral nervous system: implications for COVID-19 and pain. *Pain Rep.* **6**, (2021).
195. Patil, M. J. *et al.* Acute activation of bronchopulmonary vagal nociceptors by type I interferons. *J. Physiol.* **598**, 5541–5554 (2020).
196. Akira, S., Uematsu, S. & Takeuchi, O. Pathogen recognition and innate immunity. *Cell* **124**, 783–801 (2006).
197. Deng, L. *et al.* Staphylococcus aureus Drives Itch and Scratch-Induced Skin Damage Through a V8 Protease-PAR1 Axis. (2023) doi:10.2139/ssrn.4318823.
198. Gu, Q. & Lee, L.-Y. House dust mite potentiates capsaicin-evoked Ca2+ transients in mouse pulmonary sensory neurons via activation of protease-activated receptor-2. *Exp. Physiol.* **97**, 534–543 (2012).
199. Hassler, S. N. *et al.* The cellular basis of protease-activated receptor 2-evoked mechanical and affective pain. *JCI Insight* **5**, (2020).
200. Jimenez-Vargas, N. N. *et al.* Protease-activated receptor-2 in endosomes signals persistent pain of irritable bowel syndrome. *Proc. Natl. Acad. Sci. U. S. A.* **115**, 7438–7447 (2018).
201. Kwong, K., Nassenstein, C., Garavilla, L., Meeker, S. & Undem, B. J. Thrombin and trypsin directly activate vagal C-fibres in mouse lung via protease-activated receptor-1. *J. Physiol.* **588**, 1171–1177 (2010).
202. Liu, Q. *et al.* The distinct roles of two GPCRs, MrgprC11 and PAR2, in itch and hyperalgesia. *Sci. Signal.* **4**, (2011).
203. Perner, C. *et al.* Substance P Release by Sensory Neurons Triggers Dendritic Cell Migration and Initiates the Type-2 Immune Response to Allergens. *Immunity* **53**, 1063-1077 7 (2020).
204. Pradhananga, S., Tashtush, A. A., Allen-Vercoe, E., Petrof, E. O. & Lomax, A. E. Protease-dependent excitation of nodose ganglion neurons by commensal gut bacteria. *J. Physiol.* **598**, 2137–2151 (2020).
205. Reddy, V. B., Iuga, A. O., Shimada, S. G., LaMotte, R. H. & Lerner, E. A. Cowhage-evoked itch is mediated by a novel cysteine protease: a ligand of protease-activated receptors. *J. Neurosci. Off. J. Soc. Neurosci.* **28**, 4331–4335 (2008).
206. Serhan, N. *et al.* House dust mites activate nociceptor-mast cell clusters to drive type 2 skin inflammation. *Nat. Immunol.* **20**, 1435–1443 (2019).
207. Hartenian, E. *et al.* The molecular virology of Coronaviruses. *J. Biol. Chem.* (2020) doi:10.1074/jbc.REV120.013930.
208. Shin, D. *et al.* Papain-like protease regulates SARS-CoV-2 viral spread and innate immunity. *Nature* **587**, 657–662 (2020).
209. Liang, Q. *et al.* An electrochemical biosensor for SARS-CoV-2 detection via its papain-like cysteine protease and the protease inhibitor screening. *Chem. Eng. J.* (2023) doi:10.1016/j.cej.2022.139646.
210. Jimenez-Campos, A. G. *et al.* A cell-based Papain-like Protease (PLpro) activity assay for rapid detection of active SARS-CoV-2 infections and antivirals. *PloS One* **19**, (2024).

211. Baraniuk, J. N. & Kim, D. Nasonasal reflexes, the nasal cycle, and sneeze. *Curr. Allergy Asthma Rep.* **7**, 105–111 (2007).
212. Strassman, A. M. & Levy, D. Response properties of dural nociceptors in relation to headache. *J. Neurophysiol.* **95**, 1298–1306 (2006).
213. Canning, B. J. *et al.* Identification of the tracheal and laryngeal afferent neurones mediating cough in anaesthetized guinea-pigs: Identification of cough receptors. *J. Physiol.* **557**, 543–558 (2004).
214. Sun, H. *et al.* KCNQ/M-channels regulate mouse vagal bronchopulmonary C-fiber excitability and cough sensitivity. *JCI Insight* **4**, (2019).
215. Iwasaki, N. *et al.* Allergen endotoxins induce T-cell-dependent and non-IgE-mediated nasal hypersensitivity in mice. *J. Allergy Clin. Immunol.* **139**, 258-268 10 (2017).
216. Kayasuga, R., Sugimoto, Y., Watanabe, T. & Kamei, C. Histamine H1 receptors are involved in mouse nasal allergic responses: a demonstration with H1 receptor-deficient mice. *Int. Immunopharmacol.* **2**, 745–750 (2002).
217. Shan, H. *et al.* Development of potent and selective inhibitors targeting the papain-like protease of SARS-CoV-2. *Cell Chem. Biol.* **28**, 855-865 9 (2021).
218. Osipiuk, J. *et al.* Structure of papain-like protease from SARS-CoV-2 and its complexes with non-covalent inhibitors. *Nat. Commun.* **12**, 743 (2021).
219. Báez-Santos, Y. M., Mielech, A. M., Deng, X., Baker, S. & Mesecar, A. D. Catalytic function and substrate specificity of the papain-like protease domain of nsp3 from the Middle East respiratory syndrome coronavirus. *J. Virol.* **88**, 12511–12527 (2014).
220. Grace, M., Birrell, M. A., Dubuis, E., Maher, S. A. & Belvisi, M. G. Transient receptor potential channels mediate the tussive response to prostaglandin E2 and bradykinin. *Thorax* **67**, 891–900 (2012).
221. Wang, H. & Woolf, C. J. Pain TRPs. *Neuron* **46**, 9–12 (2005).
222. Caterina, M. J. *et al.* Impaired nociception and pain sensation in mice lacking the capsaicin receptor. *Science* **288**, 306–313 (2000).
223. Barbosa Bomfim, C. C. *et al.* CGRP inhibits SARS-CoV-2 infection of bronchial epithelial cells, and its pulmonary levels correlate with viral clearance in critical COVID-19 patients. *J. Virol.* **98**, (2024).
224. Flamier, A., Bisht, P., Richards, A., Tomasello, D. L. & Jaenisch, R. Human iPS cell-derived sensory neurons can be infected by SARS-CoV-2. (2023) doi:10.1016/j.isci.2023.107690.
225. Moayedi, Y. The cellular basis of mechanosensation in mammalian tongue. *Cell Rep* **42**, 112087 (2023).
226. Pachitariu, M. *et al.* Suite2p: beyond 10,000 neurons with standard two-photon microscopy. in *In bioRxiv* 061507 (2017). doi:10.1101/061507.
227. Wilson, S. R. *et al.* TRPA1 is required for histamine-independent, Mas-related G protein-coupled receptor-mediated itch. *Nat. Neurosci.* **14**, 595–602 (2011).
228. Chandrabalan, A. *et al.* Human osteoarthritis knee joint synovial fluids cleave and activate Proteinase-Activated Receptor (PAR) mediated signaling. *Sci. Rep.* **13**, (2023).

229. Chen, X., Zhang, B., Wang, T., Bonni, A. & Zhao, G. Robust principal component analysis for accurate outlier sample detection in RNA-Seq data. *BMC Bioinformatics* **21**, 269 (2020).
230. Usoskin, D. *et al.* Unbiased classification of sensory neuron types by large-scale single-cell RNA sequencing. *Nat. Neurosci.* **18**, 145–153 (2015).
231. Shimada, S. G. & LaMotte, R. H. Behavioral differentiation between itch and pain in mouse. *Pain* **139**, 681–687 (2008).
232. Chaplan, S. R., Bach, F. W., Pogrel, J. W., Chung, J. M. & Yaksh, T. L. Quantitative assessment of tactile allodynia in the rat paw. *J. Neurosci. Methods* **53**, 55–63 (1994).
233. Tsunozaki, M. *et al.* A “toothache tree” alkylamide inhibits Aδ mechanonociceptors to alleviate mechanical pain. *J. Physiol.* **591**, 3325–3340 (2013).
234. Dixon, W. J. The Up-and-Down Method for Small Samples. *J. Am. Stat. Assoc.* **60**, 967–978 (1965).
235. Hargreaves, K., Dubner, R., Brown, F., Flores, C. & Joris, J. A new and sensitive method for measuring thermal nociception in cutaneous hyperalgesia. *Pain* **32**, 77–88 (1988).
236. Wrapp, D. *et al.* Cryo-EM structure of the 2019-nCoV spike in the prefusion conformation. *Science* **367**, 1260–1263 (2020).
237. Walls, A. C. Structure, function, and antigenicity of the SARS-CoV-2 spike glycoprotein. *Cell* **183**, 1735 (2020).
238. Shang, J. *et al.* Structural basis of receptor recognition by SARS-CoV-2. *Nature* **581**, 221–224 (2020).
239. Zhang, L. Crystal structure of SARS-CoV-2 main protease provides a basis for design of improved α-ketoamide inhibitors. *Science* **368**, 409–412 (2020).
240. Yin, W. *et al.* Structural basis for inhibition of the RNA-dependent RNA polymerase from SARS-CoV-2 by remdesivir. *Science* **368**, 1499–1504 (2020).
241. Zhang, Y. & Kutateladze, T. G. Molecular structure analyses suggest strategies to therapeutically target SARS-CoV-2. *Nat Commun* **11**, 2920–2924 (2020).
242. Gordon, D. E. *et al.* A SARS-CoV-2 protein interaction map reveals targets for drug repurposing. *Nature* **583**, 459–468 (2020).
243. Zhong, X. *et al.* Amino terminus of the SARS coronavirus protein 3a elicits strong, potentially protective humoral responses in infected patients. *J. Gen. Virol.* **87**, 369–373 (2006).
244. Lu, B. *et al.* Humoral and Cellular Immune Responses Induced by 3a DNA Vaccines against Severe Acute Respiratory Syndrome (SARS) or SARS-Like Coronavirus in Mice. *Clin. Vaccine Immunol.* **16**, 73–77 (2009).
245. Andersen, K. G., Rambaut, A., Lipkin, W. I., Holmes, E. C. & Garry, R. F. The proximal origin of SARS-CoV-2. *Nat. Med.* **26**, 450–452 (2020).
246. Channappanavar, R., Fett, C., Zhao, J., Meyerholz, D. K. & Perlman, S. Virus-specific memory CD8 T cells provide substantial protection from lethal severe acute respiratory syndrome coronavirus infection. *J Virol* **88**, 11034–11044 (2014).
247. Wang, H. SARS-CoV-2 proteome microarray for mapping COVID-19 antibody interactions at amino acid resolution. *ACS Cent Sci* **6**, 2238–2249 (2020).

248. Ward, D. An integrated in silico immuno-genetic analytical platform provides insights into COVID-19 serological and vaccine targets. *Genome Med* **13**, 4–12 (2021).
249. Siu, K.-L. Severe acute respiratory syndrome coronavirus ORF3a protein activates the NLRP3 inflammasome by promoting TRAF3-dependent ubiquitination of ASC. *FASEB J* **33**, 8865–8877 (2019).
250. Chan, C.-M. The ion channel activity of the SARS-coronavirus 3a protein is linked to its pro-apoptotic function. *Int J Biochem Cell Biol* **41**, 2232–2239 (2009).
251. Yue, Y. SARS-coronavirus open reading frame-3a drives multimodal necrotic cell death. *Cell Death Dis* **9**, 904–915 (2018).
252. Ren, Y. The ORF3a protein of SARS-CoV-2 induces apoptosis in cells. *Cell Mol Immunol* **17**, 881–883 (2020).
253. Silvas, J. A. *et al.* Contribution of SARS-CoV-2 Accessory Proteins to Viral Pathogenicity in K18 Human ACE2 Transgenic Mice. *J. Virol.* **95**, 10.1128/jvi.00402-21 (2021).
254. Castaño-Rodriguez, C. *et al.* Role of Severe Acute Respiratory Syndrome Coronavirus Viroporins E, 3a, and 8a in Replication and Pathogenesis. *mBio* **9**, 10.1128/mbio.02325-17 (2018).
255. Lu, W. Severe acute respiratory syndrome-associated coronavirus 3a protein forms an ion channel and modulates virus release. *Proc Natl Acad Sci USA* **103**, 12540–12545 (2006).
256. Schwarz, S., Wang, K., Yu, W., Sun, B. & Schwarz, W. Emodin inhibits current through SARS-associated coronavirus 3a protein. *Antivir Res* **90**, 64–69 (2011).
257. *Electrophysiology of Unconventional Channels and Pores*. (Springer International Publishing, 2015).
258. Nieva, J. L., Madan, V. & Carrasco, L. Viroporins: structure and biological functions. *Nat Rev Microbiol* **10**, 563–574 (2012).
259. Scott, C. & Griffin, S. Viroporins: structure, function and potential as antiviral targets. *J Gen Virol* **96**, 2000–2027 (2015).
260. Nakane, T. Single-particle cryo-EM at atomic resolution. *Nature* **587**, 152–156 (2020).
261. Holm, L. & Sander, C. Dali: a network tool for protein structure comparison. *Trends Biochem Sci* **20**, 478–480 (1995).
262. Dang, S. *et al.* Cryo-EM structures of the TMEM16A calcium-activated chloride channel. *Nature* **552**, 426–429 (2017).
263. Paulino, C., Kalienkova, V., Lam, A. K. M., Neldner, Y. & Dutzler, R. Activation mechanism of the calcium-activated chloride channel TMEM16A revealed by cryo-EM. *Nature* **552**, 421–425 (2017).
264. Zhang, M. *et al.* Structure of the mechanosensitive OSCA channels. *Nat. Struct. Mol. Biol.* **25**, 850–858 (2018).
265. Jojoa-Cruz, S. *et al.* Cryo-EM structure of the mechanically activated ion channel OSCA1.2. *eLife* **7**, e41845 (2018).
266. Chung, M.-K., Güler, A. D. & Caterina, M. J. TRPV1 shows dynamic ionic selectivity during agonist stimulation. *Nat Neurosci* **11**, 555–564 (2008).

267. Banke, T. G., Chaplan, S. R. & Wickenden, A. D. Dynamic changes in the TRPA1 selectivity filter lead to progressive but reversible pore dilation. *Am J Physiol Cell Physiol* **298**, 1457–1468 (2010).
268. Xu, L., Tripathy, A., Pasek, D. A. & Meissner, G. Ruthenium red modifies the cardiac and skeletal muscle Ca2+ release channels (ryanodine receptors) by multiple mechanisms. *J Biol Chem* **274**, 32680–32691 (1999).
269. Choi, W., Clemente, N., Sun, W., Du, J. & Lu, W. The structures and gating mechanism of human calcium homeostasis modulator 2. *Nature* **576**, 163–167 (2019).
270. Pope, L., Lolicato, M. & Minor, D. L. Polynuclear ruthenium amines inhibit K2P channels via a 'finger in the dam' mechanism. *Cell Chem Biol* **27**, 511-524 4 (2020).
271. Xie, L.-H., John, S. A. & Weiss, J. N. Spermine block of the strong inward rectifier potassium channel Kir2.1: dual roles of surface charge screening and pore block. *J Gen Physiol* **120**, 53–66 (2002).
272. Suma, A., Granata, D., Thomson, A. S., Carnevale, V. & Rothberg, B. S. Polyamine blockade and binding energetics in the MthK potassium channel. *J Gen Physiol* **152**, 6726 (2020).
273. Surprenant, A., Rassendren, F., Kawashima, E., North, R. A. & Buell, G. The cytolytic P2Z receptor for extracellular ATP identified as a P2X receptor (P2X7. *Science* **272**, 735–738 (1996).
274. Karasawa, A., Michalski, K., Mikhelzon, P. & Kawate, T. The P2X7 receptor forms a dye-permeable pore independent of its intracellular domain but dependent on membrane lipid composition. *Elife* **6**, 3393 (2017).
275. Hadfield, J. Nextstrain: real-time tracking of pathogen evolution. *Bioinformatics* **34**, 4121–4123 (2018).
276. Müller, M. A. & Wang, K. Human Coronavirus NL63 Open Reading Frame 3 encodes a virion-incorporated N-glycosylated membrane protein. *Virol J* **7, 6**, 42 (2010).
277. Wang, K. PEDV ORF3 encodes an ion channel protein and regulates virus production. *FEBS Lett* **586**, 384–391 (2012).
278. Zhang, R. *et al.* The ORF4a protein of human coronavirus 229E functions as a viroporin that regulates viral production. *Biochim. Biophys. Acta BBA - Biomembr.* **1838**, 1088–1095 (2014).
279. Miao, G. *et al.* ORF3a of the COVID-19 virus SARS-CoV-2 blocks HOPS complex-mediated assembly of the SNARE complex required for autolysosome formation. *Dev. Cell* **56**, 427-442.e5 (2021).
280. Ghosh, S. *et al.* β-Coronaviruses Use Lysosomes for Egress Instead of the Biosynthetic Secretory Pathway. *Cell* **183**, 1520-1535.e14 (2020).
281. Zhao, J., Zhao, J. & Perlman, S. T Cell Responses Are Required for Protection from Clinical Disease and for Virus Clearance in Severe Acute Respiratory Syndrome Coronavirus-Infected Mice. *J. Virol.* **84**, 9318–9325 (2010).
282. Dietl, P., Haller, T. & Frick, M. Spatio-temporal aspects, pathways and actions of Ca2+ in surfactant secreting pulmonary alveolar type II pneumocytes. *Cell Calcium* **52**, 296–302 (2012).

283. del Mármol, J., Rietmeijer, R. A. & Brohawn, S. in *Potassium Channels: Methods and Protocols*.
284. Xu, T. ProLuCID: an improved SEQUEST-like algorithm with enhanced sensitivity and specificity. *J Proteom* **129**, 16–24 (2015).
285. Tabb, D. L., McDonald, W. H. & Yates, J. R. DTASelect and Contrast: tools for assembling and comparing protein identifications from shotgun proteomics. *J Proteome Res* **1**, 21–26 (2002).
286. Park, S. K., Venable, J. D., Xu, T. & Yates, J. R. A quantitative analysis software tool for mass spectrometry–based proteomics. *Nat Methods* **5**, 319–322 (2008).
287. McDonald, W. H. MS1, MS2, and SQT—three unified, compact, and easily parsed file formats for the storage of shotgun proteomic spectra and identifications. *Rapid Commun Mass Spectrom* **18**, 2162–2168 (2004).
288. Peng, J., Elias, J. E., Thoreen, C. C., Licklider, L. J. & Gygi, S. P. Evaluation of multidimensional chromatography coupled with tandem mass spectrometry (LC/LC–MS/MS) for large-scale protein analysis: the yeast proteome. *J Proteome Res* **2**, 43–50 (2003).
289. Schöneberg, J. ATP-dependent force generation and membrane scission by ESCRT-III and Vps4. *Science* **362**, 1423–1428 (2018).
290. Ritchie, T. K. Chapter 11—Reconstitution of membrane proteins in phospholipid bilayer nanodiscs. *Methods Enzym.* **464**, 211–231 (2009).
291. Mastronarde, D. N. Automated electron microscope tomography using robust prediction of specimen movements. *J Struct Biol* **152**, 36–51 (2005).
292. Guo, H. Electron-event representation data enable efficient cryoEM file storage with full preservation of spatial and temporal resolution. *IUCrJ* **7**, 860–869 (2020).
293. Zheng, S. Q. MotionCor2: anisotropic correction of beam-induced motion for improved cryo-electron microscopy. *Nat Methods* **14**, 331–332 (2017).
294. Zivanov, J., Nakane, T. & Scheres, S. H. W. A Bayesian approach to beam-induced motion correction in cryo-EM single-particle analysis. *IUCrJ* **6**, 5–17 (2019).
295. Zivanov, J. New tools for automated high-resolution cryo-EM structure determination in RELION-3. *Elife* **7**, 163 (2018).
296. Rohou, A. & Grigorieff, N. CTFFIND4: fast and accurate defocus estimation from electron micrographs. *J Struct Biol* **192**, 216–221 (2015).
297. Punjani, A., Rubinstein, J. L., Fleet, D. J. & Brubaker, M. A. cryoSPARC: algorithms for rapid unsupervised cryo-EM structure determination. *Nat Methods* **14**, 290–296 (2017).
298. Punjani, A., Zhang, H. & Fleet, D. J. Non-uniform refinement: adaptive regularization improves single-particle cryo-EM reconstruction. *Nat Methods* **17**, 1214–1221 (2020).
299. Asarnow, D., Palovcak, E. & Cheng, Y. doi:10.5281/zenodo.3576630.
300. Bepler, T. Positive-unlabeled convolutional neural networks for particle picking in cryo-electron micrographs. *Nat Methods* **16**, 1153–1160 (2019).
301. Stagg, S. M., Noble, A. J., Spilman, M. & Chapman, M. S. ResLog plots as an empirical metric of the quality of cryo-EM reconstructions. *J Struct Biol* **185**, 418–426 (2014).

302. Herzik, M. A., Wu, M. & Lander, G. C. High-resolution structure determination of sub-100kDa complexes using conventional cryo-EM. *Nat Commun* **10**, 1032–1039 (2019).
303. Emsley, P., Lohkamp, B., Scott, W. G. & Cowtan, K. Features and development of Coot. *Acta Crystallogr Biol Crystallogr* **66**, 486–501 (2010).
304. Liebschner, D. Macromolecular structure determination using X-rays, neutrons and electrons: recent developments in Phenix. *Acta Crystallogr Struct Biol* **75**, 861–877 (2019).
305. Williams, C. J. MolProbity: more and better reference data for improved all-atom structure validation. *Protein Sci* **27**, 293–315 (2018).
306. Terwilliger, T. C., Ludtke, S. J., Read, R. J., Adams, P. D. & Afonine, P. V. Improvement of cryo-EM maps by density modification. *Nat Methods* **17**, 923–927 (2020).
307. Pettersen, E. F. UCSF Chimera—a visualization system for exploratory research and analysis. *J Comput Chem* **25**, 1605–1612 (2004).
308. Smart, O. S., Neduvelil, J. G., Wang, X., Wallace, B. A. & Sansom, M. S. HOLE: a program for the analysis of the pore dimensions of ion channel structural models. *J Mol Graph* **14**, 354–360 (1996).
309. Kelley, L. A., Mezulis, S., Yates, C. M., Wass, M. N. & Sternberg, M. J. E. The Phyre2 web portal for protein modeling, prediction and analysis. *Nat Protoc* **10**, 845–858 (2015).
310. Goddard, T. D. UCSF ChimeraX: meeting modern challenges in visualization and analysis. *Protein Sci* **27**, 14–25 (2018).

Appendix

The following poems were written alongside, and often in response to, the research in this dissertation. In that sense, perhaps, they are a form of research themselves: a way to understand what it means to become a scientist.

They seek not to describe biology, but to inhabit its curiosities and explore its challenges and contradictions. But most of all, they strive to be, in the words of a dear friend, *respectably ridiculous*.

Ethogram of a Rub

"There are so many ridiculous ways to articulate the mouse rubbing and then you talk about neutrophils and you're respectable again." – P. Parikh

I. The Nose Rub

so much depends
upon

a hundred-millisecond nose
rub

an ellipse of the front paw

in between a sneeze
and a wipe

II. An Ontological Crisis

What is a rub?
Is it a sign of irritation?
A grooming behavior?
Is it wiping one's nose after a sneeze?
Is it wiping away the runny from the nose?
Can you even distinguish a *rub* from a "rub", from grooming?
Does a rub ~mean~ anything?
If a mouse rubs all the time[1], is a rub still significant?
And if a mouse is always rubbing,
what if it doesn't rub?

[1]See Chapter III, Supplemental Figures 3 and 4.

III. The rose is red for the first time in English poetry for a hundred years

A Rub is a rub is a rub is rub is a
A rub is not a wipe, or maybe it is that type.

And that is all it is– a rub.
And yet, there is a rub.

I am not a neuroscientist

What do you want to be?
A neuroscientist?
A physiologist?
A venture capitalist?
Or, perhaps a card-carrying immunologist?

Can I just be me?

Je n'avais rien appris à dessiner, sauf les boas fermés et les boas ouverts.[1]

The presumptuousness of such a question.
How can you ask me to define myself,
as a scientist nonetheless,
when I am plagued
with the proclivities of a poet.

If a physiologist seeks to understand how we feel,
a poet seeks that we feel,
that I feel,
that you feel.
When a neuroscientist explains how we see and hear,
a poet reports
that which we do not see and hear.

Is there space, in the confines of this discipline,
for a poet masquerading as a scientist?
The scientist asks how,
a poet asks why.
and I–
what happens if we try?

Do you call yourself a neuroimmunologist?

What I want to say is:
I go by Sonali
and I like to ask questions.

Oh, a sensory neurobiologist. Well, soon you can be a microbiologist too.

As though the right title
will help them place me
here or there,
or away to the left.

[1] *"I had never learned to draw anything, except boa constrictors from the outside and boa constrictors from the inside."* From *Le Petit Prince* by Antoine de Saint-Exupéry.

D.E.I., you proclaim.
What if I want to be a lizard named kitty,
or a boa constrictor eating an elephant?
Or does your equity mean something else–
where we all get our chance
to pick the word that walls our curiosity.
Diversity is welcome
so long as it can be included
in our taxonomy.

Are you the kind of sensory biologist
that studies interoception or exteroception?
Depends.
Is your nose inside or outside your body?
And anyway, does it matter if I think my nose is outside
and you yours inside?
And what of the viruses that are outside the body
and then inside our cells
and then outside again,
as though the virus is on our side at all.

Who gets to decide, anyway, what is inside and outside,
that side or this side,
when only boxes have sides.

«J'ai besoin d'un mouton. Dessine-moi un mouton.»
Alors, faute de patience, comme j'avais hâte de commencer le démontage de mon moteur, je griffonnai ce dessin-ci.
Et je lançai,
«Ça c'est la caisse. Le mouton que tu veux est dedans.»[2]

Should we poke holes so she can breathe?
Let her imagine that too.

So I shaved the sides of the box,
until it was round.

Will pivot from Neuroscience to Immunology.
Will pivot from feeling the winds of the Pacific to those of the Atlantic.
Will pivot from this side of the bed to that.
Will pivot from thinking about lunch at the sun's position defined as Greenwich Mean Time 19:00 to 16:00.

[2] *"I need a sheep. Draw me a sheep."*
So, lacking patience and eager to begin dismantling my engine, I scribbled this drawing.
And I said,
"This is the box. The sheep you want is inside."
From *Le Petit Prince* by Antoine de Saint-Exupéry.

Will pivot from old ideas to new ideas,
and back to old.
Will pivot from yesterday to tomorrow.
Will pivot until the world is spinning,
and it's all part of the same blur.

What if, instead,
we named not what we are,
but where we are looking–
not knowing whether we'll find
the clouds, the sun, the mountains, the earth,
the ocean,
or where they meet to
forget what they were
and become something else.

What do you want to be?
I want to be.

I want to be free.

Aerosolized Capsaicin

(for Ba)

You said,
I only cough a little
when my mother makes salsa,
so this must be less.

(Equivalent to about two seeds of a jalapeño, in case you wondered).

But I tried to say,
your mother's chili is not like this chili.

They screened pools on pools
just to find,
that one receptor for pain and heat and chili.

Tell me what screen will you design
to find
the sole receptor
for all the things your mother's chili binds.

Somewhere you'll discover another sweet receptor,
a warmth transducer,
a channel for tenderness
a catalyst for grief,
the mechanism that yields life.

Maybe there is
a labeled line
along the hand-brain axis
for temperature coding.

But along what axis does my nostalgia encode the way
my grandmother's chili warmed my soul, while sweet in my stomach?

Maybe instead, there is a temporal code where
I hear the last whistle of the pressure cooker,
just before the smell reaches me–
and no later–
her voice saying,
ready.

How is it that in the lab, chili stings
but her chili soothed the ache

and only in its absence,
causes pain?

But like that chili,
the affinity for mine
was so high,
I never thought to measure.

An affinity assumed.
A dissociation constant
I now feel.

Low Hanging Fruit(s)

"Mrs. Walker brought a persimmon to class
and cut it up
so everyone could taste
a Chinese apple. Knowing
it wasn't ripe or sweet, I didn't eat
but watched the other faces.

My mother said every persimmon has a sun
inside, something golden, glowing,
warm as my face."

–Li-Young Lee, *Persimmons*

I

bright and yellow with a hint of green no bruises in sight, firm to the touch and even to a good squeeze, you'll have to yank to split it open, but then it'll separate with ease, no strings attached, flesh and peel distinct and then you bite into it, a little tart, though some palatable sweetness, but mostly, it tastes like nothing but tough organic mush. but then there's the one forgotten about until you're swatting fruit flies away from your coffee and you can smell the pungent sweetness of the fruit cloaked in darkness, it's like if a ripe banana was a chocolate chip cookie this is a double chocolate chip cookie burnt to a crisp, so do you dare pick it up, lest its sticky extract coats your fingers never to be washed off, alas when you do find the courage to pick it up, some semblance of an outer skin peels off, flesh and skin still indistinguishable, but curiosity tickles and you take a bite, just a small one and it gives way to your teeth, sinking in the way your toes sink into the sand at the beach, and the mush crawls around your gums but then you wonder how anything could be sweeter than sugar until it's sliding down your throat and you try not to gag.

II

If you offer a child
an orange that is neither sweet nor sour,
one that is just a little too firm,
he'll drop all of his perfectly crisp apple slices, even the one from his mouth,
to reach for your slice of orange.

He'll eagerly bite in,
and then he'll look at you.
You've taken his apples,
and he's left with your orange.

You offer another.
He'll hesitate, but even he knows
two slices of
an orange that is neither sweet nor sour,
one that is just a little too firm,
is better than one.

III

have you ever chased
after that huge ball of light
do it, I dare you

when you think you're close
your wings of wax no more, you'll
have hit the ground, hard

stand up, I dare you
the bones will heal and then you'll
do it all again

more bruised each time like
a red delicious, once sweet,
mushed, but still with shine

IV

Reach for the low hanging fruit, they said.
So you learned rocket science.

But you had doubts. Was this even a fruit tree? What's the right season? Have the squirrels taken all the fruit? How high can you reach before it's no longer low hanging? Still, you keep reaching anyway. Low hanging if you're tall, I guess.

And when you finally taste the fruits of your labor, expecting sweet and satisfying, you get grit grinding between your teeth and a saltiness that coats your tongue,
and somehow,
all you want is more.

Because you have tasted the moon.
And now there's a fire in you
no fruit could ever satisfy.

Outstanding

If you were to ask me if I'd like to take a seat at the table,
I think I'd say,
No thank you.
I prefer to be out,
standing.